Optical Properties of the Square Superlattice Photonic Crystal Structure and Optical Invisibility Cloaking

A Thesis
Presented to
The Academic Faculty

by

John L. Blair

In Partial Fulfillment
of the Requirements for the Degree of
Doctor of Philosophy in the
School of Material Science Engineering

Georgia Institute of Technology
December 2010

Optical Properties of the Square Superlattice Photonic Crystal Structure and Optical Invisibility Cloaking

Approved by:

Dr. Christopher J. Summers, Advisor
School of Materials Science and Engineering
Georgia Institute of Technology

Dr. W. Brent Carter
School of Materials Science and Engineering
Georgia Institute of Technology

Dr. Rosario Gerhardt
School of Materials Science and Engineering
Georgia Institute of Technology

Dr. Wounjhang Park
Department of Electrical and Computer Engineering
University of Colorado at Boulder

Dr. Brent K. Wagner
Electro-Optical Systems Laboratory
Georgia Tech Research Institute

Date Approved: August 23, 2010

DEDICATION

Dedicated to my husband, Michael J. Lowery, who managed to keep me sane through this trying and expensive process, in spite of the innumerable setbacks and dramas that occurred during the process of its completion.

ACKNOWLEDGEMENTS

Foremost I would like to thank Dr. Chris Summers. When I felt that everyone else on the planet had given up on me (including myself), he provided encouragement, motivation, and latitude which made this work successful. I would also like to thank Dr. Won Park for the opportunity to participate in exciting research, and for all his help with numerical simulations and presentations. Additional thanks go to Devin Brown and the cleanroom staff at GT that helped support my nano-fabrication work. Lastly, I am thankful for all the support I received from family and friends during this process. Everyone was rooting for me to complete my thesis, and it was valuable to have the extra kindness when I ran into difficulties.

Table of Contents

List of Tables

List of Figures

Summary

Two-dimensional (2D) and three dimensional (3D) photonic crystal (PC) structures are becoming increasingly important for creating the next generation of optical telecommunications and computing devices. Photonic crystals are periodic structures which are found in nature, and which can also be recreated through various material science growth and fabrication processes. The optical performance of photonic crystals is typically controlled by manipulation of the photonic band structure of the devices. The photonic band structure can be used to control the refraction, collimation, dispersion, and many other optical performance parameters. Operation of PC devices at visible or infrared-red communications wavelengths of 1.3um or 1.55um is desirable for their use in industry and military applications.

The first part of this research investigates the optical properties and design of a square superlattice photonic crystal. Previous research in our group has involved a variation of this structure known as a triangular superlattice, and showed that this structure has novel refraction properties due to the folding of bands. This work builds on that research by investigating a square lattice variation of that structure to determine its optical properties and performance. Also, the properties resulting from both static tuning using atomic-layer deposition (ALD) and active tuning of these structures have been investigated and their application to novel devices is presented.

The second part of this research details the design and development of a new optical invisibility cloaking structure. The cloak is a metamaterial ground-plane structure that enables light incident on a raised bump or feature to be reflected as if the area was a flat surface, rendering objects placed behind the bump invisible to incoming light. This is

one of the first demonstrations of cloaking behavior at optical frequencies, as opposed to previous work done primarily in the microwave regime. The investigation consists of design, fabrication, and characterization of the several variants of the structure to determine its optical properties and performance. Also, the ALD technique of static tuning will be applied to the cloaking structure and the changes in performance will be examined in detail.

1 INTRODUCTION TO PHOTONIC CRYSTALS

1.1 Photonic Crystals Defined

Photonic crystals are the optical analogy of an electronic crystal lattice. A crystalline lattice consists of a set of small basic building blocks of atoms or molecules that are repeated in space. The crystal structure presents a periodic potential to an electron propagating through it, and the conduction properties of the crystal are therefore dependent upon the geometry. In general, the lattice introduces bandgaps into the energy structure of the crystal. Due to Bragg-like diffraction from planes of atoms, electrons are forbidden to propagate within certain energy ranges in particular directions. For a lattice potential that is strong enough, the gap may extend in all possible directions, resulting in a complete three-dimensional band gap. An example of this is a semiconductor, which has a complete band gap between the valence and conduction bands. In a photonic crystal the periodic "potential" is due to a periodic repetition of macroscopic dielectric media of different dielectric constants instead of atoms. If the dielectric constants are sufficiently different to provide a strong contrast (a refractive dielectric contrast of at least two for 2D structures and three or greater for 3D structures), and there are minimal losses in the material, the scattering at the interfaces can produce many of the same phenomena for photons (or light modes) as the atomic potential does for electrons. Thus, if it is possible to design and construct photonic crystals with specific photonic band gaps (PBGs), it is possible to control and manipulate light by preventing it from propagating in certain directions at specified energies. A photonic crystal that prevents light modes from

propagating at a particular frequency for any polarization or angle is said to have a complete photonic band gap (PBG).

1.2 History of Photonic Crystals

Photonic crystal structures were first introduced in 1987 by the work of Yablonovitch and John [1-2]. They proposed the possibility of photon confinement and light emission suppression by using an optical material whose dielectric constant was periodically modulated in three-dimensions. In 1990, Ho et al. [3] theoretically predicted a structure that would have a full PBG. This structure consisted of a diamond lattice of dielectric spheres in an air background that could also be inverted. In 1991 Yablonovitch et al. [4] reported that a full PBG could also be formed in a face-centered cubic (fcc) lattice. The structure was created by drilling dielectrics to form a three-dimensional lattice called "Yablonovite", which exhibited a full PBG at microwave frequencies. They also introduced a technique to perform band calculation on these structures by a method known as the "supercell method" [5]. Shortly after Pendry et al. [6] in 1992 developed a transfer matrix method that used a combination of finite element analysis and multilayer analysis to analyze the transmission characteristics in PCs.

In the early 1990's it was very difficult to produce nano-periodic structures operating at optical frequencies due to the limits of fabrication and computing technology. The field began to grow with the discovery of new PBG structures and progress in computational modeling techniques. Also, improvements in fabrication technologies helped to overcoming the challenges of developing crystals that could operate at optical frequencies. Another area of research that furthered discoveries in the

field was the study of metal photonic crystal structures that could operate in the microwave range. It was not until 1998 and later that the field began to mature, due primarily to progress in the semiconductor industry and improvements in nanotechnology.

Many different 2D and 3D synthetic PC structures are now being investigated with the expectation that practical optical devices will be developed from the research. Some of the most promising 2D structures are the 2D slab (due to ease of fabrication using standard cleanroom materials and processes) and the PC-cladded fiber (one of the first practical industrial applications of 2D PCs). The first demonstrated 2D slab structures consisted of a thin film semiconductor hole structure sandwiched between materials with a low refractive index to obtain confinement of laser light [7-8]. Other demonstrations of 2D PC slab devices are line defect waveguides [9-10] and a point-defect coupled cavity waveguide [11] shown in Figure 1-1.

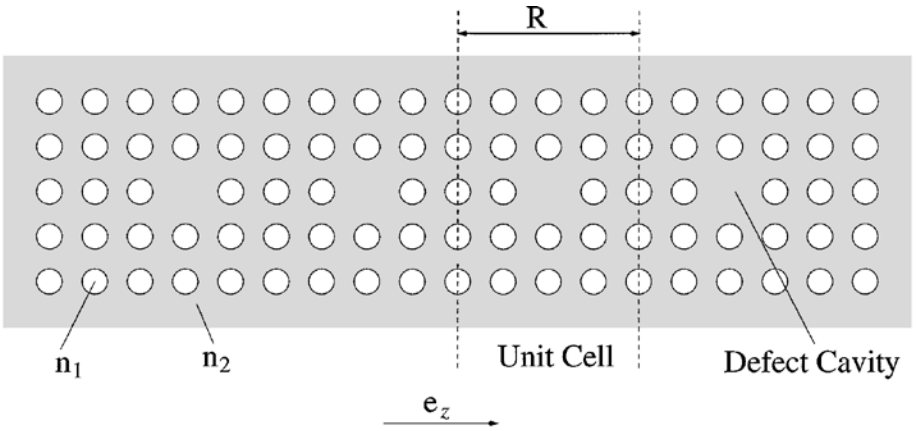

Figure 1-1: Coupled-resonator structure realized by coupling individual defect cavities together in a 2D photonic crystal [11].

The PC optical fiber waveguide structure was recently created to use PBG properties to help confine light to a silica core, instead of only relying on total internal reflection

confinement [12-13]. These fibers are able to achieve single-mode propagation over an extremely wide wavelength range, with a small spot size and large structural dispersion. Current manufactured fibers are exhibiting losses on the order of <1dB/km, competitive with that of standard optical fibers. An example of a PC fiber is shown in Figure 1-2.

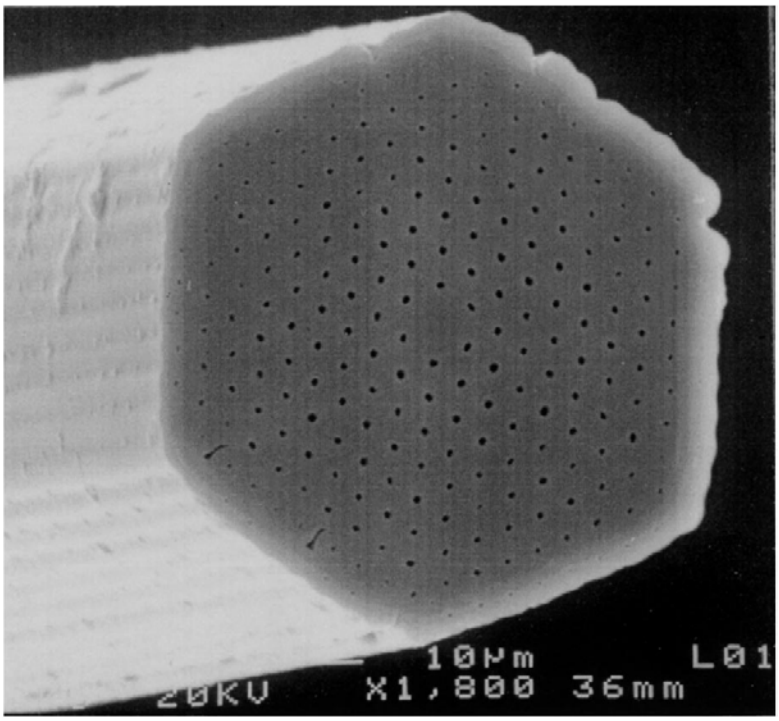

Figure 1-2: Scanning electron microscope image of the end of a photonic crystal fiber, showing the central core where a hole has been omitted. The pitch L is 2.3 mm, and the fiber is 40 mm across [12].

3D PCs have yet to find an industrial application and are very demanding to fabricate. However, structures such as the opal / inverse opal, spiral / chiral, and FCC-holographic are showing promise. Opal crystals have been under investigation for a relatively long time by many groups [14-18], and are inverted [19] by infiltration of high refractive index material into an opal structure, which enabled a full PBG to be obtained more consistently and at lower refractive index values. An inverted opal structure is shown in Figure 1-3. The exposure of polymer PCs to scanning lasers enabled the first holographic

PCs to be developed [20-22]. The chiral 3D PCs shown in Figure 1-4 consist of a periodic array of square spiral posts in a tetragonal lattice and have been demonstrated to provide a large, full 3D PBG [23]. The PBG performance of all of these 3D PCs is strongly dependent upon the structural dielectric index contrast.

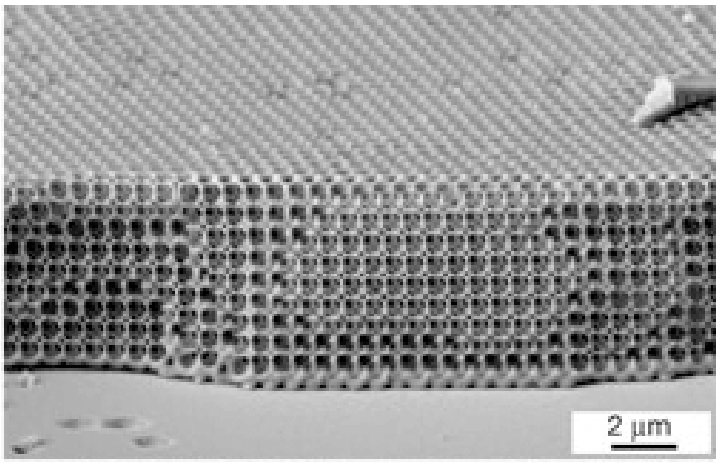

Figure 1-3: Inverse opal structure showing the (100) sample edge, revealing the structure to be f.c.c. [16].

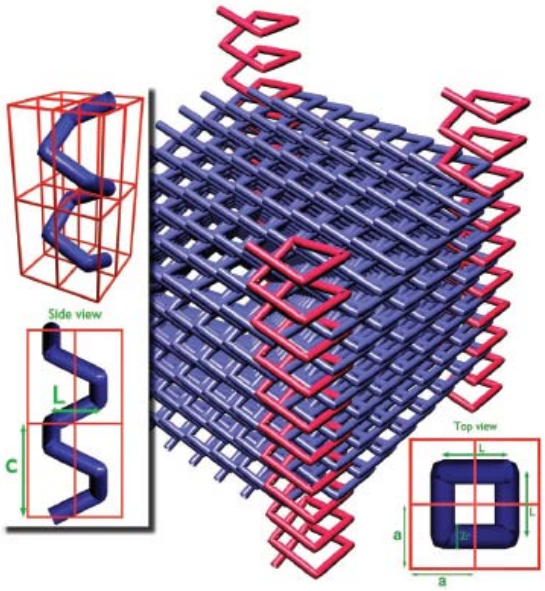

Figure 1-4: Example of a square chiral photonic crystal structure created by the glancing-angle deposition method [23].

Another emerging area of PC research involves novel biologically-inspired structures. The PC nature of butterfly scales as shown in Figure 1-5 have been

researched by a number of groups [24-27], with findings indicating that the reflective colors in some butterfly wings are due to 2D and 3D PBG effects. The iridescence observed from beetles [28] and dragonfly wings [29] have also been found to have a PC explanation. Natural PC structures have also been found in diatoms [30], bird feathers [26], flowers [31-32], insect eyes [33], jellyfish [34], and even teeth [35]. The thrust of much of the current work is to determine how these structures are able to exhibit the properties of photonic crystals, and how similar structures can be created and simulated. Another approach to analysis of these natural PCs could be through an organic to inorganic material replication of the structure, followed by characterization. Replication of natural PC structures thorough ALD will be another focus of the proposed research.

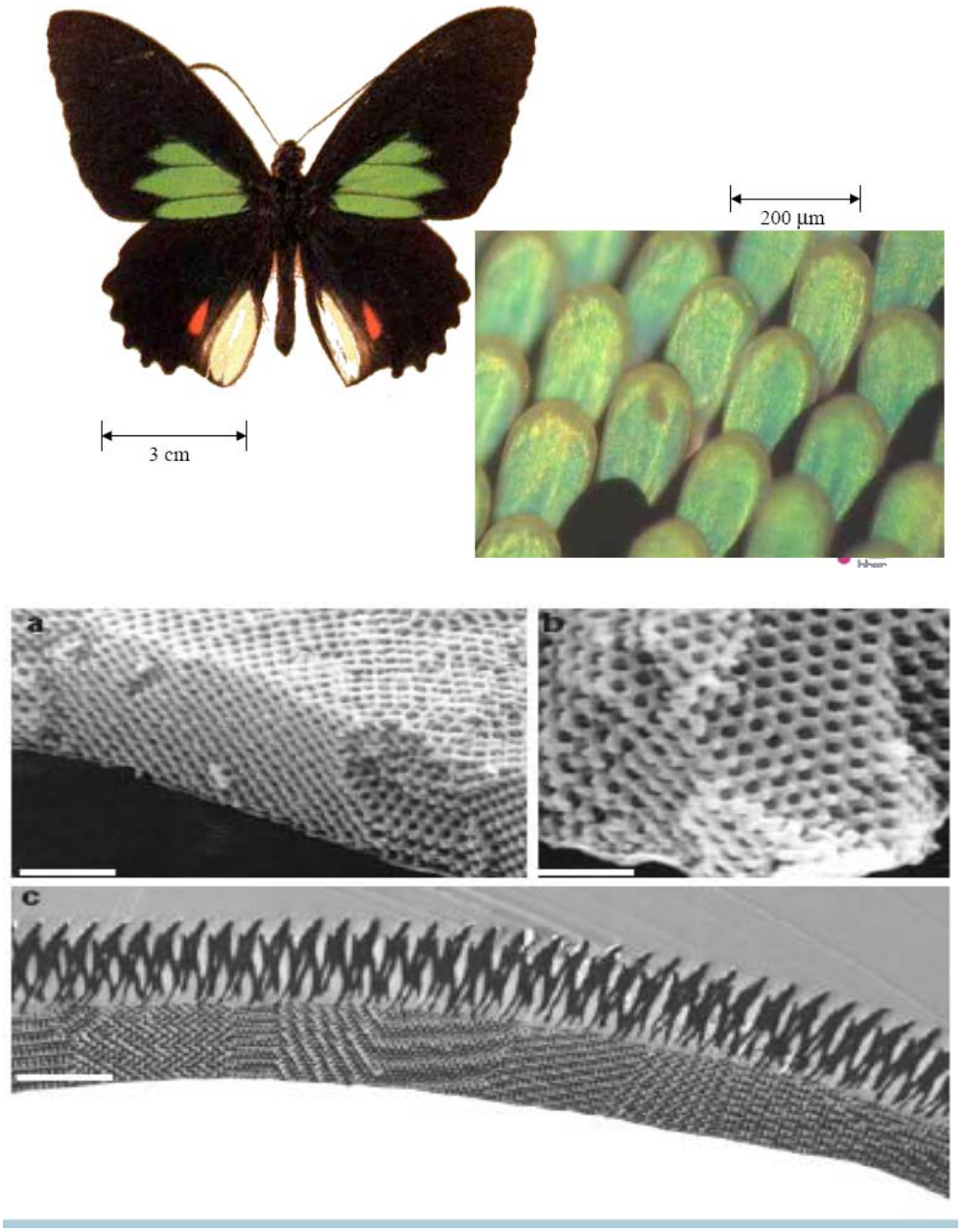

Figure 1-5: The green colour of Parides sesostris butterfly is created by a photonic crystal. a, b, **SEMs of the exposed photonic crystal after the superficial ridging has been removed.** c, **a TEM showing a 50 nm section through the scale shown in** a; **the ridging is intact whereas the neighbouring but differently oriented domains of identical 3D structure are distinguished by contrasting 2D patterns (here, the darkly contrasted material is cuticle) [27].**

1.3 Properties of Interest in Photonic Crystals

In order to fully understand and describe the properties of photonic crystals, we use and combine the principles of solid state physics and electromagnetics to characterize the structures. The dispersion relation of a radiation field:

$$\omega = ck \tag{1}$$

relates the relationship between the angular frequency ω, the speed of light c, and the wave number k:

$$k = \frac{2\pi}{\lambda_0} \tag{2}$$

where λ_0 is the free space wavelength. If the radiation field is in a uniform material with refractive index n, the dispersion relation in the material can be obtained by replacing c with an expression for the velocity of light in the material v:

$$v = \frac{c}{n} \tag{3}$$

and the free space wavelength λ_0 by the wavelength in the material:

$$\lambda = \frac{\lambda_0}{n} \tag{4}$$

In a photonic band-gap material that has periodic dielectric modulation in one to three dimensions, we can calculate which radiation modes exist in the material, per frequency range in k-space for a given polarization. The density of states (DOS) gives this information by relating the group velocity of a wave packet dω/dk (that can be obtained from the dispersion relation) to the allowed modes. For a given polarization the DOS is given by based on Equations (2)-(4):

$$D(\omega) = \frac{Vk^2}{2\pi^2}\frac{dk}{d\omega} = \frac{V\omega^2}{2\pi^2 v^3} \quad (5)$$

The key property of photonic crystals is that the DOS can be exploited to control the modes allowed to propagate in the material structure. In certain cases the structure can be designed so the DOS goes to zero for a range of photon energies and polarization. This phenomenon gives rise to the PBG where specific modes are not allowed to propagate throughout the structure.

The optical properties of a PC can be characterized by a photonic band diagram, analogous to the electronic band structure used to characterize the electrical and optical properties of a semiconductor. The band structure is typically plotted as the normalized allowed photon frequencies, $\omega_{n,}$ vs. the photon wave vector, k. The band structure calculations are an eigenvalue problem that consists of solving the macroscopic Maxwell's equations in a PC periodic dielectric medium. Symmetries within the structure allow the problem to be reduced to a smaller computational area called the Brillouin zone (BZ). We can confine characterization directions along the boundaries of the irreducible Brillouin zone. The complexity of the BZ is dependent upon the symmetries inherent in the periodic unit cell structure. For 3D PCs the light can be confined without regard to polarization conditions if a PBG is created at the same frequency range in all directions. Thus, the focus of the study on 3D PCs is on the creation and manipulation of 3D PBGs. The third dimension adds considerable complexity, however. For 2D PCs, the lack of a third dimension allows only transverse-electric (TE) and transverse-magnetic (TM) modes to couple into the structure. These two polarizations result in two groups of eigenmode solutions to the eigenvalue problem. Since the modes are now polarization dependent, it becomes more difficult to obtain a

PBG in the same frequency range due to the overlapping of modes. Hence 2D PC structures are not exploited for their PBG properties, but they can have many novel properties of interest such as superprism and supercollimation effects, which are easier to manipulate than in 3D PCs. A schematic of these phenomena is shown in Figure 1-6, comparing the properties of a random dielectric configuration to an ordered PC dielectric configuration.

Removing the third propagation direction allows simplification of the band structure and analysis. In a 2D PC the dispersion surfaces (analogous to Fermi surfaces in electronic crystals) can be represented by a plot of the in-plane k vector vs. the normalized frequency $\omega = a/\lambda$. Also, 2D PCs reduce the complexity of the numerical simulation requirements by shrinking the size of the unit cell and from the application of the periodic Bloch conditions.

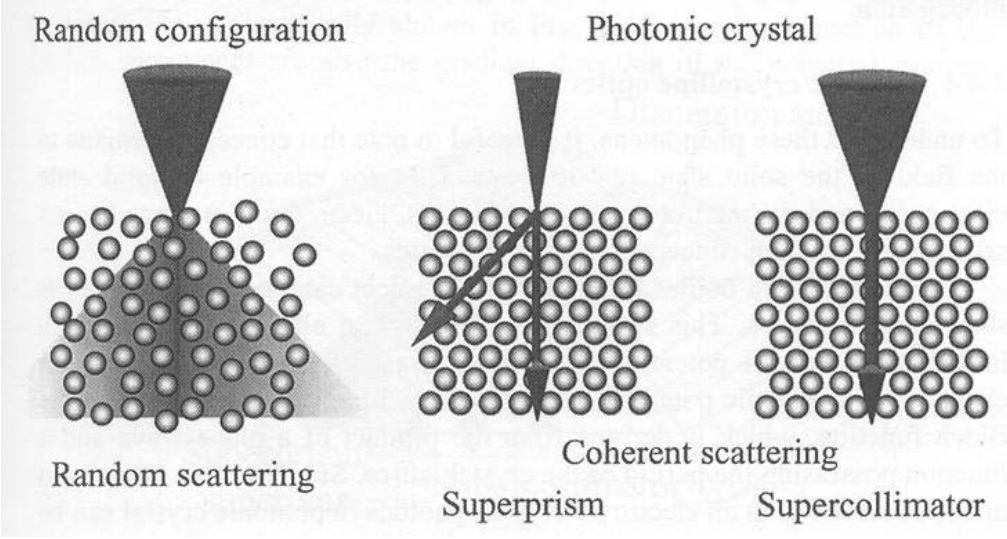

Figure 1-6: A comparison of ordinary (incoherent) scattering and (coherent) scattering in photonic crystals [36].

An example of a photonic crystal structure illustrating the above concepts is a 2D square lattice of dielectric pillars in an air medium. This structure illustrates the basic

concepts of the density of states and the photonic band gap. In real-space the square lattice structure is defined by the lattice constant a (spacing between holes), the hole radius r_a, and the dielectric constants of the holes ε_a (Si) and surrounding medium ε_b (air) as shown in Figure 1-7(a). A conversion to reciprocal space reveals the first irreducible Brillouin zone shown in Figure 1-7(b). The band structure for the TE polarization is shown in Figure 1-8, along with the calculated density of states. Note that although the structure shows three bandgaps, they are not complete gaps since TE eigenmodes and those modes with off-plane wave vectors have eigenfrequencies inside these gaps.

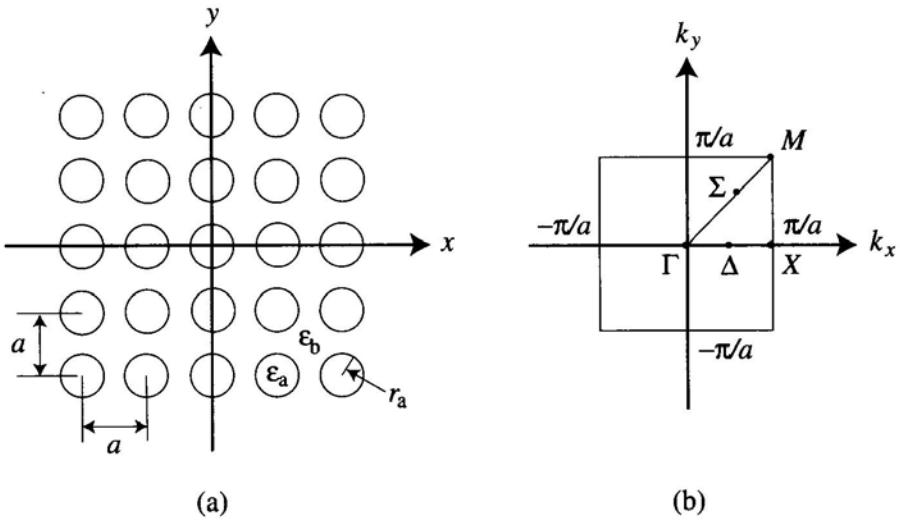

Figure 1-7: (a) 2D square PC lattice geometry, (b) first Brillouin zone of the square lattice [37].

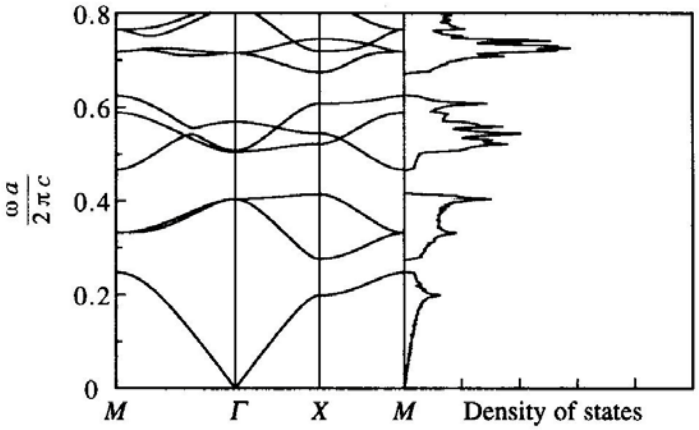

Figure 1-8: TE band structure and DOS for the square lattice PC [37].

1.3.1 Giant Refraction (Superprism Effect)

2D PCs exhibit novel properties due to their non-spherical wave vector contours (a.k.a. equi-frequency contours or dispersion surfaces). This representation is obtained by taking the surface contour of one band in k-space and slicing it to create equal frequency curves. The allowed propagating wave vector can be determined by drawing a vector perpendicular to the interface that intersects the allowed wave vector curve in the material. In an isotropic material, the equi-frequency contours are circular or elliptical, leading to normal refractive behavior. In PCs, the periodic dielectric structure leads to contours that have a varying curvature. One example of the effect of contour curvature is the ability of PCs to produce negative refraction and giant refraction (also called superprism) effects on light entering the crystal structure. An illustration of this effect is shown in Figure 1-9. As an example consider refraction from a prism of glass. In an ordinary prism 0.1º of the dispersion angle corresponds to a 1% difference in wavelength. Contrast this to a PC, where it is possible to obtain greater than 50º of dispersion angle for the same 1% difference in wavelength, an increase of 500 times that of the prism. The effect is that the angular deviation of light in a PC is large for small changes in incident angle. This phenomenon is called the superprism effect. Figure 1-10 shows a typical dispersion curve for a PC, and illustrates the effect. For the smaller incident angle in (b), a larger reflection angle of the refracted light is obtained compared to figure (a), all due to the shape of the dispersion curve.

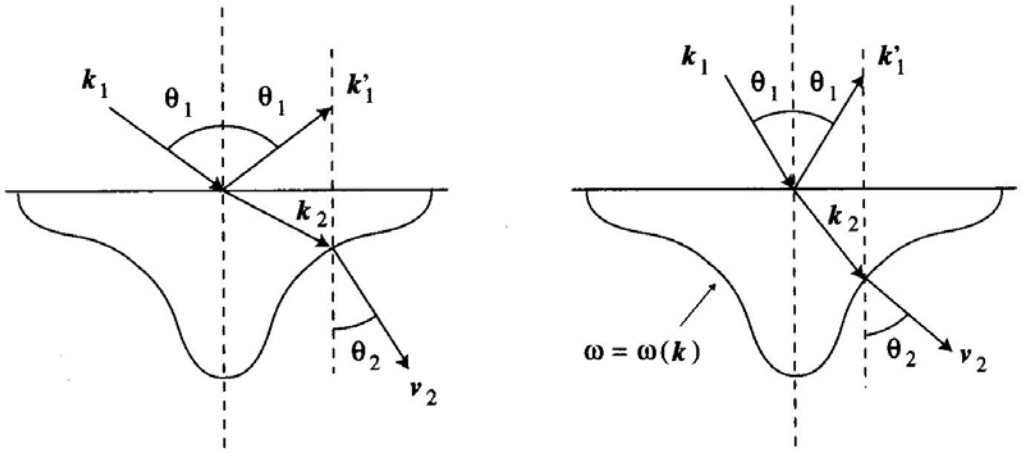

Figure 1-9: Schematic illustration of refraction at the surface of a photonic crystal [37].

1.3.2 Supercollimation Effects

If the incident angle in Figure 1-9 is positioned for a PC dispersion contour with a particular curvature, the beam can be made to self-collimate as if the material is acting as a lens. Depending on the shape of the equi-energy surfaces, the PC can act as a convex (focus), flat (self-collimation) or concave (defocus) lens. Light propagation in a supercollimator has similar characteristics to the confinement of light in fiber optics. The propagation direction can be maintained even under conditions of changing positions and incident angles by several degrees. Such an ideal fiber-like light collimator cannot occur in ordinary linear crystals where nonlinearity effects like self-focusing are not produced.

Supercollimation and focusing effects can be illustrated by the equi-frequency contours for the first band in the square lattice of pillars PC structure in Figure 1-10. Near the center the frequency is the lowest, corresponding to wavelengths of light that are much larger than the periodicity of the lattice. In this regime, the wave sees an average dielectric constant, and the allowed wave vector is circular as in an isotropic material. As the wave vector reaches a value that is near the edge of the BZ along the $\Gamma - M$ direction

in reciprocal space, the shape gradually changes from a circle to a shape resembling a square. Near the top of the first band, near the M point, the allowed wave vector shifts once again towards a circle, but now the center is located on the M point rather than on the Γ point. That is, there is a reverse in the curvature near the M point. The dispersion contour at the M point now acts like a convex lens, and can be used to produce negative index and supercollimation effects.

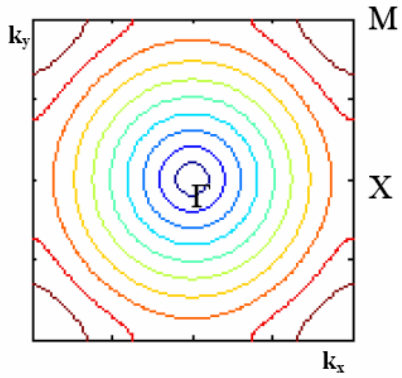

Figure 1-10: Allowed wave vector contours for the first band of the square lattice of pillars PC [38].

1.4 Goal of this work

The first goal of this work is to investigate the optical behavior and propagation effects in an entirely new superlattice photonic crystal structure, the square superlattice. Previous work on the triangular superlattice [39] showed that the structure exhibited novel propagation effects that could be exploited in the device with a static structure design. Furthermore, an investigation into the tuning of both superlattice structures will be conducted to determine how the optical properties of the device can be altered by infiltration of optical materials. The infiltration of medium index TiO_2 ($n = 2.31$) and low index Al_2O_3 ($n = 1.8$) will be investigated in Chapter 5 as a way to statically tune the square superlattice properties. In addition, further research on infiltration and device

construction using nonlinear and electro-optic materials will help to provide an understanding of how superlattice structures can enable dynamic tuning of the PC properties of interest. This work will include accurate modeling and simulation of the structures using a systematic approach.

The second main goal of the research is to prove that the mathematical optical frequency ground-plane cloaking concept proposed by Li and Pendry [40] could be fabricated into an actual device and measured, thereby proving that the real-world device performance would match that predicted by theory. This was accomplished by first converting the mathematical model of the structure into an actual device structure that can be modeled. The structure will then be numerically simulated to determine its performance at optical frequencies. The challenge lies in the experimental portion of the research, in which the nano-scale cloaking device is fabricated and its performance measured to determine if the real-world device performance matches that predicted numerically.

2 BACKGROUND

The analysis of the operation of photonic crystals requires the use of the electromagnetic, solid state physics, and optical theory. While the behavior of photons in the dielectric medium of a photonic crystal can be described by the use of Maxwell's equations, the periodicity of the structure requires the application of solid state physics theory to the behavioral description as well. In addition, the use of wavevector diagrams and analysis of the refractive properties of photonic crystal devices requires the use of several principles of optics theory.

This chapter provides a mathematical and theory background for further analysis of the triangular and square superlattice photonic crystal structures in the proceeding chapters. First, the formulation of Maxwell's equations into eigenvalue equations that enable solutions to the band structure of the square superlattice will be presented. The solutions to this equation will then be discussed, and an example on the application of propagating electromagnetic modes in a slab of glass material covered. Next, two numerical computational methods will be discussed that are used to solve for the mode structures in photonic crystals, namely the plane-wave expansion method (PWE) and the finite-difference time-domain methods (FDTD).

2.1 Maxwell's Equations as an Eigenvalue Problem

Maxwell's equations are well known for describing the properties of macroscopic electromagnetism in a concise mathematical formulation. The equations are given by:

$$\nabla \cdot \vec{B} = 0 \tag{6}$$

$$\nabla \times \vec{E} + \frac{\partial \vec{B}}{\partial t} = 0$$

$$\nabla \cdot \vec{D} = \rho$$

$$\nabla \times \vec{H} - \frac{\partial \vec{D}}{\partial t} = \vec{J}$$

Here we will use the equations to describe the propagation of light in a photonic crystal structure. For the purpose of the work in this thesis we will constrain the analysis to a mixed dielectric medium that consists of regions of homogeneous dielectric material that is invariant in time (no free charges or currents) but not in space. The relative positions of the regions of dielectric material can be described by their position vector $\vec{r}$. We will also consider the material to be isotropic, non-magnetic and lossless, i.e. a linear material with a real and positive permittivity, and unity permeability that is not dependent upon the frequency of radiation. The constitutive relations for $\vec{D}$ and $\vec{B}$ are then given by:

$$\vec{D}(\vec{r}) = \epsilon_0 \epsilon(\vec{r}) \vec{E}(\vec{r})$$

$$\vec{B}(\vec{r}) = \mu_0 \mu(\vec{r}) \vec{H}(\vec{r}) \approx \mu_0 \vec{H}(\vec{r}) \tag{7}$$

Combining these with Maxwell's equations yields:

$$\nabla \cdot \vec{H}(\vec{r}, t) = 0$$

$$\nabla \cdot (\epsilon(\vec{r}) \vec{E}(\vec{r}, t)) = 0$$

$$\nabla \times \vec{E}(\vec{r}, t) + \mu_0 \frac{\partial \vec{H}(\vec{r}, t)}{\partial t} \tag{8}$$

$$\nabla \times \vec{H}(\vec{r}, t) - \epsilon_0 \epsilon(\vec{r}) \frac{\partial \vec{E}(\vec{r}, t)}{\partial t} = 0$$

Since these equations are linear, the spatial dependence can be separated from the time dependence by treating $\vec{H}$ and $\vec{E}$ as harmonic plane waves. The real part of this complex-valued field is the actual physical field.

$$\vec{H}(\vec{r},t) = \vec{H}(\vec{r})e^{-i\omega t}$$
$$\vec{E}(\vec{r},t) = \vec{E}(\vec{r})e^{-i\omega t} \tag{9}$$

Here $H(r)$ and $E(r)$ are the plane wave parts of the equations, with $\vec{H}_0$and $\vec{E}_0$ being constant vectors:

$$\vec{H}(\vec{r}) = \vec{H}_0 e^{i\vec{k}\cdot\vec{r}}$$
$$\vec{E}(\vec{r}) = \vec{E}_0 e^{i\vec{k}\cdot\vec{r}} \tag{10}$$

These equations are now substituted into the equations in (8) yielding:

$$\nabla \cdot \vec{H}(\vec{r}) = 0$$
$$\nabla \cdot (\epsilon(\vec{r})\vec{E}(\vec{r})) = 0$$
$$\nabla \times \vec{E}(\vec{r}) - i\omega\mu_0\vec{H}(\vec{r}) = 0 \tag{11}$$
$$\nabla \times \vec{H}(\vec{r}) + i\omega\epsilon_0\epsilon(\vec{r})\vec{E}(\vec{r}) = 0$$

The divergence equations specify that the fields consist of electromagnetic waves that are traverse. Mathematically, this gives the condition that both the electric and magnetic fields are transverse to the direction of propagation, i.e. $\vec{H}\cdot\vec{k}$ and $\vec{E}\cdot\vec{k}$ must equal zero.

The curl equations can be decoupled from each other by a division and curl operation to remove the dependence on $\vec{E}(\vec{r})$. Performing these operations and substituting the relation $c = \frac{1}{\sqrt{\epsilon_0\mu_0}}$ yields a single master equation that is dependent upon $\vec{H}(\vec{r})$ only:

$$\nabla \times \left(\frac{1}{\epsilon(\vec{r})} \nabla \times \vec{H}(\vec{r}) \right) = \left(\frac{\omega}{c} \right)^2 \vec{H}(\vec{r}) \tag{12}$$

This is an eigenvalue equation, where operations on the eigenfunction yield the function itself multiplied by a constant known as the eigenvalue. After solving for the magnetic field, the electric field value can be recovered by solving:

$$\vec{E}(\vec{r}) = \frac{i}{\omega \epsilon_0 \epsilon(\vec{r})} \nabla \times \vec{H}(\vec{r}) \tag{13}$$

The master eigenvalue equation is similar to the time-independent Schrödinger eigenvalue equation in that both problems can be solved through the use of Hermitian operators and plane wave solutions. There are several differences however, between the solutions of the two equations which should be addressed. The first difference is that in quantum mechanics the potential function is scalar, and often times seperable, leading to simpler single direction solutions. The potential in the Maxwell equation is different in that it is a vector, making analytical solutions more difficult to obtain and require the use of numerical analysis simulations. Another major difference lies in the scalability of the two different equations. In the case of quantum mechanics, the fundamental length scale of the Bohr radius limits the scalar potential solutions to a particular microscopic size range. The macroscopic Maxwell equations are unconstrained by such a length scale, and are usually normalized to the lattice constant length described by the variable *a*. This fact allows the Maxwell equation solutions to be easily scaled, up or down, in both length scale and frequency of operation without changing the properties of interest, making them much more flexible in the analysis of various electromagnetic structures.

2.2 Solid-State Electromagnetism in Photonic Crystals

Photonic crystals have discrete transitional symmetry, similar to atoms or molecules in a crystal. Thus, their analysis can be treated in terms of solid state physic principles. In the case of an atomic structure, the symmetry translates in all dimensions and is said to be continuous. We will consider the band structure of continuous symmetry structure first for analysis. The solutions, or modes, are plane waves classified by the wave vector k and an integer band number, n. These plane waves are solutions of the master equation (12) having eignevalues of:

$$\left(\frac{\omega}{c}\right)^2 = \frac{|\vec{k}|^2}{\epsilon} \tag{14}$$

Solving for ω gives the dispersion relation:

$$\omega = \frac{c|\vec{k}|}{\sqrt{\epsilon}} \tag{15}$$

This equation is also called the light line, and will be described in the following example. Consider the modes of a continuous plane of glass having thickness a and dielectric constant ϵ = 11.4 as shown in Figure 2-1. The band diagram showing the electromagnetic modes propagating in the structure is created by plotting the normalized radiation frequency $\omega a/2\pi c$ versus the normalized parallel wave vector $k_{\|}$ given by $ka/2\pi$. The band structure is computed by solving the master equation (12) numerically. The modes that are not confined to the glass, extending into the air and out to infinity, must resemble a superposition of free-space plane waves having frequencies of:

$$\omega = c|k| = \sqrt{k_{\|}^2 + k_{\perp}^2} \tag{16}$$

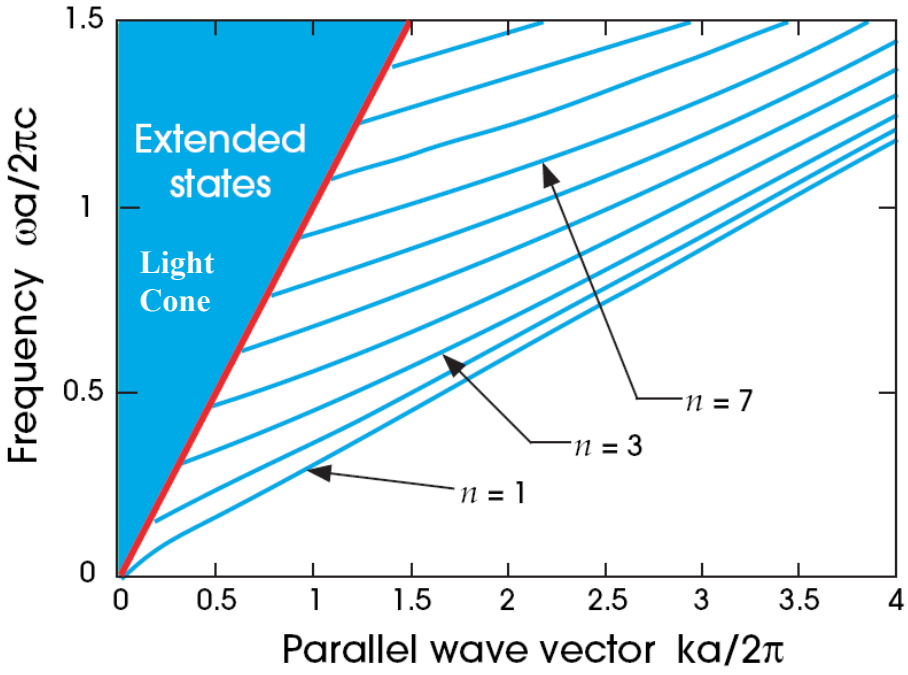

Figure 2-1: Band diagram for a plane of glass in air with thickness *a* and ε = 11.4. Blue lines correspond to guided modes in the glass, while the shaded blue region is the continuum of states that extend both into the glass and the surrounding air. The red line is the light line. Bands are given for a single polarization of the H field [41].

In this case $k_{\perp}$ is real and can take any value. If $k_{\parallel}$ is fixed, there are an infinite number of modes above the light line $w = ck_{\parallel}$, due to the fact that the structure has continuous symmetry, that is, the structure is considered to be one dimensional since there is no change to the structure over both the x and y directions. The band structure region above $w > ck_{\parallel}$ is called the light cone, where the modes are solutions of Snell's law:

$$n_1 \sin\theta_1 = n_2 \sin\theta_2 \tag{17}$$

Solutions in this region require $\sin\theta_2 > 1$ where there are no real solutions, thus the light rays are totally reflected. This is known as the critical angle:

$$\theta_c = \sin^{-1}\left(\frac{n_2}{n_1}\right) \tag{18}$$

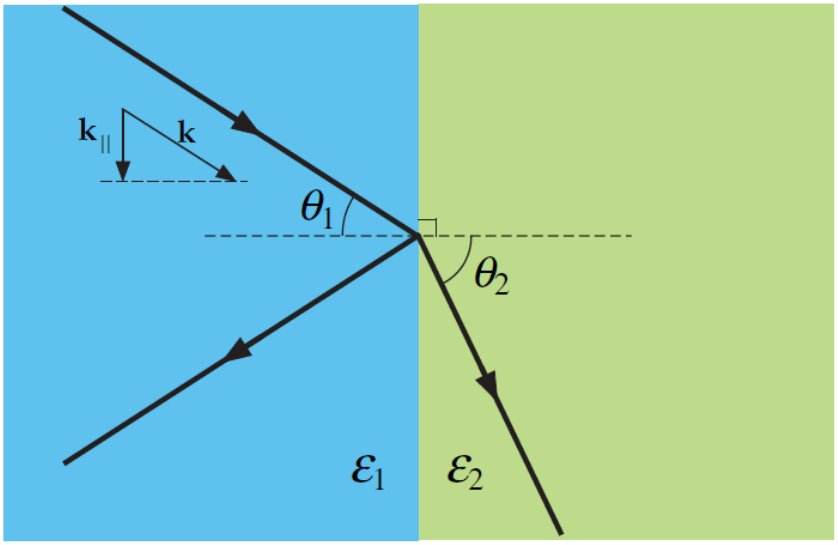

Figure 2-2: Diagram showing a flat interface between two dielectric regions ε_1 and ε_2, with the light ray having an incident angle of θ_1 and a refracted angle of θ_2. For $\varepsilon_2 < \varepsilon_1$, there is no solution for Snell's Law, and the light undergoes total internal reflection. In all cases $k_\parallel$ is conserved [41].

Solutions exist only for $n_2 > n_1$, indicating that total internal reflection occurs only within the medium with the higher index. The continuous band of modes above the light cone are called the unguided modes, because they are not contained within the slab structure but instead propagate outside the guiding medium of the glass.

The plane of glass introduces new solutions below the light line for $w < ck_\parallel$ due to the fact that referactive index of glass n_2 is larger than that of the surrounding air medium. In this region the only solutions are those with an imaginary $k_\perp$:

$$k_\perp = \pm i\sqrt{k_\parallel^2 - \frac{\omega^2}{c^2}} \tag{19}$$

These are modes that decay exponentially (evanescent waves) away from the glass, and are localized inside the slab. These modes are called the guided or index-guided modes, that form a discrete set of bands for a given $k_\parallel$. As $|k_\parallel|$ increases, the number of guided

bands increases until the ray optics limit of the critical angle is obtained, leading to totally internally reflected rays.

In the case of a photonic crystal structure with discrete transitional symmetry, the structure is described by unit cell geometry. The unit cell is a basic unit with repeating geometry within the larger photonic crystal structure and is defined by the normalized length unit a. The band diagram is constructed as before by solving Equation (12) numerically. The eigenfunction solutions are again plane waves, however the repeating geometry of the structure makes the solutions invariant over multiples of 2π/a, creating a degenerate set of solutions. This difference allows the solutions to be obtained through the use of reciprocal lattice vectors given notated as $\vec{b}$ vectors, the computation of which will be described more completely in the next chapter. Any linear combination of degenerate eigenfunctions can be combined into a single eigenfunction with the inclusion of a periodic modulation function $\vec{u}_{\vec{k}}(\vec{r})$ that describes the transitional geometry of the structure. The plane wave solutions now take the form:

$$\vec{H}_{\vec{k}}(\vec{r}) = e^{i\vec{k}\cdot\vec{r}}\vec{u}_{\vec{k}}(\vec{r}) \tag{20}$$

This result is known as Bloch's theorem [42]. Here $\vec{k}$ is called the Bloch wave vector and is given by:

$$\vec{k} = k_1\vec{b}_1 + k_2\vec{b}_2 + k_3\vec{b}_3 \tag{21}$$

The invariance of the plane wave solutions over multiples of 2π/a limits the set of non-redundant solutions to a region known as the Brillouin zone in reciprocal space. This is a consequence of the combination of three primitive lattice vectors $(\vec{a}_1, \vec{a}_2, \vec{a}_3)$ spanning the real space, and can be described by a repeating vector $\vec{R} = la_1 + ma_2 + na_3$, where l, m, n are integers. These real primitive lattice vectors give rise to three primitive

reciprocal lattice vectors given by $(\vec{b}_1, \vec{b}_2, \vec{b}_3)$ that span the reciprocal lattice and form the basis for the irreducible Brillouin zone. As a consequence, $\vec{u}_{\vec{k}}(\vec{r})$ is also invariant over $\vec{R}$, creating the set of Bloch plane wave solutions:

$$\vec{u}_{\vec{k}}(\vec{r}) = \vec{u}_{\vec{k}}(\vec{r} + \vec{R}) \tag{22}$$

As in the case of continuous transitional symmetry, there is conservation of the wave vector $\vec{k}$, but in the case of the discrete transitional symmetry of a photonic crystal the conservation is periodic. The addition of the reciprocal lattice vector does not change the eigenstates of the system or the propagation direction of the electromagnetic wave. One difference occurs in the band diagram of the photonic crystal over a continuous symmetry crystal however. The modes above the light line are now no longer continuous, but form a discrete set of bands similar to those modes below the light line.

A more detailed reciprocal space analysis of our system of interest, the square superlattice, as well as a band diagram analysis will follow in the proceeding chapters.

2.3 Dispersion Contours

The band diagram for a photonic crystal is actually a multi-dimensional surface that can be "sliced" to create dispersion contours. This is an analogy of the Fermi surface in solid state physics. A two-dimensional photonic crystal is actually a three dimensional structure, having symmetry in the two in-plane k vectors. The band structure for a two-dimensional photonic crystal is described by these two k vectors and the frequency ω, forming a three-dimensional band contour surface. By intersecting a fixed ω frequency plane with the band contour, a dispersion surface, also known as a dispersion contour, is

created. Multiple equi-frequency contour plots can be created by this method, creating a diagram that indicates the allowable wavevectors in the photonic crystal medium. These dispersion contours allow wave vector propagation refraction information to be obtained through the use of k-vector line constructions.

In the case of a isotropic homogeneous medium, the contours are congruent circles, due to the fact that the dispersion relation is linear in this case and is given by $w = ck/\sqrt{\varepsilon}$. Thus the circle radii can be related to the refractive index of the medium given by $k = wn/c$, since the dispersion curve forms an inverted cone surface. These contour surfaces are similar in an anisotropic birefringent medium, but in this case the birefringency between the opposite optical axis directions gives rise to two different refractive indexes, causing the equi-frequency dispersion contours to be ellipses rather than circles. For a photonic crystal structure, the anisotropy in $\varepsilon(\vec{r})$ is transitionally periodic, leading to more complicated dispersion curves that cannot be described by simple conic sections. Regardless of the shape of the curve, the electromagnetic group velocity and refraction propagation effects can be determined by solving for the gradient at a specific point on the dispersion contour:

$$v_g = \nabla_{\mathrm{k}}\omega(\mathrm{k}) = \frac{\partial\omega}{\partial\mathrm{k}} \tag{23}$$

Here $w(k)$ is a point on the contour and v_g is the normal to the tangent of the dispersion contour, pointing in the direction of increasing ω and making an angle θ_r with the construction line.

More details on the derivations and the refraction response of our photonic crystal of interest, the square superlattice, will be discussed in Chapters 3-5.

2.4 Numerical Analysis Background

There are several numerical simulation methods that are available to solve the eigenvalue formulation of Maxwells equation given by equation (12) used to compute the band structure of photonic crystals. Some methods involve solving of the equation directly, but most involve iterative techniques as the typical geometry of a photonic structure is not easily mathematically reduced. The two main classes of numerical simulation methods are based on either frequency-domain or time-domain solution methods. As with all numerical methods, there are advantages and disadvantages to each technique, one of the most important being the complexity of the formulation and the time required to solve equation (12) for a particular photonic crystal geometry. Frequency-domain methods typically offer a simulation speed advantage over time-domain methods, but this is dependent upon the size of the computational domain. Frequency-domain methods such as plane-wave expansion (PWE) scale exponentially with the size of the computation domain, while time-domain methods such as finite-difference time-domain (FDTD) calculations scale linearly. Therefore, the size of the computation domain is important in determining which method is best for quickly solving for a particular photonic crystal geometry.

Since solving for the photonic crystal band structure is similar to calculations used to solve for electronic crystal band structures in solid state physics, many of the same techniques can be used for both types of simulations. Unlike solid state physics calculations which rely on specific algorithms, the calculations for the photonic crystal structure are considered exact. This is due to the fact that photons are non-interacting boson particles, while electrons used to describe solid state physics structures are

fermions that interact with each other. The accuracy of the numerical calculation is then only a direct function of the dielectric function $\epsilon(\vec{r})$ that is used to directly describe the particular photonic crystal geometry.

In this research, we primarily utilize the PWE and FDTD simulation methods for specific numerical calculations, depending on which is much advantageous for the data we wish to extract. We will describe both methods briefly in the following sections, including the advantage and disadvantages of each.

2.4.1 Plane-Wave Expansion Simulations

To solve an eigenvalue equation using the plane-wave expansion (PWE) method, the magnetic field $\vec{H}$ in equation (12) is expanded into plane waves utilizing Bloch's theorem:

$$\vec{H}(\vec{r}) = \sum_{\vec{G}} \sum_{\lambda=1}^{2} h_{\vec{G},\lambda} \hat{e}_{\lambda} \, e^{i(\vec{k}+\vec{G})\cdot\vec{r}} \tag{24}$$

Here $\vec{k}$ is the a Brilloiun zone (BZ) wavevector, $\vec{G}$ is a reciprocal lattice vector in the BZ, and $\hat{e}_1, \hat{e}_2$ are unit vectors perpendicular to $(\vec{k}+\vec{G})$ that satisfy the tranversality requirement that $\nabla \cdot \vec{H} = 0$. This Bloch formulation is possible because in the case of photonic crystals, $\epsilon(\vec{r})$ is a periodic function that describes the crystal's geometry. The eigenvalue equation (12) can now be converted into a matrix equation that can be solved:

$$\sum_{\vec{G}`,\lambda`} H^{\lambda,\lambda`}_{\vec{G},\vec{G}`} \, h_{\vec{G}`,\lambda`} = \left(\frac{\omega}{c}\right)^2 h_{\vec{G},\lambda} \tag{25}$$

Here $H^{\lambda,\lambda`}_{\vec{G},\vec{G}`}$ is given by:

$$H_{\vec{G},\vec{G}`} = \left|\vec{k}+\vec{G}\right|\left|\vec{k}+\vec{G}`\right|\epsilon^{-1}_{\vec{G},\vec{G}`}\begin{bmatrix} \hat{e}_2\cdot\hat{e}_{2`} & -\hat{e}_2\cdot\hat{e}_{1`} \\ -\hat{e}_1\cdot\hat{e}_{2`} & \hat{e}_1\cdot\hat{e}_{1`} \end{bmatrix} \quad (26)$$

In this formula, $\epsilon^{-1}_{\vec{G},\vec{G}`}$ is the Forier transform of the dielectric function $\epsilon(\vec{r})$. Equation (25) can now be solved by using matrix diagonalization methods, which gives the mode coefficients and frequencies for the dispersion relation of the photonic crystal under analysis.

Shortcomings to this method are that the PWE method is not a time dependent method, therefore it cannot show the time evolution of a field propagating through the structure. Calculation of reflection and transmission requires extra steps in this method. The biggest shortcoming to this method is that PWE does not work well with three dimensional structures that have finite dimension, or do not have periodicity in all directions, such as the slab waveguide structure we will explore later. For a non-periodic structure, the boundary conditions are also non-periodic, which makes the plane wave method not applicable to the calculation. A work-around is to use a supercell that contains a large area of free space surrounding the repeating photonic crystal dielectric structure $\epsilon(\vec{r})$. This extra free space provides a buffer between each cell when the dielectric structure is repeated in space. Adding the extra free space comes at a computational cost since the unit cell is now much larger, as well as a loss of accuracy for specific frequencies that can be contained within the supercell dimensions. For real-world type photonic crystal devices, such as slab structures, time-domain methods are needed to get better accuracy for both the guided and unguided modes in the photonic crystal structure. The method we turn to for solving these complex 3D structures in the FDTD method.

2.4.2 Finite-Difference Time Domain Simulations

One of the strengths of FDTD is the large amount of boundary conditions available when performing electromagnetic calculations, making them ideal for the simulation of three-dimensional structures. These type of calculations were originally used for devices that operated in the radio and microwave regime, such as antennas and waveguiding structures. Since Maxwells equations scale linearly with frequency, the application to optical frequencies was easily possible. The FDTD method was first adapted for photonic crystals by Chan in 1995.

The technique for simulating a three-dimensional repeating cell structure consists of discretizing the single cell $\epsilon(\vec{r})$ dielectric function into a mesh of electromagnetic field calculation points. At each calculation point, the electric field $\vec{E}$ and magnetic field $\vec{H}$ are calculated, given the set of initial field and boundary conditions. These calculation points can be written in Cartesian coordinates, and consist of six coupled equations:

$$\frac{\partial H_x}{\partial t} = \frac{1}{\mu}\left(\frac{\partial E_y}{\partial z} - \frac{\partial E_z}{\partial y}\right) \tag{27}$$

$$\frac{\partial H_y}{\partial t} = \frac{1}{\mu}\left(\frac{\partial E_z}{\partial x} - \frac{\partial E_x}{\partial z}\right) \tag{28}$$

$$\frac{\partial H_z}{\partial t} = \frac{1}{\mu}\left(\frac{\partial E_x}{\partial y} - \frac{\partial E_y}{\partial x}\right) \tag{29}$$

$$\frac{\partial E_x}{\partial t} = \frac{1}{\epsilon}\left(\frac{\partial H_z}{\partial y} - \frac{\partial H_y}{\partial z} - \sigma E_x\right) \tag{30}$$

$$\frac{\partial E_y}{\partial t} = \frac{1}{\epsilon}\left(\frac{\partial H_x}{\partial z} - \frac{\partial H_z}{\partial x} - \sigma E_y\right) \tag{31}$$

$$\frac{\partial E_z}{\partial t} = \frac{1}{\epsilon}\left(\frac{\partial H_y}{\partial x} - \frac{\partial H_x}{\partial y} - \sigma E_z\right) \tag{32}$$

Given these equations, Yee in 1996 calculated the derivatives numerically to second-order accuracy spatially (spread through the computation space) and temporally (over a given time increment) [43]. Following Yee's notation we can describe each mesh calculation point given by Cartesian coordinates (i, j, k) as:

$$(i, j, k) = (i\Delta x, j\Delta y, k\Delta z) \tag{33}$$

Temporal functions with time designated as the fourth variable are formulated as:

$$F^n(i, j, k) = F(i\Delta \mathrm{x}, \mathrm{j}\Delta \mathrm{y}, \mathrm{k}\Delta \mathrm{x}, \mathrm{n}\Delta \mathrm{t}) \tag{34}$$

Here $\Delta x, \Delta y$, and Δz are the spatial increments in Cartesian coordinates, Δt is the time increment, and n is used to designate the time point in the calculation. The function F^n is either the electric field $\vec{E}$ or magnetic field $\vec{H}$ we wish to solve for. Maxwell's equations are linear in our formulation, so we can use a Taylor series expansion of F by specifying a fixed time interval $t_n = n\Delta t$ and then expand around the spatial point x_i to obtain the spatial derivative for the field values:

$$\frac{\partial F^n(i, j, k)}{\partial x} = \frac{F^n\left(i + \frac{1}{2}, j, k\right) - F^n\left(i - \frac{1}{2}, j, k\right)}{\Delta x} + O|(\Delta x)^2| \tag{35}$$

This formula expresses the time steps as increments of $\pm\frac{1}{2}\Delta x$, with $O|(\Delta x)^2|$ being the remainder term, approaching zero as the square value of the increment. Given this time increment, we now fix the computation point in space at (i, j, k) and take the first derivative of this expression with respect to time:

$$\frac{\partial F^n(i,j,k)}{\partial t} = \frac{F^{n+\frac{1}{2}}(i,j,k) - F^{n-\frac{1}{2}}(i,j,k)}{\Delta t} + O|(\Delta t)^2| \tag{36}$$

We now substitute Equations (35) and (36) into our Maxwell equation formulations (27)-(32). To get more spatial accuracy in our calculation, we shift the $\vec{H}$ and $\vec{E}$ field calculation points around in our mesh space in a Yee cell configuration, shown in. This configuration will help reduce the remainder term in Equation (35) as we evaluate the field over our $\pm\frac{1}{2}\Delta t$ time steps. Upon substitution we obtain the following equations for the fields at each time step:

$$\begin{aligned} H_x^{n+\frac{1}{2}}\left(i,j+\frac{1}{2},k+\frac{1}{2}\right) \\ &= H_x^{n-\frac{1}{2}}\left(i,j+\frac{1}{2},k+\frac{1}{2}\right) \\ &+ \frac{\Delta t}{\mu\left(i,j+\frac{1}{2},k+\frac{1}{2}\right)\Delta x} \cdot [E_y^n\left(i,j+\frac{1}{2},k+\frac{1}{2}\right) \\ &- E_y^n\left(i,j+\frac{1}{2},k\right) + E_z^n\left(i,j,k+\frac{1}{2}\right) \\ &- E_z^n\left(i,j+1,k+\frac{1}{2}\right)] \end{aligned} \tag{37}$$

$$
\begin{aligned}
&E_x^{n+1}\left(i+\frac{1}{2},j,k\right) \\
&\quad = [1-\frac{\sigma\left(i+\frac{1}{2},j,k\right)\Delta t}{\epsilon\left(i+\frac{1}{2},j,k\right)}]E_x^n\left(i+\frac{1}{2},j,k\right) \\
&\quad + \frac{\Delta t}{\epsilon\left(i+\frac{1}{2},j,k\right)\Delta x}\cdot[H_z^{n+\frac{1}{2}}\left(i+\frac{1}{2},j+\frac{1}{2},k\right) \\
&\quad - H_z^{n+\frac{1}{2}}\left(i+\frac{1}{2},j-\frac{1}{2},k\right) \\
&\quad + H_y^{n+\frac{1}{2}}\left(i+\frac{1}{2},j,k-\frac{1}{2}\right) \\
&\quad - H_y^{n+\frac{1}{2}}\left(i+\frac{1}{2},j,k+\frac{1}{2}\right)]
\end{aligned}
\tag{38}
$$

The simulation progresses in time by calculating each successive time step point based on the value from a previous field calculation point, alternating between the electric and magnetic field values. Given a set of initial condition for the fields, the time steps are incremented until a siunsiodal steady state condition is arrived at for each mesh calculation point.

The stability and accuracy of the FDTD simulations is a function of the chosen time and space increments, thus for accurate results the space increment must be a small fraction of the minimum wavelength of the fields or spatial geometry. This is to ensure that the field values do not change abruptly which can lead to error point calculations. The coarseness of the dielectric function is important, as large changes in the dielectric function $\epsilon(\vec{r})$ between the mesh calculation points will also lead to errors. The stability of time step algorithm is given by a Δt for a maximum phase velocity v_{max} which satisfies the following equation:

$$v_{max}\Delta t \leq \left(\frac{1}{\Delta x^2}+\frac{1}{\Delta y^2}+\frac{1}{\Delta z^2}\right)^{-\frac{1}{2}} \tag{39}$$

For simplicity in PC calculations, all values are typically normalized by the lattice constant a and the speed of light c since Maxwells equations scale linearly with frequency. In this case v_{max} becomes equal to 1, also simplifying the calculation.

The calculation starts at spatial points that are randomly distributed in the mesh. As the simulation proceeds, the field values at each of these points are stored. When the system has reached sinusoidal steady state conditions at all field points, two operations can be performed. The first operation is to take the data directly at this point and use it for viewing the evolution of the field components over time. The second operation is to obtain the resonant frequency points which require additional steps. First, an integration operation over time is performed on the fields. The fields are then Fourier transformed to yield the resonant frequencies in the spectrum. In the case of PCs, the resonant frequencies denote the band points of the structure, and can used to calculate the dispersion contours of the device. The use of the FDTD method will be further detailed in the calculations used in Chapter 4 and 5 for the superlattice structures being investigated.

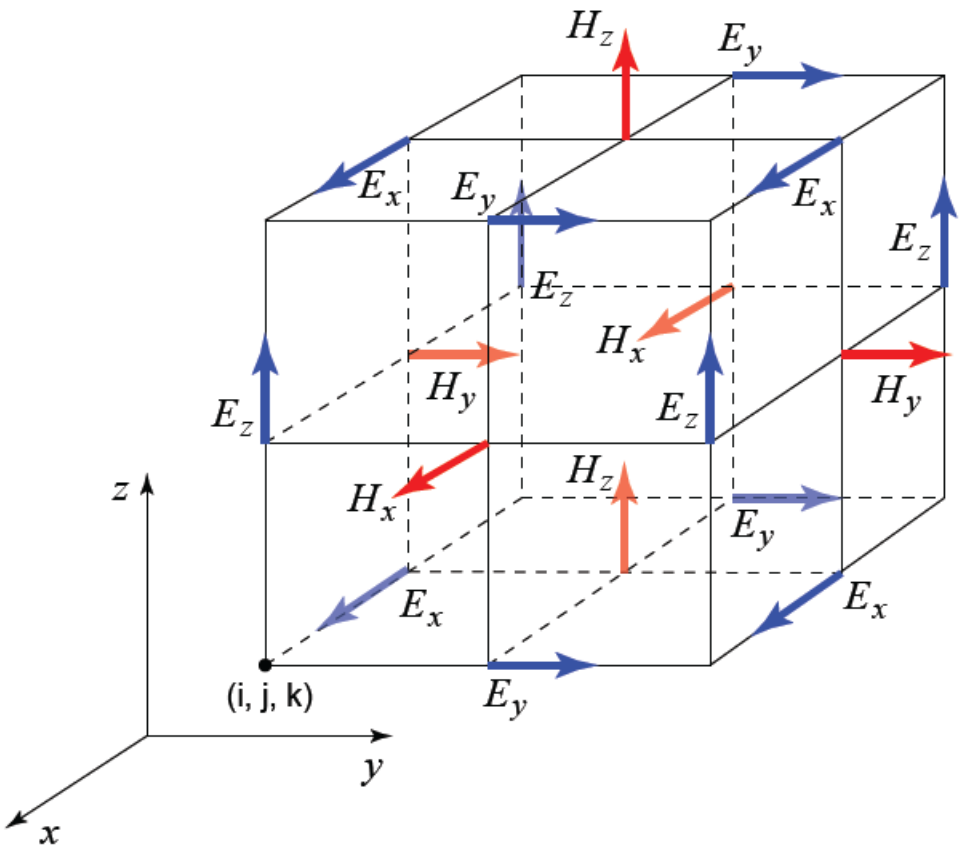

Figure 2-3: Yee cell configuration indicating the position of the field components in the FDTD calculation [43].

2.5 Atomic Layer Deposition (ALD) Technology

Atomic layer deposition (ALD) is a chemical gas phase thin film deposition method based on alternate saturative surface reactions. The difference from other chemical vapor deposition (CVD) techniques is that in ALD the source vapors are pulsed into the reactor alternately, one at a time, separated by purging or evacuation periods. The effect is that each precursor exposure step saturates the surface of the sample with a single molecular layer of the exposed precursor. This process results in self-limiting film growth that has excellent conformality and uniformity. The thickness of the film can be accurately controlled through the number of cycles and the hold and purge times. A SEM image of an ALD coating of 300nm of Al_2O_3 on Si is given in Figure 2-4, showing the conformality and trenching ability that can be obtained by the ALD process.

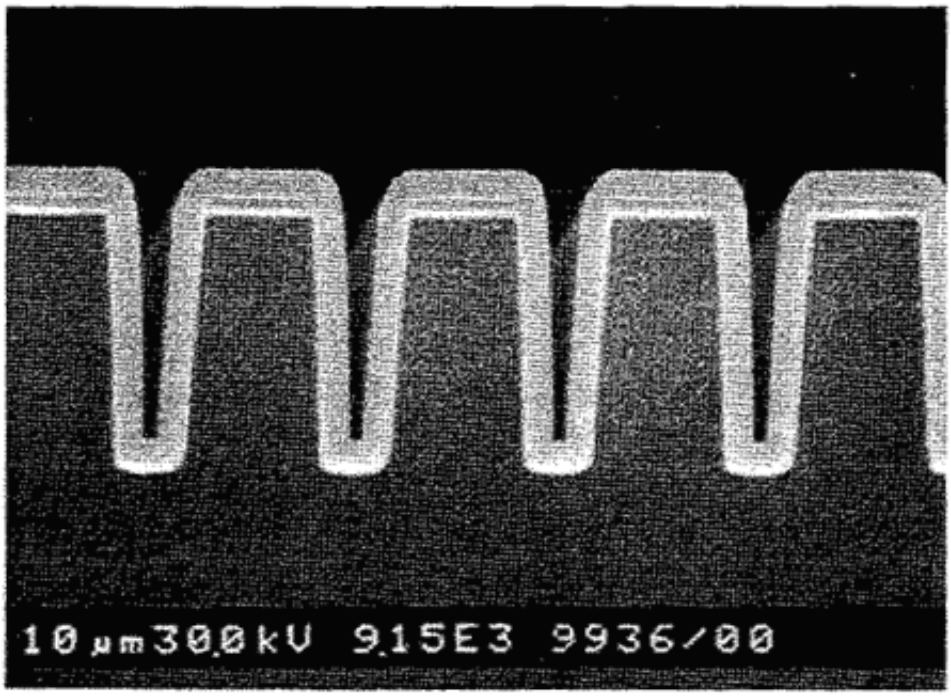

Figure 2-4: SEM image of an ALD coating of 300nm of Al_2O_3 on Si [44].

An flow chart diagram and surface chemistry reaction of the ALD growth process for TiO_2 is shown in Figure 2-5. The process is a self-limiting growth cycle of Ti attaching to the hydroxyl groups on an oxide surface, forming HCl gas as a by-product. The temperature range for this process is quite wide and from low temperature at 94C to higher temperatures of 600C, making it useful for infiltration into a number of materials such as polymers, that are temperature sensitive.

$$n(-OH)(s) + TiCl_4(g) \rightarrow (-O-)_n TiCl_{4-n}(s) + nHCl(g)$$

$$(-O-)_n TiCl_{4-n}(s) + (4-n)H_2O(g) \rightarrow (-O-)_n Ti(OH)_{4-n}(s) + (4-n)HCl(g)$$

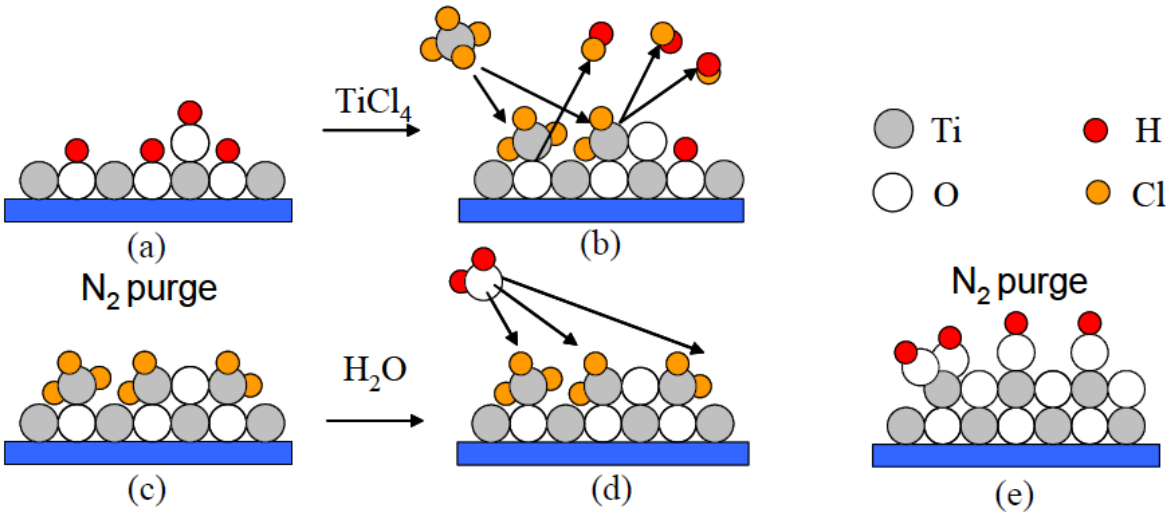

Figure 2-5: Growth cycle of TiO_2 on an oxide coated Si surface.

There are many benefits to using ALD over conventional CVD techniques. The self-limiting growth mechanism ensures that the precursor fluxes do not need to be uniform over the substrate. The flux only needs to be large enough so that the chemisorption layer becomes saturated. The excess precursor is purged out of the system after each step, avoiding the uneven buildup of material over time. This process provides

excellent conformality, reproducibility, and trench filling capability. Films can be deposited in monolayers using ALD, providing nanometer control over thickness. Also, many ALD process can be performed over a relatively wide temperature range, making it easier to find common growth temperatures for a number of different materials. There is one primary disadvantage to ALD however - the film deposition process is significantly slower than CVD methods. Fortunately the current technology trend is towards nanoscale film thicknesses, so the slow growth rate is not as significant when weighed against the benefits of ALD.

ALD processes may be performed in many kinds of reactors over a wide pressure and temperature range. The main parts of an ALD reactor are: 1) transport gas supply, 2) sources of precursor in gas, liquid, or the solid phase, 3) flow and sequencing control of the sources, 4) reaction chamber, 5) temperature control for heated sources and the reaction chamber, and 6) vacuum pump and exhaust equipment. The focus of work is to perform ALD runs at relatively low temperatures (<150 °C) and medium vacuum (25 to 1x10-3 Torr) conditions. Two reactors are available for the growth of optical materials. One system is for the growth of titania (TiO_2) and alumina (Al_2O_3), the other for growth of gallium phosphate (GaP), gallium nitride (GaN), and zirconium nitride (Zr_3N_4).

Most of the PC structures under investigation consist of Si (effective index of n=3.45 for crystalline Si) structures over a SiO_2 (n=1.45) substrate. The ALD films selected for use are compatible with these materials and have specific optical and mechanical properties that can be exploited. We are specifically interested in working in the optical (380-740nm) and near infrared (740nm-2um) wavelength regimes. Titania was selected as an ALD growth material due its medium index (n=2.31), and its ability to

withstand high temperatures and acids. Titania can also be converted into other phases such as anatase and rutile which have higher indices of refraction. Alumina has a lower index (n=1.6) and can also withstand high temperatures. Gallium phosphate is a high index material (n=3.3) that has electro-optical and photoluminescent properties. It can also be doped with nitrogen to create a phosphor that emits in the green. Zirconium nitride is also high index (n=3.3) and is transparent into the orange range. Gallium nitride has an index lower than GaP (n=2.3-2.6), but is more conformal and transparent at optical frequencies. Other optical materials that can be deposited by ALD may also be investigated at a later time.

3 THE SQUARE SUPERLATTICE PHOTONIC CRYSTAL STRUCTURE

3.1 Introduction to the Superlattice Photonic Crystal Structure

The inspiration for the design of both the triangular (also called hexagonal) superlattice and the square superlattice is derived from the work of Park and Summers in 2002 [45]. In this work a dynamically tunable PC structure was designed that increased the tunability of the optical properties of a 2D triangular lattice PC. In this scheme, an alternating bias was placed on adjacent [1 0] rows of the triangular lattice whose holes were filled with an electro-optic material such as a liquid crystal. When the bias is applied, the effective index of alternating rows of holes creates a periodic modulation in the refractive index of the structure. Figure 3-1 shows the interdigital biasing scheme of the device, where the different colors indicate different biases. This structure became known as a superlattice photonic crystal structure (SL-PC), based on the fact that the periodicity of the different indices of refraction enables the optical response properties of the device to be altered through the reduction in symmetry.

An alternative approach to creating a superlattice structure through the infiltration of electro-optic material in the holes is to change the size of the holes themselves. This changes the effective index of alternating rows similar to the biased structure, but in this case the hole sizes are static or fixed, removing the ability to dynamically change the refractive index and therefore the optical properties of the device. This type of structure is known as a static superlattice photonic crystal structure (SSL-PC), and it can be used to demonstrate optical refraction effects similar to the biased structure. An advantage of the

SSL structure is that it is much simpler to fabricate and operate, while still providing the interesting refractive behavior of the original biased device.

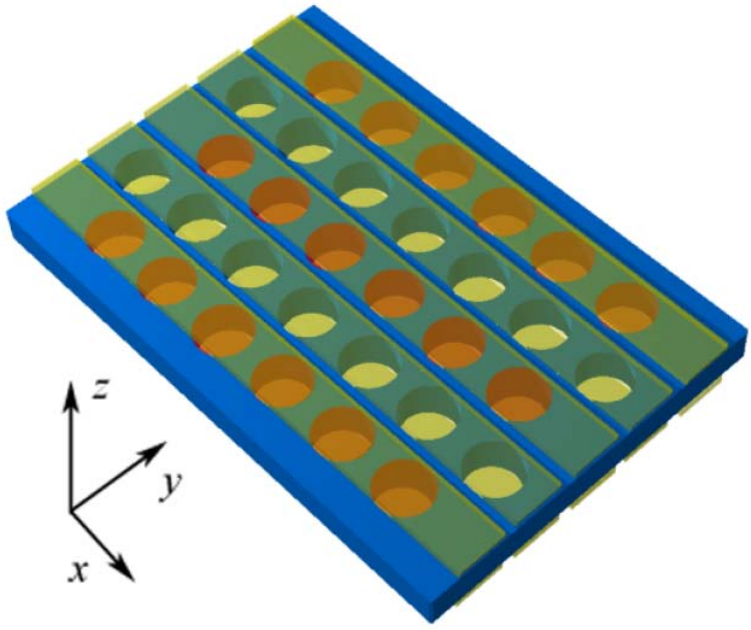

Figure 3-1: Structure of the interdigital biased superlattice structure consisting of modulating the refractive index of alternating [1 0] rows of a 2D triangular lattice photonic crystal.

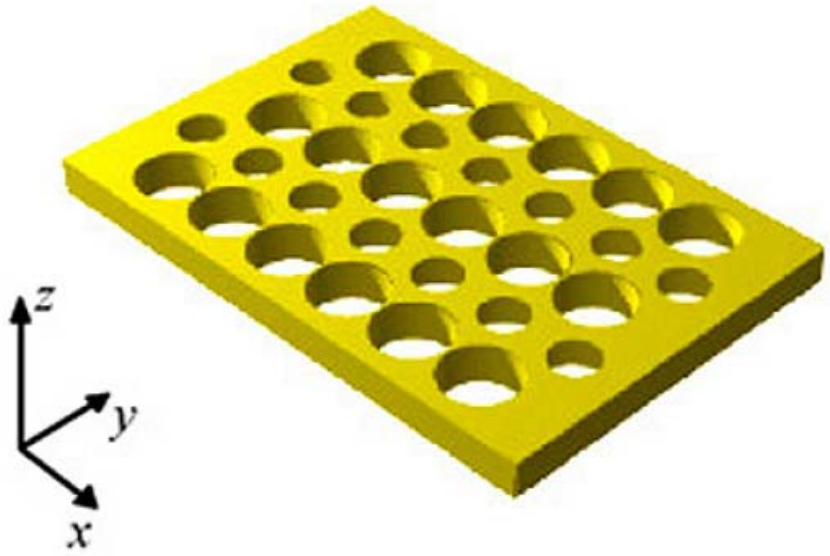

Figure 3-2: Structure of the triangular static superlattice photonic crystal. Modulation in the refractive index of the device is accomplished by modifying the hole radius in alternating [1 0] rows of the triangular lattice photonic crystal.

The first static superlattice photonic crystal design as shown in Figure 3-2 was based on a triangular photonic crystal lattice of holes [39], in which alternating rows of holes were changed in radius to control the optical properties of the device. The details of this structure are covered in the next two sections as a prelude to introducing a new superlattice structure and its properties, the square superlattice. The square superlattice is similar to the triangular superlattice in that the radius of holes in alternating rows are altered, but in this case the underlying lattice is square rather than a triangular lattice. In addition, both the triangular and square lattice will be used later in the thesis research to investigate their properties when different configurations of active optical materials are added, so the basic properties of both will be covered in this section.

3.2 Goals of the Square Superlattice Research

The first goal of this work is to investigate the optical behavior and propagation effects in an entirely new superlattice photonic crystal structure, the square superlattice. Previous work on the triangular superlattice [39] showed that the structure exhibited novel propagation effects that could be exploited in the device with a static structure design. Furthermore, an investigation into the tuning of both superlattice structures will be conducted to determine how the optical properties of the device can be altered by infiltration of optical materials. The infiltration of medium index TiO_2 and low index Al_2O_3 will be investigated in Chapter 5 as a way to statically tune the square superlattice properties. In addition, further research on infiltration and device construction using nonlinear and electro-optic materials will help to provide an understanding of how superlattice structures can enable dynamic tuning of the PC properties of interest. This

work will include accurate modeling and simulation of the structures using a systematic approach.

3.3 Real Space and Reciprocal Space Representations of Photonic Crystal Lattices

3.3.1 The triangular lattice

The analysis of the triangular lattice and the triangular superlattice is presented as a basis for discussing further structures. The real space and reciprocal space representations of the triangular lattice are shown in Figure 3-3. In real space the circles are typically cylinders of air in a background medium of higher dielectric constant, but the structure can also be reversed to a set of pillar structures in air. In this research the focus will be on investigating the former configuration, a structure of holes in a dielectric medium. The lattice structure is described by two basis vectors $\overrightarrow{a1}$ and $\overrightarrow{a2}$ making an angle of 120 degrees:

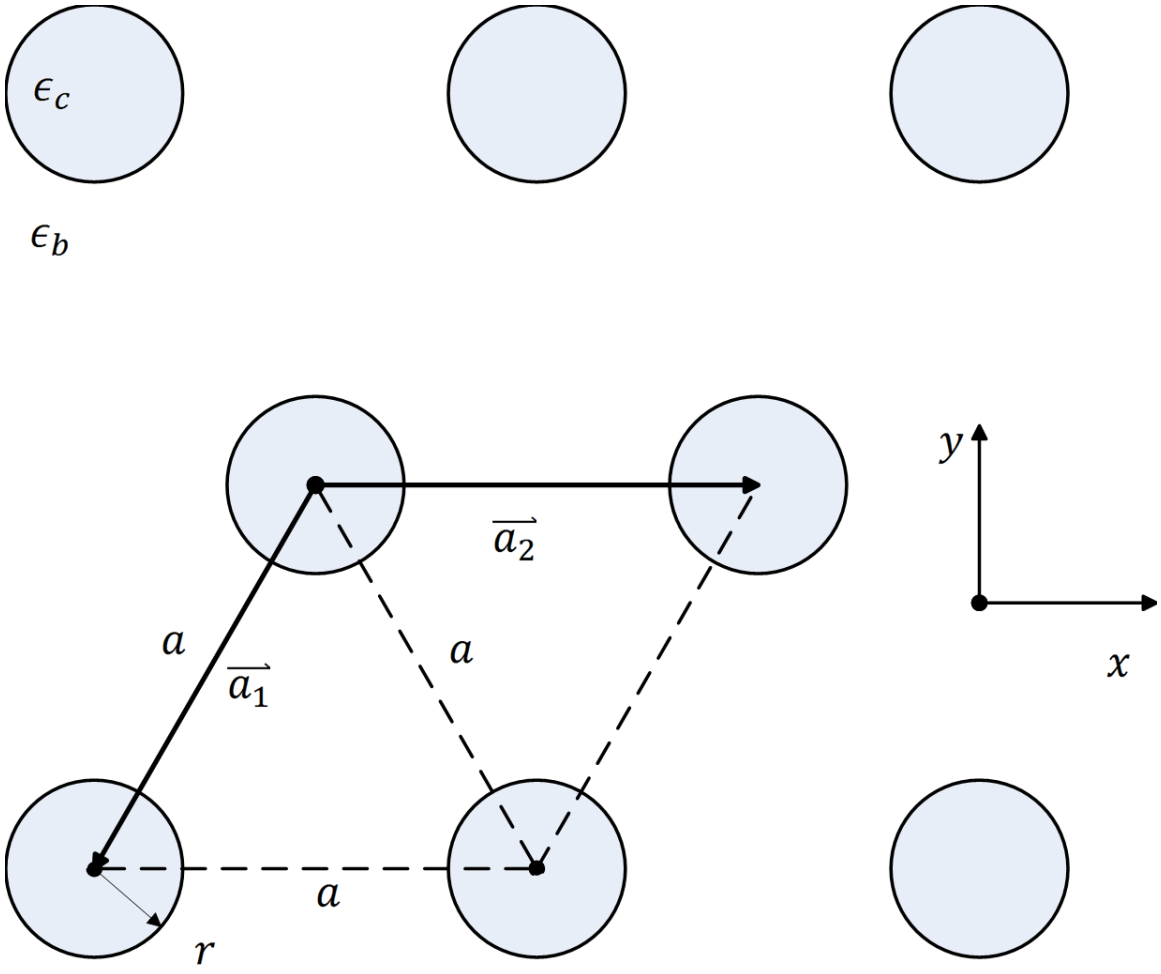

Figure 3-3: Diagram of the real space representation of the triangular lattice photonic crystal

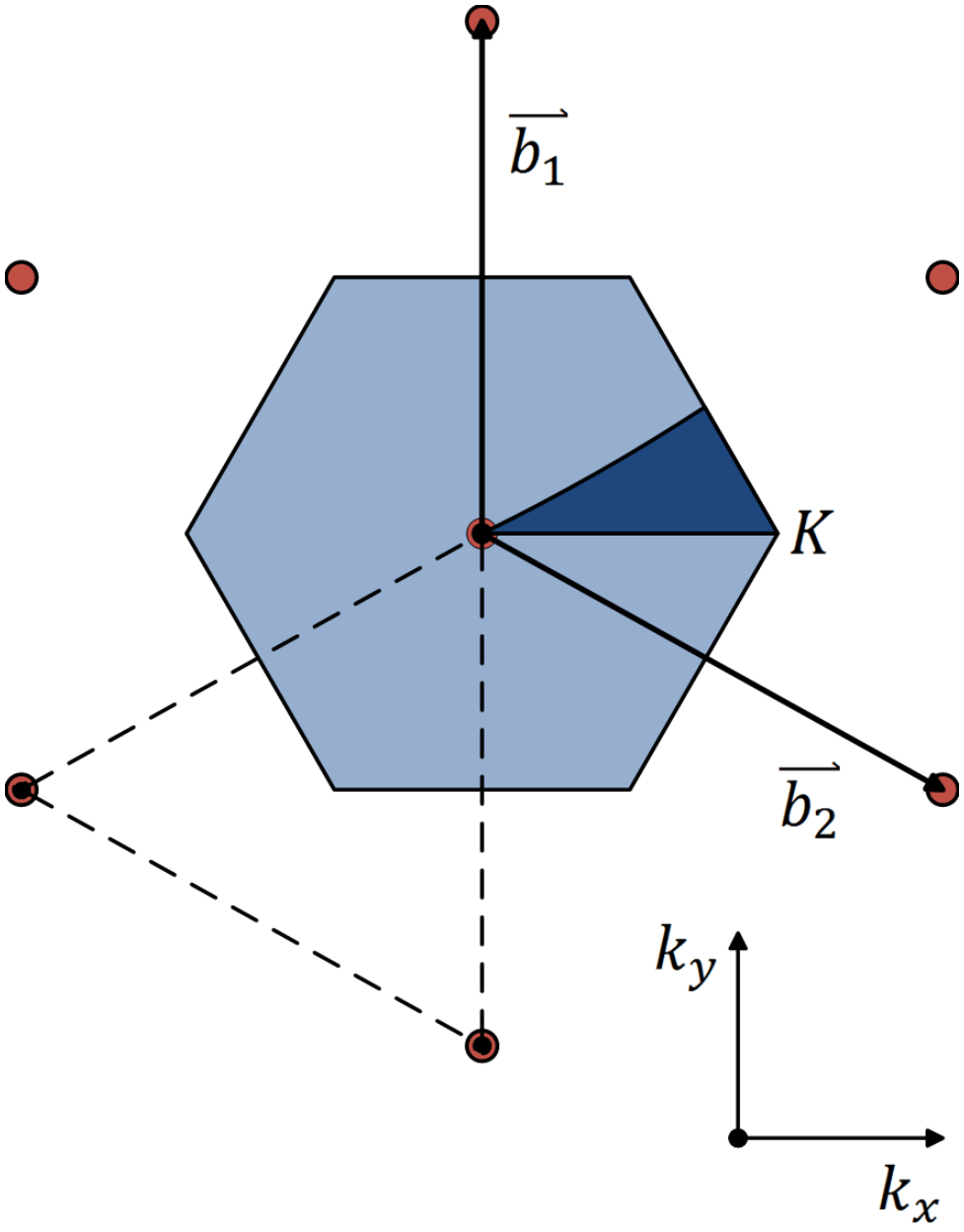

Figure 3-4: Diagram of the reciprocal space representation of the triangular lattice photonic crystal

$$\overrightarrow{a_1} = a\left(\frac{1}{2}, \frac{\sqrt{3}}{2}\right) \tag{40}$$

$$\overrightarrow{a_2} = a(1,0) \tag{41}$$

The reciprocal lattice vectors of the real space structure are calculated from the following equations [46-47]:

$$\overrightarrow{b_1} = 2\pi \frac{\overrightarrow{a_2} \times \overrightarrow{a_3}}{\overrightarrow{a_1} \cdot (\overrightarrow{a_2} \times \overrightarrow{a_3})} \tag{42}$$

$$\overrightarrow{b_2} = 2\pi \frac{\overrightarrow{a_3} \times \overrightarrow{a_1}}{\overrightarrow{a_1} \cdot (\overrightarrow{a_2} \times \overrightarrow{a_3})} \tag{43}$$

$$\overrightarrow{b_3} = 2\pi \frac{\overrightarrow{a_1} \times \overrightarrow{a_2}}{\overrightarrow{a_1} \cdot (\overrightarrow{a_2} \times \overrightarrow{a_3})} \tag{44}$$

For a 2D structure $\overrightarrow{a_3} = (0,0,1)$, and equations (8)-(10) reduce to simpler forms:

$$\overrightarrow{b_1} = \frac{2\pi}{(a_{1,x}a_{2,y} + a_{1,y}a_{2,x})}(a_{2,y}, -a_{2,x}) \tag{45}$$

$$\overrightarrow{b_2} = \frac{2\pi}{(a_{1,x}a_{2,y} + a_{1,y}a_{2,x})}(-a_{1,y}, a_{1,x}) \tag{46}$$

Here $a_{j,x}$ and $a_{j,y}$ are the x and y coordinates of the $j = 1,2$ point. Using the above equations to calculate the reciprocal lattice vectors of the triangular lattice yields:

$$\overrightarrow{b_1} = \frac{2\pi}{a}\left(0, \frac{2\sqrt{3}}{3}\right) \tag{47}$$

$$\overrightarrow{b_2} = \frac{2\pi}{a}\left(1, -\frac{\sqrt{3}}{3}\right) \tag{48}$$

The reciprocal lattice of the triangular photonic crystal is a triangular subsection of the hexagonal first Brillouin zone (BZ) as indicated by the shaded light blue area in Figure 3-4. This region is obtained by creating a bisecting line construction that effectively halves the distance between adjacent reciprocal lattice points. The irreducible BZ is

represented by the dark blue triangle and is a consequence of the symmetry of the reciprocal lattice points. This region represents all the eigenmodes of the structure, the other areas in the first BZ are simply folded versions of this zone. The high symmetry directions of the irreducible BZ sides are typically labeled as Γ, M, and K and are shown on the figure.

3.3.2 The triangular static superlattice

The triangular photonic crystal lattice is now modified to reduce the size the adjacent rows of holes, the larger having a radius r_1 in row i and a smaller radius of r_2 in row j. The schematic of this triangular superlattice structure is shown in Figure 3-5. This results in one hole of the triangle lattice formed by the basis vectors being smaller than the other two, resulting in the relations:

$$\frac{r_2}{r_1} \leq 1 \tag{49}$$

$$\Delta r = r_2 - r_1 \tag{50}$$

The introduction of the smaller row of holes changes the periodicity of the lattice in the y-direction, which in turn requires a change in the real space unit basis vectors:

$$\overrightarrow{a_1} = a(0, \sqrt{3}) \tag{51}$$

$$\overrightarrow{a_2} = a(1,0) \tag{52}$$

The basis vectors now define a rectangular unit cell indicated by the dashed rectangle. Inserting the components of these unit vectors into the 2D reciprocal lattice vector equations yields new reciprocal lattice vectors:

$$\overrightarrow{b_1} = \frac{2\pi}{a}\left(0, \frac{\sqrt{3}}{3}\right) \tag{53}$$

$$\overrightarrow{b_1} = \frac{2\pi}{a}(1,0) \tag{54}$$

The new reciprocal lattice is rectangular in shape similar to the real space basis lattice as shown in Figure 3-6. Again, the light blue shaded region indicates the first BZ and the dark blue shaded region the irreducible BZ. In order to verify that the rectangular reciprocal lattice structure is valid, we need to verify that there exists Bragg reflections at the reciprocal lattice points which is only true as long as the holes in rows i and j have different properties such as different radii or ε. This validation is performed by calculating the geometrical structure factor, $S_{\vec{K}}$ given by solid state physics [47]:

$$S_{\vec{K}} = \sum_{j=1}^{n} f_j(\vec{K}) e^{i\vec{K}\cdot\vec{d}_j} \tag{55}$$

Here $\vec{K}$ is the reciprocal lattice vector, f_j is the form factor, and $\vec{d}_j$ is the real-space coordinate of the j^{th} holes. In this case there are two different hole radii $n = 2$, which gives us two different form factors $f_1(\vec{K})$ and $f_2(\vec{K})$. The reciprocal lattice vector can be expressed as a linear combination of the primitive lattice vectors $\overrightarrow{b_1}$ and $\overrightarrow{b_2}$ each multiplied by an integer n_1 and n_2, yielding a general expression for $\vec{K}$:

$$\vec{K} = n_1\overrightarrow{b_1} + n_2\overrightarrow{b_2} \tag{56}$$

For the two different hole radii r_1 and r_2, one hole is chosen as the origin for simplicity:

$$\overrightarrow{d_1} = a(0,0) \tag{57}$$

$$\overrightarrow{d_2} = \frac{a}{2}(1,\sqrt{3}) \tag{58}$$

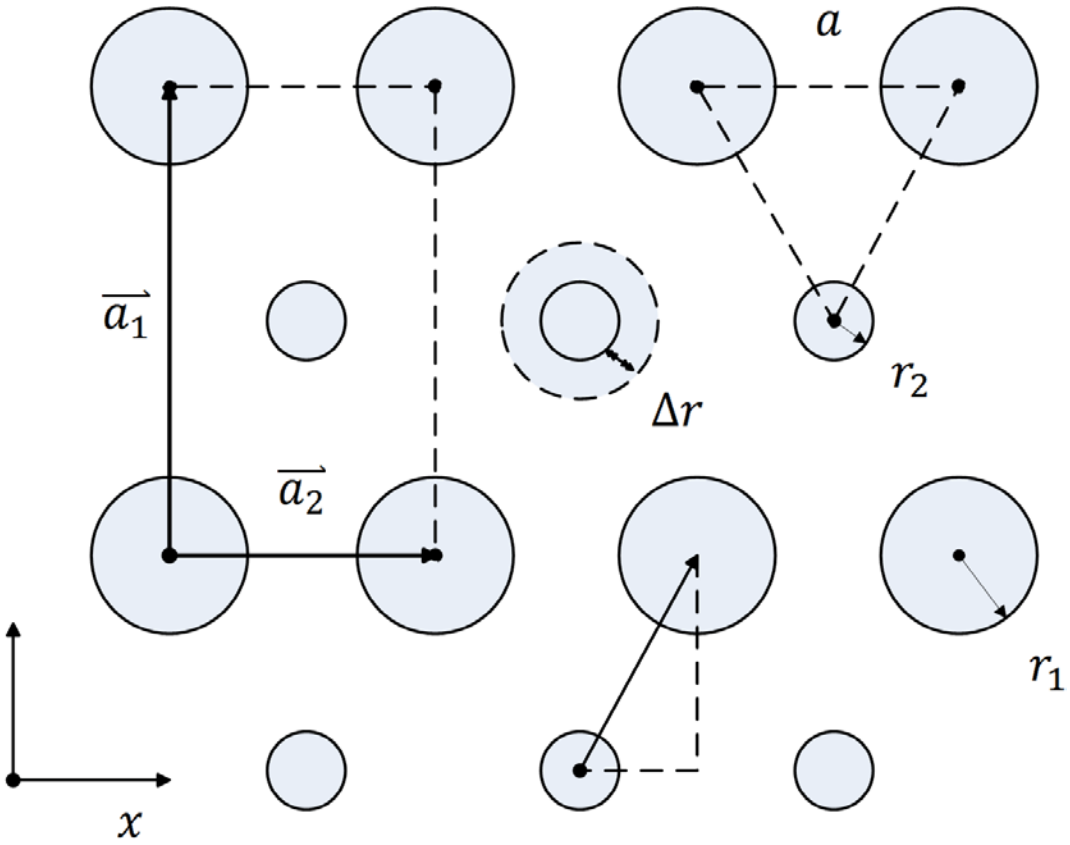

Figure 3-5: The real space representation of the triangular static superlattice, showing the defining parameters.

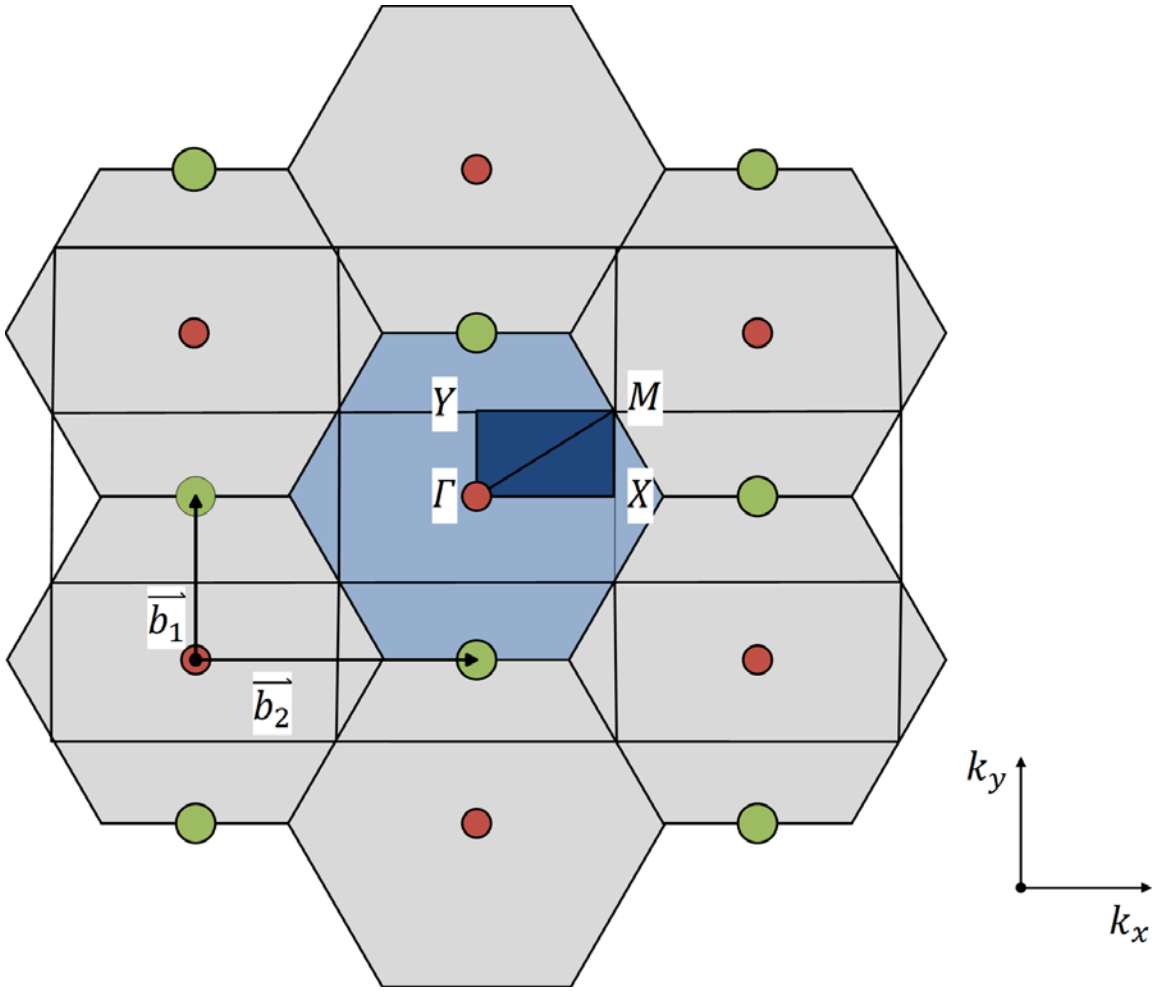

Figure 3-6: Schematic showing the reciprocal lattice representation of the triangular static superlattice. The red circles indicate the reciprocal lattice points for the underlying triangular lattice basis and the green circle are new reciprocal lattice points created by the introduction of the superlattice structure.

Solving for the geometrical structure factor:

$$S_{\vec{K}} = f_1(\vec{K})e^{i(n_1\vec{b_1}+n_2\vec{b_2})\cdot\vec{d_1}} + f_2(\vec{K})e^{i(n_1\vec{b_1}+n_2\vec{b_2})\cdot\vec{d_2}} \tag{59}$$

$$= f_1(\vec{K}) + f_2(\vec{K})e^{i(\pi n_1+\pi n_2)}$$

$$= f_1(\vec{K}) + (-1)^{(n_1+n_2)}f_2(\vec{K})$$

To check that the reciprocal space model is correct, we set $r_1 = r_2$, in which case $f_1(\vec{K}) = f_2(\vec{K}) = f(\vec{K})$:

$$S_{\vec{K}} = f(\vec{K})(1 + (-1)^{(n_1+n_2)}) \tag{60}$$

$$= \begin{cases} f(\vec{K}), & if\ (n_1 + n_2)\ is\ even \\ 0, & if\ (n_1 + n_2)\ is\ odd \end{cases}$$

In the reciprocal lattice diagram for the triangular superlattice the red colored circles represent reciprocal lattice points for which $(n_1 + n_2)$ is even, and the larger green circles represent the points where $(n_1 + n_2)$ is odd. In the case where the radii of the holes are equal, we can see that the green circle lattice points vanish, reducing the structure back to a triangular lattice reciprocal space consistent with the derivation above.

The addition of the row of reduced radii holes into the triangular lattice changes the symmetry of the real-space lattice from six-fold to two-fold. This reduction in symmetry is reflected in the change of first BZ from a hexagonal to a rectangular unit cell. The irreducible BZ becomes a one-quarter subset of the first BZ and is indicated by the darker shaded region lying inside it. The corner points Γ, M, X, and Y are the high symmetry points of the irreducible BZ. While the Γ point is equivalent in both the triangular and triangular superlattice reciprocal space, only four of the six M points are shared between the two. Both the Y and the X symmetry points are not present in the triangular lattice and have to be introduced. The X symmetry point lies along two of the

six Γ-K directions parallel to the $\overrightarrow{b_1}$ lattice vector in the triangular superlattice reciprocal space. The X point is located slightly inward from the K point, in between the two endpoints. The Y point lies along the two of the six Γ-M directions and is again between the two endpoints. In the final BZ analysis there are two equivalent Y and X points, four equivalent M points and a single Γ located within the first BZ area.

The analysis of the triangular and triangular superlattice photonic crystal structures provides a basis for analyzing the square and square superlattice photonic crystal structures. The mathematical analysis will follow a similar path, starting with the square lattice basis, then examining the changes to the structure as the square superlattice modification is added to it.

3.3.3 The square lattice

The square lattice consists of holes that are spaced evenly both horizontally and vertically with their centers forming a square as shown in Figure 3-7. The unit cell lines are drawn from the radii of four adjacent holes with the following base vectors:

$$\overrightarrow{a_1} = a(0,1) \tag{61}$$

$$\overrightarrow{a_2} = a(1,0) \tag{62}$$

Using the reciprocal lattice equations to solve for the base reciprocal lattice vectors yields:

$$\overrightarrow{b_1} = \frac{2\pi}{a}(0,1) \tag{63}$$

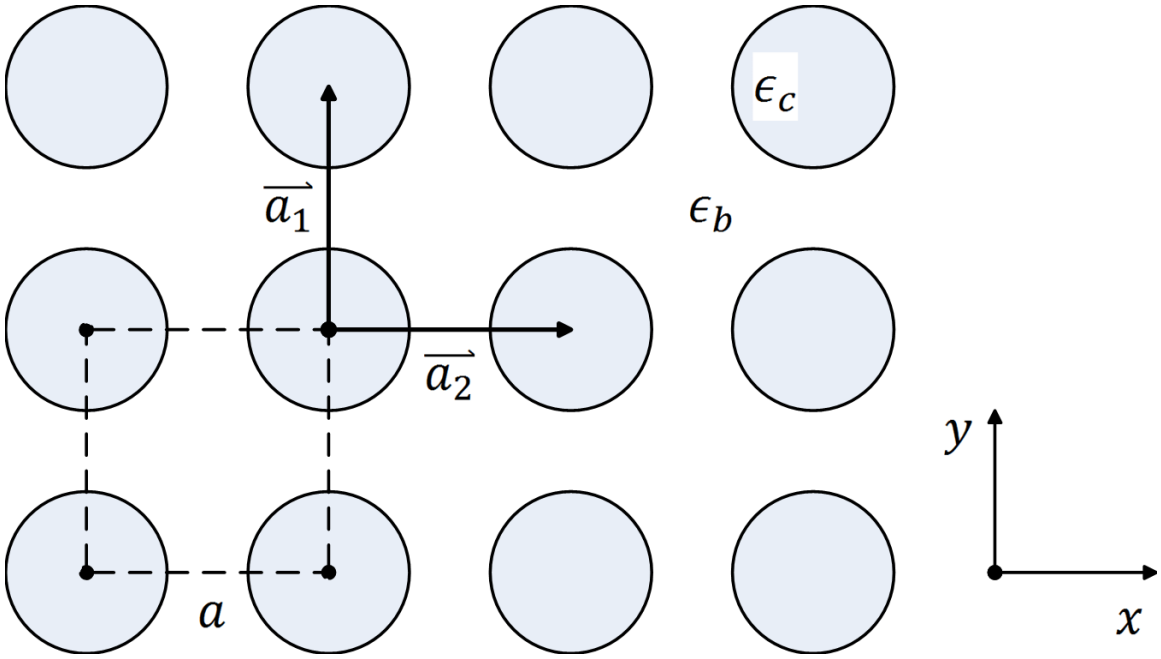

Figure 3-7: The geometry of the square photonic crystal lattice in real space

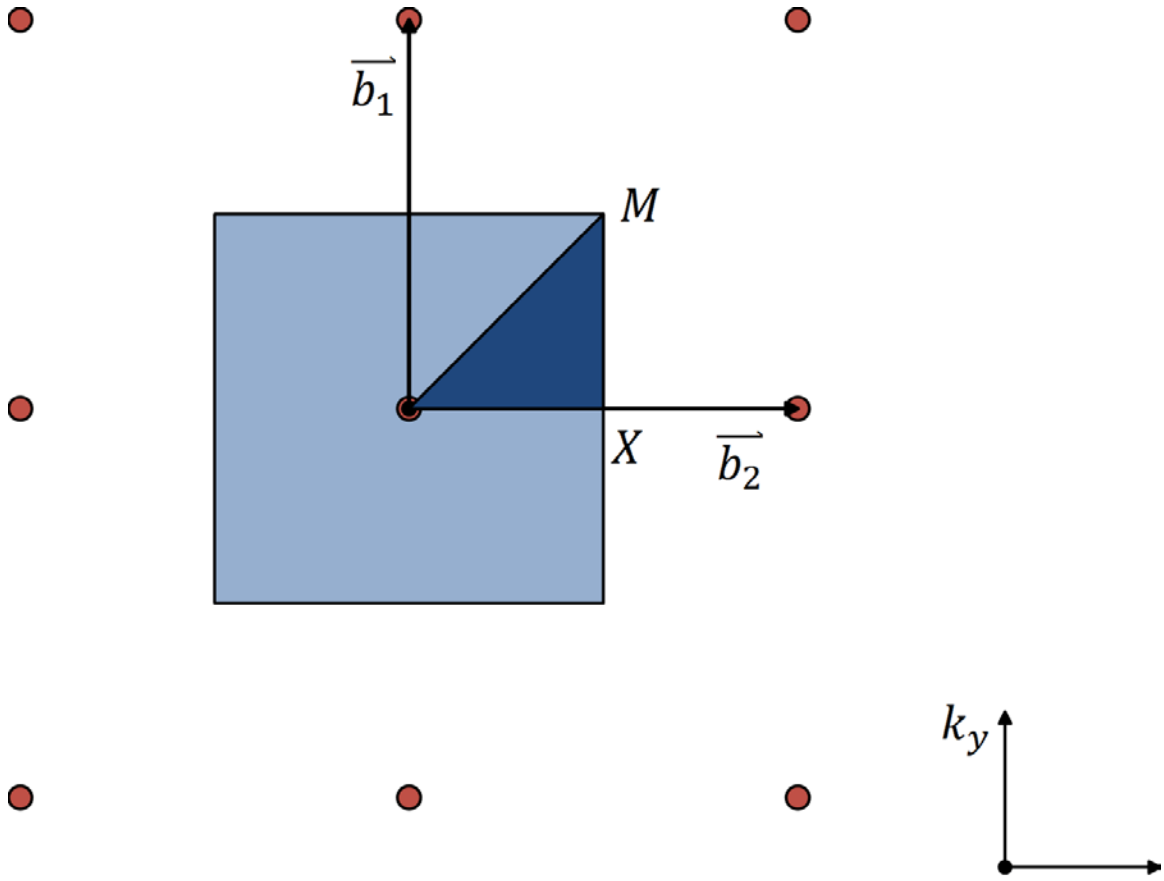

Figure 3-8: Diagram of the reciprocal space representation of the square lattice. The irreducible BZ is a triangle with three high symmetry points.

$$\overrightarrow{b_2} = \frac{2\pi}{a}(1,0) \tag{64}$$

The base reciprocal lattice vectors are in the same direction as the real space lattice vectors, however they are scaled by a factor of $2\pi/a^2$. The first BZ construction is shown in Figure 3-8. The four-fold symmetry of the square reciprocal lattice creates a triangular shaped irreducible BZ that is bounded by the high symmetry points Γ, X, and M. There are eight irreducible BZs contained in the first BZ of the square lattice, creating four identical X and M points for a given Γ.

3.3.4 The square static superlattice photonic crystal

The square photonic crystal lattice is now modified to reduce the size of the adjacent rows of holes as was previously done with the triangular lattice previously. Again, the larger holes have radius r_1 in row i and the smaller radius r_2 in row j. The schematic of this square superlattice structure is shown in Figure 3-9. In this case two holes of the square lattice formed by the basis vectors are smaller than the other two as before:

$$\frac{r_2}{r_1} \leq 1 \tag{65}$$

$$\Delta r = r_2 - r_1 \tag{66}$$

The introduction of the smaller row of holes again changes the periodicity of the lattice in the y-direction, which in turn requires changing the real space unit basis vectors:

$$\overrightarrow{a_1} = a(0,2) \tag{67}$$

$$\overrightarrow{a_2} = a(1,0) \tag{68}$$

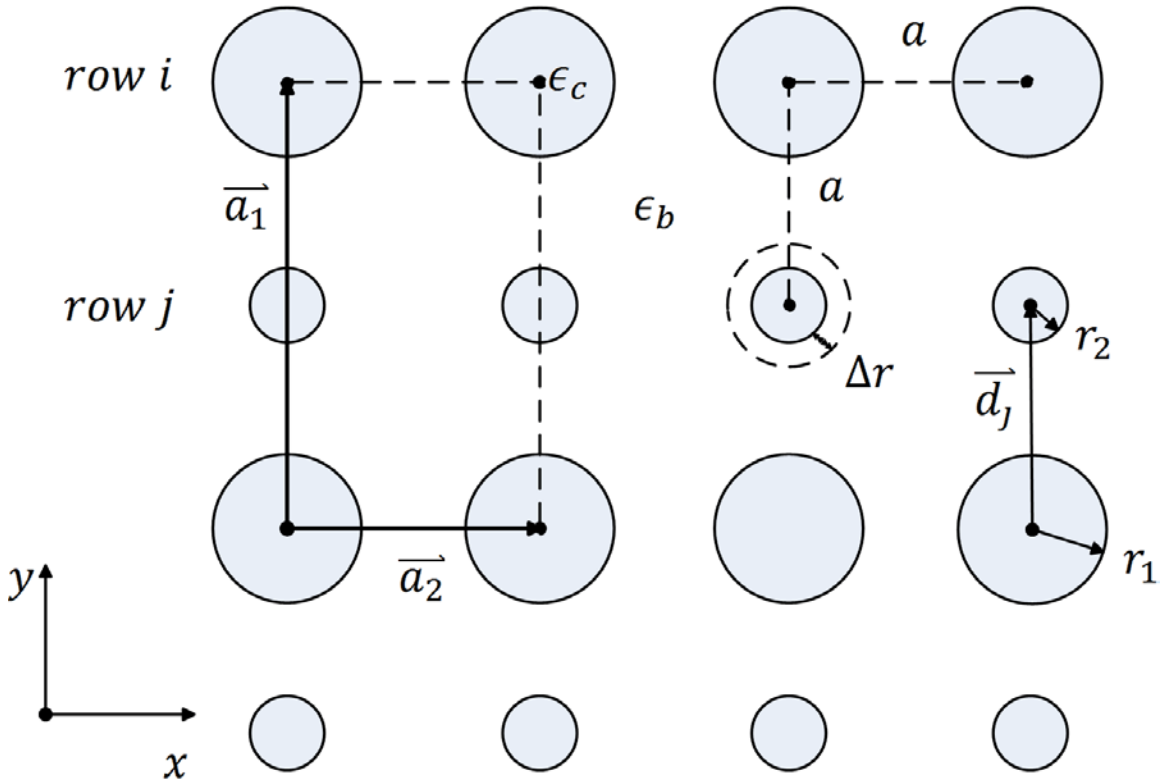

Figure 3-9: Diagram of the real-space representation of the static square superlattice with applicable parameters.

The basis vectors now define a rectangular unit cell similar to the triangular static superlattice as indicated by the dashed rectangle. In this case there are two smaller holes on either side of the unit cell, as opposed to the triangular superlattice where there is a single smaller hole in the middle. Inserting the components of these unit vectors into the 2D reciprocal lattice vector equations yields new reciprocal lattice vectors:

$$\overrightarrow{b_1} = \frac{2\pi}{a}\left(0, \frac{1}{2}\right) \tag{69}$$

$$\overrightarrow{b_1} = \frac{2\pi}{a}(1,0) \tag{70}$$

The new reciprocal lattice is rectangular in shape, similar to the real space basis square lattice as shown in Figure 3-10. Again, the light blue shaded region indicates the first BZ and the dark blue shaded region the irreducible BZ. In this case the irreducible BZ is changed from a triangle to smaller rectangle. In order to verify that the rectangular reciprocal lattice structure is valid, the geometrical structure factor and reciprocal lattice vector, $S_{\vec{K}}$ and $\vec{K}$, were calculated:

$$S_{\vec{K}} = \sum_{j=1}^{n} f_j(\vec{K}) e^{i\vec{K}\cdot\vec{d}_j} \tag{71}$$

$$\vec{K} = n_1\overrightarrow{b_1} + n_2\overrightarrow{b_2} \tag{72}$$

For the two different hole radii r_1 and r_2, one hole is chosen at the origin for simplicity as before. Note that now the position vectors are parallel to each other:

$$\overrightarrow{d_1} = a(0,0) \tag{73}$$

$$\overrightarrow{d_2} = a(0,1) \tag{74}$$

Solving for the geometrical structure factor:

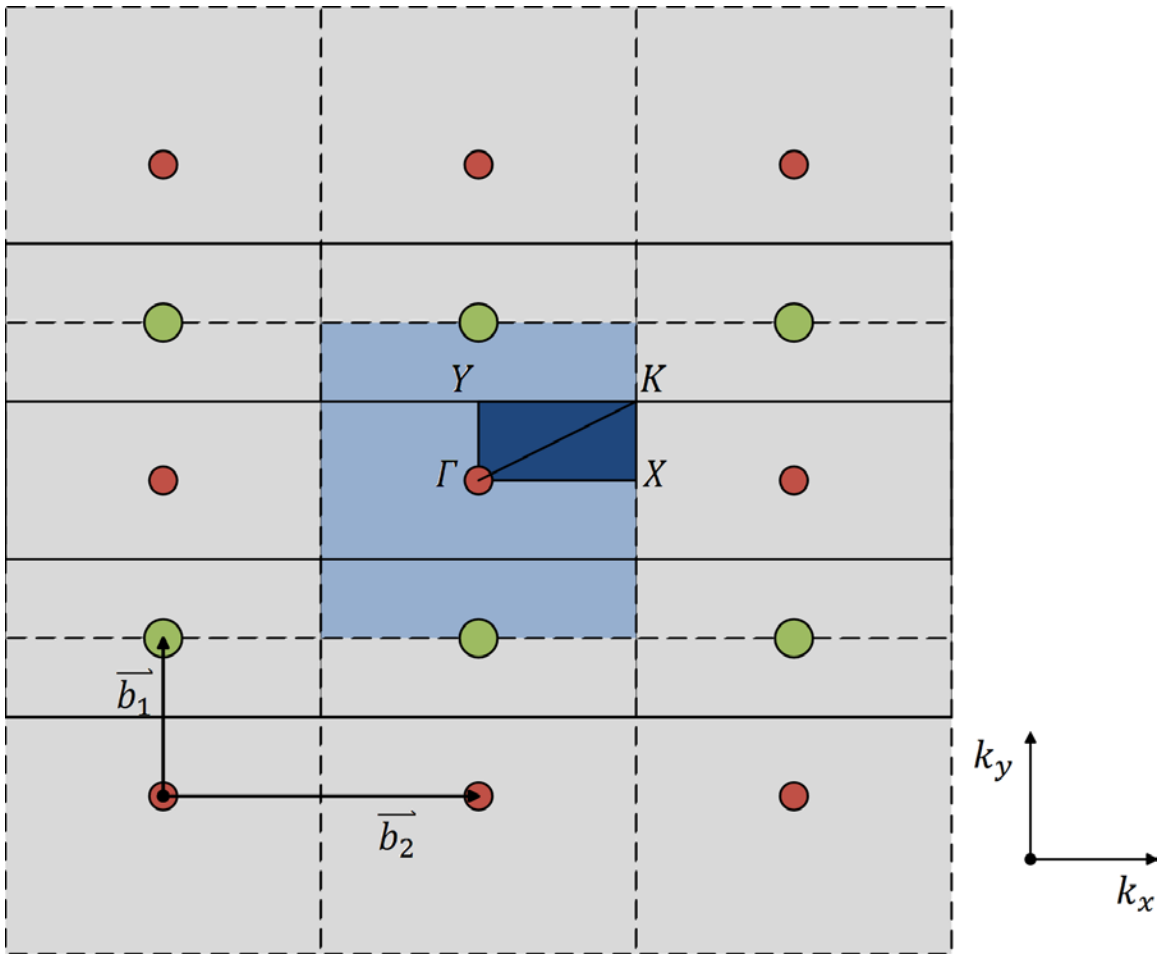

Figure 3-10: Reciprocal space of the square static superlattice. The red circles come from the underlying square lattice basis, and the green circles are new reciprocal lattice points arising from the addition of the superlattice structure.

$$S_{\vec{K}} = f_1(\vec{K})e^{i(n_1\vec{b_1}+n_2\vec{b_2})\cdot\vec{d_1}} + f_2(\vec{K})e^{i(n_1\vec{b_1}+n_2\vec{b_2})\cdot\vec{d_2}} \tag{75}$$

$$= f_1(\vec{K}) + f_2(\vec{K})e^{i(\pi n_1)}$$

$$= f_1(\vec{K}) + (-1)^{(n_1)}f_2(\vec{K})$$

In the case of the square static superlattice, the n_2 term drops out, indicating that there is no k_x dependence on the structure factor. A check is performed as in the case of the triangular superlattice photonic crystal to verify that the reciprocal space model is correct by setting $r_1 = r_2$, in which case $f_1(\vec{K}) = f_2(\vec{K}) = f(\vec{K})$:

$$S_{\vec{K}} = f(\vec{K})(1 + (-1)^{(n_1)}) \tag{76}$$

$$= \begin{cases} f(\vec{K}), & if\ n_1\ is\ even \\ 0, & if\ n_1\ is\ odd \end{cases}$$

This result is different from the triangular superlattice photonic crystal because here the structure factor is dependent upon only one index, a multiple of the basis vector in the reciprocal space k_y direction. As seen in the square superlattice reciprocal lattice diagram, the odd numbered indexes refers to the green circles found in alternating rows halfway between the red circles which are the reciprocal lattice points from the underlying square lattice basis. The addition of superlattice points shrinks the first BZ, shaded in light blue, to an area half the size in k_y. When these additional lattice points are removed, we are left with the original square lattice reciprocal space and the first BZ returns back to a square area, consistent with the derivation.

As in the case of the triangular superlattice, there is a reduction in symmetry when the alternating rows of smaller holes are added. The superlattice addition reduces the symmetry of the square lattice structure from four-fold to two fold, changing the irreducible BZ from a triangular cell to a smaller rectangular cell. There are four

irreducible BZs within the larger first BZ area, similar again to the triangular lattice. However, there are some differences with regard to high symmetry points. In this case only two of the four X points remain equivalent. In the k_y direction the reduction in the size of the BZ gives a new symmetry point located between Γ and X, which is designated Y in keeping with the triangular superlattice designation. Moreover, the M point from the square lattice is no longer a part of the irreducible BZ as the corner is shifted halfway down to a new point which is designated by the new letter K. Since the Γ-K vector runs along a different direction than the original Γ-M direction, the band structure along it is expected to be changed. Based on the new symmetry designations, there are now four equivalent K directions and two equivalent Y directions located within the first BZ. The Γ point remains unchanged as in the case of the triangular superlattice.

3.4 Folding Effects in Brillouin Zone Dispersion Contours

The reduction in symmetry introduced as a result of the new primitive lattice vectors in both the square and triangular lattice leads to an effect known as BZ folding. Since all k-points inside the BZ are defined as an integer multiple of $\overrightarrow{b_1}$ and $\overrightarrow{b_2}$ as defined by the Bloch theorem, the points now lying outside of the new smaller BZ have to be translated inward. In the case of the triangular superlattice, k-points from the hexagonal first BZ of the triangular lattice are folded into the smaller rectangular first BZ in both reciprocal lattice vector directions. This effect is shown in Figure 3-11 for a single normalized frequency dispersion contour of the second band in a triangular lattice PC. The blue lines represent the original triangular lattice band, while the dotted red lines represent the new triangular superlattice band structure that has been folded. The regions

of the original band that fall in both zones remain un-translated. The full dispersion contour becomes a combination of the two curves and is shown in Figure 3-12. The folding effect leads to higher curvature contours at the BZ edges, the exact shape of the contour being dependent on the superlattice strength, i.e. the Δr between the larger and smaller holes in the structure.

In the case of square superlattice the degree of folding is reduced because the reduction in symmetry is different. In the case of the triangular superlattice there is a reduction from six-fold to two-fold symmetry, leading to BZ folding in both reciprocal lattice directions. In the square superlattice there a change from four-fold symmetry to two-fold symmetry – the consequence of the reduced original square lattice symmetry is that the BZ folding is now restricted to a single reciprocal lattice direction $\overrightarrow{b_1}$. This leads to a similar dispersion contour folding as shown in the triangular superlattice, except in this case the folding is restricted to the Γ-Y direction. Another difference between the superlattices is that in the case of the triangular lattice all the irreducible BZ directions point to an original symmetry point of the underlying triangular lattice. In the square superlattice, the smaller BZ results in a completely new lattice direction Γ-K which has different properties than the Γ-M direction.

The purpose of researching these structures is to exploit the folding effects of the BZ dispersion contours to obtain new and enhanced refractive effects not seen in the underlying basis lattices. A more detailed analysis of the dispersion contours and the effects of their folding will be explored in the next chapter.

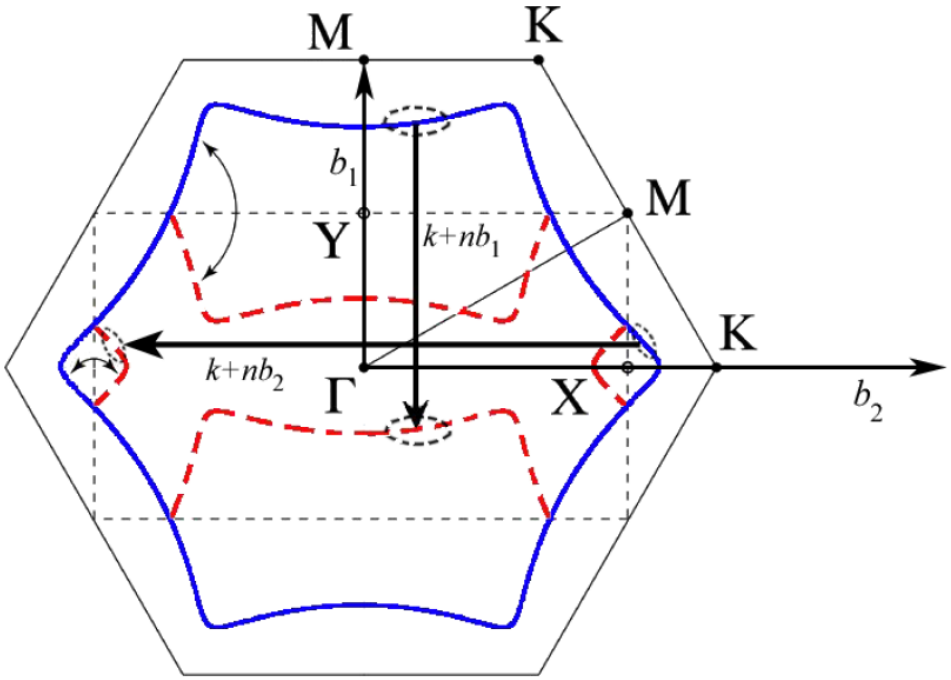

Figure 3-11: Example of a dispersion contour of the triangular superlattice created from the folding of the bands from the underlying triangular lattice basis [39].

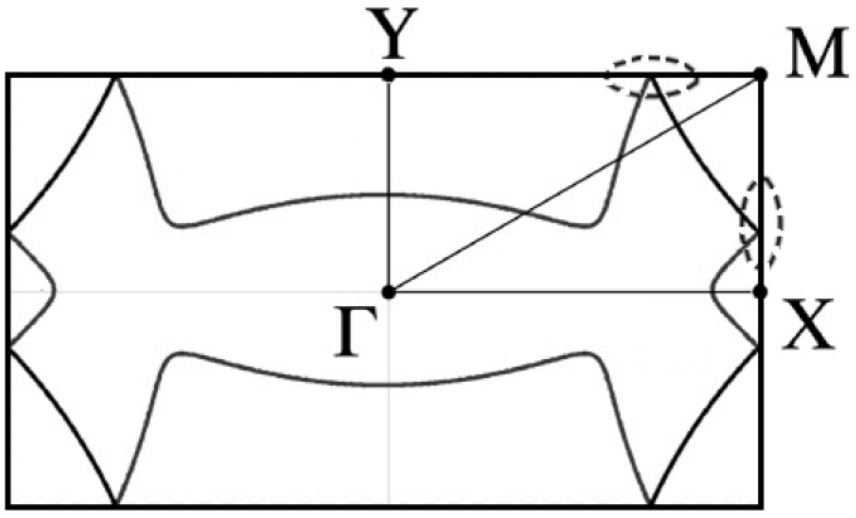

Figure 3-12: Triangular superlattice dispersion contour detailing folding effects at the edges of the BZ [39].

3.5 Folding Effects in Brillouin Zone Band Diagrams

The dispersion contours are obtained directly from the band structures of lattices under investigation by creating equi-frequency surfaces. More insight can be gained into how these contours are created by examining the folding that occurs directly from the band structure of the superlattices. In the triangular superlattice there are two folding direction to examine. The first direction is the Γ-Y band and is shown in Figure 3-13. The Γ-Y band structure is created by the folding of k-points running from the Y to M points in the triangular lattice BZ. Numerical PWE simulations were run for the TE bands using MPB with the parameters of $\epsilon_b = 12.0$ and $\epsilon_c = 1.0$ (silicon with air holes), and normalized hole radii $r_1 = 0.30a$ and $r_2 = 0.35a$. For the Γ-Y direction, the Γ-M band structure is first plotted, then folded into the band structure around the midpoint Y to obtain the triangular superlattice band structure. This folding of the bands creates a more complicated band structure in which each band follows a path from Γ to Y and back to Γ with increasing frequency. A similar band folding effect in the Γ-X direction is shown in Figure 3-14, only in this case the folding passes through the X-K and K-M points, creating folding centered around the midpoint X.

For the square superlattice, folding occurs only in the Γ-Y direction but follows a similar construction as in the case of the triangular lattice. The result of the folding the bands around the Y point is shown in

Figure 3-15. The folding of the underlying square lattice band structure again leads to a new set of folded bands that are more complicated in shape, which will lead to different device refractive properties.

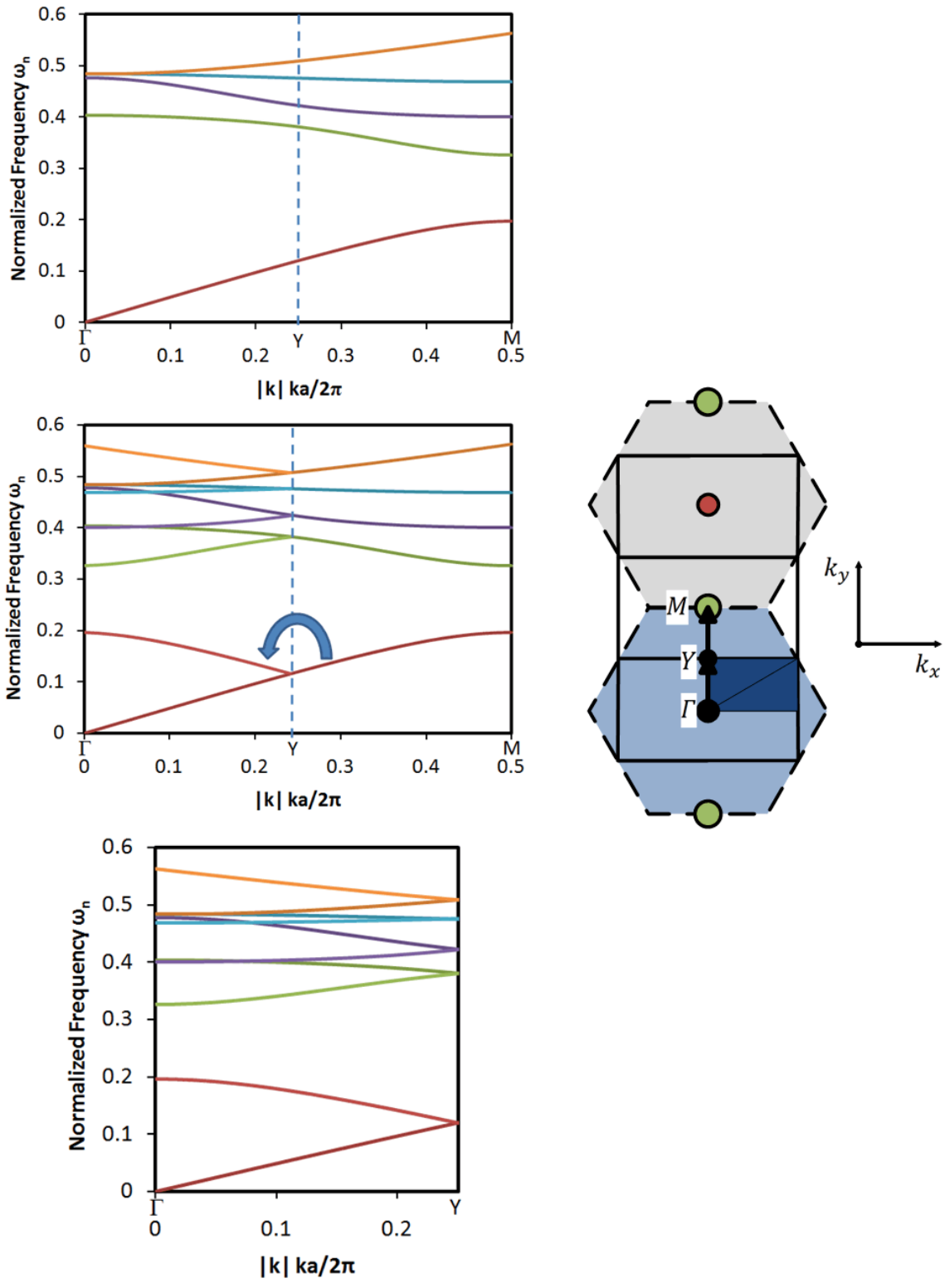

Figure 3-13: Band diagrams showing the folding of the Γ-M band in the triangular lattice creating the Γ-Y band in the triangular superlattice [39].

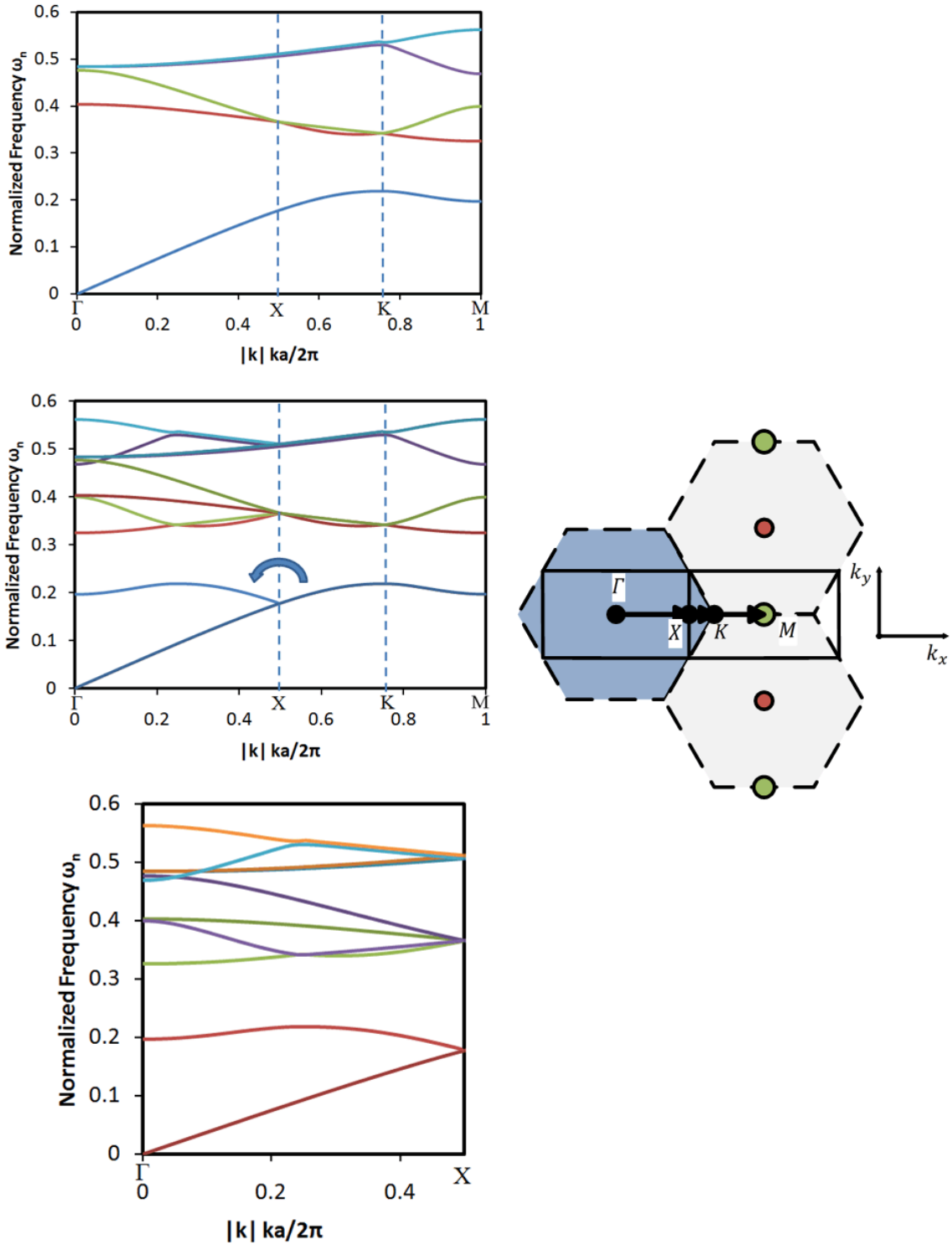

Figure 3-14: Band diagrams showing the folding of the Γ-K-M band in the triangular lattice creating the Γ-X band in the triangular superlattice [39].

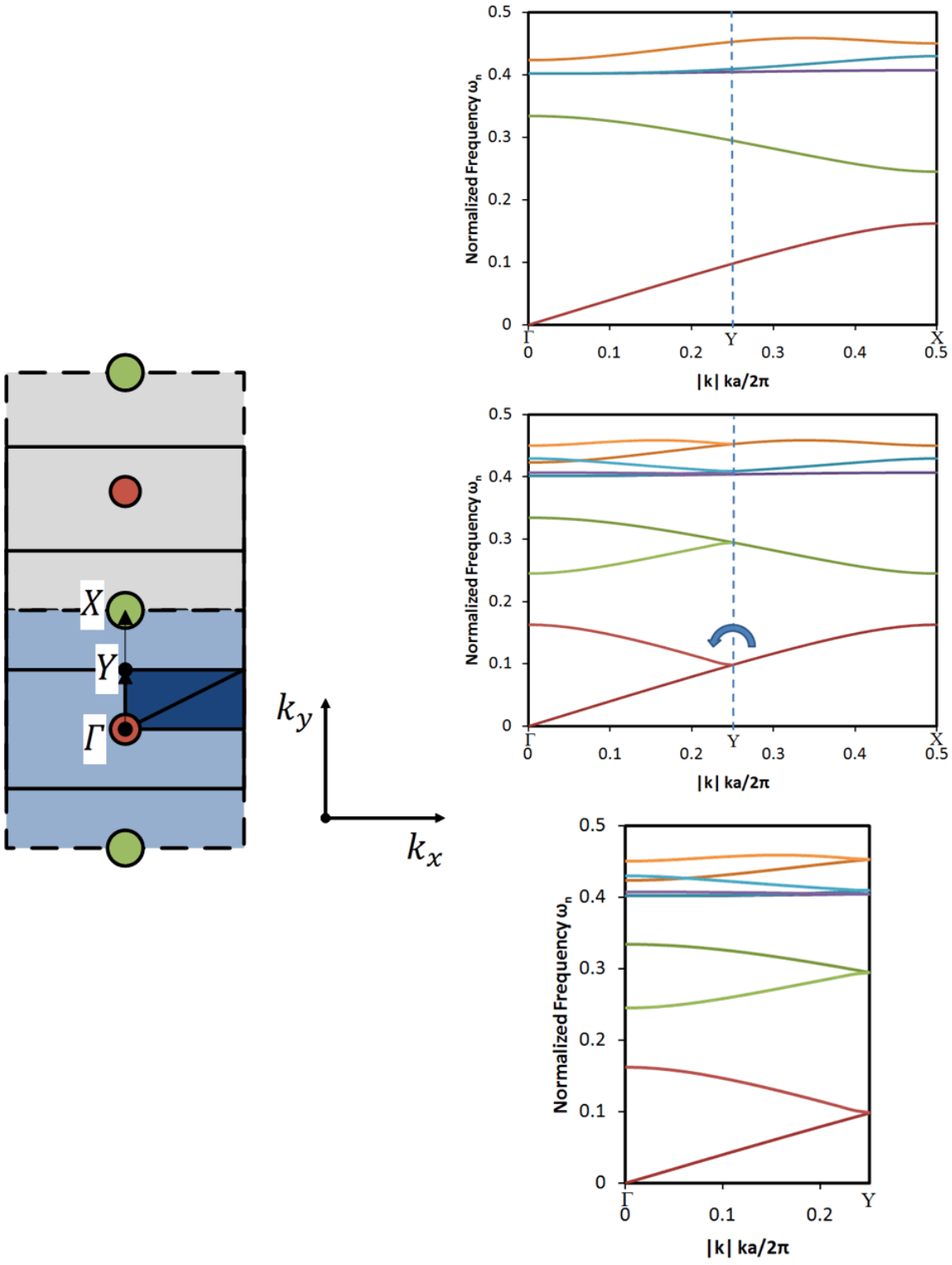

Figure 3-15: Band diagrams showing the folding of the Γ-X band in the square lattice creating the Γ-Y band in the square superlattice.

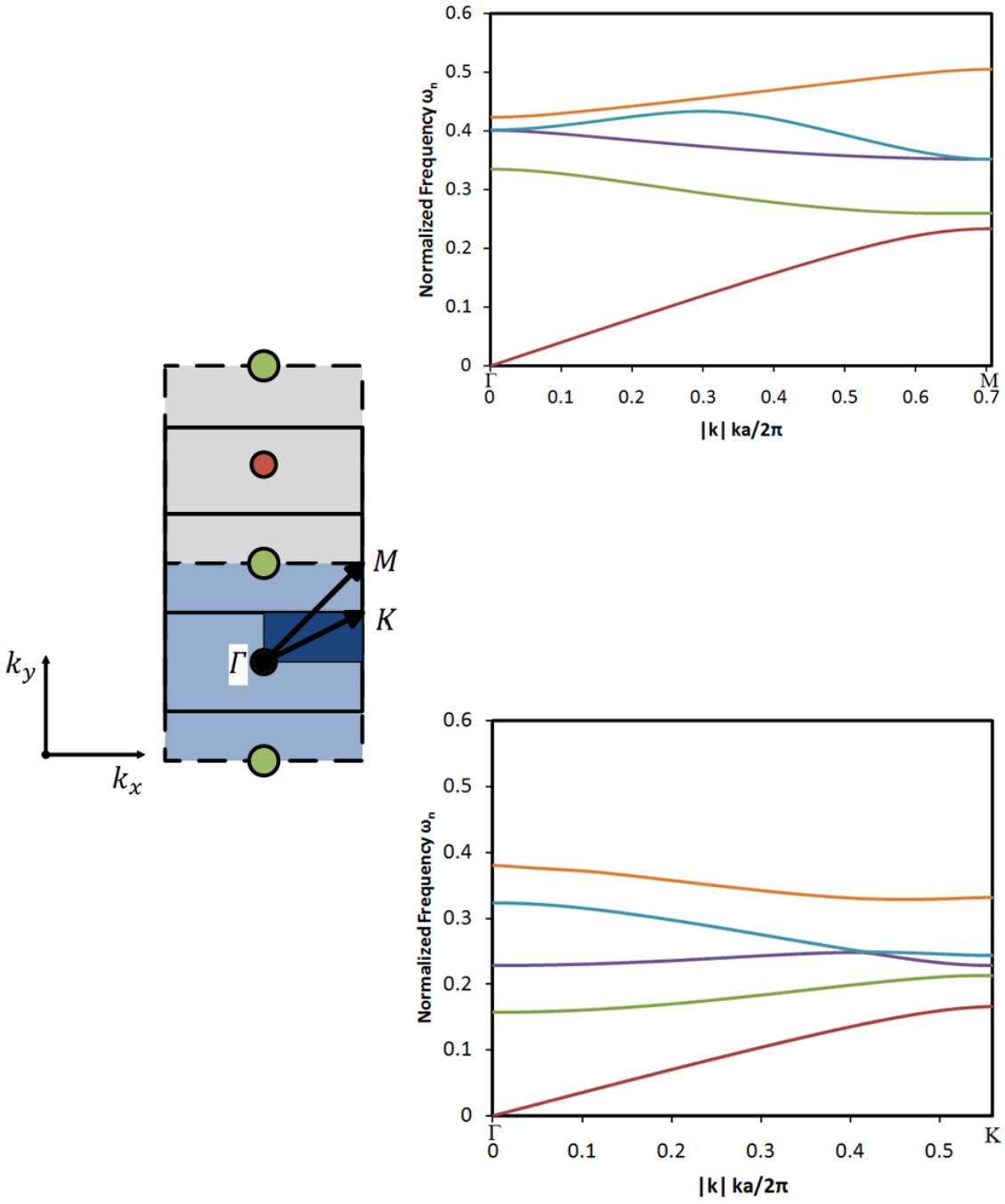

Figure 3-16: Band diagrams showing the Γ-M band in the square lattice and the new Γ-K band in the square superlattice.

In the case of the Γ-K direction, there is no folding, only a different band structure due to change in from direction from the Γ-M vector. Both band structures are shown in Figure 3-16, and have different shapes and different normalized k-vector lengths.

The changes in band structure due multiple crossings, anti-crossings (band repulsion effects), and the splitting of degenerate states in the superlattice structures lead to complicated device dispersion properties that will be investigated in the Chapters 4 and 5.

4 Photonic Band Properties of the Static Square Superlattice Photonic Crystal

4.1 The Superlattice Strength

Photonic crystals (PCs) possess a *k*-space dispersion surface, analogous to the Fermi surface, which is dramatically different from an isotropic material, opening up the possibility of giant refraction effects, huge dispersion (the superprism effect), and large modifications of the photon group velocity [48-53]. In a typical PC, these light propagation effects are passive since they depend upon refractive index, lattice period, and feature size. In our research, a simple modification to the square and triangular lattice PC enables these effects to be modified significantly from both a static and dynamic tunability aspect.

The concept of *superlattice strength* [45, 54-55] was first introduced in the work of Park and Summers [45] in a conference proceeding. In this work, a triangular lattice of holes with identical radii was index modulated by changing the refractive indexes of alternating rows of holes through the addition of electo-optic material inside them. In this case the change in refractive index Δn between rows of adjacent holes is dynamic when a bias is placed across them. Superlattice effects are observed in this structure when the structure factor is non-zero, indicating that the holes in rows i and j have different properties. In the case of the dynamic superlattice, the difference in properties between adjacent rows is the effective dielectric constant, which can be modified in real time by adjusting the level of bias that is placed on them dynamically. The figures included in Section 3.1 provide a reference for this structure.

For the static triangular and square superlattices, tuning can be initiated by using electro-optic material as the slab or hole in the device. The property difference between rows is the hole radius Δr. While the static superlattice refractive index properties cannot be changed in real time, the difference in hole sizes still leads to the observation of the superlattice effect, that is, a change in Δn between opposite rows of holes. The index difference becomes a function of the size of the smaller r_2 hole area or volume due to the addition of the higher index background material compared to the r_1 holes. The difference in hole radii $\Delta r = r_1 - r_2$ is referred to as the static superlattice strength and is designated by the ratio of r_2/r_1. The superlattice strength increases as the ratio of r_2/r_1 decreases. To provide a basis for comparison between the refractive effects of the triangular and square superlattice in this work, r_1 was held constant at 0.35a, while r_2 varied from 0.35a to 0.15a. The main body of work focuses on two different superlattice strengths: $r_2/r_1 = 0.30a/0.35a = 0.857$ and $r_2/r_1 = 0.20a/0.35a = 0.571$.

This chapter will focus primarily upon the analysis of the square superlattice structure band diagrams and dispersion contours for the superlattice strengths mentioned above to provide a basis for understanding static and active structure tuning analysis. The difference between Δn values obtained in a static superlattice versus an active superlattice structure will be discussed in more detail in the refractive index effects chapter.

4.2 Photonic Band Structure of an Ideal Square Superlattice

We begin our analysis of the photonic band structure of the square superlattice photonic crystal by considering the analysis of the structure by 2D models. This

approach allows the use of PWE methods that greatly reduce the band structure computation time while giving a concise model of the frequency behavior for a square or other superlattice device. The primary simulation tool used for the 2D analysis was MPB (MIT-Photonic-Bands). These simulations were initially computed using idealized material indexes to understand the general band structure of the device.

The 2D simulations are then repeated in the following sections using a more realistic material index stackup. Using a technique known as the effective index method, 3D FDTD simulations were run to obtain an approximate average index for the structure for a specific frequency range of interest. This index value is then substituted into the 2D PWE simulation to simulate the stackup, which in this case is the slab waveguide structure. The 3D FDTD simulations were computed using the FDTD method provided by the MEEP (MIT) program. Graphs are included for both the 2D and 3D simulations for comparison. Since the calculation time for the PWE simulations is shorter and has less stray points for nearly identical results over the frequency bands of interest, this was the main method used for band analysis.

The idealized 2D model consists of a unit cell structure of air holes (ε=1) in a high index Si background material (ε =12.0). The x and y dimensions of the cell are 1a by 2a, with the air hole r_1 located at (0,0) and the air hole r_2 at (0,1). Infinite boundry conditions are placed in the plane to simulate the overall device. As mentioned above, r_1 was held constant at 0.35a, while r_2 was varied from 0.35a to 0.15a. For identical holes sizes r_1 = r_2 = 0.35a, we obtain a double-sized version of the unit cell of a basic square lattice, which will show folding effects in this case since the BZ directions overlap. We are primarily interested in computing the bands for the square superlattice BZ direction as

described in Chapter 3. The superlattice effect we are interested in is exhibited as we reduce the size, and therefore the effective index, of the r_2 holes. The analysis of the band structure focuses on two different r_2 radius changes, creating two different superlattice strengths: $r_2/r_1 = 0.30a/0.35a = 0.857$ and $r_2/r_1 = 0.20a/0.35a = 0.571$. Figure 4-1 shows the geometry of the unit cell structure for square superlattice photonic crystal with a superlattice strength of 0.857.

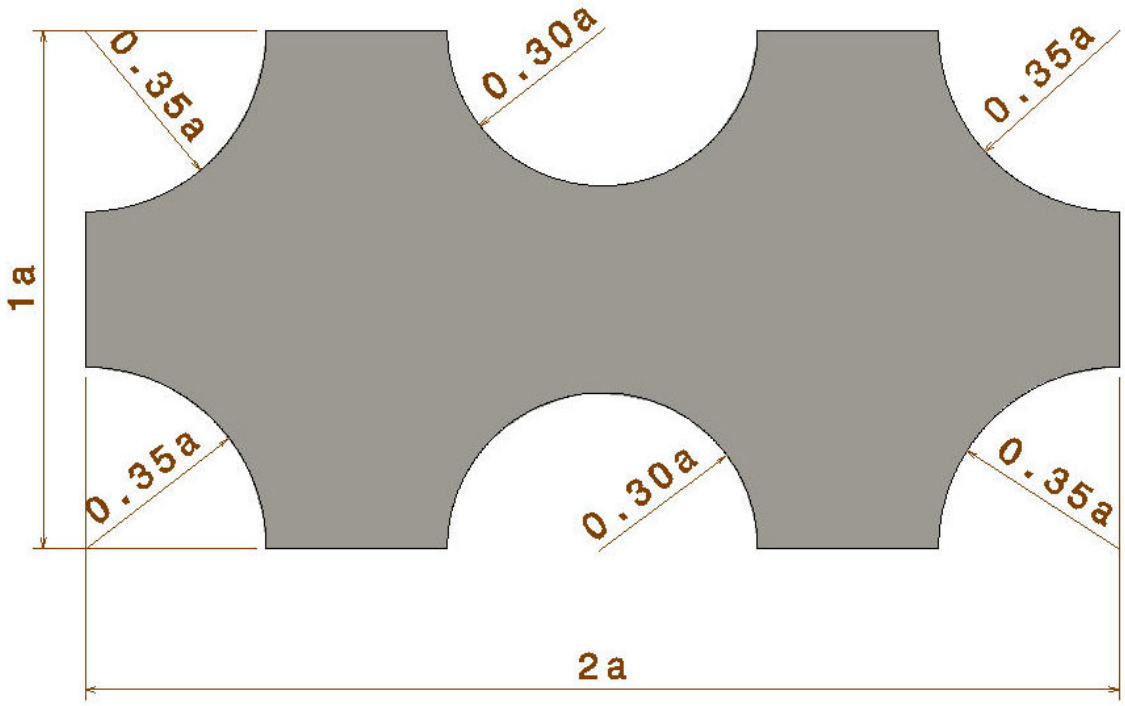

Figure 4-1: Diagram of the 2D square superlattice crystal structure with a superlattice strength of r_2/r_1 = 0.30a/0.35a = 0.857. This unit cell geometry is repeatedly used in many MPB simulations.

The first ten bands of the square superlattice for TE polarization and TM polarization were computed and are shown in the following six figures. In the case of the TE polarization, the electric field is parallel to the 2D plane of the device, normal to the magnetic field vector H_z following the normal photonic crystal convention. The TM

polarization conditions are simply the reverse of the TE vector directions, the magnetic field being parallel to the 2D plane of the device, normal to Ez. The TE polarization band diagrams are shown in Figure 4-2 for r_2/r_1 = 0.35a/0.35a = 1.0, Figure 4-3 for r_2/r_1 = 0.30a/0.35a = 0.857, and Figure 4-4 for r_2/r_1 = 0.20a/0.35a = 0.571. The TM polarization band diagrams are shown in Figure 4-5 for r_2/r_1 = 0.35a/0.35a = 1.0, Figure 4-6 for r_2/r_1 = 0.30a/0.35a = 0.857, and Figure 4-7 for r_2/r_1 = 0.20a/0.35a = 0.571.

As a general observation, we can note that the band structure for the r_2/r_1 = 1.0 in both polarizations is identical to the basic square lattice band structure, the difference being that the diagram shows folding effects due to the reduced BZ that is utilized in the analysis of superlattice band structure. In addition, as with the basic square lattice band diagram behavior, there are two full band gaps rather than a single full band gap that was seen in a basic triangular lattice band diagram [39]. The fact that there is no full TM band gap, only what will be referred to as a pseudo-band gap that covers a specific set of BZ directions, is indicative of the behavior of the basic square lattice where a full band gap exists for only one polarization. In the case of a lattice of air holes, full band gap behavior is exhibited only in the TE polarization condition. If the structure were reversed to create a square lattice of pillars in air, the situation would be reversed and the full band gap would occur only under TM polarization conditions.

Several observations regarding the superlattice influence on the band behavior of the structure can be made. First, the width of the both the first and second full PBG for the TE polarization bands decreases rapidly as the superlattice strength is increased. By the time the superlattice strength reaches approximately 0.85, the gap running from Γ-X-K closes completely. At this point the full TE PBGs reduce to pseudo-bandgaps covering

only the first section of the band diagram. Further increasing the superlattice strength results in a reduction in the width of the remaining pseudo-PBGs. In the case of the TM band structure, there are no full PBGs, thus the effect of increasing the superlattice strength only reduces the width of the pseudo-PBGs. This effect is similar to that seen in the TE polarization bands when the full PBGs close and the structure is reduced to pseudo-PBGs. We can examine the rate of decrease in the width of the TE PBGs as

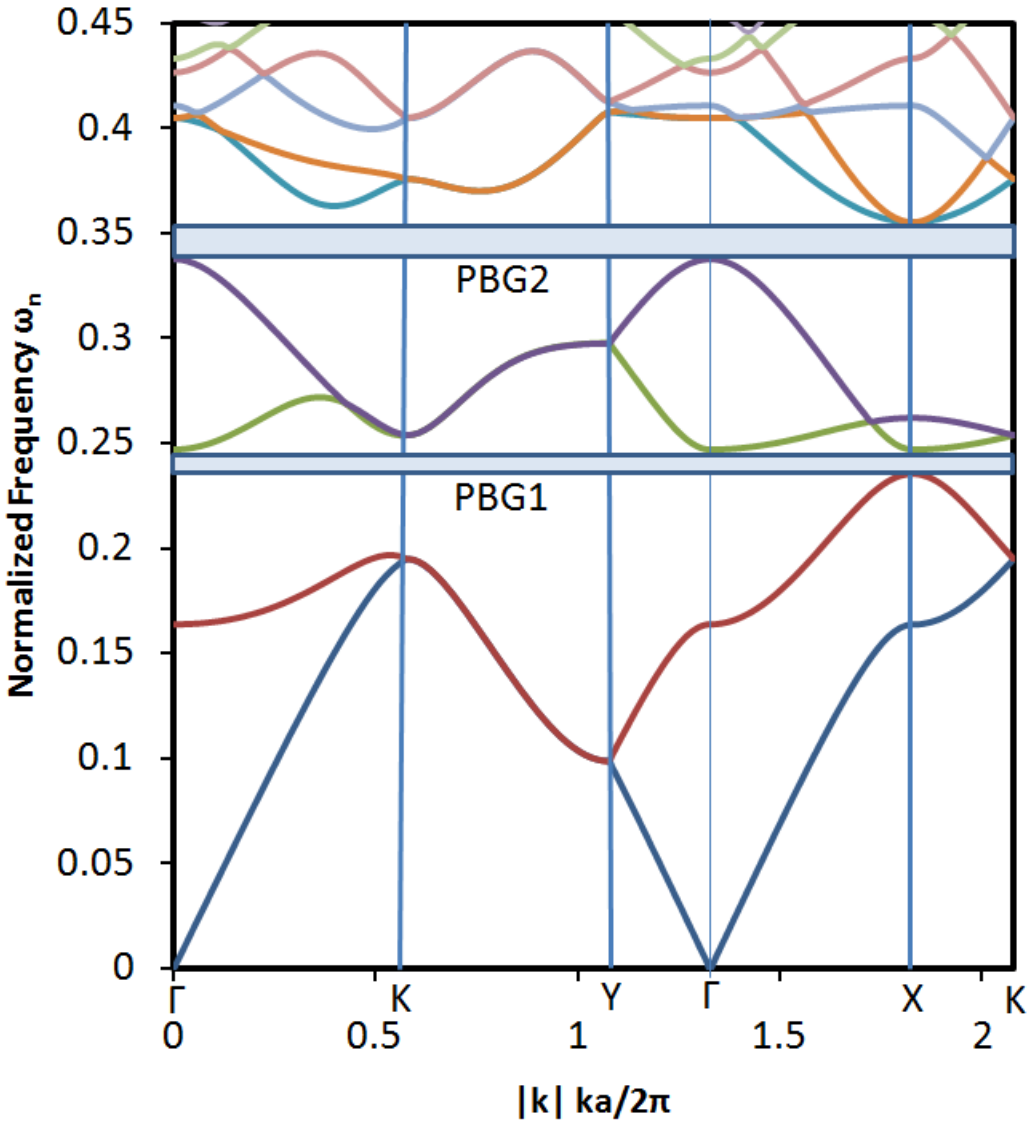

Figure 4-2: Photonic band structure plot for TE polarization condition for the case where r_2/r_1 = 0.35a/0.35a = 1.0.

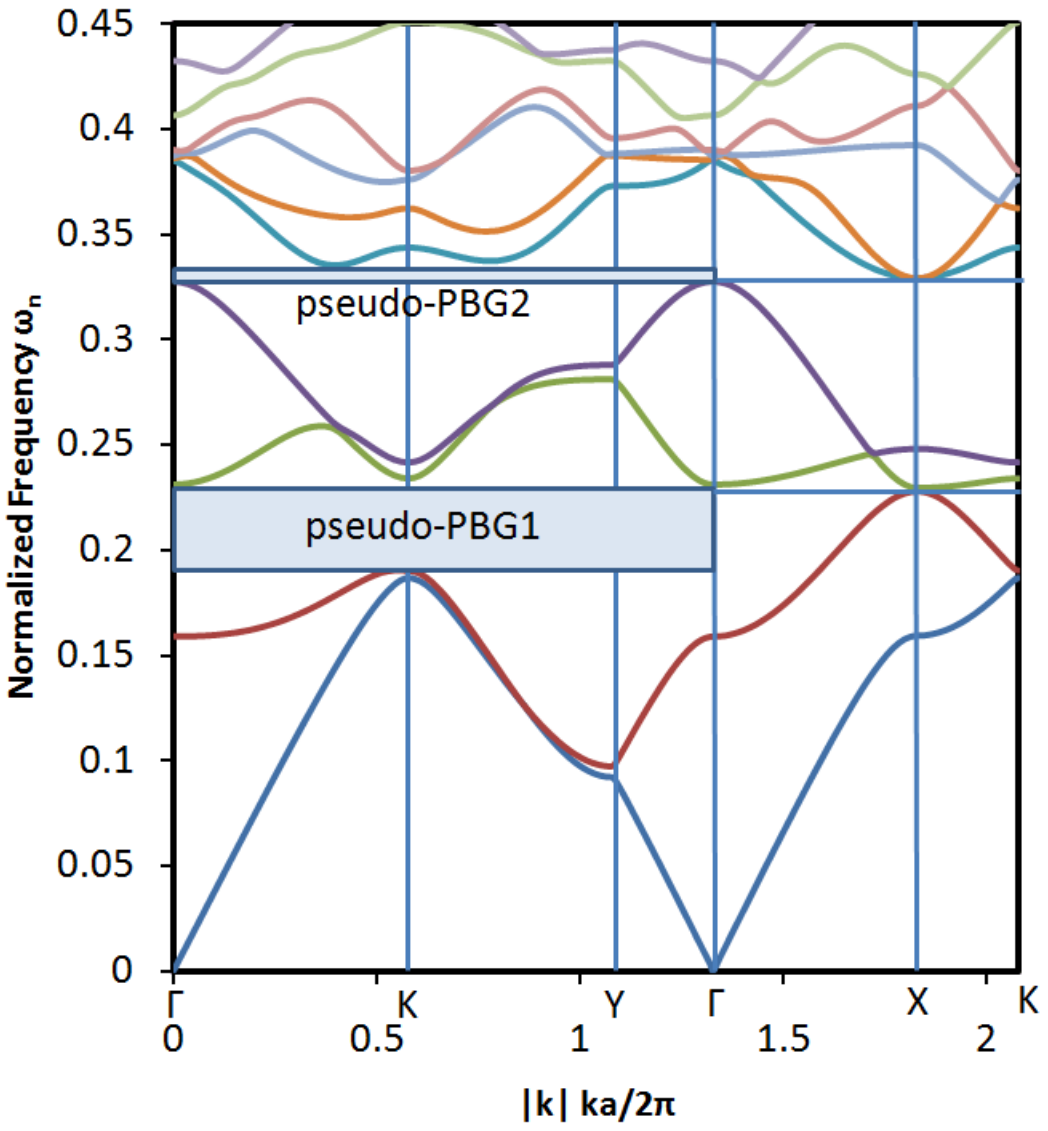

Figure 4-3: Photonic band structure plot for TE polarization condition for the case where r_2/r_1 = 0.35a/0.30a = 0.857.

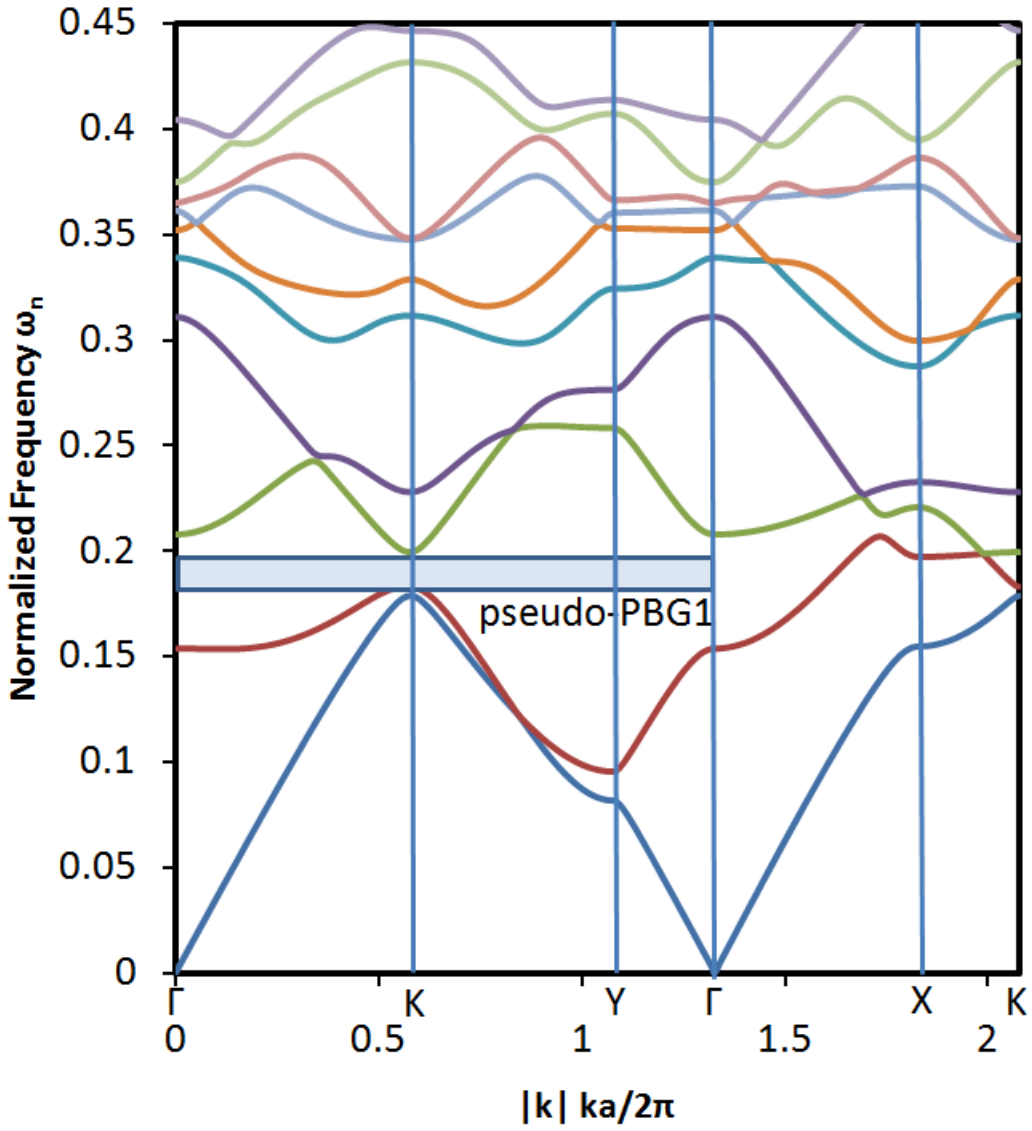

Figure 4-4: Photonic band structure plot for TE polarization condition for the case where r_2/r_1 = 0.35a/0.20a = 0.571.

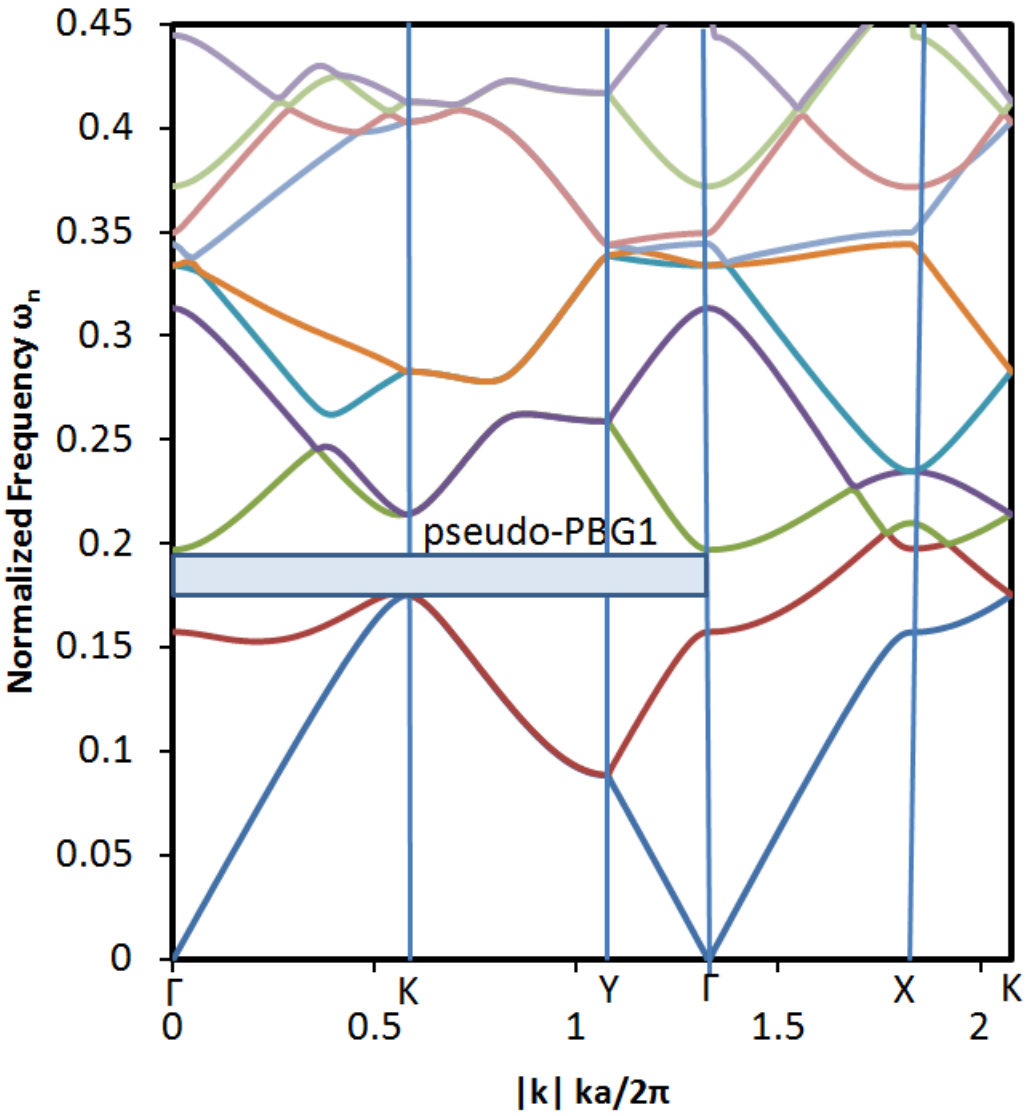

Figure 4-5: Photonic band structure plot for TM polarization condition for the case where r_2/r_1 = 0.35a/0.35a = 1.0.

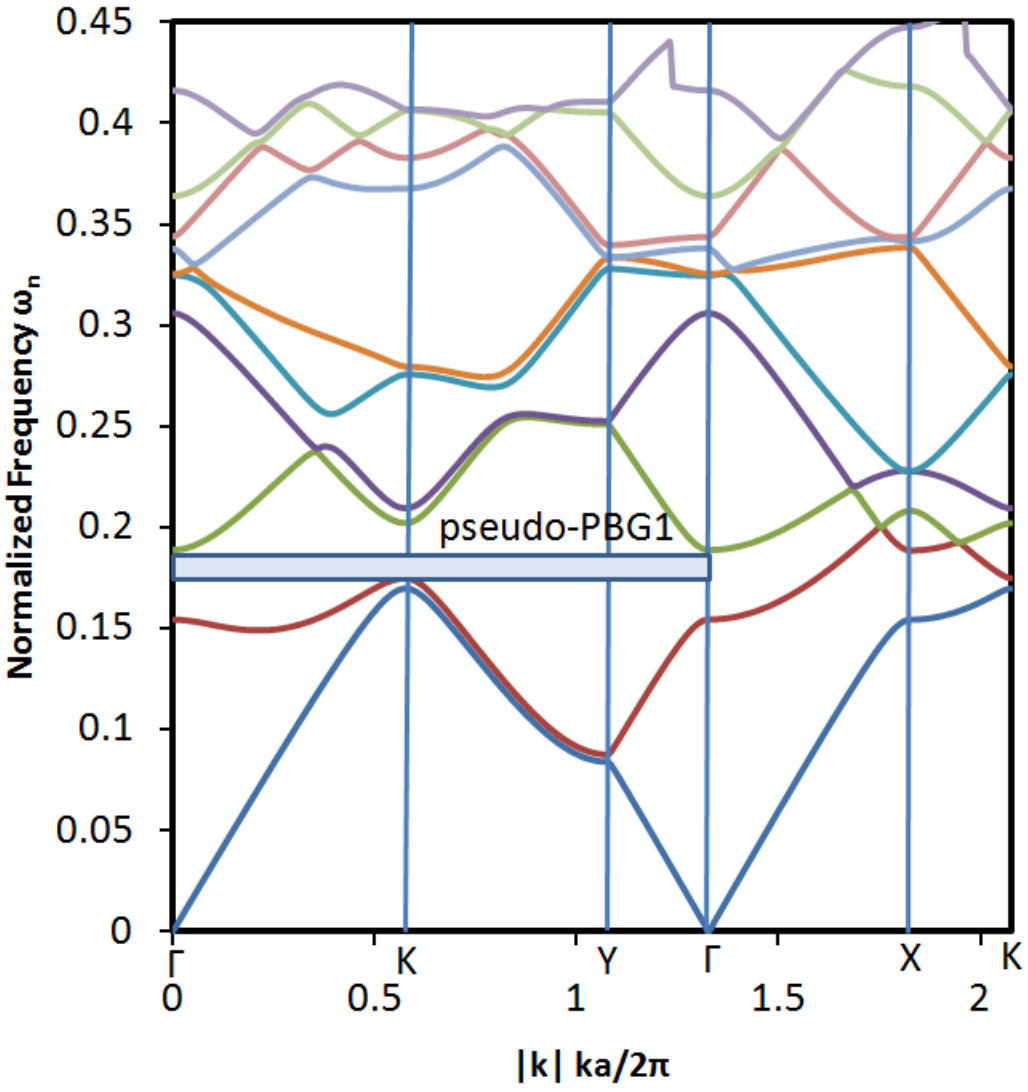

Figure 4-6: Photonic band structure plot for TM polarization condition for the case where r_2/r_1 = 0.35a/0.30a = 0.857.

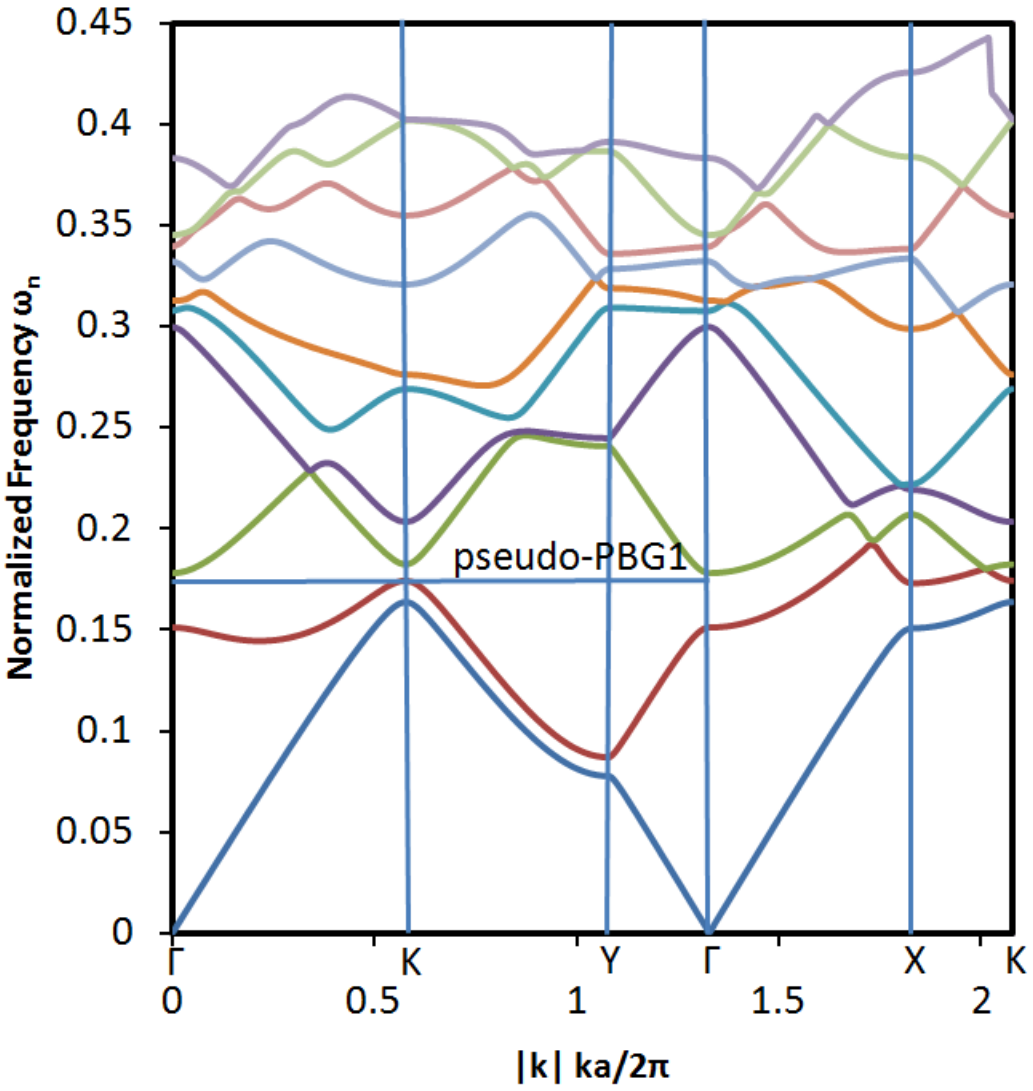

Figure 4-7: Photonic band structure plot for TM polarization condition for the case where r_2/r_1 = 0.35a/0.35a = 0.571.

function of superlattice strength. In this case we look at the normalized frequency difference between the lower band limit at the Γ point and the upper band limit at the X point, which are the upper and lower boundaries that determine the width of the PBGs. Figure 4-8 plots the width change of the first full PBG for TE polarization as a function of increasing superlattice strength. Similarly, Figure 4-9 shows the same width change for TE polarization of the second full PBG as a function of increasing superlattice strength. The plots are shown for three different initial superlattice strengths of $r_1 = 0.4$ and 0.35, where r_2 is varied. No full PBGs exist for $r_1 = 0.3$. As shown in the graphs, the width of both PBGs decreases rapidly as the superlattice strength is increased. For a superlattice strength change of 1 to 0.857 and a given $r_1 = 0.4$, the width of the first PBG decreases by 57.7%, while that for the second PBG decreases by 61.1%. Increasing the superlattice strength to 0.571 completely eliminates the first and second full PBG for $r_1 = 0.4$, so the effect of further increasing the superlattice strength reduces the full PBGs to pseudo-PBGs.

Another observation of the square superlattice band behavior is that several of the upper bands split inside the BZ. This behavior can be found in bands for both TE and TM polarizations. Of special interest are bands three and four, which split apart as the superlattice strength is increased at the K-point. In keeping with work done on the triangular superlattice [39], the third band is designated as the 3s band and the fourth band as the 3p band. This nomenclature was chosen because the field patterns for these bands resemble atomic orbitals, as we will see shortly.

This band splitting is detailed in Figure 4-10 that shows both bands for TE polarization, and in Figure 4-11 for the TM polarization condition. The dashed ellipse

highlights the area of interest, showing that for a superlattice strength of unity the bands are joined at the K-point, but gradually separate as the square superlattice strength is increased.

We analyze the amount of band splitting as the superlattice strength is increased at the K-point by a method similar to the PBG width analysis. By holding r_1 fixed at r_1 = 0.4, 0.35, and 0.3, and varying r_2, plots of the splitting variation were obtained as a function of superlattice strength. This is illustrated in Figure 4-12 for the 3s-3p TE bands in Figure 4-13 for the 3s-3p TM bands. As evidenced in the graphs, the magnitude of splitting is proportional to the relative difference between the hole sizes r_1 and r_2. All the curves show a similar trend towards a greater degree of band splitting as the superlattice strength is increased.

To further investigate the underlying basis for band splitting behavior in square superlattice photonic crystal, we turn to the field patterns of the device to investigate the electromagnetic energy distribution. We start by analyzing the H_z field component of square lattice photonic crystal structure under TE polarization conditions to serve as a basis for this investigation. The H_z component of the TE field was chosen for visualization because it is normal to the 2D plane of the structure, yielding views of the E_x and E_y fields in the crystal.

Field patterns plots of photonic bands 3 and 4 for a standard dimensioned 1*a* x 1*a* unit cell square lattice are shown in Figure 4-14(a) and Figure 4-14(b), respectively. The air holes are referenced by black circle outlines in the figures, labeled rows *i* and *j*, in keeping with the superlattice crystal structure convention. Regions of positive field amplitude are shown in red and marked with '+' signs, while those of negative field

amplitude are shown in blue and marked with '-' signs. Zero crossings, or nodes, are indicated by white values, indicating zero field amplitude at these points. In these plots, the harmonic field pattern has phase fronts that are normal to the Γ – K direction. The fields are primarily concentrated in the dielectric region surrounding the holes, with nodes inside the holes indicating little field energy present in the air regions. When transversing across a single *i* or *j* row of holes in a horizontal direction, the field oscillates between positive and negative amplitudes between each hole. Also, oscillation occurs in the horizontal direction.

By changing the square lattice unit cell to a 1*a* x 2*a* dimension, a square superlattice photonic crystal structure is effectively created with a superlattice strength of 1.0. The energy distributions are shown in Figure 4-14 (c) for band 3, the 3s band, and Figure 4-14 (d) for band 4, or the 3p band. When these fields are summed, the field pattern matches that of band 3 in the 1x1 square lattice shown in Figure 4-14 (a). It has been proven that the summed energy density of the 3s and 3p field in the triangular superlattice are equal to the energy density of band 3 of the original triangular lattice in work conducted by C. Neff [39]. Although the same calculation has not been performed here, in the case of the square superlattice the results appear nearly identical in comparison to the earlier work. The summed energy density match provides evidence that the 3s and 3p bands are degenerate. This degeneracy is manifested by the fact that the two field patterns are identical under transitional symmetry.

We now investigate the effect of the superlattice strength on the field distribution in the square superlattice photonic crystal structure. Figure 4-15 (a) and (b) show the field patterns for a superlattice strength of 0.857. As the dielectric area around the

smaller holes in row j is increased, the field intensities are redistributed within the high dielectric constant of Si to take up the additional space available to support the degenerate modes. This reshaping is a consequence of the Variational Theorum in electromagnetics, which infers that high-frequency modes will remain and are carried in areas of high dielectric constant. In this case the modes take on a more rectangular shape as the r_2 hole size is reduced. Further reduction of the superlattice strength to 0.571 increases the rectangularity of the modes, as illustrated in Figure 4-15 (c) and (d). These rectangular mode shapes are not similar to the orbital shapes found in the triangular superlattice work, but the 3s and 3p orbital notation will continue to be used for consistency with the previous work.

While the 2D PWE is completely accurate for bands under the light line, i.e. the guided modes, it is not as accurate for the unguided modes above the light line. Since we are primarily interested in the guided modes of the 3s and 3p bands of our structure for refractive purposes in a real-world device, the PWE simulation will suffice for modeling purposes. However, we require a more realistic model of the device to accurately simulate device behavior for a series of fabricated devices. To accomplish this we have used a comprehensive series of 3D FDTD simulations and the effective index method in the next section. The effective index method enables us to take into account the finite thickness of a fabricated device by providing an average index that accurately and effectively models an actual 3D device.

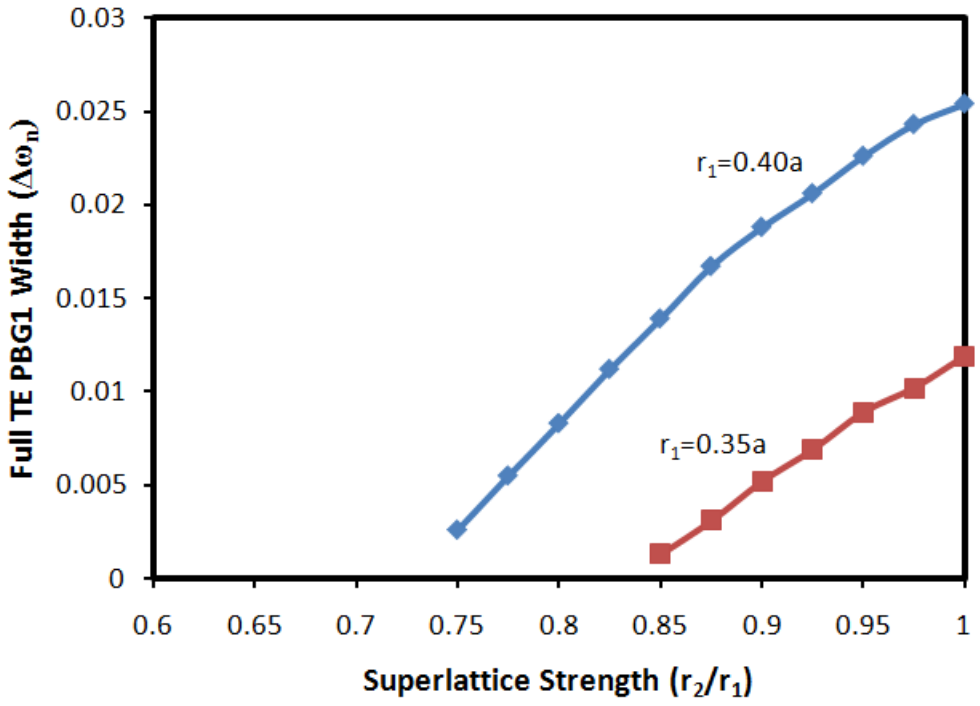

Figure 4-8: Plot detailing the effect of the square superlattice strength on the width of the first full TE PBG for r1 = 0.4 and 0.35.

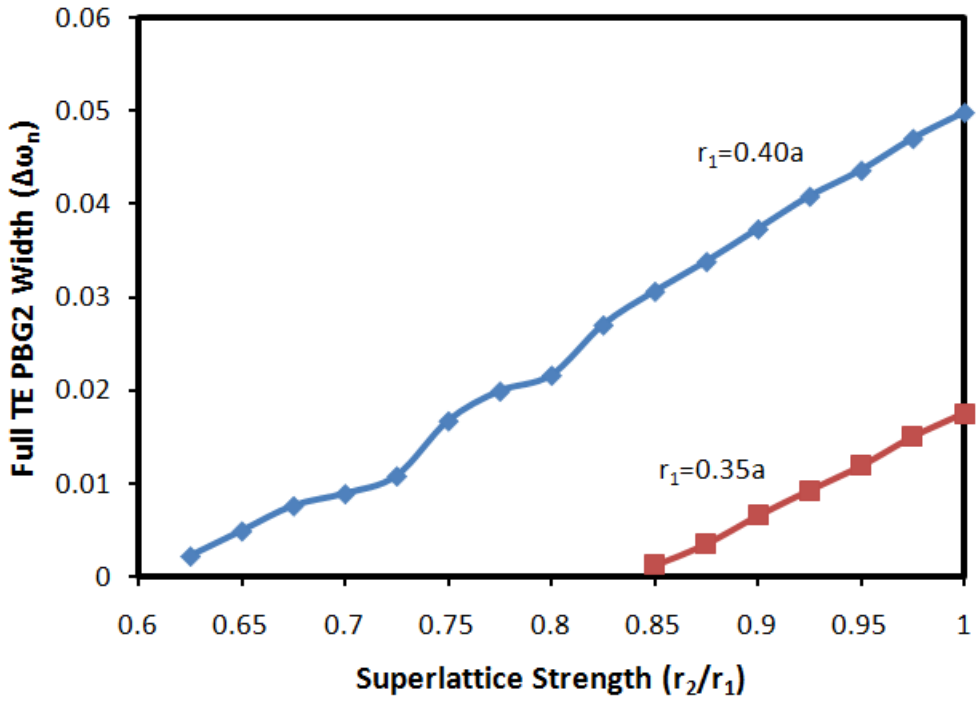

Figure 4-9: Plot detailing the effect of the square superlattice strength on the width of the second full TE PBG for r1 = 0.4 and 0.35.

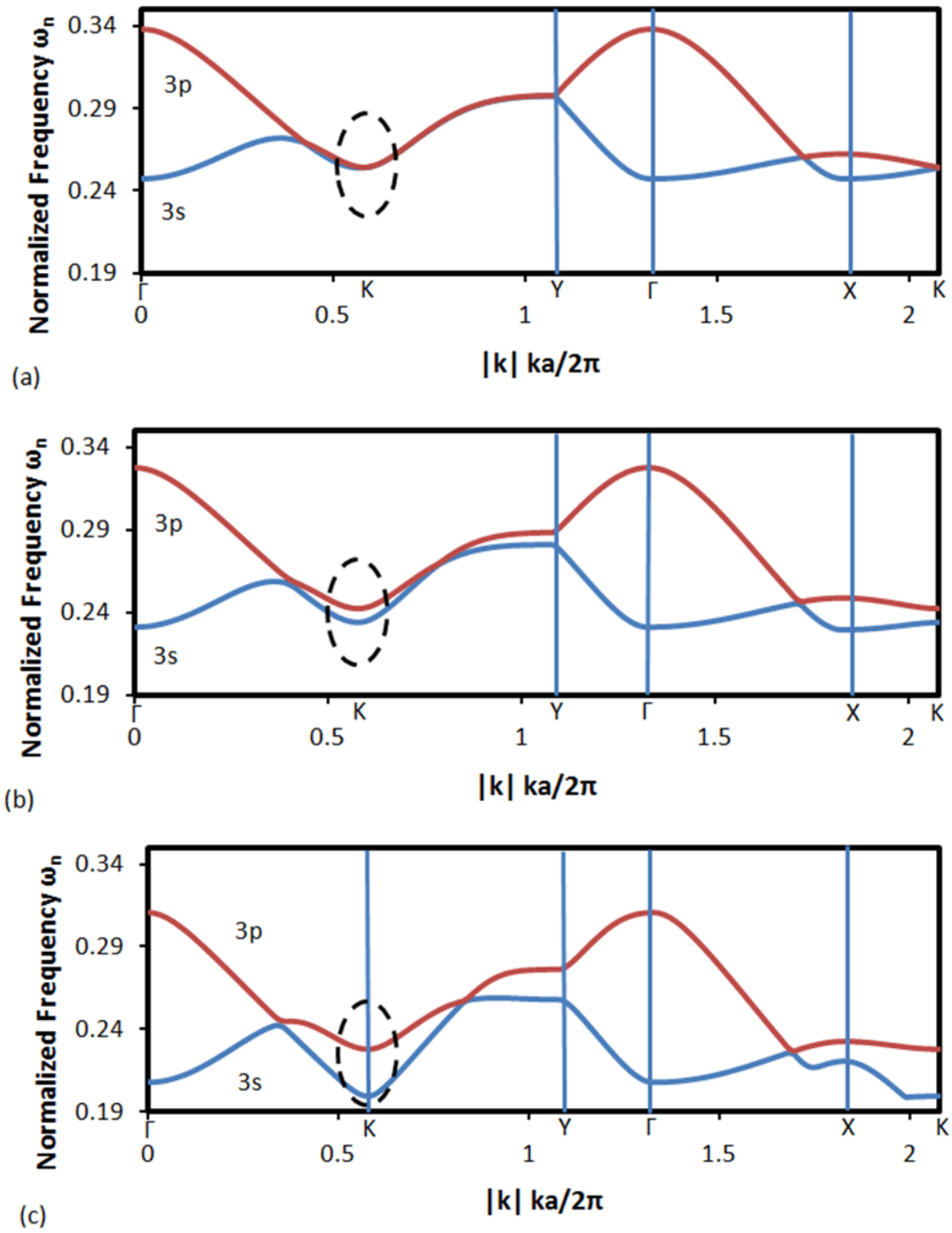

Figure 4-10: Detailed plots of the TE square superlattice band structure for the 3s and 3p bands for superlattice strengths of (a) 1.0, (b) 0.857, and (c) 0.571, illustrating the band splitting effect.

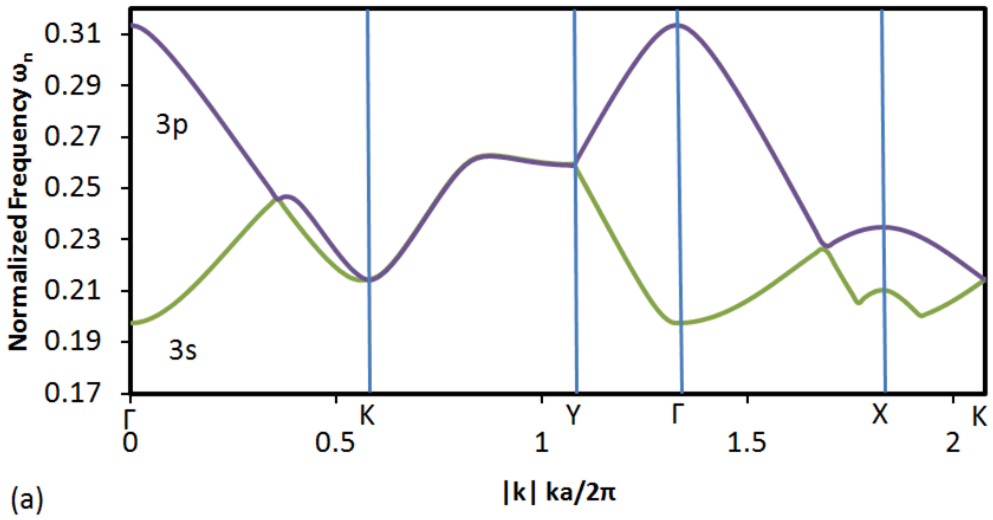

(a)

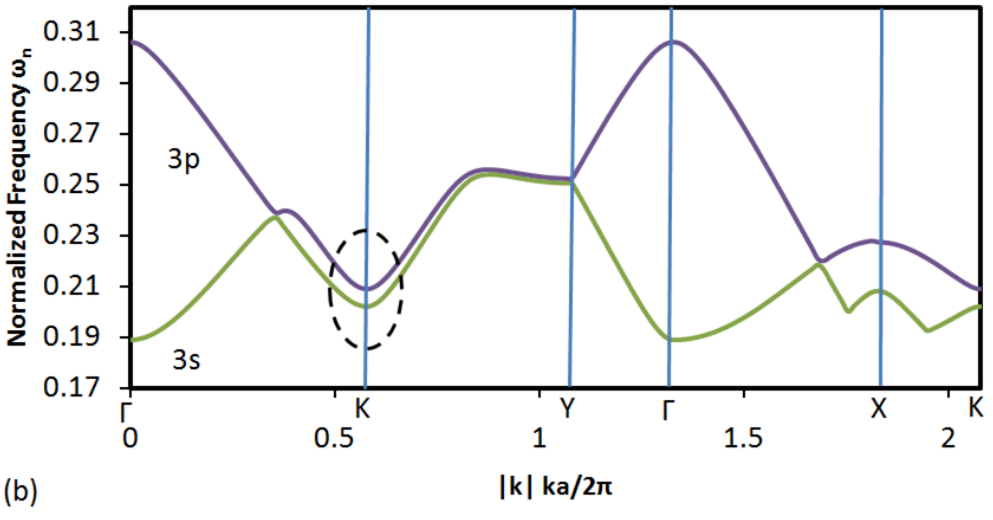

(b)

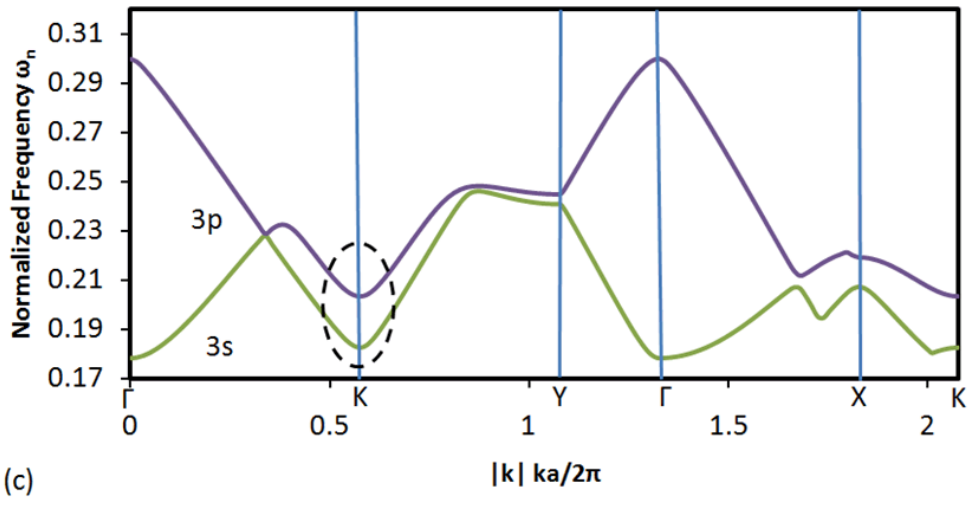

(c)

Figure 4-11: Detailed plots of the TM square superlattice band structure for the 3s and 3p bands for superlattice strengths of (a) 1.0, (b) 0.857, and (c) 0.571, illustrating the band splitting effect.

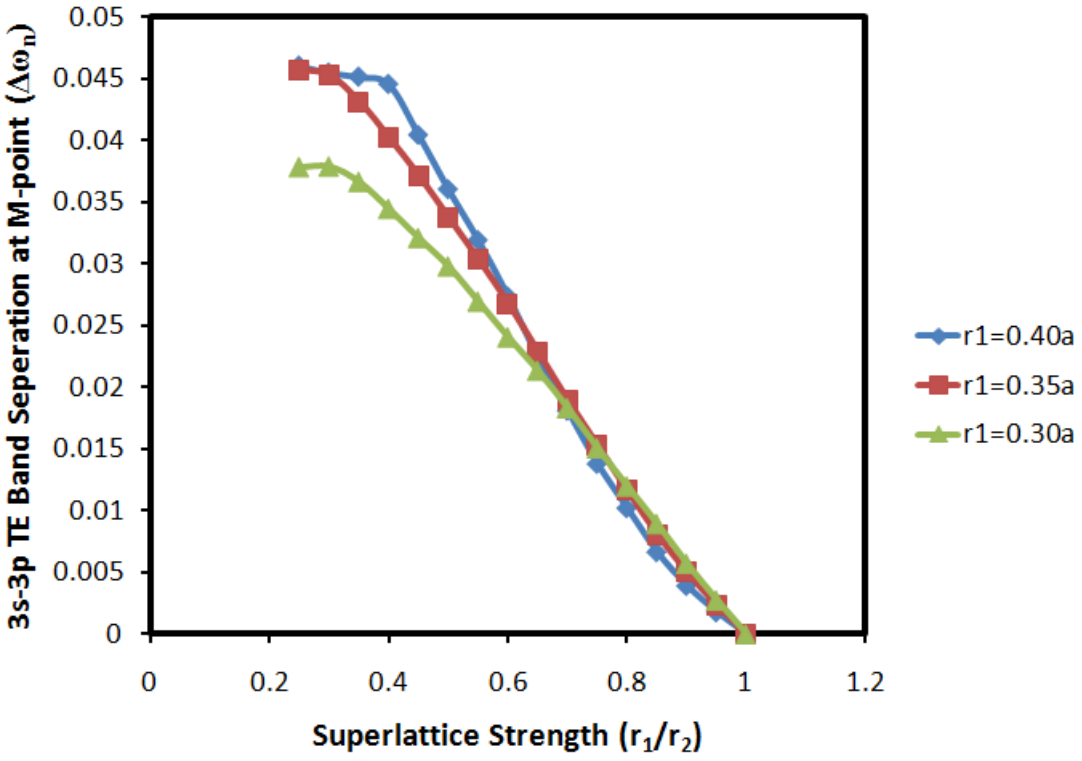

Figure 4-12: Variation of the frequency gap between the 3s (band 3) and 3p (band 4) bands at the K point with square superlattice strength for r1 = 0.4, 0.35, and 0.3 for TE polarization.

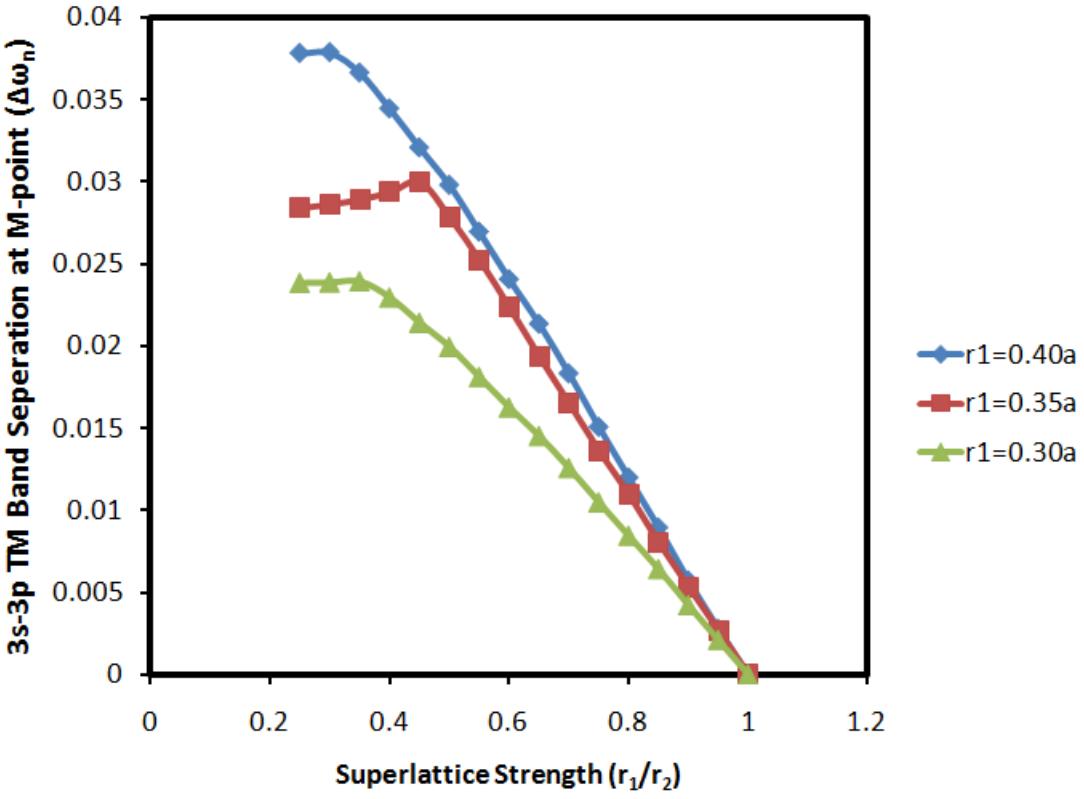

Figure 4-13: Variation of the frequency gap between the 3s (band 3) and 3p (band 4) bands at the K point with square superlattice strength for r1 = 0.4, 0.35, and 0.3 for TM polarization.

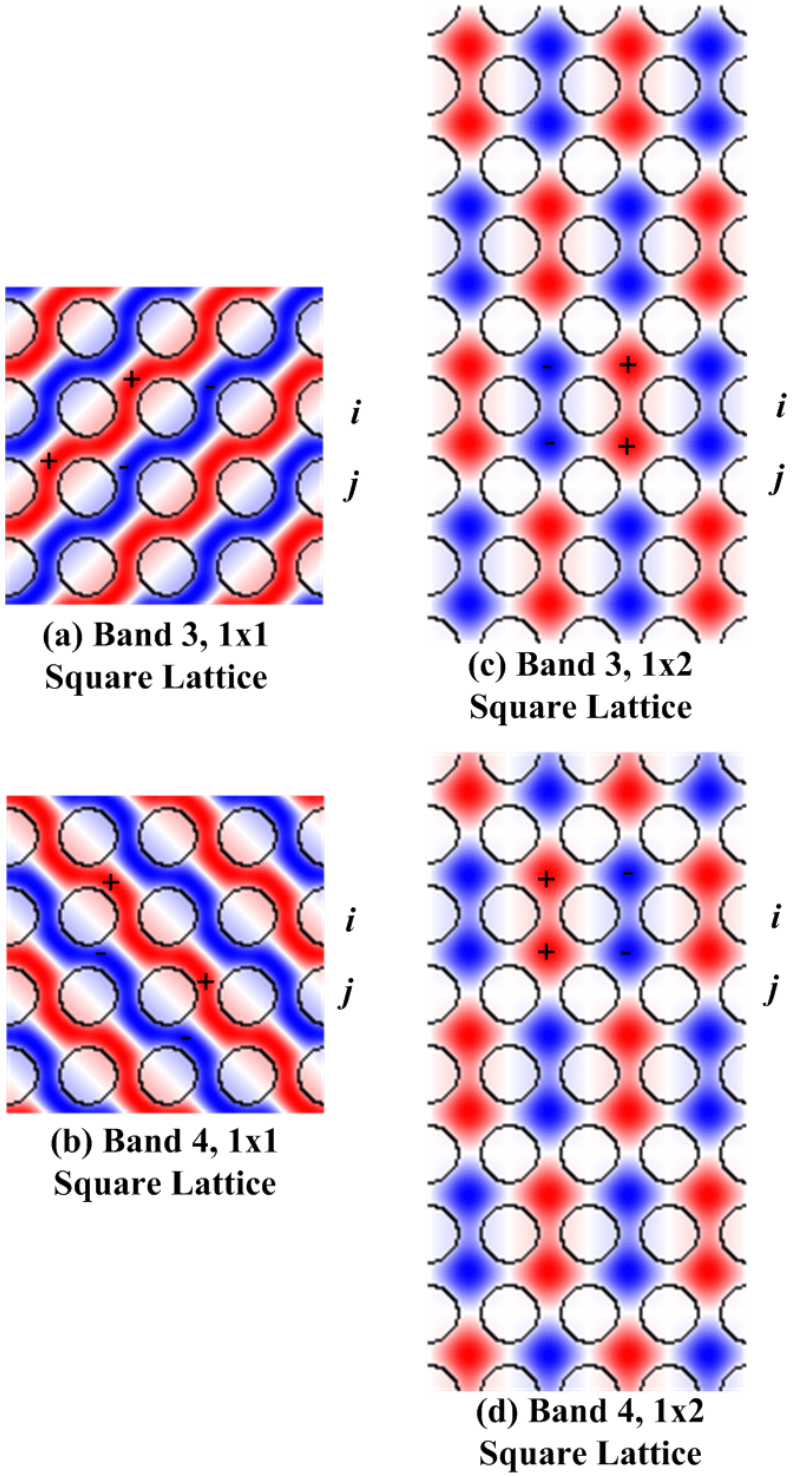

Figure 4-14: Field profiles of the square lattice photonic crystal structure for bands 3 (a) and 4 (b) for a 1x1 unit cell with TE polarization conditions, showing the H_z field component. After changing to a 1x2 unit cell to simulate square superlattice conditions, the field profiles for bands 3 (c) and 4(d) are modified significantly.

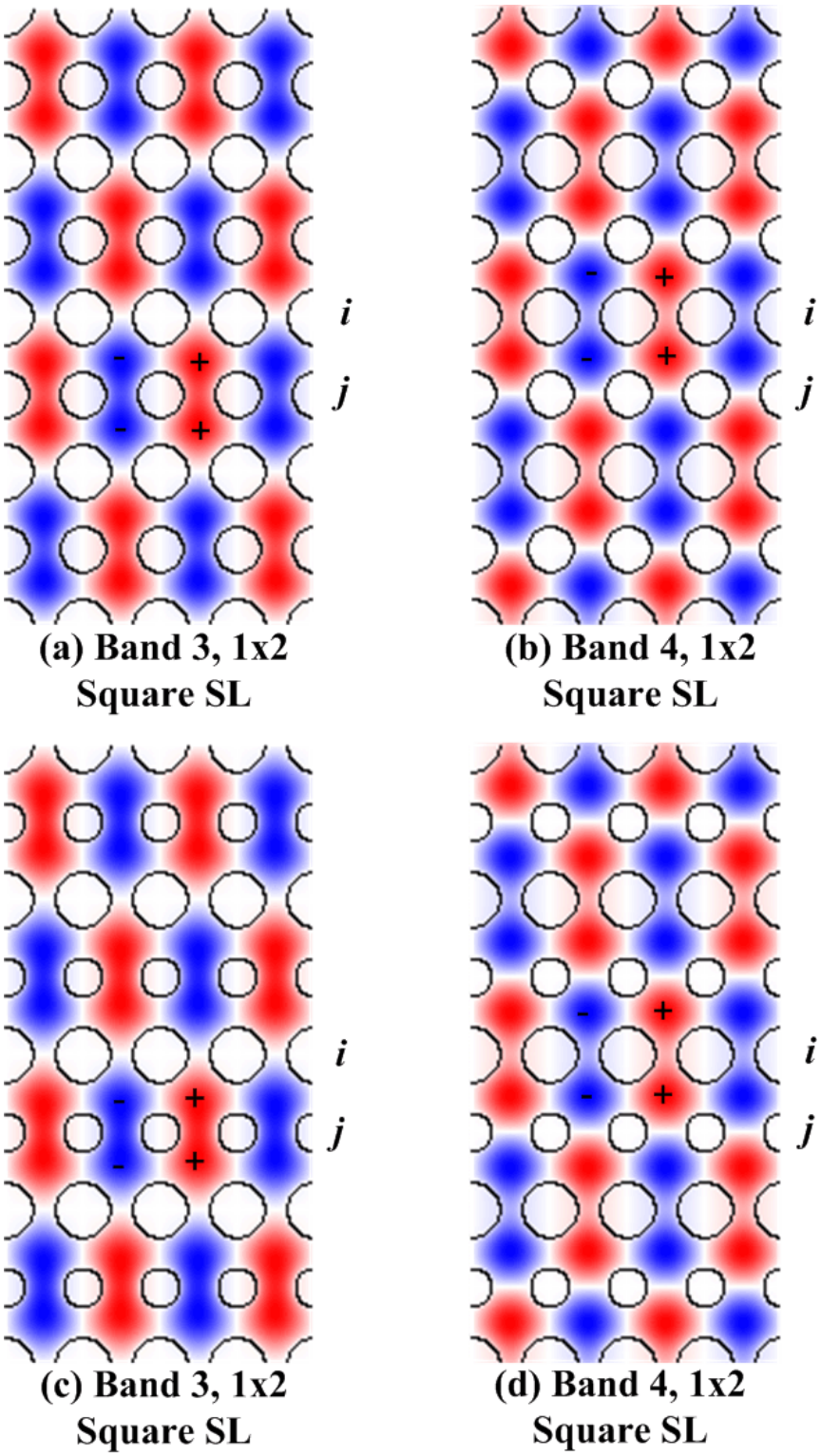

Figure 4-15: Field profiles of the square superlattice lattice photonic crystal structure for bands 3 (a) and 4 (b) for a 1x2 unit cell with TE polarization conditions and a superlattice strength of 0.857, showing the H_z field component. Similar profiles are shown for a superlattice strength of 0.571 for bands 3 (c) and 4(d).

4.3 Photonic Bands of a 3D Slab Waveguide Square Superlattice Structure

We now focus on a more realistic 3D model of the square superlattice device that better matches an actual fabricated device, known as the slab waveguide stackup. This stackup is illustrated in Figure 4-16. It consists of a slab of Si with a height of h = 0.5a and an index of n = 3.464 (ε = 12.0) surrounded top and bottom by 2a air layers (n = 1.0). No holes are present in this simulation as we are only interested in getting the effective, or average index, of the layered structure that the device will be fabricated on. Holes will be incorporated in the 2D simulated structure once we have the effective index of this stackup. This layered structure is similar to the SOI (silicon-on-insulator) stackup that is used to fabricate the device, the only difference being that the bottom layer is SiO2 (n = 1.5) rather than air. The difference between the two layered stackups, in terms of average index, is fairly small so the simpler slab waveguide stackup is adequate for 3D modeling purposes. This particular stackup will provide the basis for refractive index calculations in the following chapter, to provide better accuracy in computing the refractive properties of an actual fabricated square superlattice device.

In the 3D model infinite boundary conditions are used in the plane of the slab, and PML (perfectly-matched-layers) are used in z-axis of the device. The PML layers provide absorption for unguided electromagnetic energy that may reflect off the upper and lower boundaries of the unit cell. To further simplify the band analysis, we place the source at z = 0, which results in only the odd-symmetry TM bands being captured.

A plot of the FDTD solutions for the TM bands is shown in Figure 4-17 for a superlattice strength of r_2/r_1 = 0.30a/0.35a = 0.857. A comparison of both the idealized 2D PWE solution and the 3D FDTD solution for the same geometry is shown in Figure

4-18. It becomes more difficult to understand how the bands separate in the 3D FDTD simulation due the scattered nature of the solutions compared to the 2D PWE simulation where the solutions are categorized by band number. The solutions in the FDTD method are scattered because they are computed by performing a Fourier transform (FT) on single k-points, resulting in erroneous points due to insufficient filtering in the spectral analysis. Note that the solutions are not identical, especially for the bands above the light line. In the case of the 3D simulation, the bands shift upwards as compared to the 2D simulation. This is due to the fact that the average index of the structure, as "seen" by the source, is lower than that of pure Si due to the inclusion of the air layers. Also note that splitting (less degeneracy) between the 3s and 3p bands increses in the 3D simulation which more accurately reflects the behavior of an slab waveguide device.

The 3D model is accurate for both the guided and unguided modes, unlike the 2D PWE method, but is much more computationally intensive. Another drawback to the 3D simulation is the band data is scattered due to computation of stray solution points. Some of these stray points are actually light line solutions, but most are errant points that are especially evident in the computation of the upper bands. We need to keep the band data categorized according to the band number as in the 2D PWE simulations, while combining this with the band data accuracy of the 3D FDTD band computations. This is accomplished by use of the effective index method described in the next section.

4.4 The Effective Index Method

It is necessary to accurately match the 3s and 3p band guided modes between the two simulations in order to precisely perform device refractive behavior analysis. In order to effectively shift the 2D bands upwards to match the 3D solution in the frequency range of these two bands, we must calculate the average index of the 3D slab waveguide structure. This was performed by an effective index analysis using the exact same 3D geometry, but removing the holes to create a bare slab structure. A 3D simulation of the bare structure was then performed from which the average index of entire stackup can be calculated. In the 3D effective index simulation we are only interested in the lowest band, which is the longest wavelength solution that effectively "sees" the stackup as an average effective index. To accurately perform this we extended the Γ – K direction out in BZ space so as to have enough points to calculate a straight line index change versus *k*. A calculation of the TM bands for the slab waveguide structure for the three repeated BZs is shown in Figure 4-19. The path of the lowest band is traced out using lines and is shown. Then we took each k-point on this lowest band line and created a table with its corresponding normalized frequency value ω. The effective index at each point was then calculated from:

$$n = \frac{k}{\omega} \tag{77}$$

The effective slab thickness for each index was then calculated based on the operating wavelength of interest for the device. Here we choose an operating wavelength of λ = 1500nm which is commonly used in telecommunications devices, and is compatible with optical fiber operating frequencies. The normalized slab thickness in our case is 0.5a, thus the effective index can be calculated by:

$$effective\ thickness\ (nm)$$

$$= \lambda * normalized\ slab\ thickness\ (0.5) * \omega \tag{78}$$

This calculation is shown in Table 1:

Table 1: Effective index and effective thickness calculations for the our slab waveguide structure.

k (norm)	ω (norm)	effective *n* (= *k*/ω)	effective ε (= *n*^2)	thickness based on fixed wavelength of 1500nm (= 1500nm * norm. slab thickness (0.5) * norm. ω)
0				
0.044118				
0.088235	0.087532	1.008036512	1.01613761	65.64888254
0.132353	0.126354	1.047481356	1.09721719	94.76512909
0.176471	0.166409	1.060462112	1.124579892	124.8068551
0.220588	0.201082	1.097007002	1.203424363	150.8114134
0.264706	0.224874	1.177129078	1.385632866	168.6556007
0.308824	0.243557	1.26797028	1.607748631	182.668041
0.352941	0.257747	1.369329619	1.875063607	193.310565
0.397059	0.269517	1.473225086	2.170392155	202.1375555
0.441176	0.279875	1.576333717	2.484827986	209.9062841
0.485294	0.289444	1.676644909	2.81113815	217.0826908
0.529412	0.298577	1.773117076	3.143944164	223.9326602
0.573529	0.307485	1.8652265	3.479069896	230.6138471
0.617647	0.316302	1.952710094	3.813076713	237.2268651
0.661765	0.325332	2.034118773	4.137639184	243.9992865
0.705882	0.333965	2.113643522	4.467488937	250.473535
0.75	0.342895	2.187258749	4.784100834	257.1712196
0.794118	0.351923	2.256507665	5.091826844	263.9424826
0.838235	0.361062	2.321581843	5.389742255	270.7966003
0.882353	0.370316	2.382703544	5.677276176	277.7369042
0.926471	0.379688	2.440086158	5.95402046	284.7657403
0.970588	0.389178	2.493946079	6.219767043	291.883286
1.014706	0.398782	2.544513188	6.474547363	299.0864482
1.058824	0.408499	2.59198616	6.718392256	306.3741849
1.102941	0.418322	2.636583342	6.951571719	313.7416023
1.147059	0.429474	2.670847272	7.133425149	322.1053209
1.191176	0.438268	2.717915731	7.38706592	328.7012702
1.235294	0.448381	2.755007932	7.590068706	336.2859967
1.279412	0.458579	2.789947736	7.78380837	343.9343365
1.323529	0.4708	2.811237719	7.90305751	353.0996515
1.367647	0.47921	2.853963019	8.145104916	359.4073529
1.411765	0.489632	2.883315869	8.313510402	367.2242576
1.455882	0.495074	2.940737404	8.647936477	371.3054295
1.5	0.504	2.976190476	8.857709751	378

Now that we have the table of effective index values versus their effective thickness, we can select the frequency range of the 2D PWE bands of interest that we wish to match. In this case we are interested in index matching the 3s and 3p bands in the 3D simulation which lie in the normalized frequency range of ω = 0.35 to ω = 0.45. Note that the effective index value obtained is frequency specific and only valid around the point ±0.5ω, outside of which the accuracy of the band match is degraded. We choose the best operating frequency that in turn provides the best 2D band match around this frequency range. This is done by calculating the lattice constant a for the several different source frequency values:

$$a = \lambda * f_{normalized} \tag{79}$$

The effective slab thicknesses are then calculated by multiplying this by 0.5, the normalized thickness value chosen in our simulation. Table 2 shows the results of this calculation:

Table 2: Calculated lattice constant a and effective slab thickness 0.5a for various source frequencies centered around the 3s and 3p bands.

ref.	λ (nm)	source frequency f (normalized)	$a = \lambda * f$ (nm)	$0.5a$ (nm)
a	1500	0.35	525	262.5
b	1500	0.375	562.5	281.25
c	1500	0.4	600	300
d	1500	0.45	675	337.5

We can now calculate the effective index given the effective 0.5a slab thickness values. This calculation is performed by plotting the effective index curve versus the effective thickness from the 3D FDTD calculations in Table 1. This is shown in Figure 4-20, and is labeled by the reference number for each source frequency point. The

intersection between the TM effective index curve at lines a - d provides the effective index values for each 3D source frequency. A list of the effective index values we obtain is shown in Table 3. The resulting values were obtained from linear interpolation between points in Table 1.

These effective index values, are then substituted for the index of Si in the 2D MPB simulations. Four 2D simulations were run using the values of effective index for points a - d in Table 2, in order to find the index that best matches both the 3s and 3p bands in the guided region around the BZ K-point. A plot of the band matches in the guided region around K-point are shown in Figure 4-21 - Figure 4-22 for the 3s band, and Figure 4-23 - Figure 4-24 for the 3p band. Note that for the 3s band the best match between the 2D and 3D solutions is at a source frequency of 0.35 (point b). However, the match for the 3p band is not as good at this point and is better matched at source frequency 0.4 (point d). To obtain the best match for both bands, 0.375 source frequency effective index was chosen. This match gives a -4.215% frequency error for the 3s band and a +4.076% error for the 3p band, within acceptable computational error.

The parameters for our 3D waveguide slab effective index calculation will now provide the best approximation for the 3s and 3p curves in our 2D simulation. The best effective index was obtained for a lattice constant of a = 562.5nm based on a center source frequency f = 0.375. The next step is to use these simulation parameters to investigate the refractive properties of the square superlattice for a variety of different slab stackups. For each slab stackup, a 3D effective index simulation will be run using a center Gaussian source frequency of f = 0.375, then matching the effective index curve we obtain with the a = 562.5nm line. It is not necessary to run the simulations at f =

0.375 since we are using a Gaussian source with a large bandwidth that will cover a wide frequency range, but for consistency we choose to use this as convention. Now the 2D PWE simulations can be run very efficiently and with high accuracy for the 3s and 3p bands for many different waveguide slab configurations. The focus of the next chapter is to use the 2D band simulation data we obtained to compute the refractive behavior of the square superlattice photonic crystal structure.

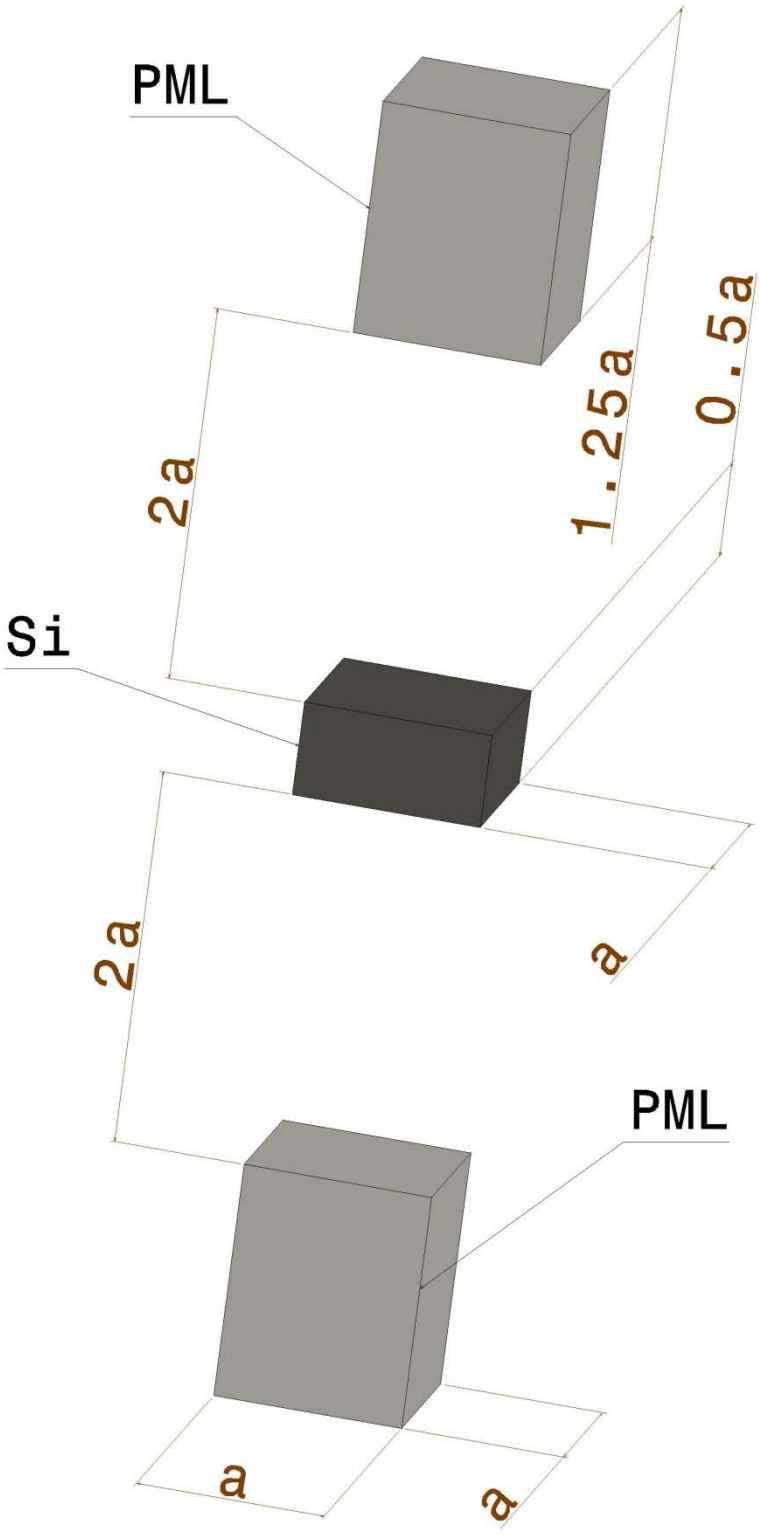

Figure 4-16: 3D slab waveguide stackup

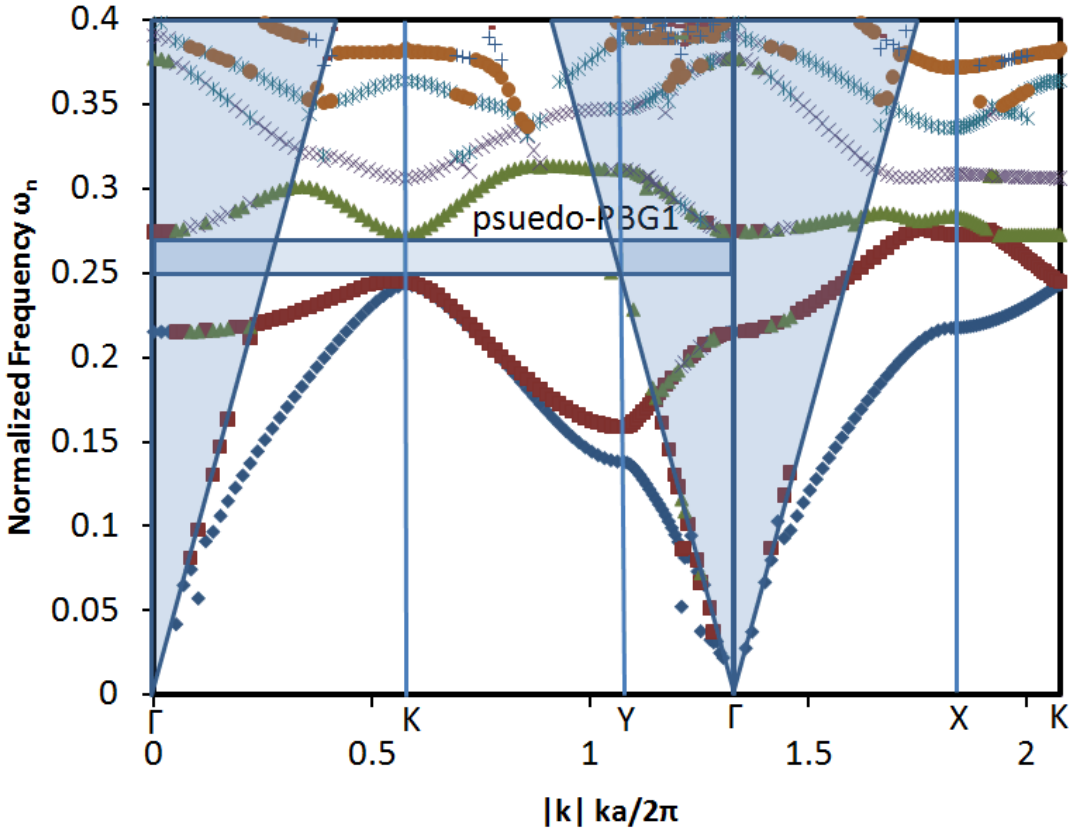

Figure 4-17: 3D FDTD TM band diagram for a square superlattice strength of r_2/r_1 = 0.30a/0.35a = 0.857.

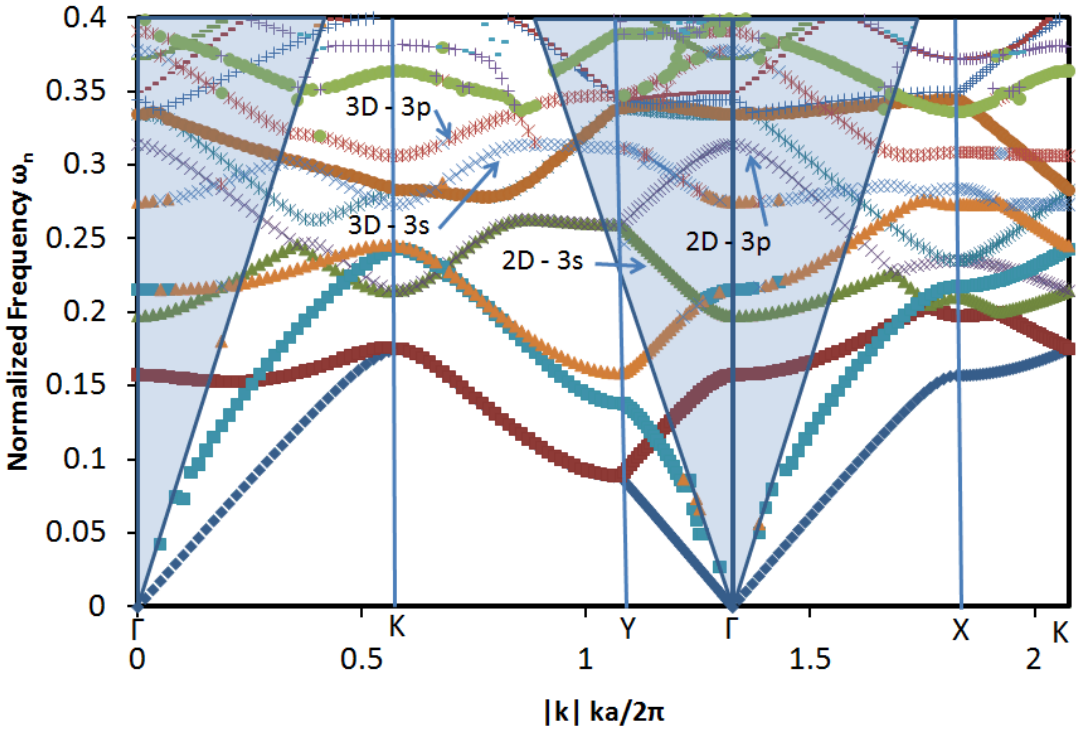

Figure 4-18: Comparison of the ideal 2D PWE and 3D FDTD computed band points. The 3s and 3p bands for each simulation are indicated for clarity.

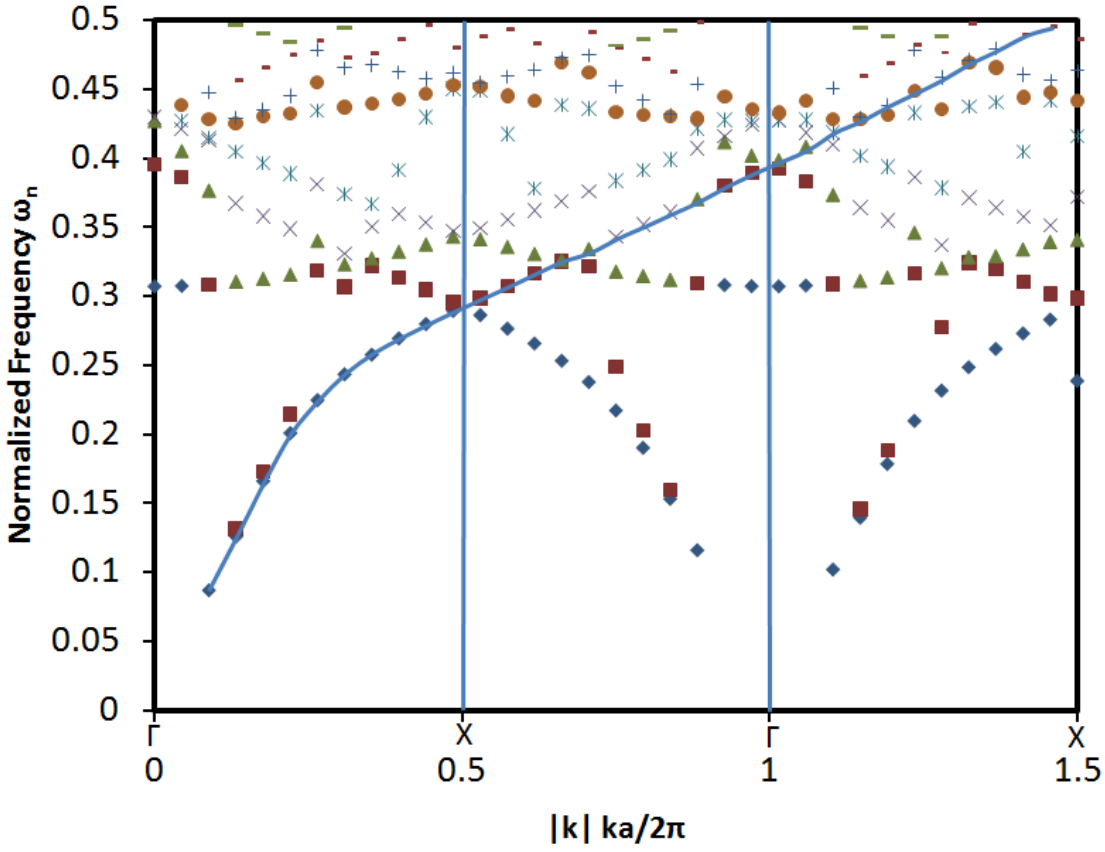

Figure 4-19: Normalized frequency versus k-value for the TM modes of a 3D FDTD slab waveguide stackup.

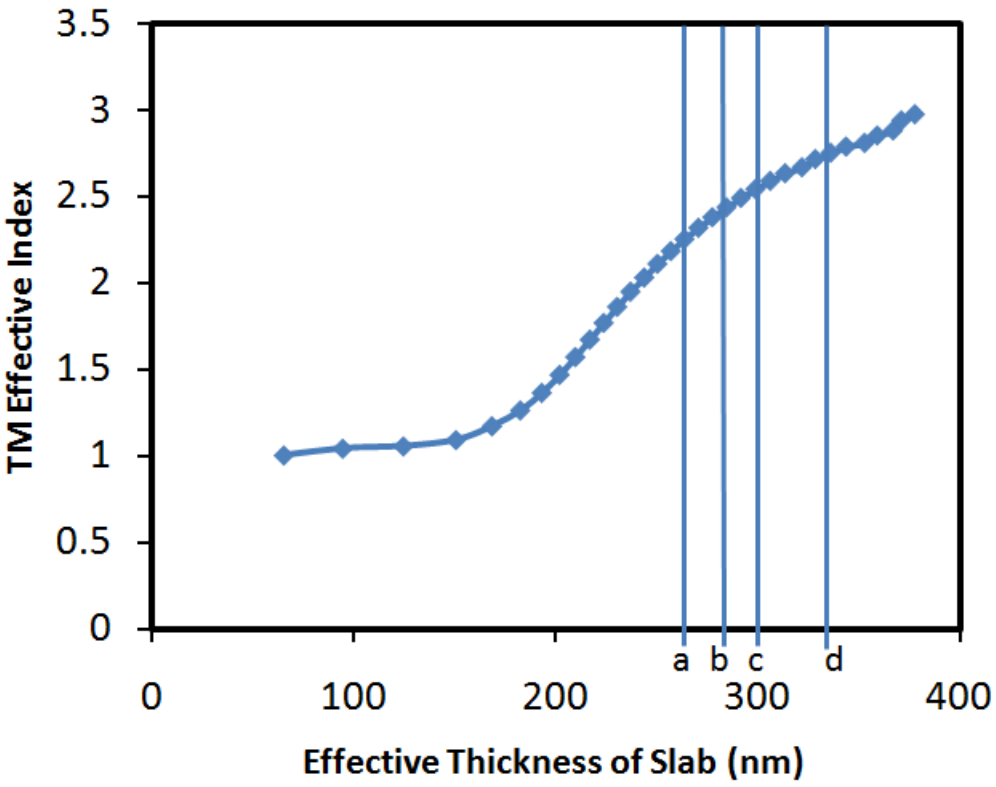

Figure 4-20: TM effective index versus effective thickness of the slab structure. Table 2 references the *a* values for the a-d values of effective index.

Table 3: Tabulation of the TM effective indexes obtained from matching the a-e line intersection with the 3D slab waveguide effective index curve.

ref.	0.5a (nm)	source frequency *f* (norm.)	calculated effective η from Table 1	calculated effective ε from Table 1
a	262.5	0.35	2.236854239	5.003516887
b	281.25	0.375	2.411554739	5.815596258
c	300	0.4	2.550506509	6.505083453
d	337.5	0.45	2.762876405	7.633486028

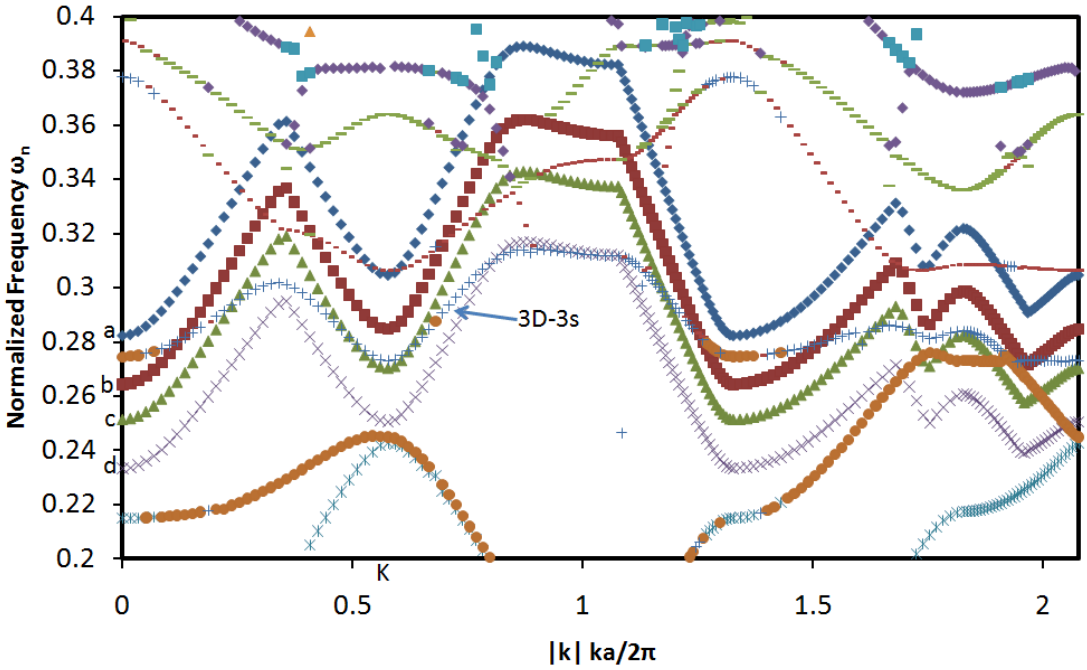

Figure 4-21: Four 2D simulations for the 3s band matched against the 3D slab waveguide 3s band.

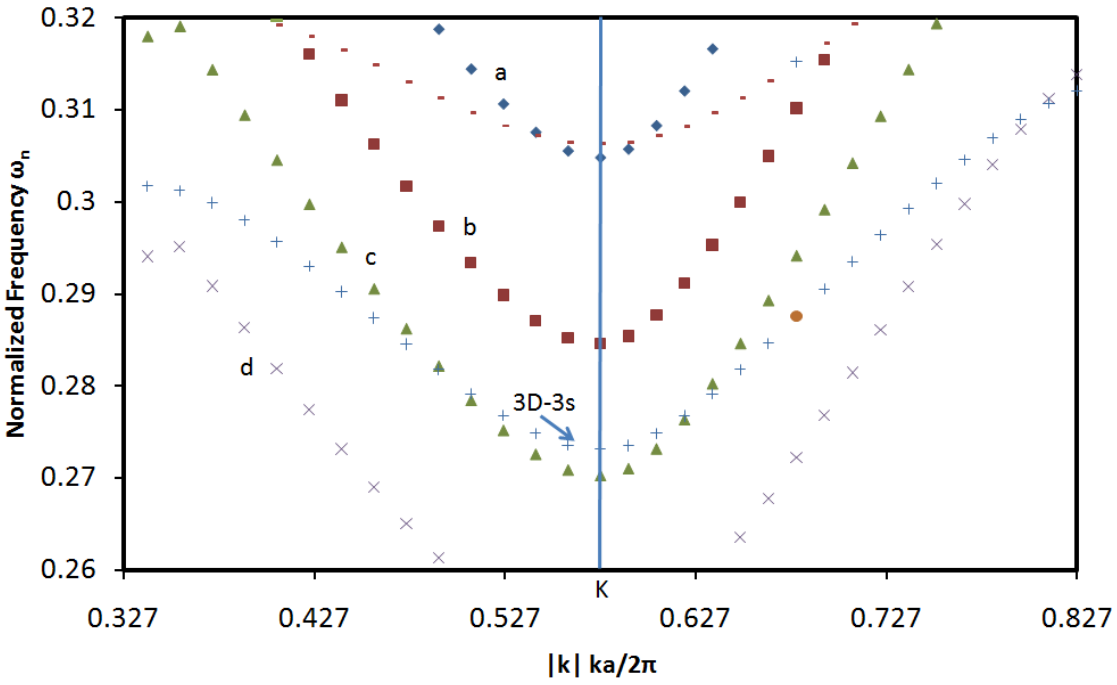

Figure 4-22: Close up view of the area around the K-point for the 3s band match.

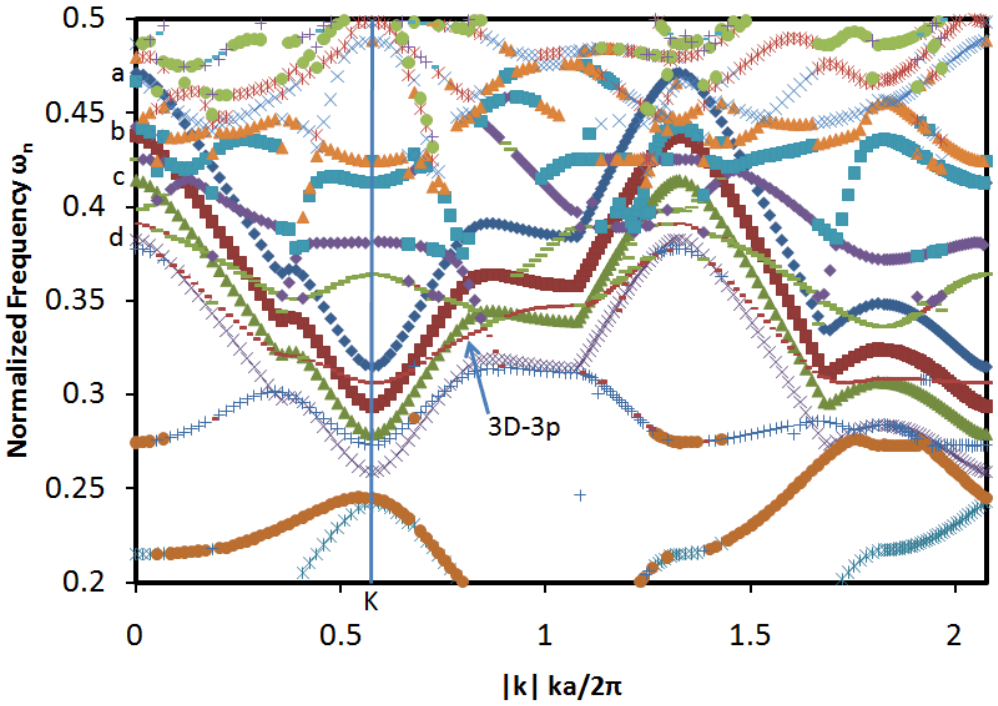

Figure 4-23: Four 2D simulations for the 3p band matched against the 3D slab waveguide 3s band.

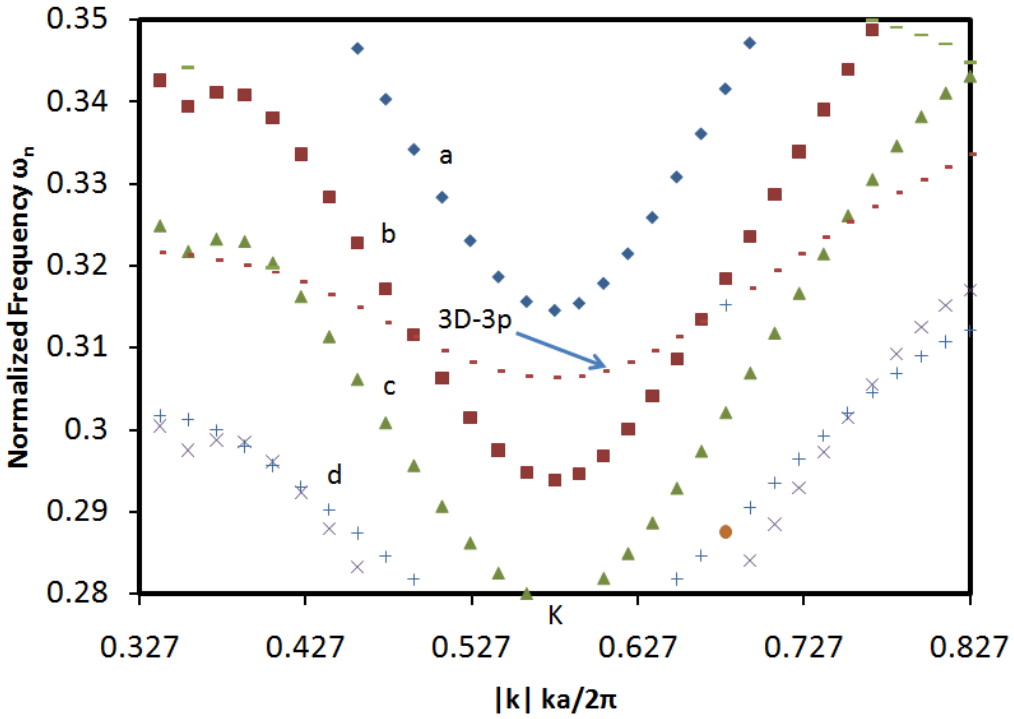

Figure 4-24: Close up view of the area around the K-point for the 3p band match.

5 Refraction Effects in the Square Superlattice

Having obtained the model parameters for correctly simulating our structures, we investigate how the square and triangular superlattice can be applied and exploited as optical refraction controlling devices. To do this, we first need to investigate the dispersion contours for these structures. Up to this point, we have investigated the photonic band structure of the square superlattice, however this does not give a full picture of how light propagates through the structure. The photonic band structure is a simplified view of the dispersion properties of the device, in that it only plots the dispersion relation along the boundaries of the BZ. In reality, the dispersion relation for a photonic crystal structure is a three dimensional surface in k-space, having k_x and k_y vector components in the plane of the device. The dispersion surface is in effect a contour plot of this three dimensional band structure, and is created by taking "slices" through the three dimensional band surface for a particular frequency of interest ω_n, representing the frequency of the light source travelling through the device. For ease of graphical analysis, the contour maps are plotted in surface relief graphs in two-dimensional form. The refraction response of the device can then be extracted from this information using wavevector analysis, which will be detailed in the following section.

To create the dispersion contour plots for the triangular and square superlattice, a two-dimensional PWE simulation method was used, as described in Chapter 4. The PWE analysis provides solutions that are automatically categorized by band number, reducing the number of spurious solutions that can lead to calculation errors as in the FDTD approach. Initially, the dispersion contours for the idealized square superlattice, with a

superlattice strength of 0.857, will be examined to obtain an overall picture of the features of interest. Mainly, we are interested in examining the degenerate 3s and 3p contour curvatures of the square superlattice to determine which bands have the opportunity to provide the most interesting dispersion contour shapes that in turn provide interesting device refractive properties. The curvature of these dispersion contours have the most interesting refractive effects, forming closed boundaries that allow for both positive and negative refraction.

After this initial analysis, the model will be modified to more faithfully represent a "real-world" slab waveguide device to more accurately assess how they would work when fabricated. To this end, the effective index model of a slab waveguide device we developed in Chapter 4 will be applied; i.e. an index change in the simulation, to more accurately describe the dispersion contours. Using this data, which more accurately describes actual device behavior, the dispersion contours of interest can be recalculated for the square superlattice. Using these improved accuracy contours, the refraction characteristics of the square structures will be calculated, focusing on a few contours of interest that illustrated the refractive behavior of the device

After modifying the dispersion contour model to represent the slab waveguide structure, an investigation into static tuning of the square superlattice will be demonstrated. Static tuning of the lattice is accomplished by the use of ALD technology, in which the structure is conformally coated with an optical material. In this case we have selected TiO_2, a dielectric with a medium range index ($n = 2.31$) as compared to the index of Si ($n = 3.46$). This ALD coating work has been performed for the triangular superlattice [56] – here we will focus on ALD modification to the square superlattice.

The changes to the dispersion contours and refraction behavior of the device will be investigated as the lattice is coated with 0 – 200nm of TiO_2.

The final analysis of the square and also the triangular superlattice will be for dynamic tunability configurations. Two different configurations will be investigated. The first configuration consists of placing sealed liquid crystal (LC) cells over both the top and bottom of the waveguide. In this case the cells will modify the effective index of the structure depending on whether they are biased on (higher index) or biased off (lower index). Changes to the dispersion contours and refractive behavior of both the square and triangular superlattice are examined. Finally, a configuration in which the entire lattice is made of electro-optic material, known as lead lanthanum zironcate titanate (PLZT) will be investigated. In this case, biasing of the entire structure will affect the overall effective index of the device and lead to changes in the dispersion contours and refraction properties. Previous work has been done for the triangular superlattice, the focus here will be the square superlattice only.

Conclusions will be drawn on the usefulness of controlling the dispersion contours both statically and dynamically following the analysis.

5.1 Calculation of PC Dispersion Surfaces and Refraction Curves by Wavevector Analysis

Wavevector analysis is performed through the use of wavevector diagrams. These wavevector diagrams have been applied to optical structures in order to determine refraction behavior at an interface between two materials. First, consider an interface between two isotropic, homogeneous materials, which will be called Region 1 and

Region 2. An infinite plane wave with angular frequency ω in Region 1 is incident at an angle $\theta_1 = \theta_i$ at the interface to Region 2. In k-space the wavevectors in the respective regions are given by:

$$k_1 = \frac{n_1 \omega}{c} \tag{80}$$

$$k_2 = \frac{n_2 \omega}{c} \tag{81}$$

If the assumption is made that $n_1 > n_2$, the interface can be considered to be in the k_x direction and the normal interface in the k_y direction. Due to the transitional symmetry of the interface, the wavevector components of the incident, reflected and refracted waves parallel to the interface must be conserved. The conservation condition can be shown by creating a construction line drawn normal to the k_x axis at the endpoint of the $k_{1\parallel}$ vector. The refracted vector k_2 is then created by adding a construction line upward to the vector endpoint from the origin making an angle $\theta_2 = \theta_r$, the refraction angle. Since the material is homogeneous and isotropic, the contour that is created for various incident angles becomes a circle. For a family of different ω values, a set of contours can be created which creates the dispersion contour plot for refraction within Region 2. If we set the parallel components of the wavevectors equal, $k_{1\parallel} = k_{2\parallel}$, as the conservation law requires, we obtain:

$$\frac{n_1 \omega}{c} \sin \theta_i = \frac{n_2 \omega}{c} \sin \theta_r \tag{82}$$

which reduces to:

$$n_1 \sin\theta_i = n_2 \sin\theta_r \tag{83}$$

In the case two isotropic, homogeneous optical materials, the equation reduces to Snell's Law. The group velocity v_g of the propagating wave in Region 2 is given by the gradient of the dispersion contour at a particular ω and is given by:

$$v_g = \nabla\omega(\vec{k}) = \frac{\partial\omega}{\partial k} \tag{84}$$

In the case of uniform circular dispersion contours, k_2 and v_g are coincident. A diagram illustrating these wavevectors and the associated dispersion contour is shown in Figure 5-1.

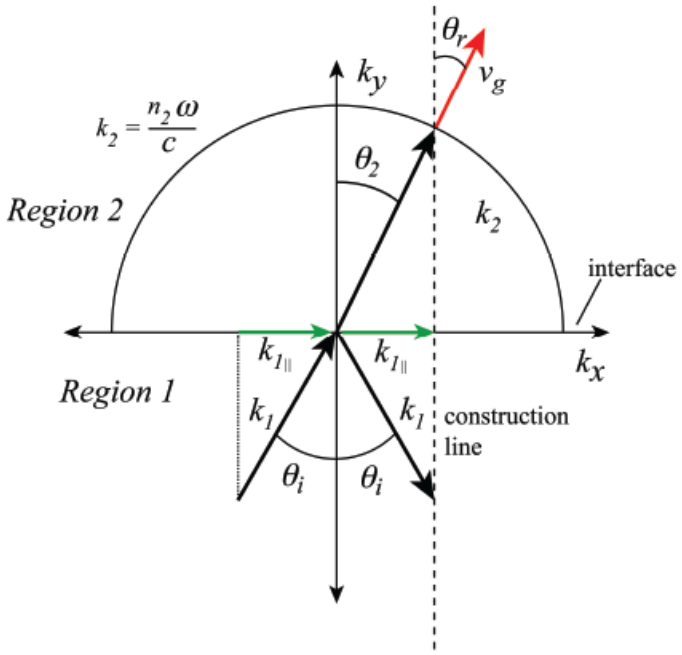

Figure 5-1: Diagram showing the use of wavevector methods to calculate the refraction of a plane wave at the interface of two different isotropic homogeneous materials.

If the material is no longer considered isotropic and homogeneous, as in the case of a PC where the material is patterned creating areas of different optical indexes, the

dispersion contour $\omega(\vec{k})$ can be of any shape. Wavevector methods, as applied to multi-dimensional PC structures, was first introduced by Russel et.al. in 1996. The conservation condition still holds in the case of PC refraction, although in this case k_2 and v_g are not coincident. Figure 5-2 shows the wavevector diagram for an arbitrary dispersion contour. Note that in this case, the direction of v_g is highly dependent upon the incident angle of the incoming radiation in the case where the contours contain sharp curvature points.

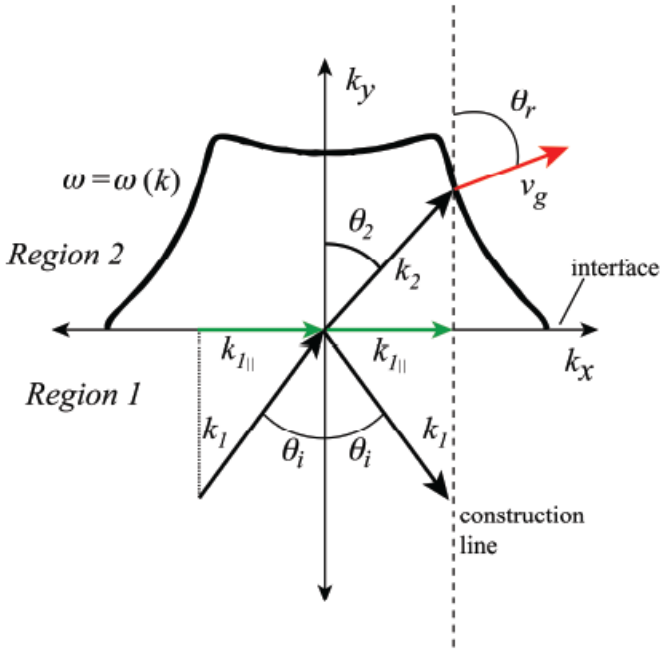

Figure 5-2: Diagram showing the use of wavevector methods to calculate the refraction of a plane wave at the interface between an isotropic homogeneous material and a complex dispersion surface similar to that of a PC.

Given a calculated dispersion contour surface, $\omega(\vec{k})$, the refraction properties of the device can be calculated by plotting θ_i , the incident wave angle, vs θ_r, the reflected wave angle. These values are computed from the conserved wavevector component $k_{1\|}$ and the derivative of the k_x and k_y components of the contour at a particular point,

specifically the slope of the tangent line at that point on the contour. The respective formulas are:

$$\theta_i = \frac{n_1 \cdot \sin^{-1}(k_{1\parallel})}{\omega} \tag{85}$$

$$\theta_r = \tan^{-1}\left(\frac{dk_y}{dk_x}\right) \tag{86}$$

Details of how dispersion contours for the square superlattice PC are calculated numerically are contained in the Section 5.2. In Section 5.3, refraction plot construction will be covered, where the slab waveguide structure of the square superlattice PC is modeled and examined in more detail.

5.2 Dispersion Contours for Ideal Square and Triangular Superlattice

The initial analysis starts by examining the dispersion contours for ideal 2D square and triangular superlattices. In this case, the 2D structure consists of air holes (n = 1) in a 2D medium of ideal index Si (n = 3.464). Creating the dispersion contours is a complex process that is based on an MPB PWE simulation of the superlattice unit cell band structures across the entire first BZ of the structure. Because the dispersion contours can be of any shape, it is important to compute as many band points as possible in both the k_x and k_y directions, to avoid gaps in the curves - especially at high curvature points that can be missed in a particular direction. Missed points in the curves can cause large spaces

between points, and since the refraction curves rely on accurate slopes, the refraction plots will be reduced in accuracy.

Once the family of bands is generated in both k-directions, the intersection between the bands and the particular contour frequency of interest is computed using MATLAB code. A sub-program that finds the intersection points was utilized inside the main body of code to generate the intersection point matrix. These points are then plotted in k-space to create the dispersion contours for the full BZ. The BZ is then repeated and folded to create a larger repeated BZ, also known in solid state physics as the repeated zone scheme, so that the curves join at the BZ edges. In this case we are interested primarily in the 3s (band 3) and 3p (band 4) dispersion curves. The curves that have the most curvature, and therefore the biggest refraction response, will be those curves near the center of the K-point (or the M-point in the triangular superlattice) that form closed contours. The focus of both the static and dynamic tuning of these closed contours forms the basis for the refraction characterization of the devices.

The dispersion contours for the ideal 2D triangular superlattice have been documented in previous research work [39]. These dispersion contours were computed for a superlattice strength of 0.857 and TE source polarization. The plots were centered around the Γ point and are shown in Figure 5-3 for all four bands. The frequency values for several curves is included on the plot for topology reference.

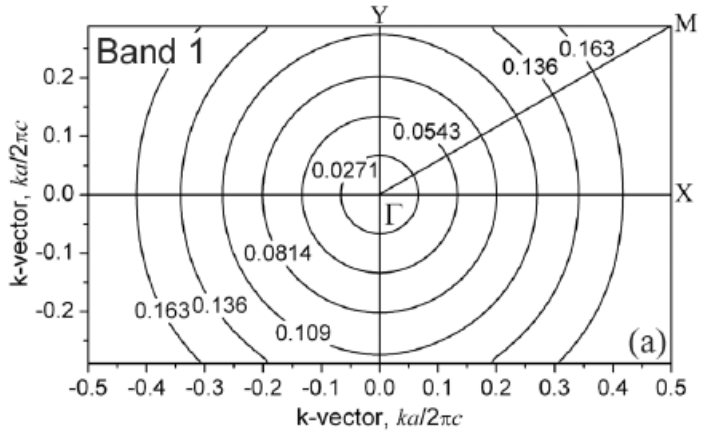
Band 1
Y
M
X
Γ
0.163
0.136
0.0543
0.0271
0.0814
0.163
0.136
0.109
(a)
k-vector, ka/2πc
k-vector, ka/2πc

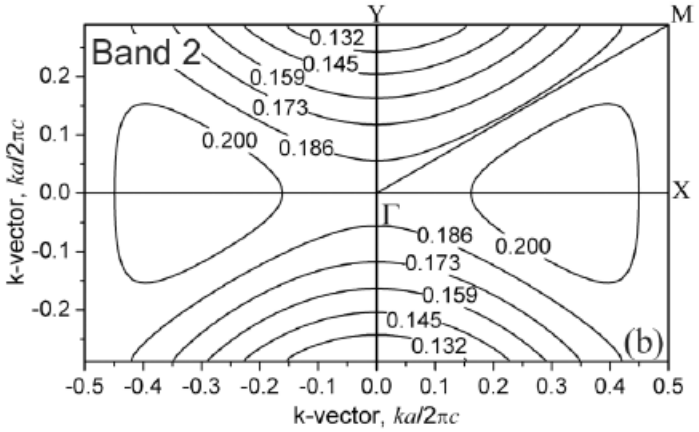
Band 2
Y
M
X
Γ
0.132
0.145
0.159
0.173
0.200
0.186
0.186
0.200
0.173
0.159
0.145
0.132
(b)
k-vector, ka/2πc
k-vector, ka/2πc

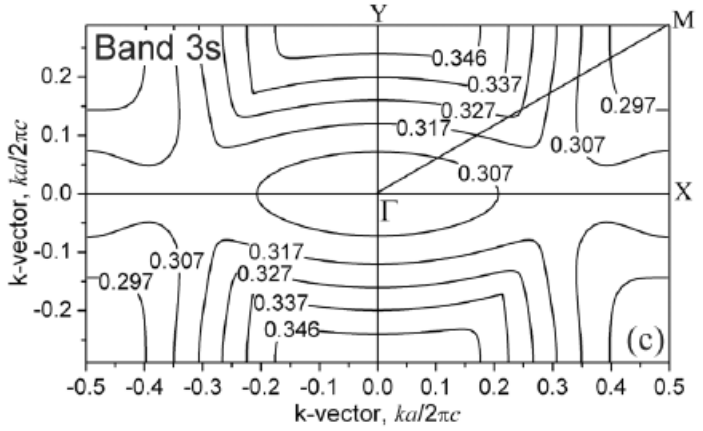
Band 3s
Y
M
X
Γ
0.346
0.337
0.327
0.317
0.307
0.297
0.307
0.307
0.317
0.327
0.337
0.346
0.297
(c)
k-vector, ka/2πc
k-vector, ka/2πc

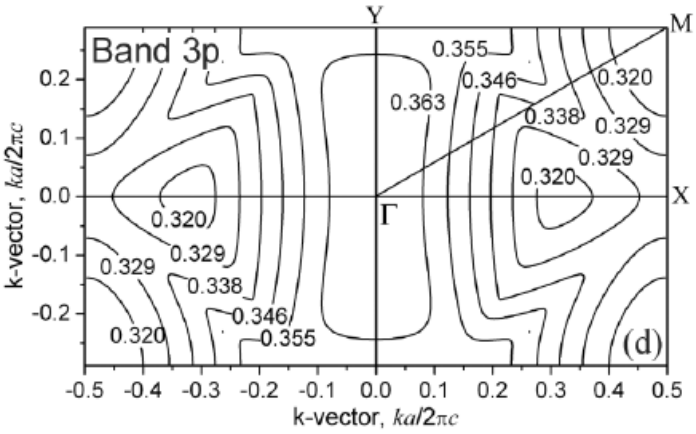

Figure 5-3: Contour maps of the dispersion surfaces inside the first Brillouin zone for the first four TE bands of a triangular superlattice. The superlattice strength is 0.857, with n = 3.464 for the Si structure and n = 1 for the air filling the holes. Curves are shown for (a) band 1, (b) band 2, (c) band 3s, and (d) band 3p [39].

To compute the triangular lattice refraction curves for light propagating along the Γ-M direction, the dispersion contours must be oriented around the M point instead, to obtain the correct orientation. There are two reasons this particular direction is primarily being investigated. First, the anisotropy of the curves at the M-point are larger than other BZ directions where the curves tend to be symmetric across the zone. The anisotropy also introduces interesting refraction behavior, such as the exhibiting both positive and negative refraction for a single frequency curve. Second, the curves around the M-point are typically within the guiding regime of the slab waveguide structure, i.e. below the light line in the band structure. Other higher frequency bands that have interesting dispersion contours tend to operate above the light line, thus they are unguided and will decay as extended states outside of the slab structure. There may be contours in other directions under the light line that exhibit interesting refractive properties. However, these contours are left for future investigations.

Once the curves are shifted to the repeated zone scheme around the M-point, the triangular lattice shows closed curves around the M point for both the 3s and 3p bands, the 3s being more "square"-like and the 3p being more "elliptical"-like. These dispersion contours are shown in Figure 5-4 for the 3s band and Figure 5-5 for the 3p band. We will revisit the refraction response of the triangular superlattice in the active tuning section of the research, specifically the LC wave-guided configuration.

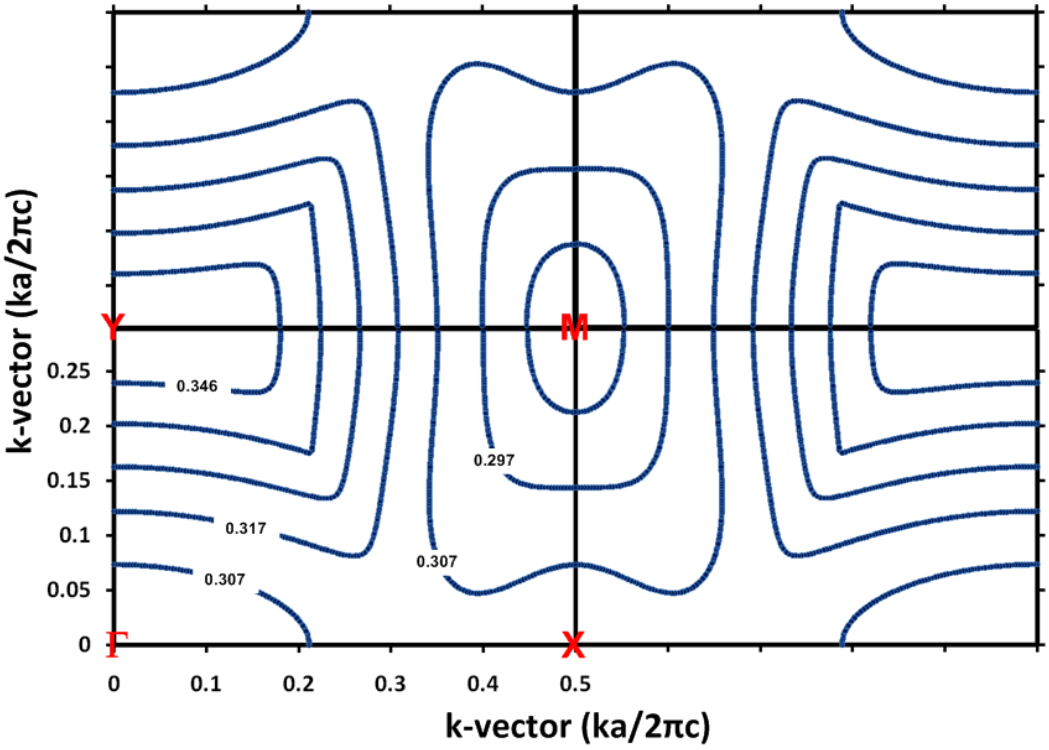

Figure 5-4: Dispersion contours of the triangular superlattice 3s band for a superlattice strength of 0.857, centered around the M-point.

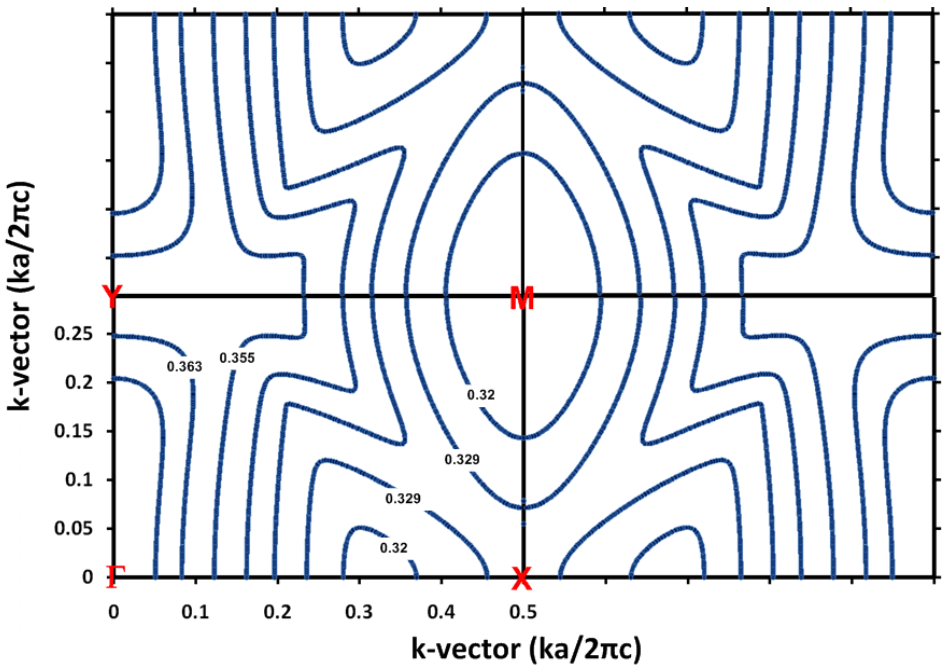

Figure 5-5: Dispersion contours of the triangular superlattice 3s band for a superlattice strength of 0.857, centered around the M-point.

We now turn to the dispersion contours for the ideal 2D square superlattice. The dispersion contours for the ideal 2D model (again, air holes (n = 1) in a 2D medium of ideal index Si (n = 3.464) are shown in Figure 5-6 - Figure 5-9 for bands 1, 2, 3 (3s), and 4 (4p) for a TE source polarization condition. In this case, the band 1 and band 2 dispersion contours are similar to those obtained from the triangular lattice. The band 3 (3s) contours shows a marked difference however, in that there are no closed contours around the K-point. A closed contour could be created around the Y-point as in the case of the triangular superlattice, however, this contour would be in the unguided region of the device and thus will not be considered since we are only interested in slab guided modes. Also, another closed contour could be created around the X-point, creating an elliptically shaped contour. This particular closed contour could be considered to be in the guided regime of the device. Unfortunately, it is small in size which limits the

frequency range over which it will provide significant refractive properties, thus it was not investigated in this work. Band 4 (3p) shows a closed contour around the K-point in the guided regime and is much larger, thus it is suitable for refraction calculations. The shape is somewhat elliptical, but has flat edges on the sides. Therefore, the band 4 (3p) dispersion surfaces, and the refractive properties of these surfaces are of interest.

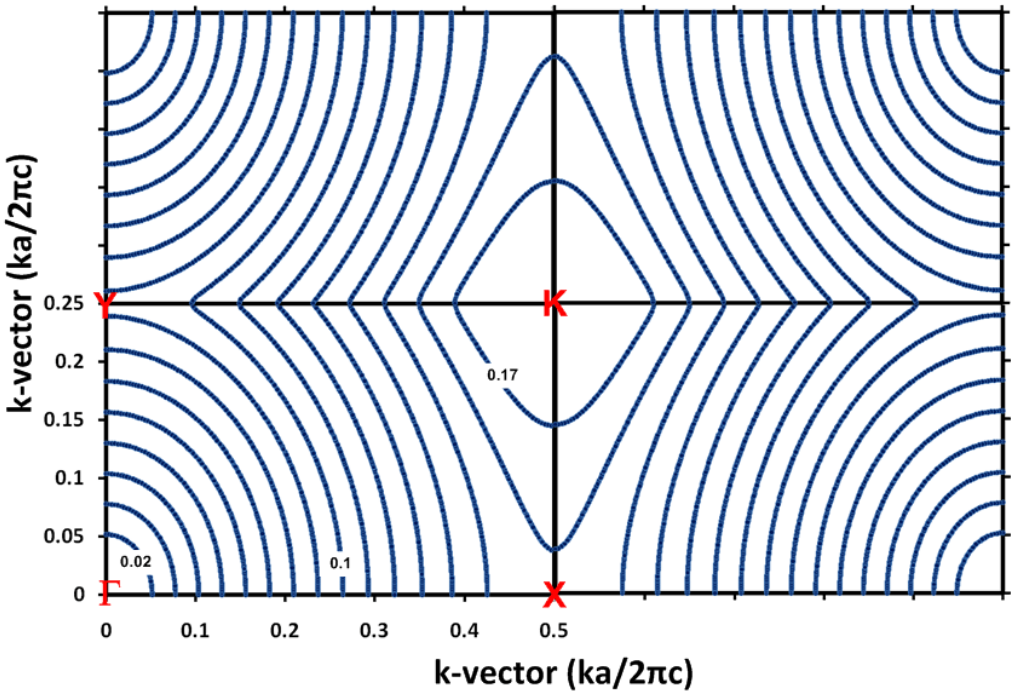

Figure 5-6: Contour maps of the dispersion surface in the first BZ for band 1 of an ideal 2D square superlattice having a strength of 0.857.

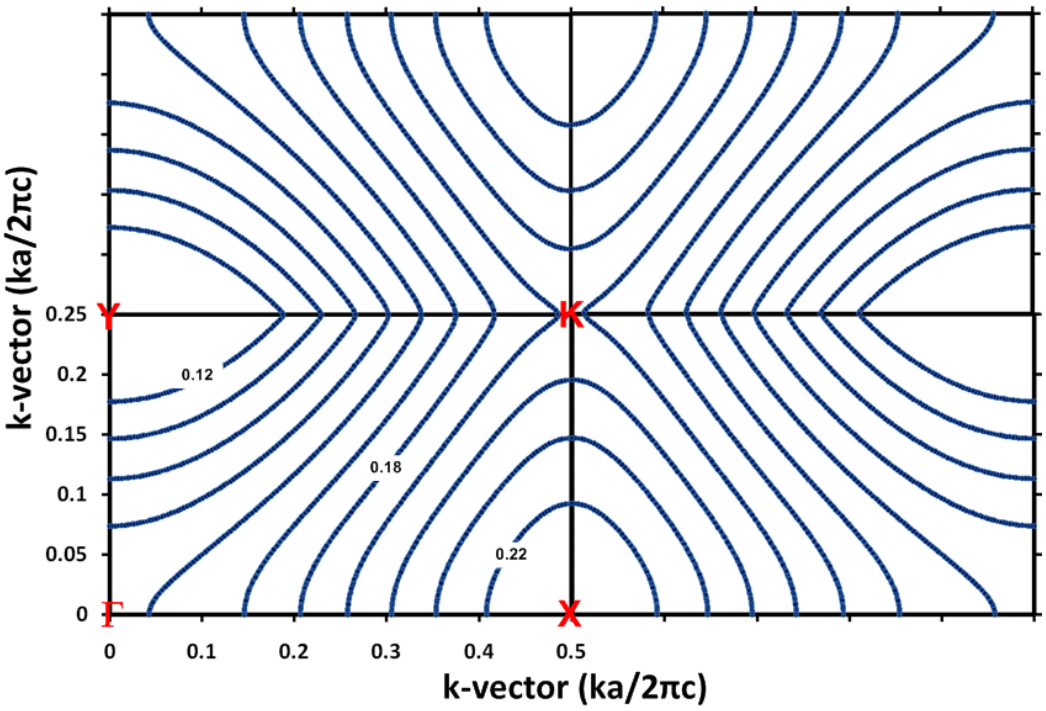

Figure 5-7: Contour maps of the dispersion surface in the first BZ for band 2 of an ideal 2D square superlattice having a strength of 0.857.

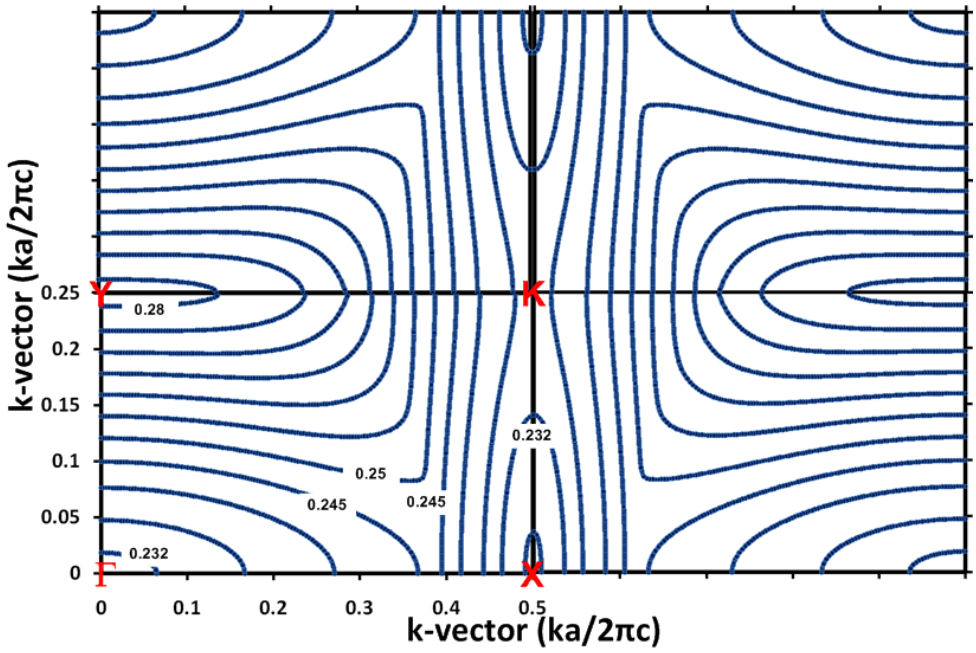

Figure 5-8: Contour maps of the dispersion surface in the first BZ for band 3 (3s) of an ideal 2D square superlattice having a strength of 0.857.

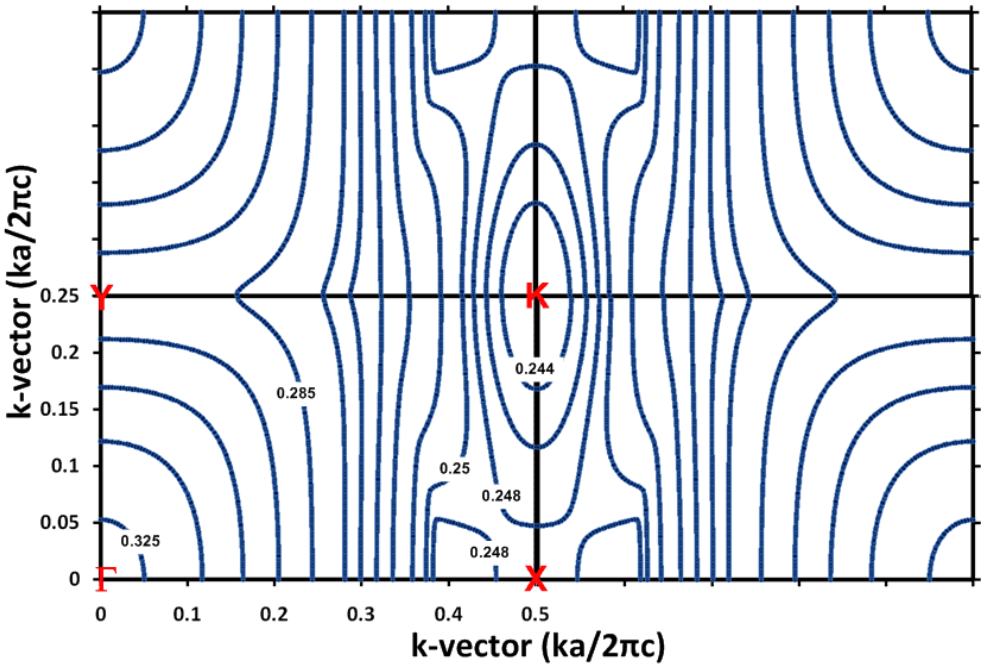

Figure 5-9: Contour maps of the dispersion surface in the first BZ for band 4 (3p) of an ideal 2D square superlattice having a strength of 0.857.

5.3 Dispersion Contours of the of Slab Waveguide Square Superlattice

Having obtained the ideal response for the square superlattice, we now focus on a more realistic 3D model of the device that more exactly matches an actual fabricated device, known as the slab waveguide stackup. It consists of a slab of Si with a height of h = 0.5a and an index of n = 3.464 (ε = 12.0) surrounded top and bottom by 2a air layers (n = 1.0) as shown previously in Figure 4-16. No holes are present in this simulation as we are only interested in calculating the effective, or average index, of the layered device structure. Holes will be incorporated in the 2D simulated structure once we have the effective index of the stackup. This layered structure is similar to the SOI (silicon-on-insulator) stackup that is used to fabricate the device, the only difference being that the bottom layer is SiO_2 (n = 1.5) rather than air. The difference between the two layered

stackups, in terms of average index, is fairly small so the simpler slab waveguide stackup is adequate for 3D modeling purposes. This particular stackup will provide the basis for refractive index calculations, to provide higher accuracy in computing the refractive properties of an actual fabricated square superlattice device.

The effective index simulation were run using a TE polarized source and a center Gaussian source frequency of $\omega = 0.375$. The effective index curve obtained using the lattice constant $a = 562.5$nm line was then utilized. An effective index of $n = 3.01$ was obtained for the TE polarized source, compared to $n = 2.41$ for the TM case. The 2D structure now consists of air holes ($n = 1$) in a 2D medium of effective index TE polarization mode compensated Si ($n = 3.01$). Lowering the index to account for the finite thickness of the slab waveguide structure causes the bands to move upwards as expected, and also to closely match the expected 3D band structure of the device. The inner dispersion curves of the device now center around $\omega = 0.276 – 0.282$ as shown in Figure 5-10, as opposed to the lower frequencies of $\omega = 0.242 – 0.248$ in the ideal 2D model case shown in Figure 5-9. Note that in the slab waveguide model, the K-point dispersion curves become more rounded, as opposed to the ideal case. Using these new frequency adjusted dispersion curves, we are now ready to compute the refraction response of the 3p square superlattice device in the next section.

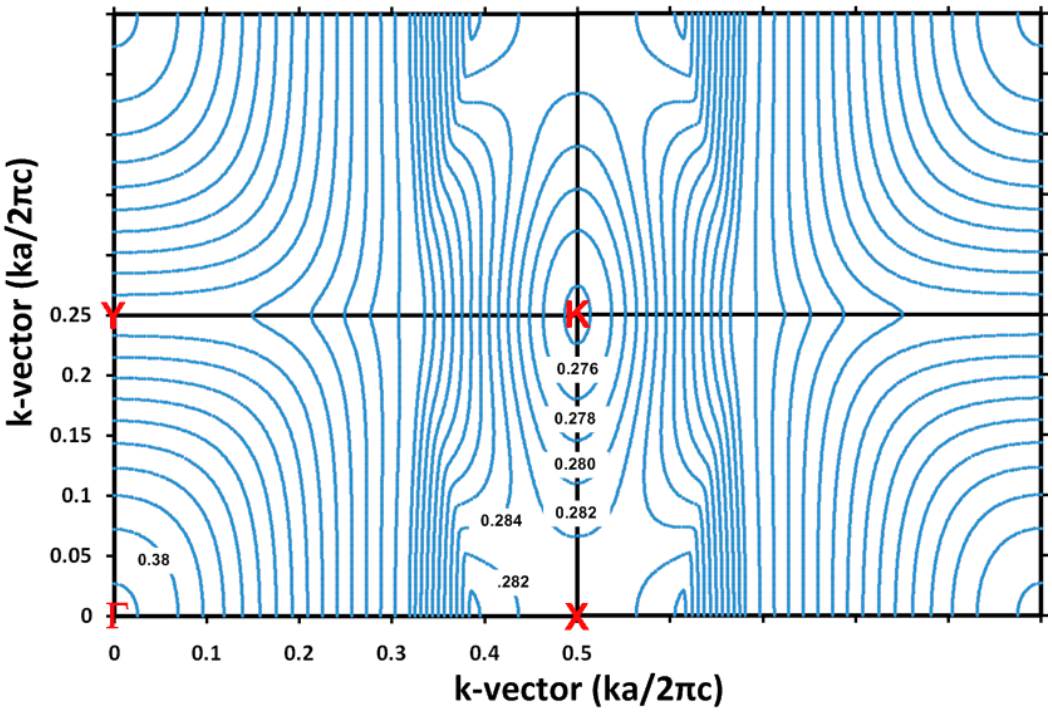

Figure 5-10: Contour maps of the dispersion surface in the first BZ for band 4 (3p) of an slab waveguide effective index modeled 2D square superlattice having a strength of 0.857.

5.4 Refraction Properties of the Square Superlattice 3p Band

The refraction properties of the 3p band for the central dispersion contours can now be computed using the accurate slab waveguide model of the square superlattice. The first step is to fold the dispersion contour from a single BZ into the repeated zone scheme to create a closed contour. This is accomplished by first sorting the curve points in sequential order in a single BZ quadrant, then using rotation functions in Matlab to create the other three quadrants of the curve. Once the closed curve is created with all the k-points arranged in sequential order, a final rotation of the entire curve is necessary to make the Γ-K direction normal to the surface. In the case of the square superlattice, the BZ rotation angle was 63.435°, as opposed to the triangular lattice where the rotation

angle was 60°. This rotation places the θ_i angle at 0 degrees, parallel to the Γ-K direction. The set of four inner 3p contours obtained from the slab waveguide model of the square superlattice shown in their rotated state in Figure 5-11.

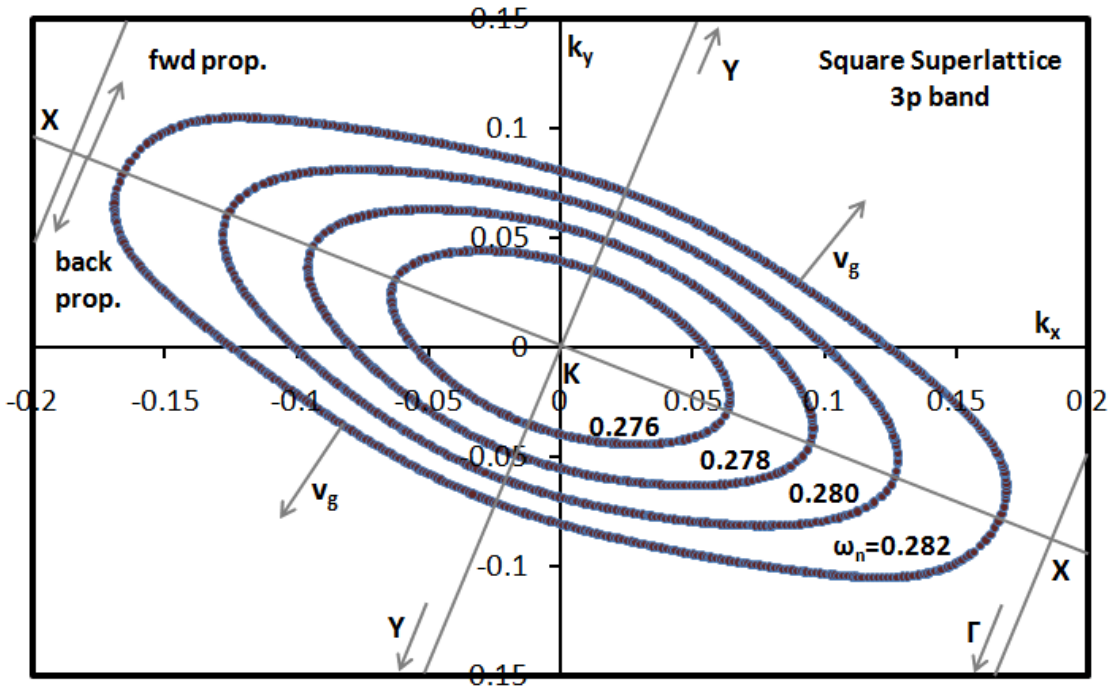

Figure 5-11: Rotated dispersion contours around the K-point for a square superlattice slab waveguide structure 3p band with TE polarization and 0.857 superlattice strength.

As illustrated in the rotated contour diagram, there can be both forward and backward propagation, based on the direction that v_g takes. The direction of v_g depends on the incident angle of the incoming light as it is effectively swept around the contour. Using the equations for θ_i and θ_r from the previous section, a plot of the incident angle of light versus the refracted angle of light can be constructed. In this case we are varying the frequency of the incoming light to make contact with each of the separate dispersion contours. Figure 5-12 shows the refraction plot for these four dispersion curves as the incident angle is changed.

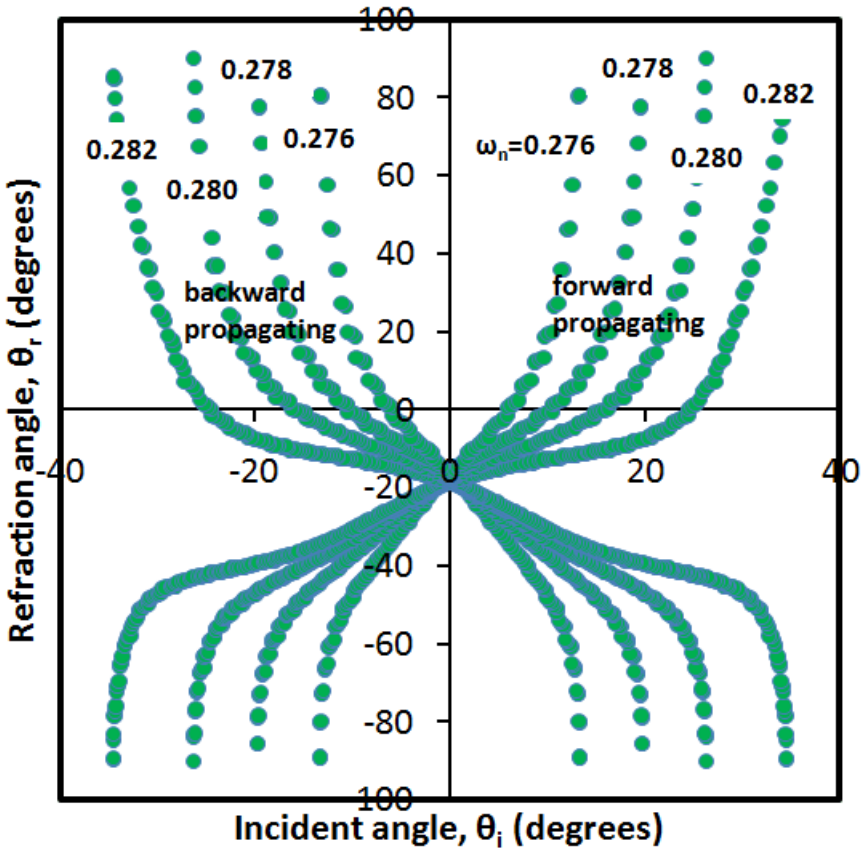

Figure 5-12: Refraction plots for the 3p band of the square superlattice slab waveguide structure, showing both the forward and backward propagating response for a superlattice strength of 0.857.

Note that by displaying the entire dispersion surface we obtain curves indicating both the forward and backward propagation in the device. In reality, the only useful refraction is for the forward propagating light. In order to modify the refraction curves, we use the top half of the rotated contour and perform the same calculations to generate the plot. In this way, only the forward propagating refraction response of the square superlattice 3p band is computed. Figure 5-13 shows the forward propagating response for two of the 3p dispersion contours. Based on the given contours, a maximum $\Delta\theta_r$ = 80.71 – (-11.35) = 92.06° at an incident angle of θ_i = 13.3° was found. The refraction in this case changes from negative to positive and the frequency of light is changed from ω

= 0.282 to ω = 0.276. In an experimental measurement of the device, the frequency of the light source requires adjustment to observe the shown refraction change. We can now examine how to tune these structures to design different refraction responses. The first investigation into tuning the square superlattice device starts with static tuning using thin-film ALD coating applications to the structure.

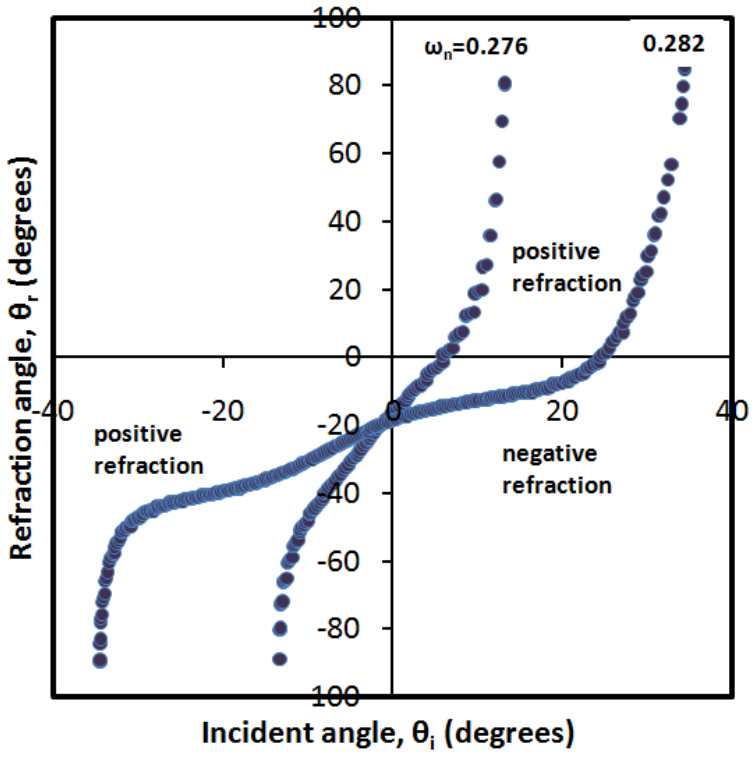

Figure 5-13: Refraction plots for the 3p band of the square superlattice slab waveguide structure, showing only the forward and propagating response for a superlattice strength of 0.857.

Now that we have a clear picture of what the refraction response is for the 3p band elliptical dispersion contours centered around the K-point, we can examine how we can tune these structures to get different refraction responses. The first investigation into tuning the square superlattice device starts with static tuning using thin-film ALD coating applications to the structure.

5.5 Static Tuning of the Refraction Properties of the Square Superlattice 3p Band Utilizing ALD

The goal of static tuning the square superlattice device is to understand how the refraction properties of the device are changed with the application of optical material to the structure. Previous work of this nature has been performed on the triangular superlattice [56]. In this set of simulations a superlattice strength of 0.857 was used for TE polarization conditions. A medium index material of TiO_2 (n = 2.31) was selected as it has a high enough index to make the tuning changes more observable. ALD is a conformal coating process, thus we start with a 5nm thickness simulation, increasing to a 200nm thickness. To make the simulation as accurate as possible, an understanding of how the structure changes as it is coated is needed. Figure 5-14 shows a side view of the gradual application of ALD layers to a photonic crystal structure. Note for a conformal coating, as the coating thickness increases the small holes fill in first, followed by the larger holes. In addition, a layer of material is also deposited on the surface of the device.

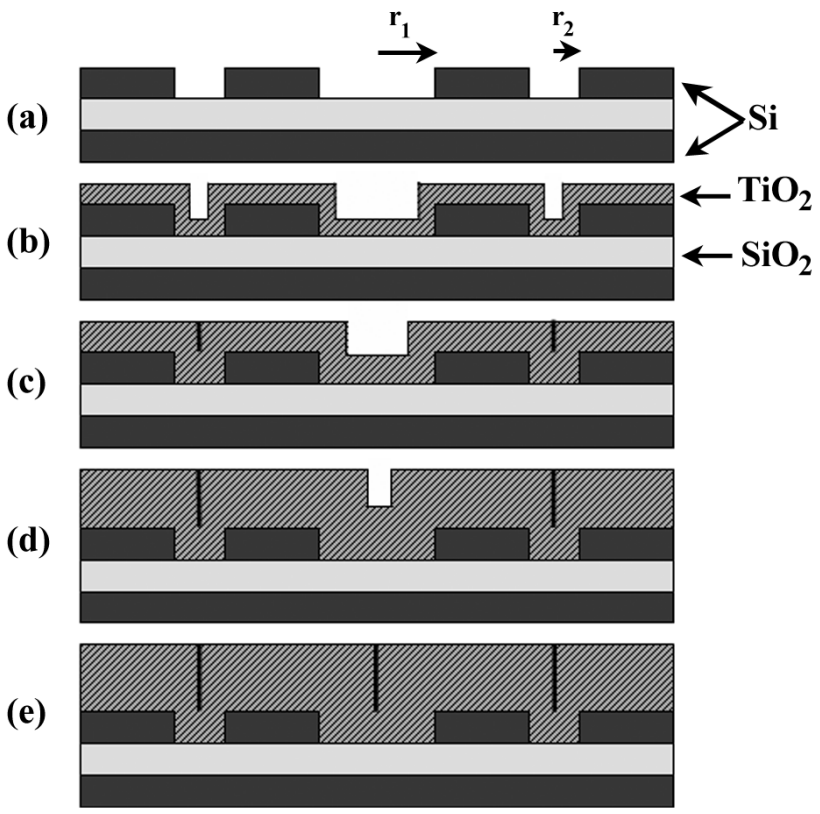

Figure 5-14: Diagram illustrating the effect of coating a superlattice structure with multiple ALD thin-film layers of TiO_2.

Creating this 3D structure in a 2D simulation requires two steps. First, the effective index model of slab waveguide is modified by adding a thickness of TiO_2 over the top of the slab. Two examples of the simulation stackup are shown in Figure 5-15 for two different thickness of TiO_2. This step required many 3D FDTD simulations using TE polarization conditions to be run with various thicknesses of coating. The effective index change is then calculated for each thickness. Table 4 relates the applied coating thickness to the normalized thickness that was used in the 3D simulations.

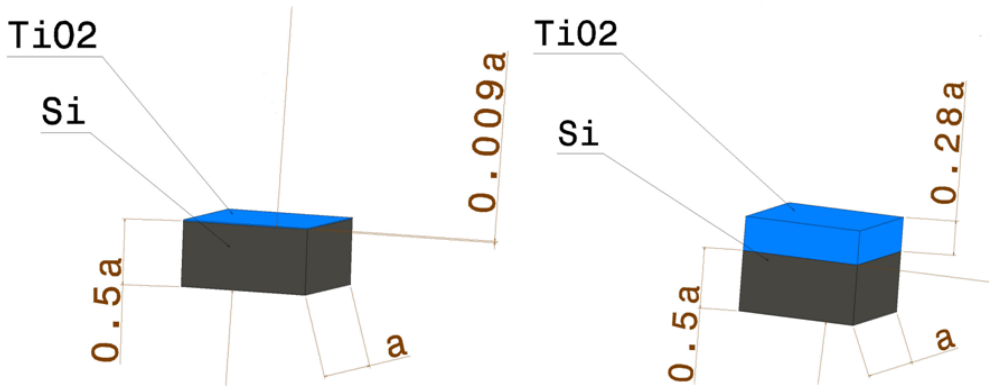

Figure 5-15: Diagram for the slab effective index slab waveguide model for two different TiO_2 coating thicknesses that was used in the 3D FDTD simulation.

Table 4: Conversion of the actual thickness of ALD deposited TiO_2 to a normalized value that is used in the 3D effective index slab waveguide simulations.

TiO_2 thickness (nm)	TiO_2 thickness (normalized)
0	0
5	0.008888889
10	0.017777778
20	0.035555556
30	0.053333333
40	0.071111111
50	0.088888889
60	0.106666667
70	0.124444444
80	0.142222222
90	0.16
100	0.177777778
110	0.195555556
120	0.213333333
130	0.231111111
140	0.248888889
150	0.266666667
160	0.284444444
170	0.302222222
180	0.32
190	0.337777778
200	0.355555556

Each 3D TE simulation produced a new effective index that takes into account the thickness of the top layer of TiO*2* material being added to the device. Table 5 shows the effective index that was calculated for each of the coating thicknesses. This data can also be graphed and is shown in Figure 5-16. The curve has an interesting shape, starting out with large effective index changes for small thickness ALD layers; then gradually decreases to smaller and smaller index changes for larger thicknesses. This is expected as the ratio of the thicknesses of Si and TiO_2 becomes larger, the effective index of the structure tends to blend together into a single material, as the effective index change with each successive layer is reduced.

Table 5: Tabulation of the effective index values obtained through the 3D simulations for various thicknesses of ALD deposited TiO_2.

TiO_2 thickness (nm)	TE effective index
0	3.010370541
5	3.014709326
10	3.019309286
20	3.026156459
30	3.031499208
40	3.037206168
50	3.04097723
60	3.044349657
70	3.048038255
80	3.049910267
90	3.051989535
100	3.053983111
110	3.055253177
120	3.056556285
130	3.057711063
140	3.058483836
150	3.059299521
160	3.05993933
170	3.060415874
180	3.060945859
190	3.061282337
200	3.061609775

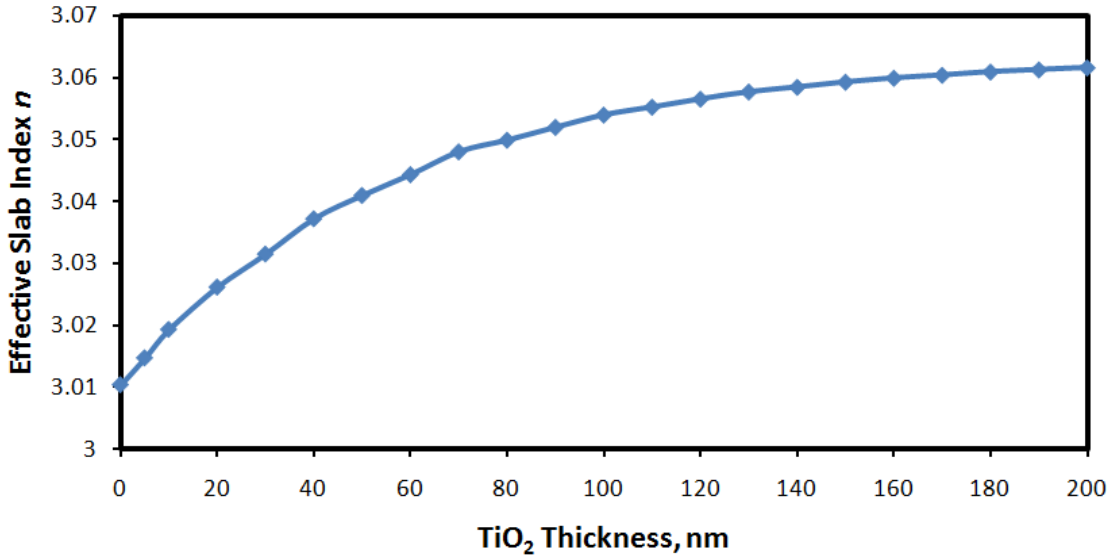

Figure 5-16: Plot of the effective index values for various thickness of ALD deposited TiO_2 given in Table 5.

The second step in creating an accurate model is to fill the holes with TiO_2 material along with using the effective index of the coating on top of the slab. Filling in the holes will take into account the additional thin film material that is added conformally inside them during the ALD process. Figure 5-17 shows the filling in of holes in a 2D triangular superlattice structure. To use the various hole filling layer thicknesses in the 2D model, they must be normalized. A table of the normalized values of the hole size where air (n = 1) is present is shown in Table 6. In the MPB simulation, the hole index is first changed to TiO_2, then overwritten by the air cylinders using the normalized values in the table, creating the annual TiO_2 structure around the outside of the holes. Another observation is that the small holes will be completely filled with TiO_2 at a coating thickness of 170nm, while the larger holes will fill at the full coating thickness of 200nm.

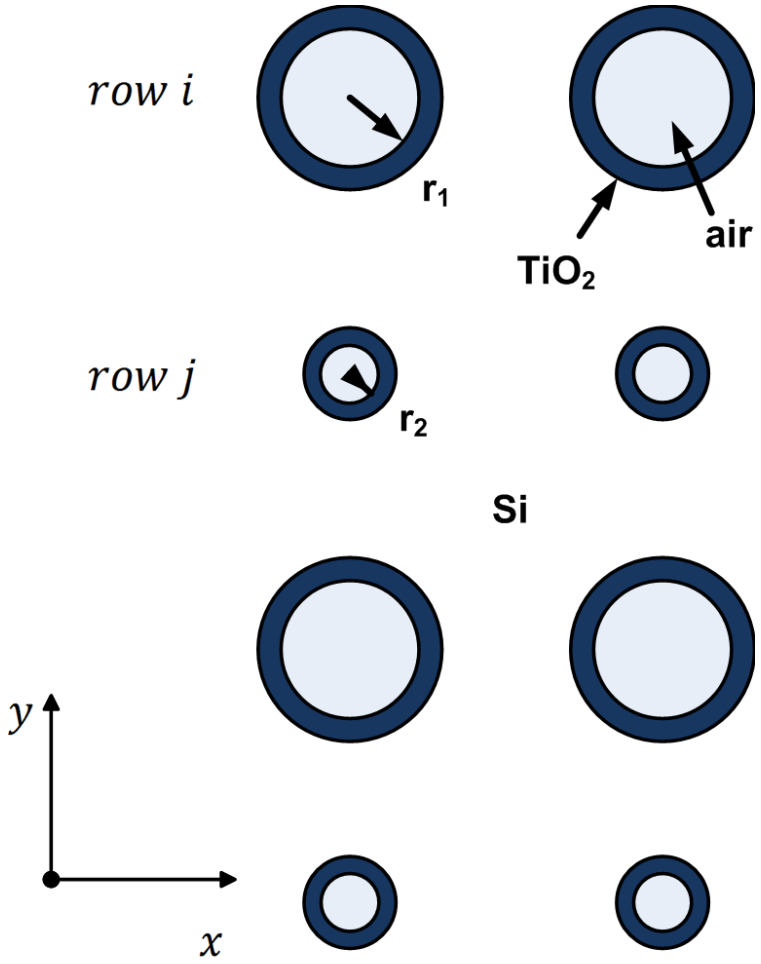

Figure 5-17: Diagram illustrating the filling of the holes in a triangular superlattice through the use of TiO_2 ALD coatings. This is the model that was incorporated into the 3D effective index values to create an accurate 2D model of the material infiltration.

Table 6: Tabulation of the real hole and normalized hole radii used in the 2D coated slab waveguide calculations.

TiO_2 thickness	Normalized r_1 radius	Actual r_1 radius	Normalized r_2 radius	Actual r_2 radius
(nm)	(normalized)	(nm)	(normalized)	(nm)
0	0.35	196.875	0.3	168.75
5	0.341111111	191.875	0.291111111	163.75
10	0.332222222	186.875	0.282222222	158.75
20	0.314444444	176.875	0.264444444	148.75
30	0.296666667	166.875	0.246666667	138.75
40	0.278888889	156.875	0.228888889	128.75
50	0.261111111	146.875	0.211111111	118.75
60	0.243333333	136.875	0.193333333	108.75
70	0.225555556	126.875	0.175555556	98.75
80	0.207777778	116.875	0.157777778	88.75
90	0.19	106.875	0.14	78.75
100	0.172222222	96.875	0.122222222	68.75
110	0.154444444	86.875	0.104444444	58.75
120	0.136666667	76.875	0.086666667	48.75
130	0.118888889	66.875	0.068888889	38.75
140	0.101111111	56.875	0.051111111	28.75
150	0.083333333	46.875	0.033333333	18.75
160	0.065555556	36.875	0.015555556	8.75
170	0.047777778	26.875	0	0
180	0.03	16.875	0	0
190	0.012222222	6.875	0	0
200	0	0	0	0

Using the combination of the effective index of the TiO_2 coating on top of the slab, and the changing the hole sizes in the 2D simulation, a full set of 3p band diagrams and dispersion contours was created for each coating thickness. We can now investigate the 3p band diagram for the various thickness of applied TiO_2 to determine how the TE bands move downwards as the coating is applied. As shown in Figure 5-18, the bands all have approximately the same shape. The spacing between bands follows the same trend as the effective index curve, showing larger downward shifts for the thinner coatings, and

then gradually showing less and less shifting for larger coating thickness where the effective index curve plateaus.

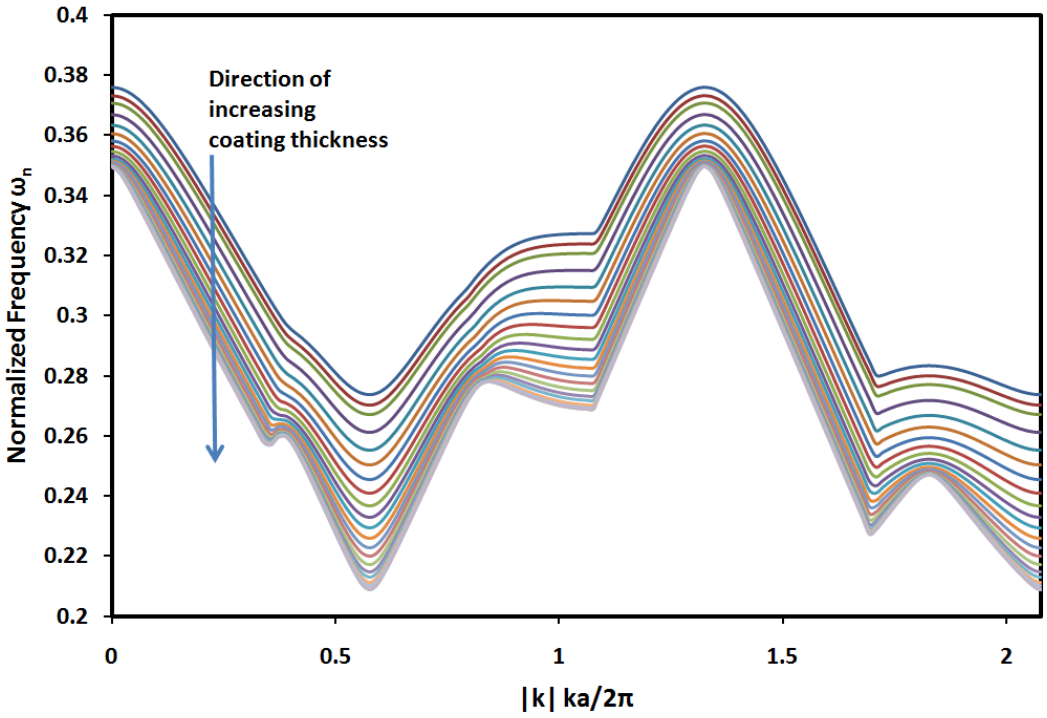

Figure 5-18: Band diagram for the 3p band of the square superlattice with strength 0.857, showing all the ALD coating thicknesses effects on the downward shifting of the bands.

We can also look at the TE band 2 and 3s bands for 0nm TiO_2 vs. 200nm TiO_2 to see how the bandgap is affected by the addition of the coatings. There is only a pseudo PBG1 for the slab 0nm coated device. As illustrated in the graph, the bandgap is completely closes at 200nm as a consequence of the upper band moving down faster than the lower bands. This band movement is a consequence of the effective index change as the various coating thickness are added. The band diagram for 0nm of TiO_2 is shown in Figure 5-19, while that for 200nm of TiO_2 is shown in Figure 5-20.

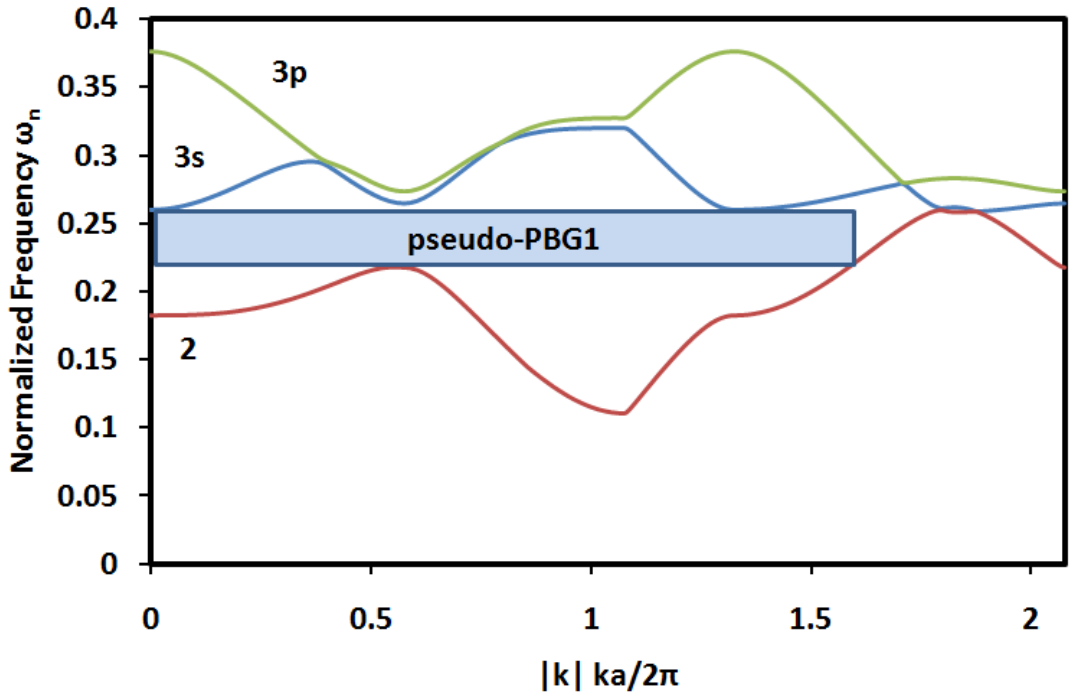

Figure 5-19: Band diagram of the 0.857 square superlattice effective index slab waveguide model for 0nm of TiO_2.

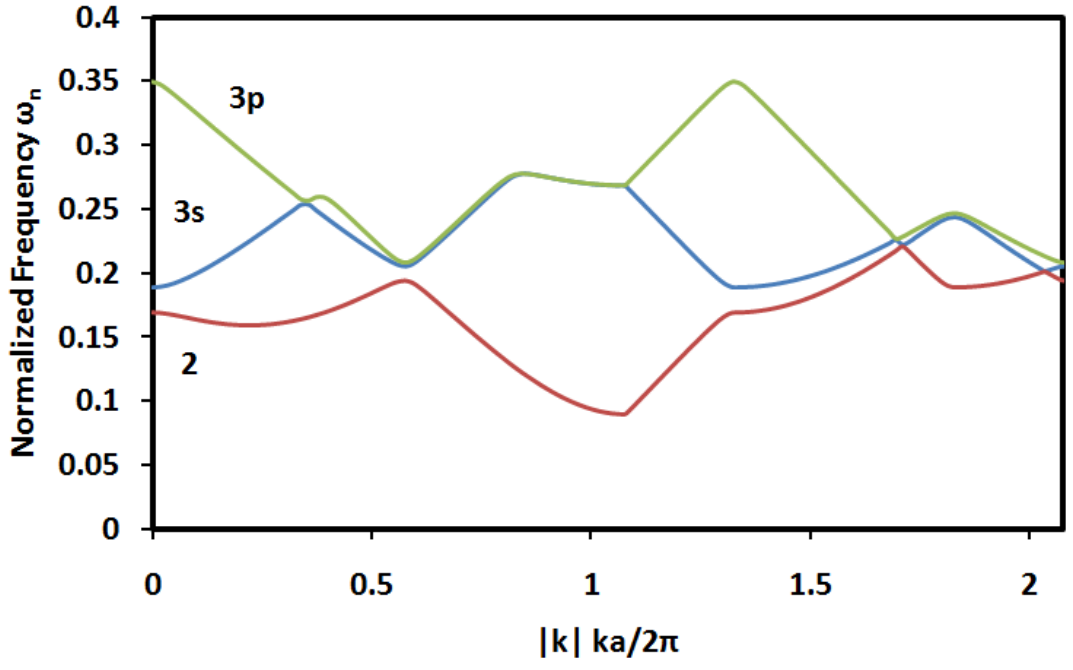

Figure 5-20: Band diagram of the 0.857 square superlattice effective index slab waveguide model for 200nm of TiO_2.

Using the graph of the various 3p bands for different coating thicknesses, we can choose a point where multiple dispersion contours cross at a single frequency. This is different from the uncoated slab waveguide where instead of varying the frequency source value, we now keep the frequency source fixed and adjust the refraction curves by the addition of the ALD layers. The dispersion contours were constructed for two sets of a single frequency but combining curves with different coating thicknesses. Refraction curves were then computed to determine the dependence on coating thicknesses.

Figure 5-21 shows the dispersion contours for three small coating thicknesses ranging from 30nm to 50nm at a fixed frequency of $\omega = 0.259$. Note that the sides of the dispersion curves are now flatter compared to the uncoated slab case. Based on the band diagram, these bands show some of the largest changes in frequency with each additional 10nm of coating. This is a direct consequence of the larger effective index changes at thin coating thicknesses. The forward refraction curves are computed for these three contours and are shown in Figure 5-22. Again, the curves show a similar trend in their areas of positive and negative refraction. An example of the refraction change that could be produced by the addition of these coatings are $\Delta\theta_r = 80.55 - (-8.08) = 88.63°$ at an incident angle of $\theta_i = 16.9°$, between the coating thicknesses of 30nm and 50nm. Between 40nm and 50nm at $\theta_i = 29.7°$, a change in refraction angle of $\Delta\theta_r = 86.84 - (-3.00) = 89.64°$ is observed. Since these devices are tuned statically after manufacture, the TiO_2 coatings could be used as a refraction angle adjustment to the final device. This could be useful when a specific desired refraction angle is needed for a particular application.

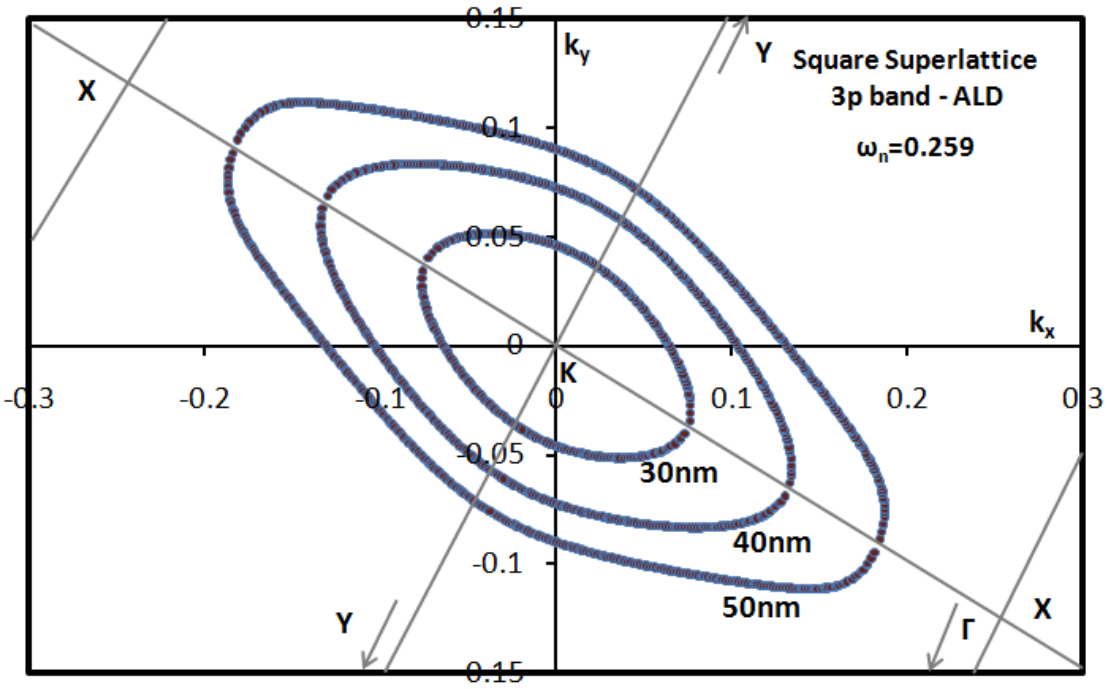

Figure 5-21: Rotated dispersion contours of a 0.857 square superlattice for 30, 40 and 50nm of ALD TiO_2 coating.

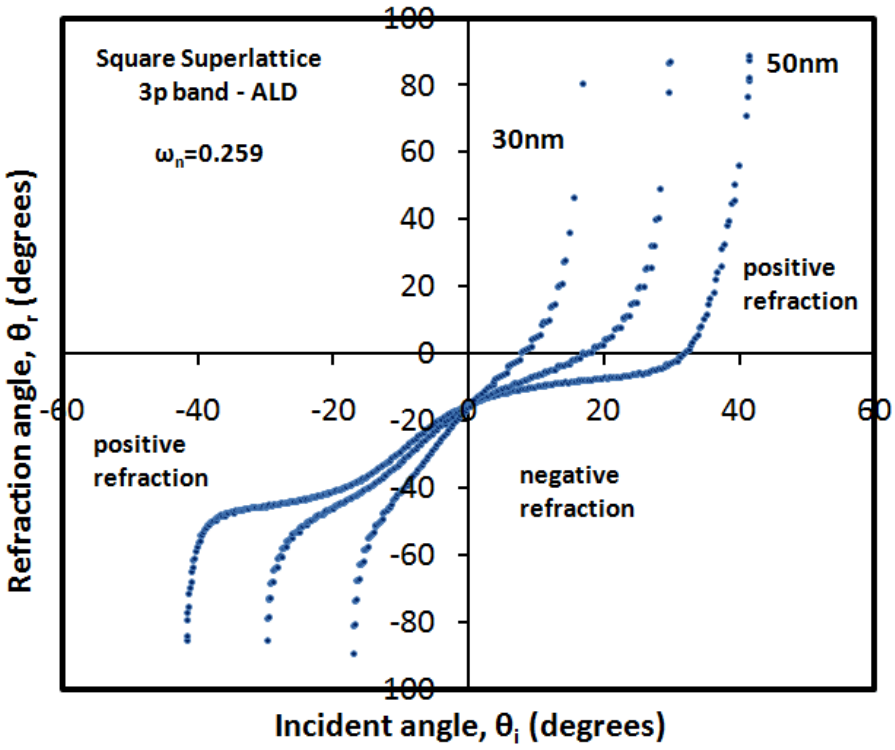

Figure 5-22: Refraction curves of a 0.857 square superlattice for 30, 40 and 50nm of ALD TiO_2 coating.

Figure 5-23 shows the dispersion contours for a series of nine coating thicknesses ranging from 60nm to 150nm at a fixed frequency of $\omega = 0.246$. The contours for thicker coatings almost overlap, due to the progressively smaller index changes involved. According to the band diagram, these bands show smaller changes in frequency with each additional 10nm of coating. The forward refraction curves computed for the nine contours are shown in Figure 5-24. The curves show a similar trend in their areas of positive and negative refraction, but now they are spaced much closer together. The area of negative refraction are reduced in size with the addition of thicker layers of TiO_2 material. Since the curves are spaced closer together, the refraction change between them is also reduced. For the 60nm and 70nm coatings and $\theta_i = 17.05°$, a refraction change of $\Delta\theta_r = 81.58 - (9.66) = 71.92°$ is computed, which is less than that for the thinner coatings. For thicker coatings between 120nm and 150nm at $\theta_i = 44.47°$, a refraction change of $\Delta\theta_r = 82.61 - (27.45) = 55.16°$ is calculated. These thicker coatings can be used to fine tune the refraction angle since the change between them, in terms of refraction, is very small.

Statically tuning the devices after manufacture may be a useful manipulation to change the direction of light output to a fixed position, and has the benefit that regardless of the nano-feature mis-sizing, the device can be tuned after manufacture. Currently, from an industry standpoint, most of the interest in PC devices today is for beam steerable and switchable applications. Following this analysis, the next investigations focused on two active tunable square superlattice configurations, one using a liquid crystal slab sandwich configuration, the other converting the entire structure to a non-linear optical material such as PLZT.

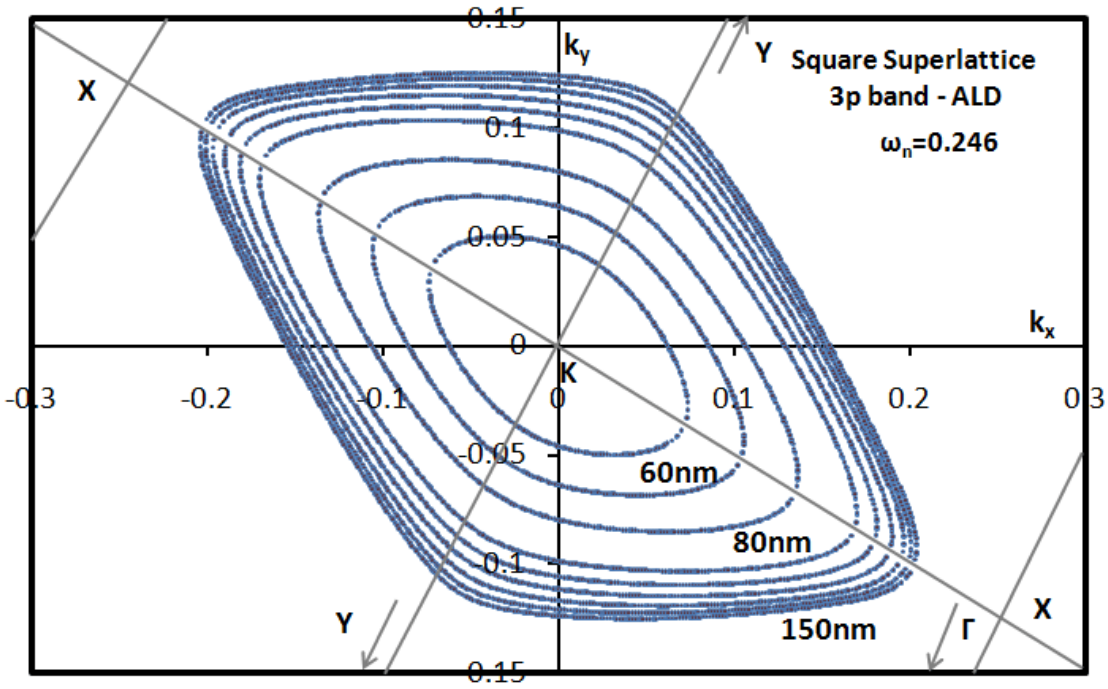

Figure 5-23: Rotated dispersion contours of a 0.857 square superlattice for 60 – 150nm of ALD TiO_2 coating.

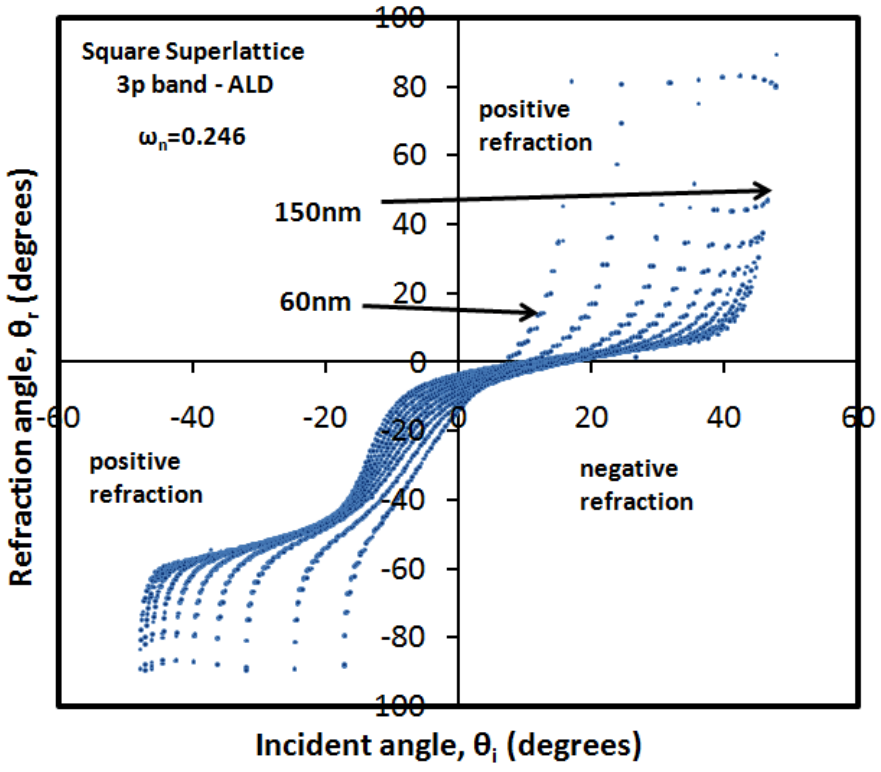

Figure 5-24: Refraction curves of a 0.857 square superlattice for 60 – 150nm of ALD TiO_2 coating.

5.6 Dynamic Tuning of the Square Superlattice Using Liquid Crystal Materials

The refractive index of PC structures can be modified through the use of electro-optic (EO) or nonlinear materials (NL) [53, 57-62] or mechanical deformation can modify the lattice period [63-64]. Experimentally, Leonard *et al.* [65] found that infiltrating a 2D triangular lattice of air pores in silicon with a liquid crystal (LC) allowed temperature dependent tunability of the air band edge frequency. However, the maximum theoretical tuning of the air band edge was not achieved because pinning of the LC molecules limited the alignment of the director to an escaped-radial configuration, which reduced the refractive index tuning to below the maximum Δn of 0.2. In the current work, we present several new lattice structures with dynamic refractive index tuning that offer significant tunability improvements over the square and triangular lattice PCs. The superlattice structures more sensitive to changes in refractive index and therefore can provide greater tuning options than the basic PC structures alone.

We first consider a tunable configuration of the square superlattice slab waveguide structure using liquid crystal materials. In this configuration, the slab waveguide structure is surrounded on top and bottom by two filled LC cells. These cells could be self contained structures with ITO glass providing the method of actively changing their index by applying a bias across the plates. For these LC cells, the index can be varied from $n = 1.5$ for the "off" condition (no bias) to $n = 2.2$ for the "on" condition (biased). The index change is a result of the LC molecules aligning themselves under applied bias, effectively increasing the optical index of the material.

The idea for implementing this structure results from the work by a startup company. They designed a beam steering waveguiding structure, originally conceived for a military hardware replacement application that was bulky. Figure 5-25 and Figure 5-26 show two pictures of the device the company was designing. In this case, there is only a liquid crystal cell on the top of the device. The waveguide core is not a photonic crystal but simply a guiding structure. In this configuration, the output light can be steered by affecting an index change on the Gaussian input beam. Here the tail of the beam is affected by the index change causing it to refract slightly from its input direction. In this design, the beam steering ratio is quite small, only 30° at a maximum.

Our design consists of using two LC cells to change the average index of the structure further than the one cell approach, while also adding the patterned square superlattice PC to the waveguiding structure. The addition of the square superlattice PC has been investigated to see if output beam steering could be increased to a value of over 60°, making it more useful for its intended application.

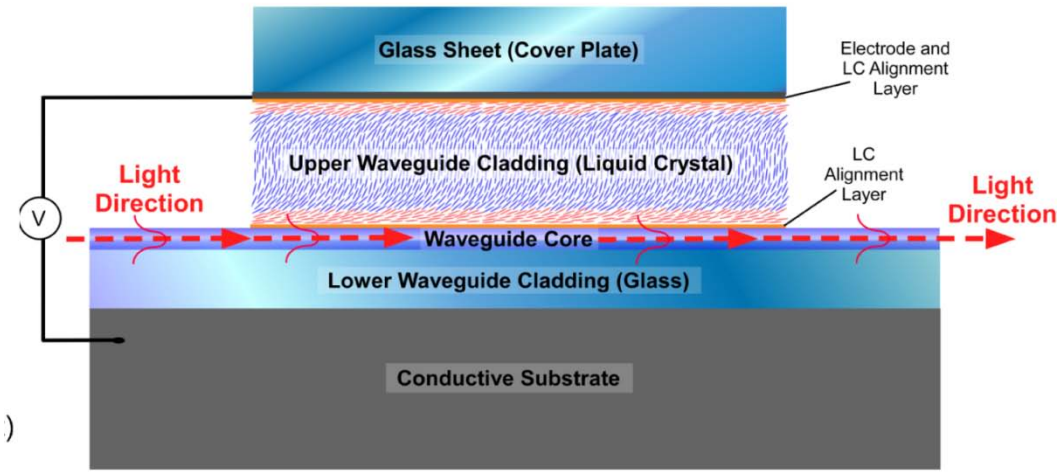

Figure 5-25: A design for a LC tunable beam steerable device.

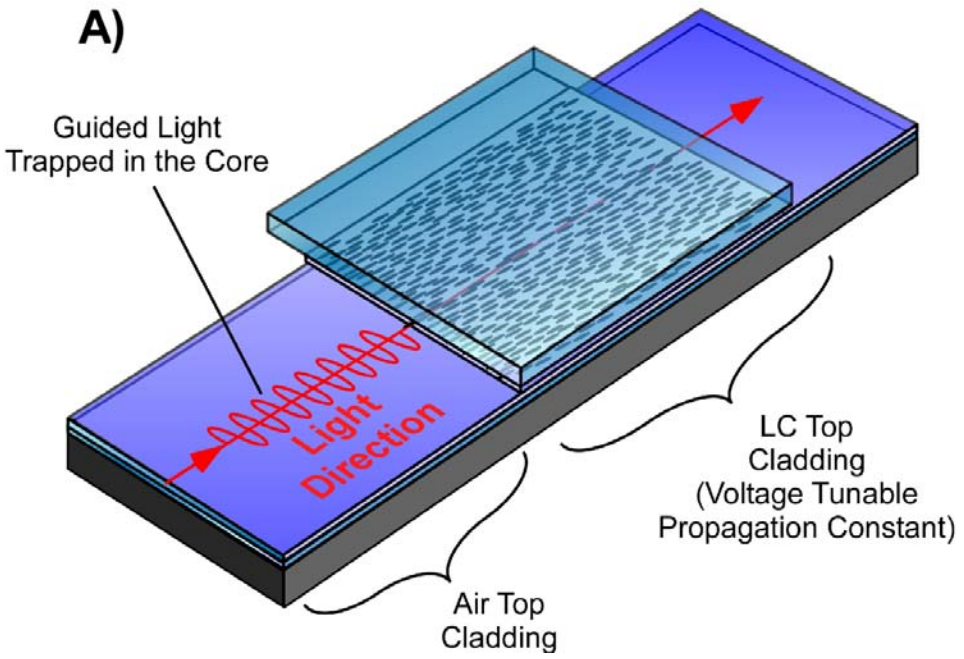

Figure 5-26: Top viewpoint of a design for a LC tunable beam steerable device.

Figure 5-27 shows the slab waveguide model modification by adding the LC cells on top and bottom. The effective index of the overall structure was calculated for both the "on" and "off" states of the LC cells to provide input for the 2D simulation of the structure. The square superlattice device was then simulated using a superlattice strength of 0.857 with TE source polarization conditions. Two effective index values were generated from the 3D FDTD simulations – for the off condition the effective index is n = 3.034 and for the on condition the effective index is n = 3.093. This results in a very small index change of only Δn = 0.059. Even though the index change is relatively small, using the square superlattice 3p refraction response increases the beam steering angle. This refraction plot is shown in Figure 5-28. For an input source frequency of ω = 0.274, at the θ_i angle of 13.05°, an active steerable beam of $\Delta\theta_r$ = 81.09 - (-7.51) = 88.60°

could be obtained even with this small index change for the square superlattice 3p band. This is a large potential refractive angle change and could be quite useful in this device application.

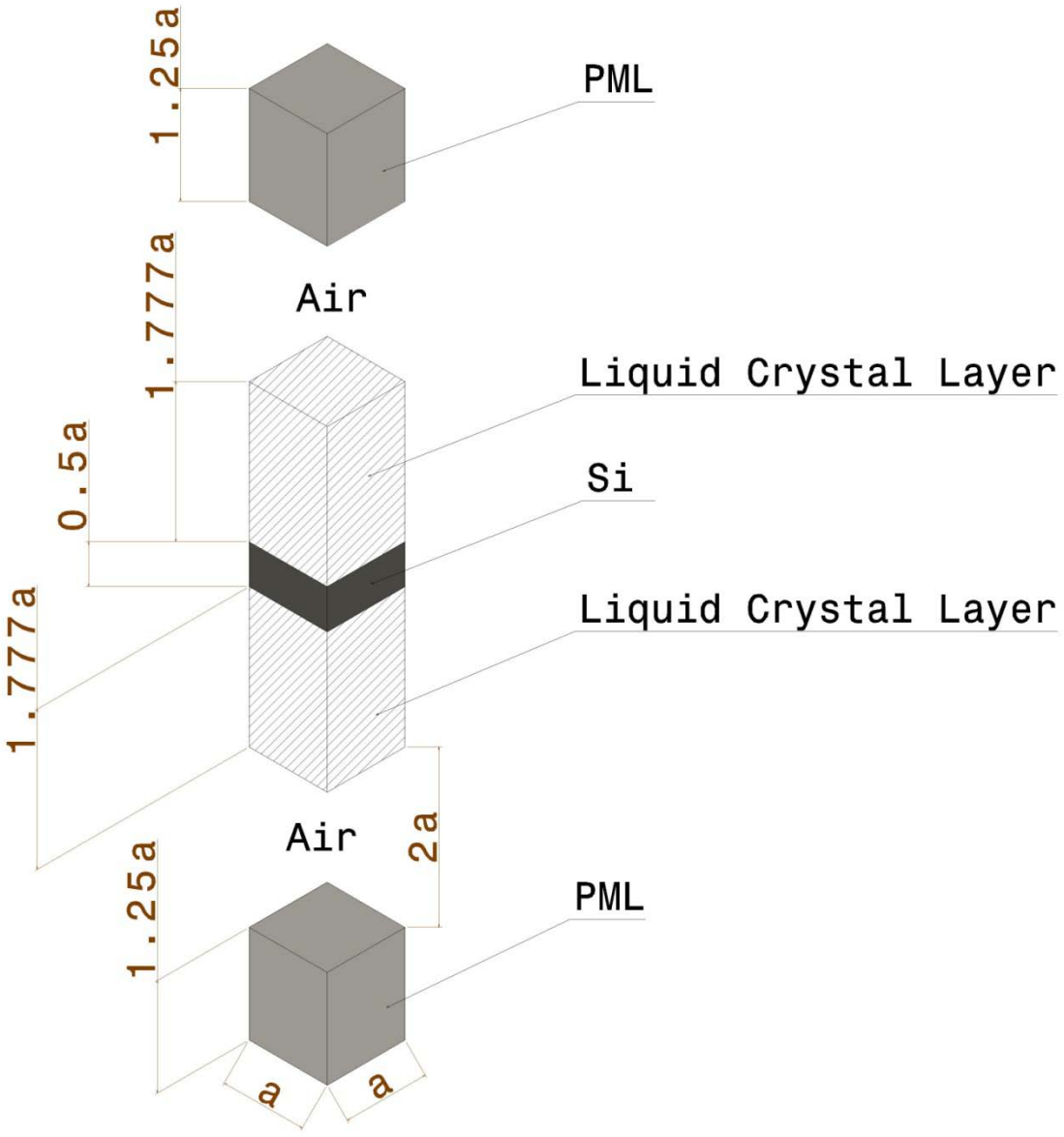

Figure 5-27: 3D effective index slab waveguide model, modified to include LC cells on the top and bottom of the slab.

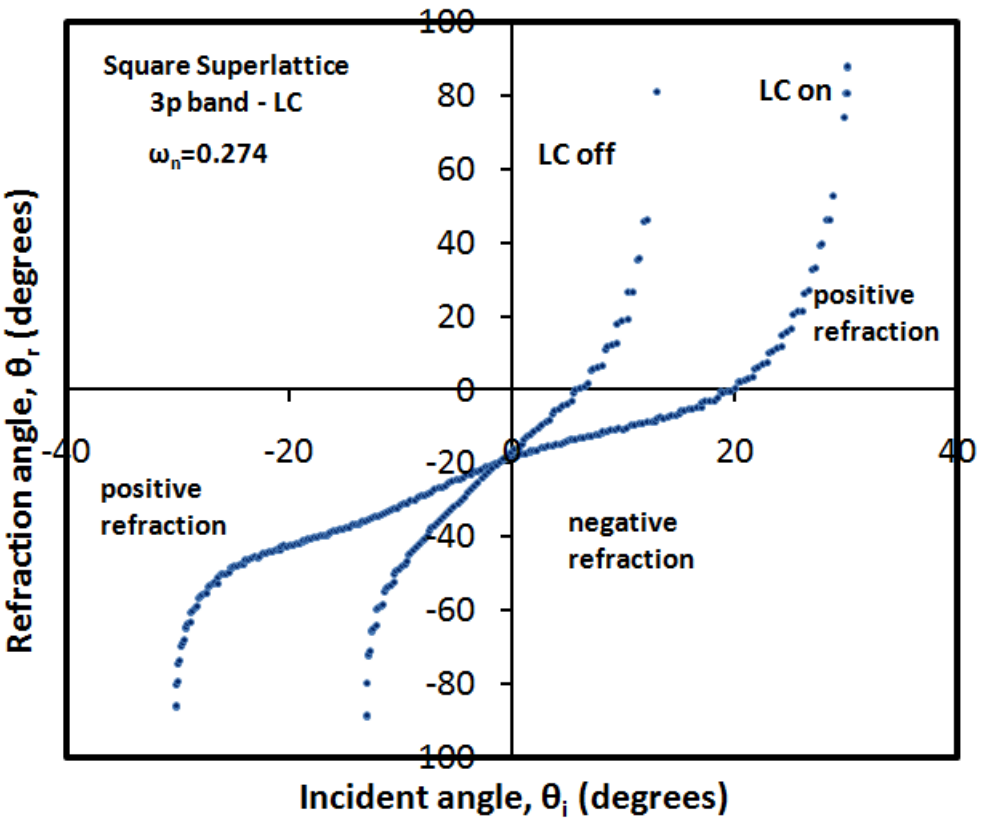

Figure 5-28: Refraction curves for the 3p band of a 0.857 square superlattice for both the on and off bias condition of the LC cells.

Using the same effective index slab model, we can also compute the refraction changes for the triangular superlattice in this configuration. In the case of the triangular superlattice, both the 3s and 3p contours can be examined as both have closed contours around the M-point. Previous work has been done on this structure using LC infiltrated holes rather than cells on the top and bottom. The issue of filling the nanoscale holes with LC is that the index change biased vs. unbiased in reality is quite small. This is due to the fact that the LC molecules are fairly large compared to the hole size, and as mentioned previously they tend to pin to the walls, thus significantly reducing the overall index change. Also, there is difficulty in infiltrating such small holes from a fabrication

perspective. Using the new scheme of placing sealed LC cells on the device, refraction calculations were run for both bands to determine if they exhibited a large refractive angle change similar to the square superlattice 3p band.

Figure 5-29 shows the refraction diagram for the 3s band of the triangular superlattice at a fixed frequency of $\omega = 0.33$. As illustrated in the graph, the curves are very close together using the same effective index values as the square superlattice. In this case a maximum change of $\Delta\theta_r = 59.31 - (21.41) = 37.90°$ at $\theta_i = 17.75°$. This is significantly less than that of the 3p band of the square superlattice. The 3p band of the triangular superlattice is similar to the square version so a larger refraction response is expected.

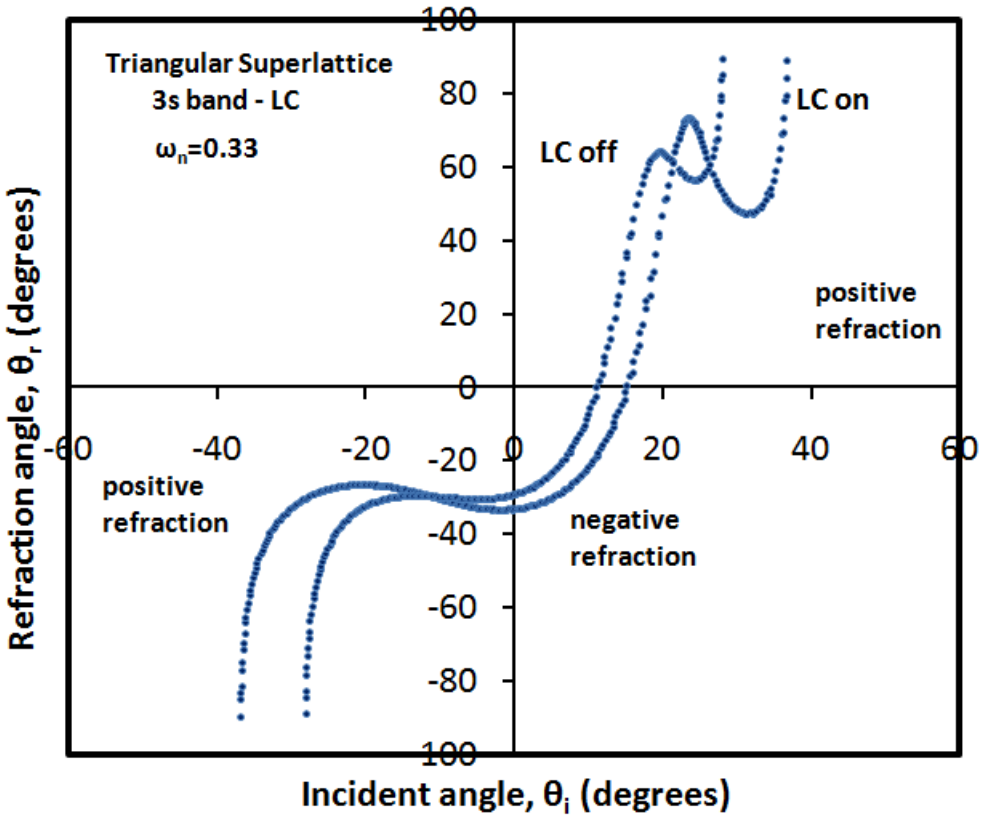

Figure 5-29: Refraction curves for the 3s band of a 0.857 triangular superlattice for both the on and off bias condition of the LC cells.

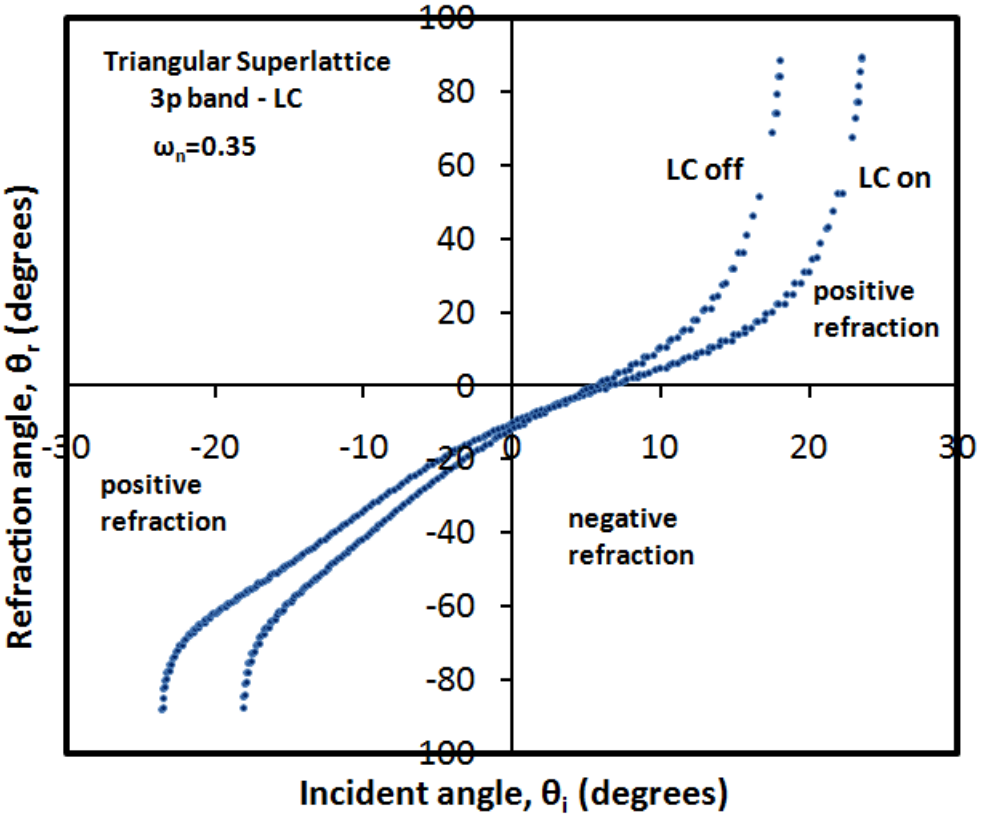

Figure 5-30: Refraction curves for the 3p band of a 0.857 triangular superlattice for both the on and off bias condition of the LC cells.

From the 3p contours of the triangular superlattice in Figure 5-30, it can be observed that these curves are also quite close together. it can be observed that these curves are also quite close together. The largest tunable refraction that can be obtained for this band is $\Delta\theta_r = 88.15 - (22.14) = 66.01°$ at $\theta_i = 18.06°$. This value is greater than that for the 3s band for the triangular superlattice, but still less than the 3p band refraction in the square superlattice. The difference between the two is $\Delta\theta_r = 88.60 - 66.01 = 22.59°$, showing that the 3p band of the square superlattice provides about 34.2% more refraction for the same change in index. The large refraction change makes this structure

potentially useful for improving refraction in the proposed LC beam steerable waveguide application.

5.7 Dynamic Tuning of the Square Superlattice Using Electro-Optic Materials

As a final active tuning investigation of the square superlattice 3p band, the entire structure can be constructed in a non-linear optical material such as PLZT (lead lanthanum zirconate titanate). This material changes index upon the application of a bias across the material. For the "off" case with no bias, the index is approximately $n = 2.49$, while for the "on" case the index is $n = 2.61$, yielding a Δn of approximately 0.12. For a more realistic model, we substitute these values into the 3D slab waveguide model to obtain an accurate effective index for the entire structure. The effective index simulations yield $n = 2.009$ for the off case and $n = 2.117$ for the on case, resulting in a Δn change of 0.108 for the structure. This is a larger refractive index change than the $\Delta n = 0.059$ that was found for the LC slab waveguide structure.

The simulation was run for TE source polarization with 0.857 superlatttice strength as before. Figure 5-31 shows the curves for both PLZT bias conditions. The maximum refraction angle in this case is $\Delta\theta_r = 86.77 - (-2.87) = 89.64°$ at $\theta_i = 10.51°$; similar in magnitude to that for LC slab waveguide configuration. Previous work on the 3p band of the triangular superlattice gave only a Δn of 55.2°, so the square superlattice 3p band improves this refraction response by 62.3%, which is significant.

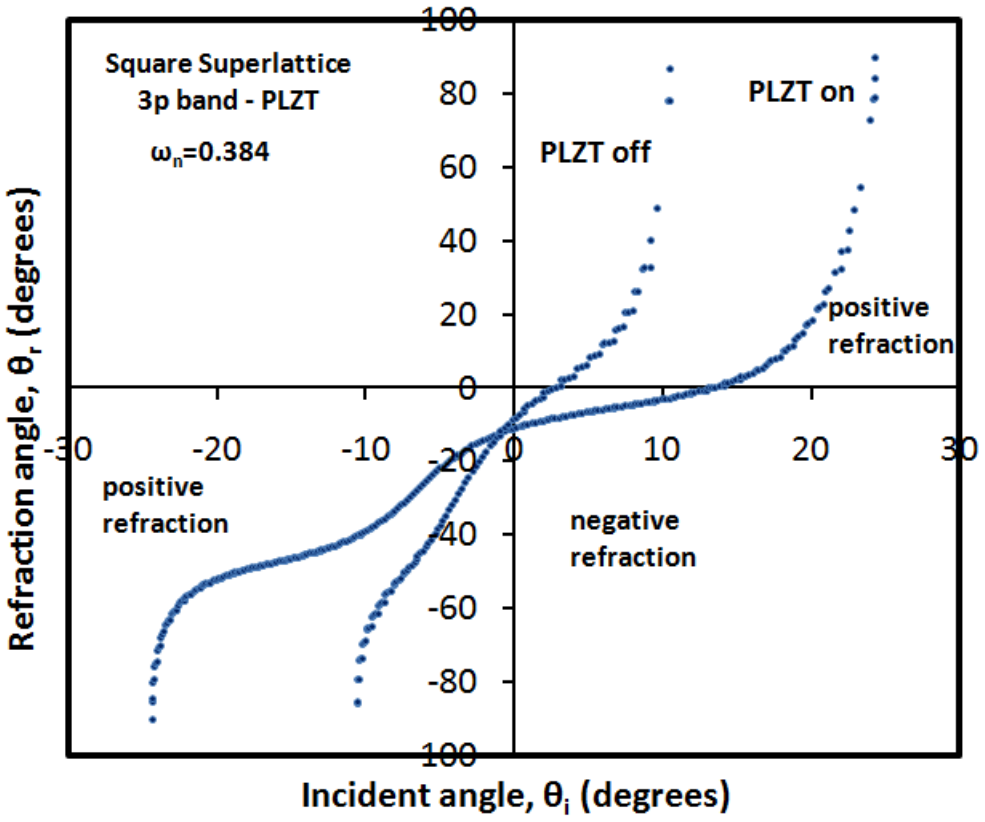

Figure 5-31: Refraction curves for the 3p band of a 0.857 square superlattice for both the on and off bias condition of the PLZT.

5.8 Conclusions and Future Work on the Square Superlattice PC Structure

Through this work we have identified that the square superlattice, specifically the 3p band, shows great potential to produce large refraction values. It has been demonstrated that refraction can be controlled statically and dynamically through the introduction of

various linear and non-linear optical materials into the structure. Several points need to be made regarding the degree of refraction that can be obtained in real fabricated devices that are subjected to real source and measurement conditions.

First, an actual real-world light source has a finite excitation beam size, rather than the infinite plane wave source that was used in the numerical simulations. Since the beam is incident on points that are near the BZ boundary, the finite beam size will cause the k-values to be spread over this region of curvature. The large curvature of the contour surface will typically lead to a large dispersion, where the actual excitation will spread rapidly and decay within the square superlattice structure. To counter this effect, either the source excitation beam and device must be made wider, or a different contour chosen to obtain the desired tunable refraction effects. These effects need to be examined closer in measurements of a fabricated square superlattice to determine how they could be minimized.

Second, the PLZT version of the device presents a fabrication challenge. PLZT is currently not compatible with cleanroom processes therefore, it could not be fabricated using these technologies, such as electron beam lithography and plasma etching. A way to mold the device using some kind of material injection or inversion technique, or making the holes with focused ion beam (FIB) technology may be possible. This fabrication work is left for future research, as the structure shows good tunability and potential applications, and would be valuable to investigate further.

In spite of these challenges, the square superlattice looks promising as a way to produce and control large refractions in a device. Work is underway to measure and characterize the refraction in these fabricated devices. An SOI version of the lattice was

recently produced using cleanroom technologies – the SEM image is shown in Figure 5-32. Unfortunately, the measurement facilities available to our group are limited to reflectivity characterizations of the device only at this time. Reflectivity measurements only allow probing of the non-guided modes of the structure, which are not valuable in determining the refractive properties of the device. In order to fully probe the refraction effects in the square superlattice, we require a transmission measurement setup. We are currently investigating setting up such a system, or utilizing equipment from another group. Further investigations and publication should follow from this additional planned measurement work.

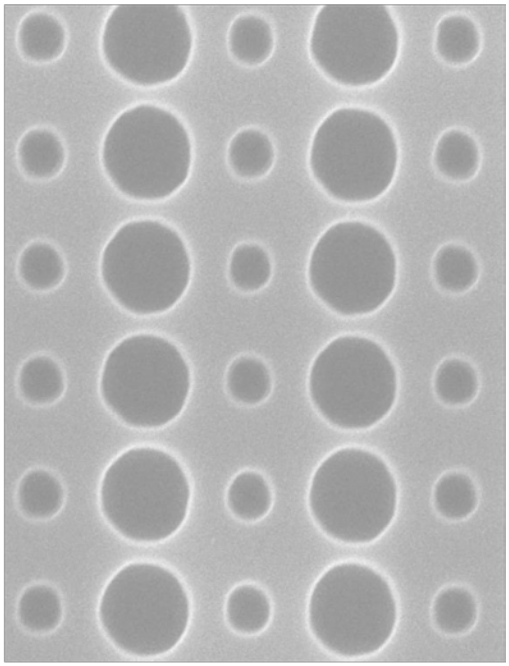

Figure 5-32: SEM image of a fabricated square superlattice PC with dielectric strength $k = r_1 / r_2 = 0.587$

In the square superlattice research work, we have primarily focused on the higher frequency bands, where the shorter operating wavelength of light in the structure is on the same scale as the Si and air dielectric features. This operating regime produces the

irregularly shaped dispersion contours that were the focus of the work. For the optical invisibility cloaking structure examined in the next section, we will primarily be focusing on the lower bands, where the operating wavelength of light in the structure is much larger than the Si and air dielectric features. In this case the light sees an average index between the two materials, creating a spatially varying index across the device. We will now turn to this new optical invisibility cloaking structure, where the index averaging method will be discussed in more detail.

6 The Optical Invisibility Cloak

6.1 Introduction to Electromagnetic Cloaking

The idea behind invisibility cloaking was originally published by Pendry *et al.* in 2006 [66]. The concept involves creating a closed space from which electromagnetic radiation is excluded. To create the cloaked area, the radiation must be steered around it. Since electromagnetic waves are constrained to travel in straight lines away from their point of origin according to Fermat's principle, a way to steer the beams around the space without violating this law must be found. This steering can be accomplished by use of mathematical transformation on the original space that creates a warped lattice as shown in Figure 6-1. Consider the original space to consist of a uniform dielectric material. The concealment space then distorts the dielectric function of the material in such a way that the electromagnetic radiation travels around the cloaking area or is reflected off the area in a uniform way. Simulated ray diagrams illustrating how the electromagnetic radiation would flow around the cloaked area are shown in Figure 6-2 (A) for a 2D circular cloaking region and in Figure 6-2 (B) for a 3D spherical cloaking region.

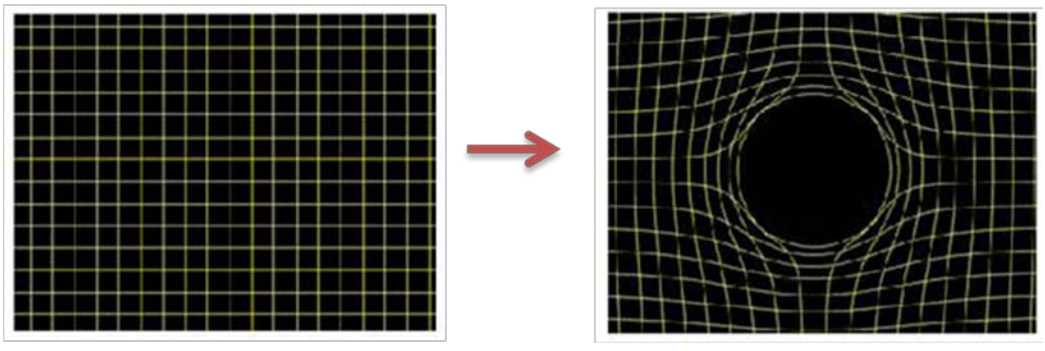

Figure 6-1: Illustration of the warping of dielectric space by a mathematical transform operation.

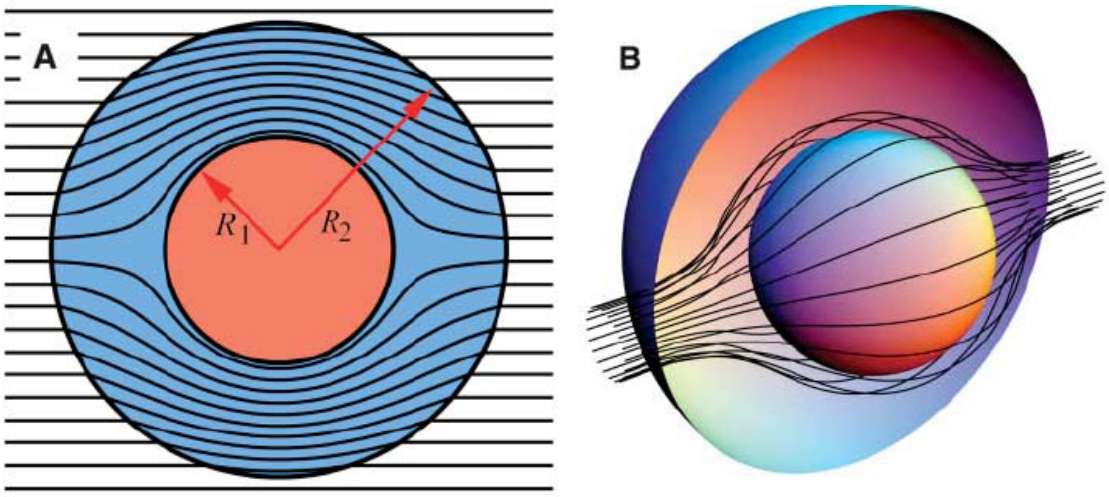

Figure 6-2: Simulated ray diagrams for electromagnetic radiation flowing around a (A) 2D circular cloaked region and (B) a 3D spherical cloaked region [66].

To accomplish this transformation, we must determine how Maxwell's equations are affected by the distortion of the dielectric space function, and therefore how the electromagnetic wave propagation is affected around the cloaked area. It turns out the Maxwell's equations have the same form, but the dielectric and magnetic constants around the space are scaled by different factors. Therefore, a transformation of the properties of a material surrounding the concealment region is equivalent to distorting the original space. The material or metamaterial that is placed around the distorted region is now the actual cloaking structure, and provides the transformation required for electromagnetic radiation to move around the cloaking region uninterrupted. These transformation techniques as applied to cloaking structures that operate at optical frequencies are considered to be part of a emerging field known as transformation optics.

The original work by Pendry et. al. [66-67] was mainly devoted to the conceptualization of the mathematical transformations, i.e. transformation optics, that

enable the computation of the material properties required to create the cloaking structure. The determination of whether the cloaking device can work at broadband frequencies or is confined to a single operating frequency is dependent upon the laws of physics. Although the phase velocity in the cloak material surrounding the void can and must be greater than the phase velocity of light in a vacuum to create the cloaking effect, it is not possible for the group velocity of the radiation in the material to exceed that of light. This requires the presence of dispersion in the cloaking material to obtain different phase and group velocities. However, all materials have dispersion properties that change with frequency, thus efficient cloaking is currently limited to a single frequency until sufficiently broadband metamaterials can be developed.

After the publication of this work indicating that an invisibility cloaking structure was mathematically and theoretically possible, work by other groups commenced to obtain a practical realization of cloaking structures. The first real-world cloak construction was developed by Schurig et al. [68] in 2006. The cloaking structure consisted of structured metamaterials that contained split ring resonators. The cloak works for an narrowband incident TE wave (here using the E_z electrical engineering notation), and its functionality is dependent only upon μ_r, μ_φ, and ε_z. Simplification of the electromagnetic parameter requirements was realized by assuming μ_φ=1, making the system of design equations spatially homogeneous and eliminating the need for any infinite parameter values, which are hard to realize experimentally. The simplifications reduced the effectiveness of the cloak somewhat, but good reduced scattering behavior was exhibited.

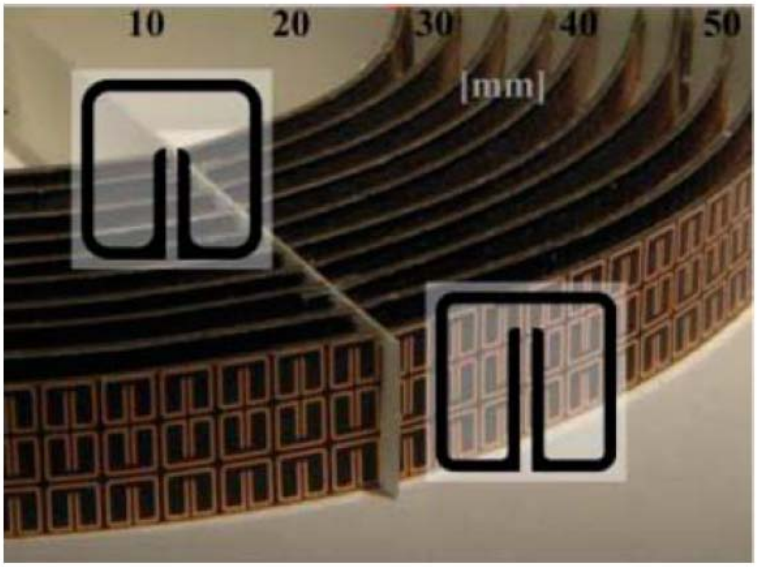

Figure 6-3: Experimental cloak consisting of split ring resonators produced by Shurig et al. [68]

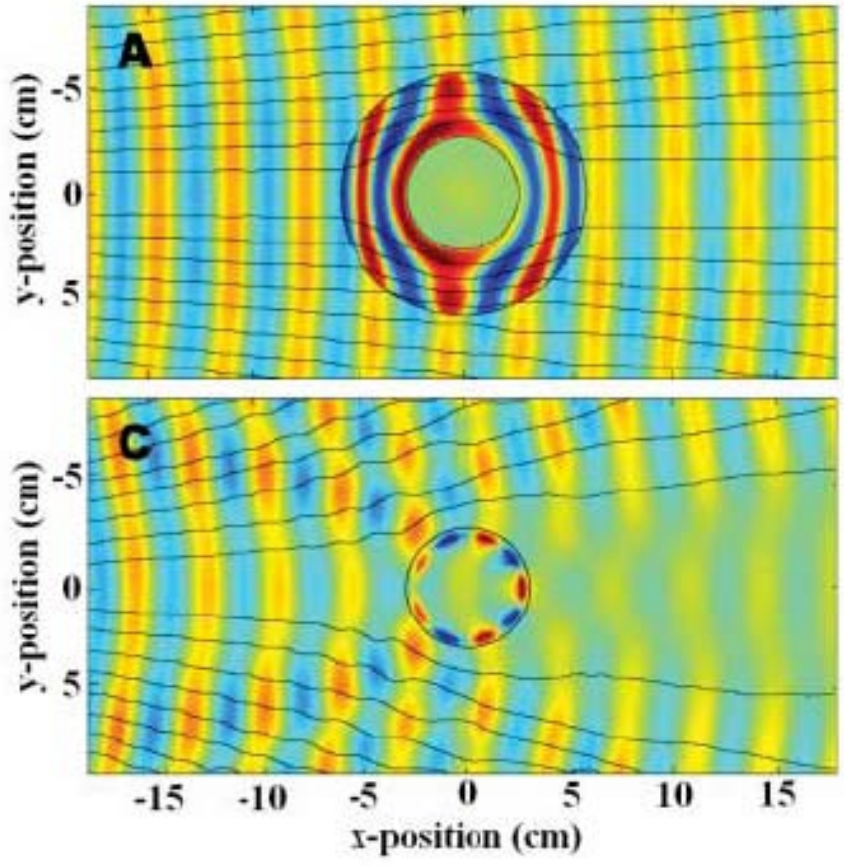

Figure 6-4: Simulated (A) and measured (C) electromagnetic cloaking performance for the structure developed by Schurig et. al. [68]

The main difficulty in creating devices that exhibit cloaking behavior lies in the fact the they require extreme values of permittivity and permeability necessary for correct device operation [69-70]. While the design of these structures for operation in the microwave frequency range requires the use of resonating metal elements [68], this strategy and material will not work for structures cloaking in the optical regime. This is due to the fact that metal materials are unable to maintain low-loss performance characteristics at higher frequencies of operation.

Recently, a new cloaking design has been theoretically proposed that reduces the required range of material property values for higher frequency device operation [40]. This design, the 'carpet' cloak, compresses a curved reflective surface into a flat reflective surface, effectively shielding objects behind the curve from view with respect to the incoming radiation source. In this case the electromagnetic energy reflects off the cloaked area, rather that travelling around it in space. The quasi-conformal mapping is performed such that transformed cells of the structure reduce the overall anisotropy of the device to a smaller range of isotropic medium indices. Thereby, this approach eliminates the need for absorptive metallic resonant elements, and thus can be fabricated using only dielectric materials. A figure for this index mapping will be shown in the next section covering the numerical theory of this cloak design. This cloaking structure was recently demonstrated to work in the microwave [71] and optical regimes [72-74]. Our goal was to adapt this design for operation at optical frequencies by scaling the device dimensions down to nanoscale dimensions. For device operation in the near infrared wavelength spectrum, features in range of 5 - 50nm need to be created within high precision tolerances to prevent undesirable shifts in the frequency of operation of the cloak.

6.2 Goals of the Optical Cloaking Research

The main goal of the research was to prove that the mathematical optical frequency ground-plane cloaking concept proposed by Li and Pendry [40] could be fabricated into an actual device and measured, proving that the real-world device performance would match that predicted by theory. This will be accomplished by first converting the mathematical model of the structure into an actual device structure that can be modeled. The structure will then be numerically simulated to determine its performance at optical frequencies. The challenge lies in the experimental portion of the research, in which the nano-scale cloaking device will be fabricated and its performance measured to determine if the real-world device performance matches that predicted numerically.

The second main goal of the research was to investigate the tunability of the structure through the use of ALD coatings and electro-optic materials to modify the operating wavelength of the structure were to be pursued. Initially these investigations were conducted numerically to test the device operation and tuning as the coatings were added to the structure. The rest of the research focuses coating the fabricated samples with ALD coatings such as TiO_2 and comparing the experimental and measurement results.

6.3 Design and Numerical Analysis of the Optical Cloak

Before the work could be begin on constructing this ground plane cloak experimentally, numerical simulation of the cloaking structure was required to determine

the index values required for the material that would make up the structure. Since the material we desire to work in is Si, we require a conformal mapping that gives us an index range of $\varepsilon \leq 12.0$, the maximum optical index of Si at a 1.55μm operating wavelength. Once we have the conformal index map that adheres to our index limits, the cloak can be constructed by area or volume averaging a Si / air structure that can be fabricated using microelectronics processing technology.

The mathematical background used to created the index map starts by converting a physical index mapped coordinate system, mapping it into a virtual index mapped coordinate system that contains the cloaking area. The two systems are shown below in Figure 6-5.

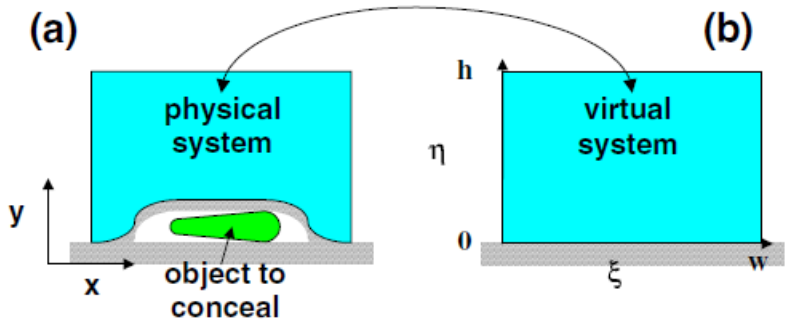

Figure 6-5: Physical and virtual systems for the ground-plane cloak design. Shaded regions are the ground planes. The physical system is perceived by the observer as the virtual system with a flat ground plane [40].

The physical system has coordinates (x,y) or (x1, x2), while the virtual coordinate system has coordinate labels of (ξ, η) or (ξ^1, ξ^2). The transform starts with the introduction of a Jacobian matrix Λ:

$$\Lambda^{i}_{i'} = \frac{\partial x^{i}}{\partial \xi^{i'}} \tag{87}$$

The covariant metric is described by g:

$$g_{i',j'} = \xi_{i'} \cdot \xi_{j'} \tag{88}$$

Or incorporating the Λ formula:

$$g = \Lambda^T \Lambda \tag{89}$$

To create the cloaking effect, the observer must see the physical system as an isotropic homogeneous medium having permittivity ε_{ref} and unit permeability (i.e. structure is non-magnetic). The electromagnetic parameters of the physical medium that are now created by the coordinate transform given by:

$$\varepsilon = \varepsilon_{ref} / \sqrt{\det(g)} \tag{90}$$

$$\left[\mu^{i\,j}\right] = \Lambda\Lambda^T / \sqrt{\det(g)} \tag{91}$$

The principal values of the permeability tensor μ_T and μ_L in the physical medium, i.e. the cloaking material, can written in terms of refractive indices:

$$n_T = \sqrt{\mu_L \varepsilon} \tag{92}$$

$$n_L = \sqrt{\mu_T \varepsilon} \tag{93}$$

These index values are for the two planes waves travelling along the principal axes. The anisotropy of the material can be described by the anisotropy factor α:

$$\alpha = \max\left(\frac{\eta_T}{\eta_L}, \frac{\eta_L}{\eta_T}\right) \tag{94}$$

Using equations (81) - (84), the formula becomes:

$$\alpha + \frac{1}{\alpha} = \frac{Tr(g)}{\sqrt{\det(g)}} \tag{95}$$

where

$$\mu_L \mu_T = 1 \tag{96}$$

We can now define an averaged refractive index n that puts the describes the system in terms of α and n instead of the electromagnetic parameters ε and μ^{ij}:

$$n^2 = \frac{\varepsilon}{\varepsilon_{ref}} = \frac{1}{\sqrt{\det(g)}} \tag{97}$$

In a cloaking structure, the compression of space in the physical domain makes the cloak anisotropic. We wish to minimize the anisotropy by choosing a suitable coordinate transform. If the transform reduces the anisotropy enough, we can drop the factor by assigning $\alpha = 1$. In this way, we reduce the terms and only keep the average refractive index term n. This reduces the physical medium to a simple dielectric profile with unit magnetic permeability. Reducing the anisotropy factor requires minimizing the Modified-Liao functional:

$$\Phi = \frac{1}{hw}\int_0^w d\xi \int_o^h d\eta \frac{Tr(g)^2}{\det(g)} \tag{98}$$

Without going into further technical proof, this functional minimizes the average and the maximum value of $Tr(g)/\sqrt{\det(g)}$ in the physical domain. That is, the anisotropy in the physical domain is now minimized. The unit cells in the transformed grid are now rectangles with a constant aspect ratio of $M{:}m$, where M is a conformal module of the physical domain, i.e. a geometric property of the physical domain with four defined boundaries). The function $m = w/h$ is now a conformal module of the virtual domain and is described by:

$$\frac{|\xi_1|}{|\xi_2|} = \frac{M}{m} \tag{99}$$

$$\sqrt{\det(g)} = |\xi_1||\xi_2| \tag{100}$$

If we now substitute equations (92) – (93) into equation (88) we obtain:

$$\frac{Tr(g)}{\sqrt{\det(g)}} = \frac{M}{m} + \frac{m}{M} \tag{101}$$

Which can also be expressed as:

$$\alpha = \max\left(\frac{M}{m}, \frac{m}{M}\right) \tag{102}$$

These equations are now independent of position . It can be proven that in the limit of $M = m$, the quasiconformal map approaches the conformal map. The quasiconformal map is required to keep the topology of the physical space unchanged without creating errant singular points in the coordinate transformation.

For an example, consider the mapping of a rectangle bounded by $0 \leq \xi^1 \leq 4$, $0 \leq \xi^2 \leq 1.5$ in the virtual domain, to the same rectangle in the physical domain with a bottom boundary specified by:

$$y_{bottom}(x) = \begin{cases} 0.2\cos\left(\frac{\pi x}{2}\right)^2 & 1 \leq x \leq 3 \\ 0 & otherwise \end{cases} \tag{103}$$

This equation describes the "bump" area on the ground plane of the physical space that defines the cloaking area, behind which the object to be hidden is placed.

Applying the mathematical transform to this physical system results in the index map shown in Figure 6-6 (a)-(b). Figure 6-6 (a) is the transfinite grid transformation, in the case that interpolation is used for a regular 40 x 15 grid. Note that in this case there is only a linear compression of the index value in the y direction. Here the anisotropy factor α ranges from 1.0 to 1.385, while n^2 ranges from 1.0 to 1.153. For device design purposes, we would like to have a fixed anisotropy, eliminating the need for a material with a more complex dielectric profile. Thus, the preferred cloak construction method is to use the quasiconformal mapped grid shown in Figure 6-6(b). In this case, the grid

lines are orthogonal to the cloaking area. This quasiconformal mapping changes the aspect ratio of each cell so that the anisotropy factor α becomes a constant of 1.042. The index value range n^2 is increased in this case to a range of 0.68 to 1.96. While we have increased the index range for the sake of minimizing the anisotropy in the structure, both n and ε remain finite without approaching zero or infinity, unlike the case for the original design where the radiation flow around the cloaking area [66]. The quasiconformal mapping in this case effective crushes the object into a plane rather than a line. The choice of Equation 96 to describe the inner boundary was chosen to achieve a smaller value of n, rather than using a boundary with sharp corners that could results in singularities in the solution.

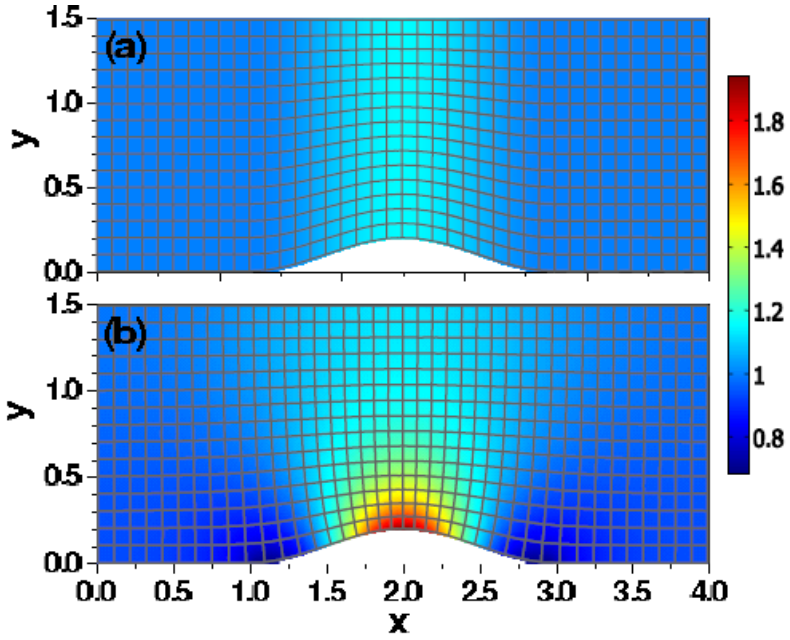

Figure 6-6: Plots of the transformed grid in a physical space with a ground plane cloak boundary described by Equation (96). Grid (a) is for a transfinite grid and (b) is the quasiconformal grid. The color map shows the values of n^2.

Now that the index values for the quasiconformal mapped cloak have been computed, the physical design of the cloak can be constructed. The small anisotropy and

finite range of n from the quasiconformal map calculations make the physical realization possible using only silicon and air as dielectric materials. For device operation in the near infrared wavelength spectrum, features in range of 5 - 50nm need to be created within high precision tolerances to prevent undesirable shifts in the frequency of operation of the cloak. To accommodate the small feature size and range in the nanoscale regime, specific design choices were made in the creation of this cloaking device to maximize performance and minimize the complexity of fabrication. The basic design strategy is to use deep sub-wavelength scale silicon nanostructures to produce a metamaterial structure with desired effective refractive index values at different points within the device. When the features are much smaller than the wavelength of light, the effective index of a composite structure is determined by properly averaging the indexes of the constituent materials. In our design, we chose our unit cell to be 150nm which corresponds to $\lambda/10$ for operation at $\lambda = 1500$nm. Each unit cell may contain an air hole or a silicon nanorod. Since the effective index of a given unit cell is given by the volume average of the indexes of silicon ($\varepsilon = 12.0$) and air ($\varepsilon = 1.0$) within the unit cell, we can simply change the size of the air hole or silicon nanorod to realize a range of effective index values required to implement the cloak structure. For a given unit cell size, air holes with varying diameters were found to provide a smaller range of effective indexes compared to nanorods. We thus chose to use silicon nanorods of various diameters to implement the all-dielectric cloak structure. The size of the nanorods were then determined using the effective medium theory. We first calculated the effective permittivity for the fundamental transverse-magnetic (TM, electric field perpendicular to the device layer) mode for the air-silicon-oxide slab waveguide, which was found to be

$\varepsilon_{SOI\text{-}TM} = 7.55$ at $\lambda_o = 1500$ nm. If the nanorods are small, the effective permittivity of the nanorod array is given by the simple volume average of the silicon slab and air, $\varepsilon_{eff} = A\varepsilon_{SOI\text{-}TM} + (1 - A)\varepsilon_{air}$ where A is the total cross-sectional area encompassed by nanorods and $\varepsilon_{air} = 1$. The range of permittivity values required for the cloak can now be realized by progressively varying the nanorod diameter throughout the structure. The validity of this simple averaging rule was confirmed by performing rigorous 3D photonic band structure calculations as verification of the method.

Simulation results for the ground-plane cloaking structure utilizing the finite-element method are provided in the original paper by Pendry *et. al.* [40]. In these simulations the index profile is created directly through the use of a dielectric matrix. Here a Gaussian beam with a 750nm wavelength is launched into the profile at an angle of 45 degrees. The real part of the total electric field pattern is shown in Figure 6-7(a), and reflects off the cloaked area as if it was a flat ground plane. Contrast this field pattern with Figure 6-7(b) in which there is only a single dielectric constant for cloak. This field pattern clearly shows the presence of the cloaking structure, splitting the incident beam into two different angles of 38 and 53 degrees.

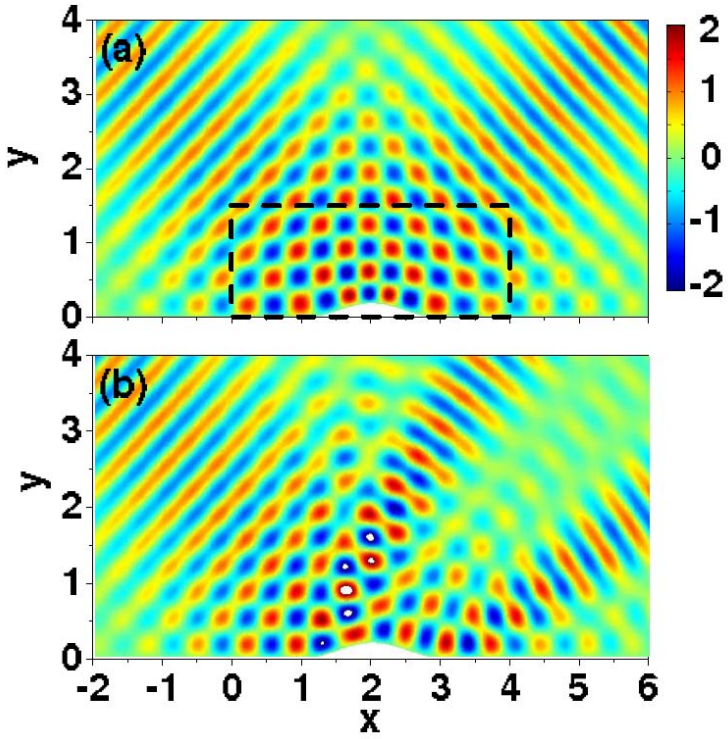

Figure 6-7: (a) Electric field pattern for the ground-plane cloaking structure with an incident Gaussian beam launched into the index mapped dielectric material at a 45 degree angle. (b) Electric field pattern when the cloaked area is reflective and index mapping is removed from the background material [40].

The performance of our nanorod cloak design was investigated by similar methods, here utilizing the FDTD simulation method. Instead of using a dielectric matrix as in the previous work, the structure was created as a matrix of Si nanorods in air, creating the original matrix profile as a discrete effective index profile. The results are shown in Figure 6-8 showing a well-defined beam analogous to the specular reflection that would be obtained from a flat mirror ground plane. This result, when compared to the simulation in the original work, shows good agreement. In this case, scattering is present due to the discrete nature of the effective index dielectric matrix. The amount of scattering in the field pattern is directly proportional to the size of the nanorod structures used in the simulation. Initially larger nanorods were used due to fabrication constraints

(to be discussed in the next section). Decreasing the size and periodicity of the nanorods reduces the scattering significantly in the simulation, due to the fact that the index profile is now more precise, especially in the area of the cloaked region. Some light leakage is present around the reflecting interface due to the less than 100% reflectivity at this point.

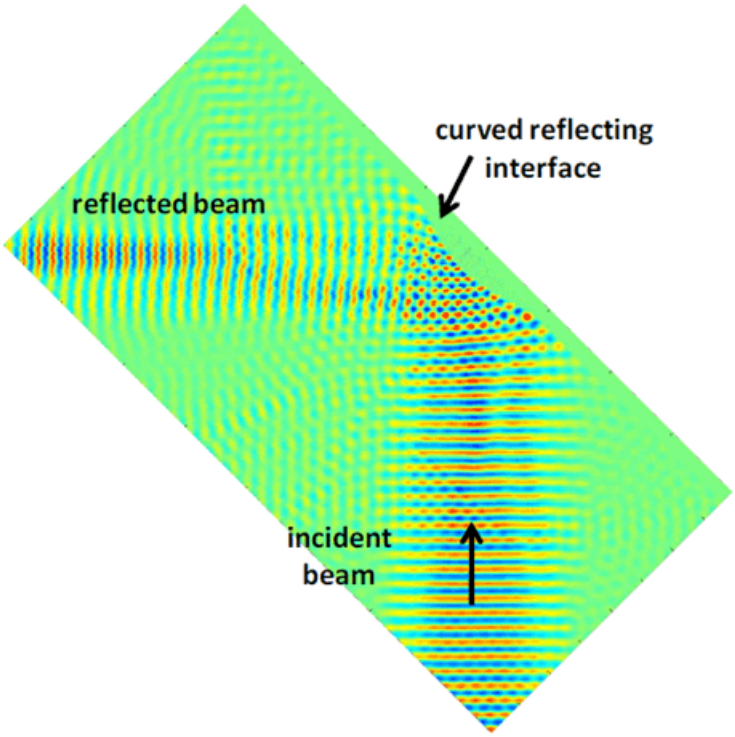

Figure 6-8: FDTD simulation showing the performance of the silicon nanorod array cloak. The frequency was set to $\omega a/2\pi c = 0.1$ which corresponds to a = 150 nm for an operating wavelength of $\lambda = 1500$ nm [72].

FDTD simulations were also performed on a reference device constructed entirely of silicon. This was done to not only confirm the original work, but to provide a field pattern reference for an actual calibration device that was to be created and measured later. The index pattern that was used was identical in size to the nanorod cloak device in Figure 6-8. Figure 6-9 shows reference device field pattern, which exhibits the same multiple reflection behavior as in the original finite element simulation. The two bright

areas at the top provide a reference point for reflection angle calculation and calibration of the incident light source into an actual measured device.

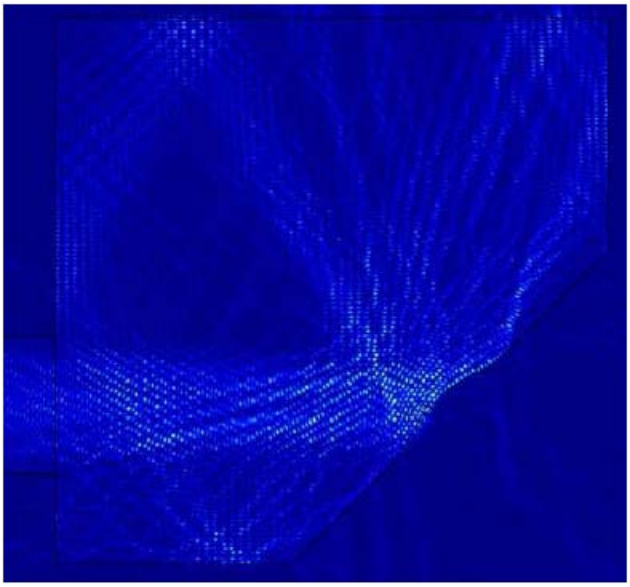

Figure 6-9: FDTD simulation for the all silicon reference sample cloak, showing multiple reflections off the cloaking area.

6.4 Fabrication Methods

To accommodate the small feature size and range in the nanoscale regime, specific design choices were made in the creation of this cloaking device to maximize performance and minimize the complexity of fabrication [72-73]. The basic design strategy is to use deep sub-wavelength scale silicon nanostructures to produce a metamaterial structure with desired effective refractive index values at different points within the device.

Three different cloak designs were created, the first two having less challenging electron beam lithography requirements to provide a design baseline for the third more

difficult to fabricate structure. All three designs required permittivity values inside the cloak ranging from 1.5 to 4.4, created using the volume averaging index method as described above. In the base design for all the cloaks, the smallest nanorods are on the order of 50nm in diameter, while the largest nanorods required very small gaps between them of approximately 20nm. As a comparison, the Si device layer is approximately 17 times the thickness of the smallest gap size. Producing these small size features in a small device area significantly increases the difficulty in fabricating these devices using current electron-beam technologies.

The cloak structures under investigation were designed specifically to be fabricated on a SOI (silicon-on-insulator) substrate in a microelectronics facility using readily available cleanroom technologies. This strategy was used because of the existing knowledge and experience available in microelectronics fabrication is extensive, so the risks involved in making these new devices to correct specifications with minimal iterations was reduced. Reducing the number of iterations required to successfully fabricate the devices was crucial to obtaining a successful outcome, and also in minimizing the device fabrication costs. The challenge of producing nanorod arrays that exhibit cloaking behavior at optical frequencies is that the feature size begins to approach the limits of modern cleanroom processing and patterning techniques for high aspect ratio structures. For example, this particular design required narrow gaps between nanorod structures that are difficult to keep from bridging in the fabrication process. In order to pattern the nano-scale devices successfully, state-of-the-art electron beam lithography (EBL) techniques have been used. The choice of resist used to pattern the device was another consideration, as the electron beam dose and other processing parameters are

critically dependent on obtaining a high contrast pattern. An additional challenge to successful device fabrication involves obtaining vertical sidewalls on nano-scale device features to reduce scattering. Meeting this challenge involved the optimization of plasma-etching techniques and etch recipes, working within the limits of the processing capabilities of the equipment.

Several approaches to the design were investigated with the goal of obtaining a reasonable tradeoff between ease of device fabrication and final performance. The choice of using nanorods over holes allows a more advantageous choice of electron beam resist, specifically the use of a negative resist with a higher selectivity ratio. The higher selectivity ratio enables deeper etching while keeping the mask intact, thereby allowing more vertical sidewalls to be fabricated during the plasma etching process. Also, the use of a negative resist allows for a faster write time as the size of the resist mask areas is significantly reduced. Another advantage of the design is that the entire structure can be patterned using the EBL system without the need for additional steps such as focused ion beam (FIB) milling and metallization [75]. In addition, since isotropy within the device is directly controlled by the nanorod pillar size and spacing, adjustments can easily be made to reduce the minimum size write requirements of the EBL patterning process, allowing for more reliable and consistent fabrication results.

The process flow for fabrication starts with the entry of the design structure into a CAD file format, followed by a conversion of the file into a .v30 format readable by the EBL system. Due to the complexity of drawing approximately 13,200 different sized circles using a manual command-line interface, the process was automated through the use of Excel spreadsheets and AutoCAD scripting functions. The surrounding

background photonic crystal design was then added through the use of array functions, and the entire structure rotated by 45 degrees to obtain the correct orientation for adding the waveguides. An image of the AutoCAD file for the overall device is shown in Figure 6-10, and a close-up detailed image of the structures contained in the file in the vicinity of the cloaking area is shown in Figure 6-11.

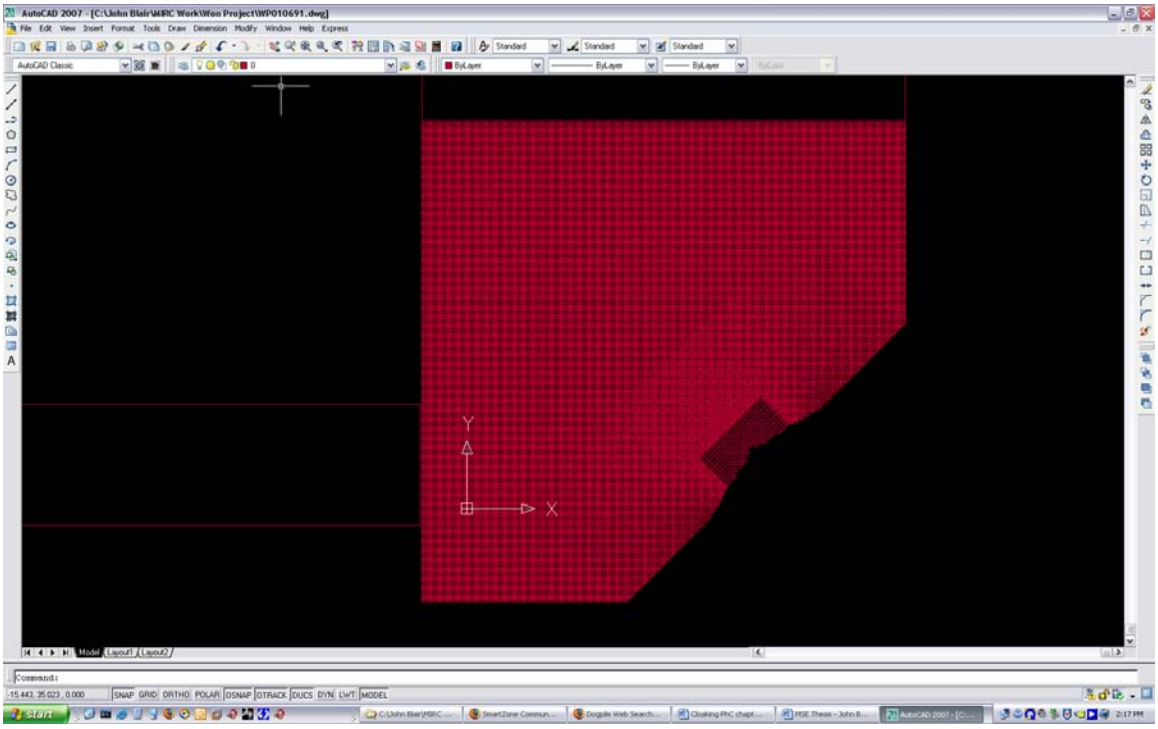

Figure 6-10: Overview of the Design A cloaking structure AutoCAD file.

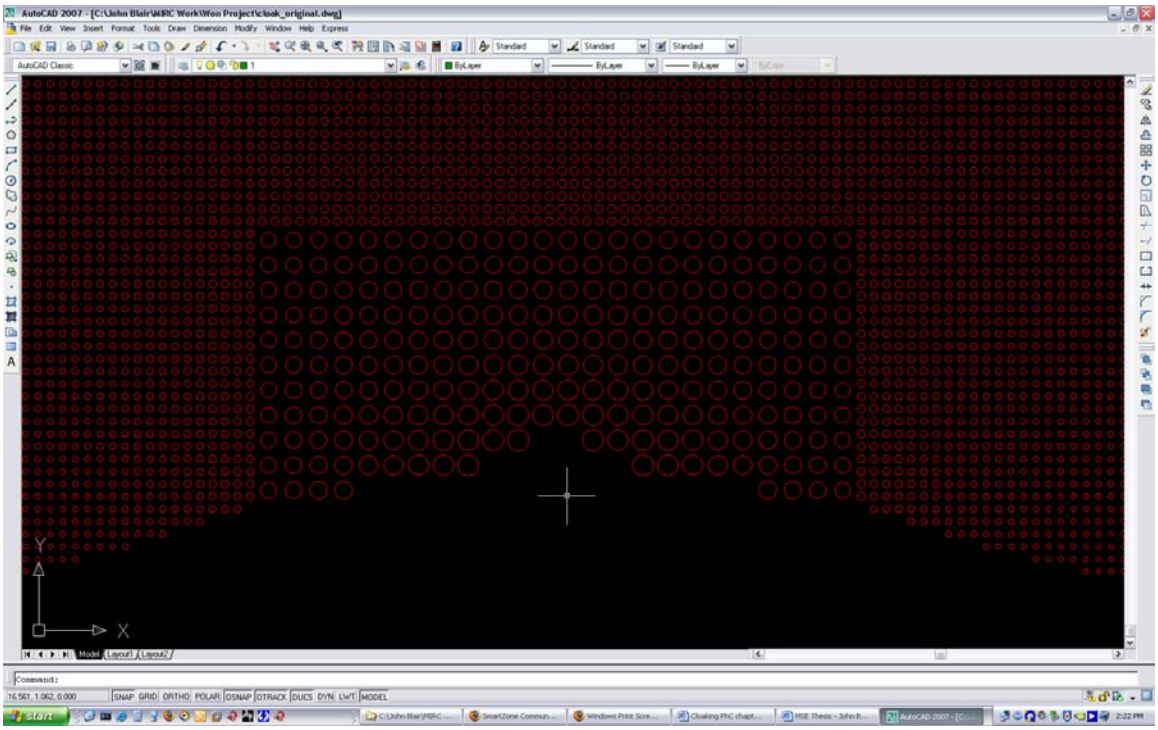

Figure 6-11: Detail of the Design A cloaking structure AutoCAD file in the vicinity of the bumped cloaking area.

Once the structure design was entered into the CAD system and converted to a .dxf format, a second conversion step was performed to convert the design to a .v30 file format through the use of proximity correction software. Proximity correction was necessary during the file conversion process to allow for dose adjustments due to the Gaussian nature of the electron beam during exposure of the structure, most importantly at the device edges and near the large waveguide areas. The proximity correction software divides the structure into 64 different dose adjustment areas, each area being a varying percentage of the base dose to compensate for the Gaussian nature of the electron beam exposure process. The dose structure output data was then placed into the EBL system control file to enable proximity corrected dose adjustments during the device patterning. However, the current version of proximity correction software does not take

into account the structure size and shape when calculating dose adjustments, and even an updated version is only able compensate for some adjustments to rectangular features. Since this design utilizes circular structures, manual adjustments were made to the proximity correction parameters during file conversion. The exact proximity correction parameters for the different designs are discussed further in the Fabrication Results section.

The SOI stack used was a 340nm thick Si layer over a 1um SiO_2 layer, which provides an adequate guiding thickness for light propagation in the 1400 - 1600nm range. A six-percent solution of hydrogen silsesquioxane (HSQ) was then applied to the surface through a spin-coating process. HSQ is a polymer-like negative-tone resist material that undergoes a transition to a more SiO_2-like material upon ebeam exposure, and has a demonstrated high resolution masking capability. For the high aspect ratio process, the spin coater was set to 5000rpm, 2500rpm/s spin up, followed by a wafer bake at 80C for four minutes to cure the resist and obtain a 100 - 110nm layer thickness. Significant care was taken to keep the wafer clean and free from contaminants prior to the application of the resist, as these could lead to defects in the final devices. The wafer was then manually cleaved into smaller pieces for processing.

Electron-beam resist patterning was performed using a JEOL JBX-9300FA EBL system running at an acceleration voltage of 100kV with a 5nm spot pitch size. A piece cassette was selected to allow for multiple device runs using a single SOI wafer. In the design the input and output waveguide line lengths were set to 3mm to allow enough room for manual line cleaving after the devices had been fabricated.

Extensive experimentation was required to determine the correct electron beam base exposure dose that would give the best feature size match without either over-exposing or underexposing parts of the device pattern. Several runs of test cloaking devices were done initially in order to optimize the ebeam dose on Si test wafers. The first set of runs was done using shorter 100um input and output lines to reduce e-beam exposure time (and thus expense). The shorter lines still provide the proximity effects that would be seen in the device with longer lines. Initial dose range was 8000μC/cm^2 - 20000μC/cm^2 for the first five devices. It was quickly determined that the initial doses were all too high for test range and the devices were overexposed creating L-shaped patterns missing fine features. Run time was about 45 min with some added calibration steps between devices.

The next set of five devices had a dose range of 1000μC/cm^2 - 8000μC/cm^2. Some calibration routines were bypassed to reduce the run time to 30 min. The best exposure dose appeared to be 2500μC/cm^2 which had showed no bridging between pillars, with the next best being 3000μC/cm^2 showing a slight bridging. The size of the fabricated pillars was compare to the design sizes, and it was found that the upper dose range of 3000μC/cm^2 had a closer match.

After many more test runs on Si, a final dose range was determined for the actual SOI run. The best electron beam dose for all three device designs was found to be in the range of 2400μC/cm^2 - 3000 μC/cm^2 after the proximity correction adjustments had been made. The CAD file was then modified to include the 3mm input and output waveguides to enable the device to be cleaved after fabrication. The ebeam write time per device was

longer, about 30-40 minutes per device, due to the longer waveguides requiring more write time.

In all of the ebeam exposure runs the device pattern was developed using a 25% solution of N-tetramethyl ammonium hydroxide (TMAH) heated to 80°C. The wafer piece was developed for 30s followed by a de-ionized water rinse for approximately 2 minutes and sample drying using N_2 gas. A visual inspection was then performed to make sure the development had been completed, and that there were no residues or contaminants left on the wafer. Before etching the device, measurement of the height of resist patterns were made using a Tencor Alpha-Step Profilometer to provide a reference point for calculating resist etch rates. The resist height patterns were identical to the original thickness of the resist layer (100-110nm) after development indicating that no resist material had been removed in the process.

Etching of the devices was performed using a STS Standard Oxide Etcher (SOE) using Cl_2 as the enchant gas. The chlorine gas flow was set to 20sccm and the plasma bias voltage set to 700V. The objective was to etch completely through the 340nm layer of Si without undercutting into the SiO_2 layer, which would destabilize the pillar structures. The etch rate of Si using this recipe was determined to be 2.6nm/s, while that of the HSQ was 0.55nm/s, resulting in a selectivity of approximately 4.75 : 1. Note that no BOE (buffered oxide etch) process was used to remove the remaining HSQ resist as this would remove the pillars as well as the resist, because the acid also attacks the underlying SiO_2 layer. The 30nm of HSQ remaining on the surface of the device was not removed due to the negligible effect it would have on the device performance due to its low index over the expected frequencies of operation.

After etching, the ends of both the input and output waveguides were cleaved to provide a clean edge for butt-coupling the laser light source to the wafer for device testing. The butt-couple allows for introduction of laser light into the device, allowing the near field pattern of the cloaking structure to be examined in detail through measurements.

6.5 Fabrication Results and Discussion

The first cloak structure, which will be referred to as Design A, was designed for a background index of 1.5. This index was chosen to test how a matched index between the underlying silicon dioxide substrate and overlying cloaking structure would affect light scattering in the device. For this design, the cloak requires the nanorod diameters to vary from 0.35a to 0.87a or 52nm to 130nm for a unit cell size a = 150nm. This section of the cloak will be labeled as the PC1 area. In Design A, a small portion of the cloak structure nanorod array was replaced with larger pillar structures that have an increased lattice constant of a = 300nm. In this sub-array, which will be notated as PC2, all feature sizes were doubled and therefore the smallest gap was increased to ~40nm, which is well within the range of e-beam fabrication capabilities. details the cloaking area for this design showing both the PC1 and PC2 arrays.

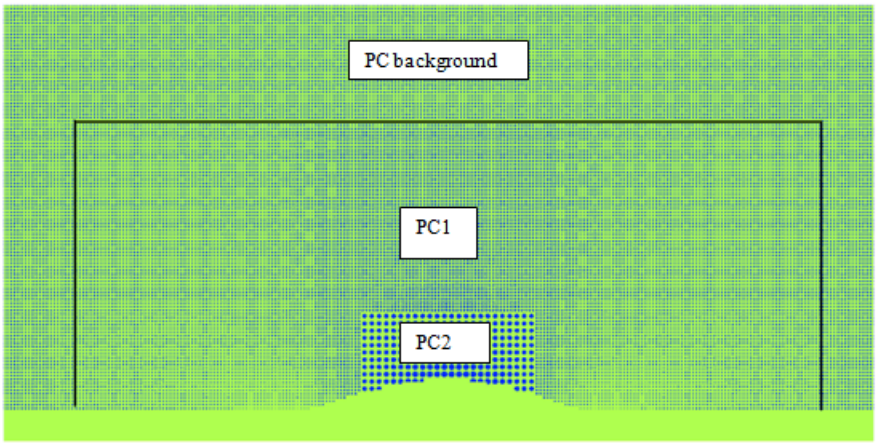

Figure 6-12: Diagram of the nanorod structure in the cloak, showing the areas of smaller lattice spacing (PC1) and larger lattice spacing (PC2).

An example block diagram figure for the Design A optical cloaking structure is shown in Figure 6-13. The device region consists of two combined areas of silicon rods in a 39.6μm x 39.6μm area, connected by a 10μm wide input and a 36.9μm wide output Si waveguide. The size of the output Si waveguide was reduced in follow-on designs to reduce the fabrication expense of the device. The 32μm x 12μm cloaking region contains the main array of 150nm spaced pillars with diameters ranging from 90.75nm to 52.18nm, and the secondary array of 300nm spaced pillars with larger diameters in the range of 184.05nm to 256.18nm. The modified spacing of the center pillars in the secondary region increased the minimum gap between adjacent structures to around 40nm, which reduced the spacing requirements and therefore the difficulties in producing the rods accurately during fabrication.

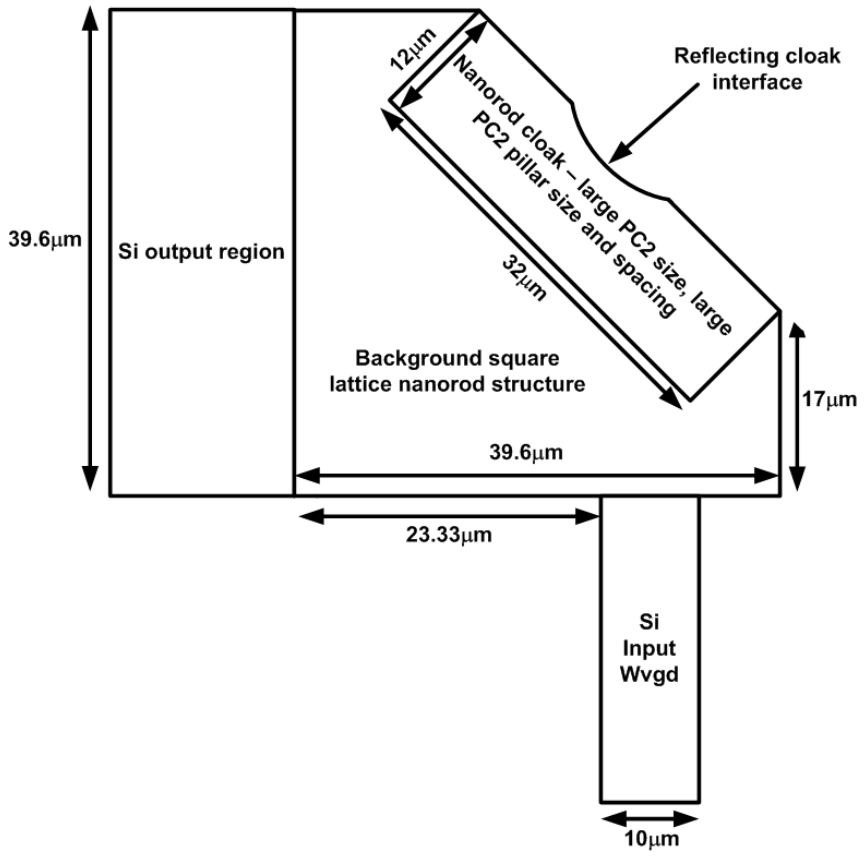

Figure 6-13: Block diagram of the Design A nanorod optical cloaking structure.

The pillar diameters were arranged such that the average refractive index creates the quasi-conformal dielectric index mapping required for the device to exhibit cloaking behavior. The uniform background nanorod array was a square lattice turned 45° to the Γ - M direction to provide a well-matched interface to the cloak structure, so as to minimize the scattering at the interface. The input waveguide width is standard for the wavelength of operation, while the output waveguide was made wider to allow some room to observe the direction of the output light, in case the reflected beam was not at the predicted angular deviation.

For Design A, the standard default forward scattering and back scattering correction for Si devices was used as a starting point. The Alpha parameter describes the forward (short range) scattering range of the electrons and is important when the aspect ratio of the device features is small. The Beta parameter describes the backward (long range) scattering of the electrons, which describes the distance the electrons travel into the substrate material. Both the Alpha and Beta parameters are set to values that are dependent upon the substrate and photoresist material that is used. The Eta parameter describes the ratio of the Beta Gaussian against the Alpha Gaussian based on their stored energies, and determines the ratio of forward to backward scattering. The reduced spacing requirements in the large pillar sub-array was expected to allow the smaller side nanorods to be reproduced with the correct dimensions using the default proximity correction parameters for a Si substrate. These parameters were originally determined from Monte Carlo simulations and extensive experimental runs of Si devices through characterization work conducted over many batches of different structures. The values that were used were Alpha = 0.05, Beta = 33.3, and Eta = 0.61.

Scanning electron microscope images were taken of the fabricated Device A structure to check their quality and final dimensions. For Design A, Figure 6-14 shows the overall fabricated device, Figure 6-15 shows a close up of the cloaking area, and Figure 6-16 is a high magnification image of the largest nanorods in the cloaking area. The nanorod diameter matched the original design within ±5% experimental tolerances once the best dose value was obtained. While the pillars were nearly perfectly vertical, some non-uniformity in top and bottom diameters was observed in the sidewalls of the nanorods especially those near the device edges, where the bottom diameter was

somewhat larger than the top. Close-up images of these non-uniformities are shown in Figure 6-17 for a larger nanorod (about an 8% difference) and Figure 6-18 (a larger 24% difference) for a smaller nanorod. This effect could be attributed to non-uniformities in the photoresist mask covering the nanorods, which caused sloping sidewalls due to the edges of the mask being thinner, and therefore more susceptible to removal during the etch process. Overall, the standard parameters for the proximity correction of the device during EBL exposure worked well for this structure fabrication.

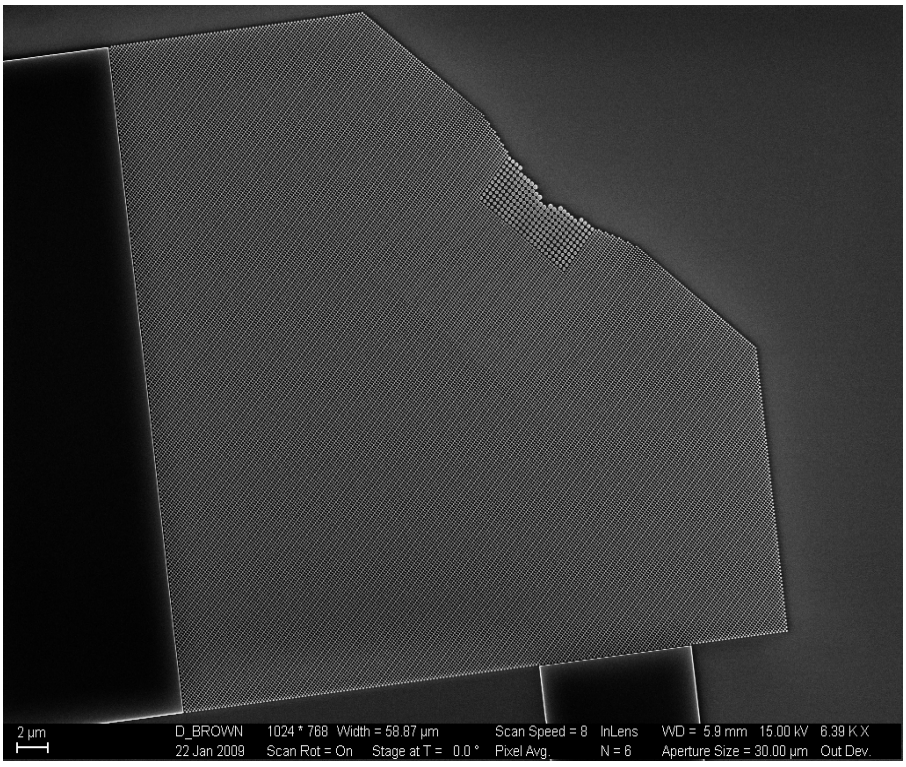

Figure 6-14: SEM of the Design A fabricated cloaking nanorod device.

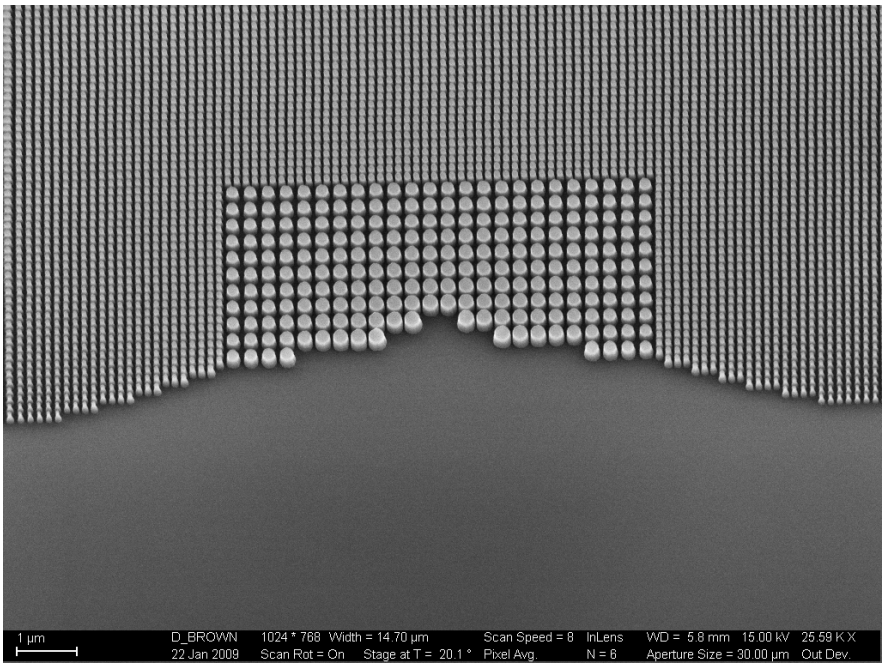

Figure 6-15: Higher magnification image of the Si pillars around the cloaking area in Design A.

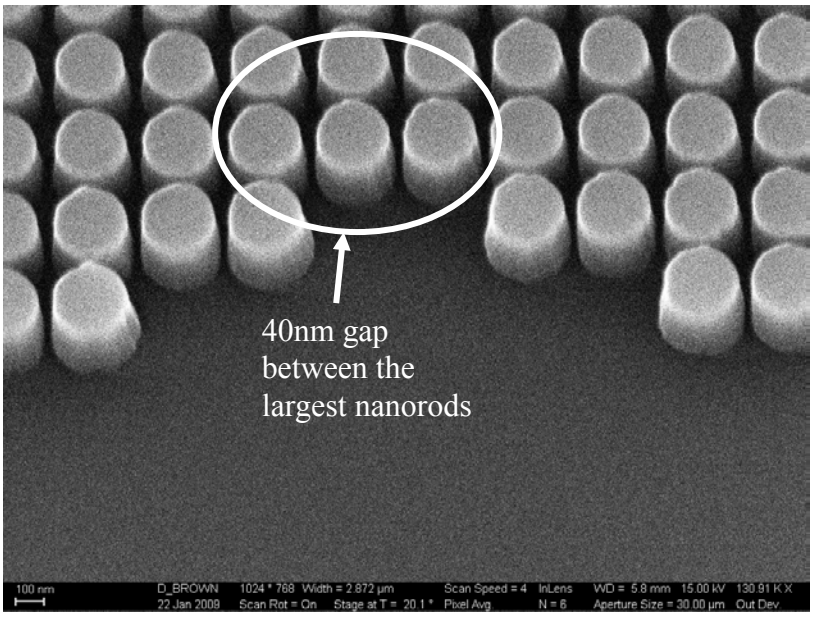

Figure 6-16: High magnification SEM image of the largest nanorods in the cloaking area of the device in Design A. Note the clear separation between nanorods at the smallest gap point of ~40nm at the center of the structure.

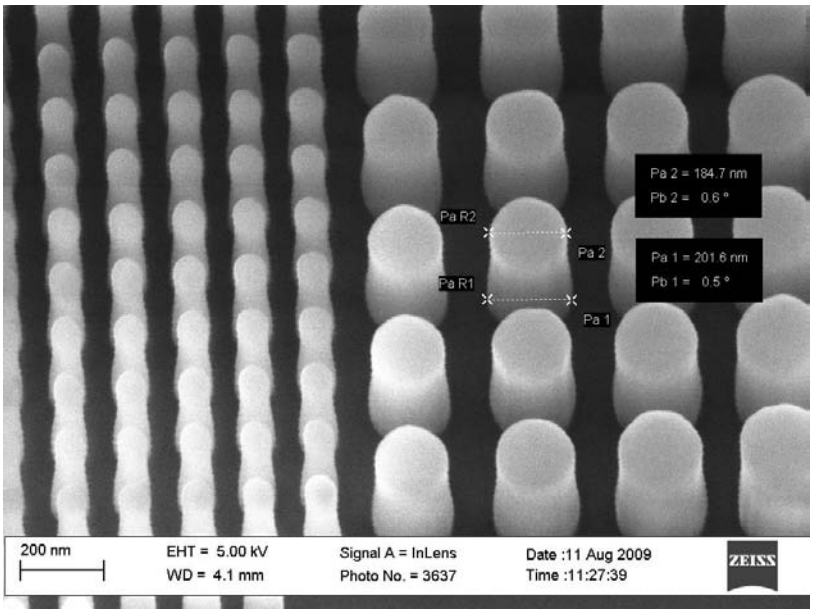

Figure 6-17: Side view of one of the larger nanorods in Device A, showing the non-uniformity obtained in the sidewall thickness as an effect of the etch process.

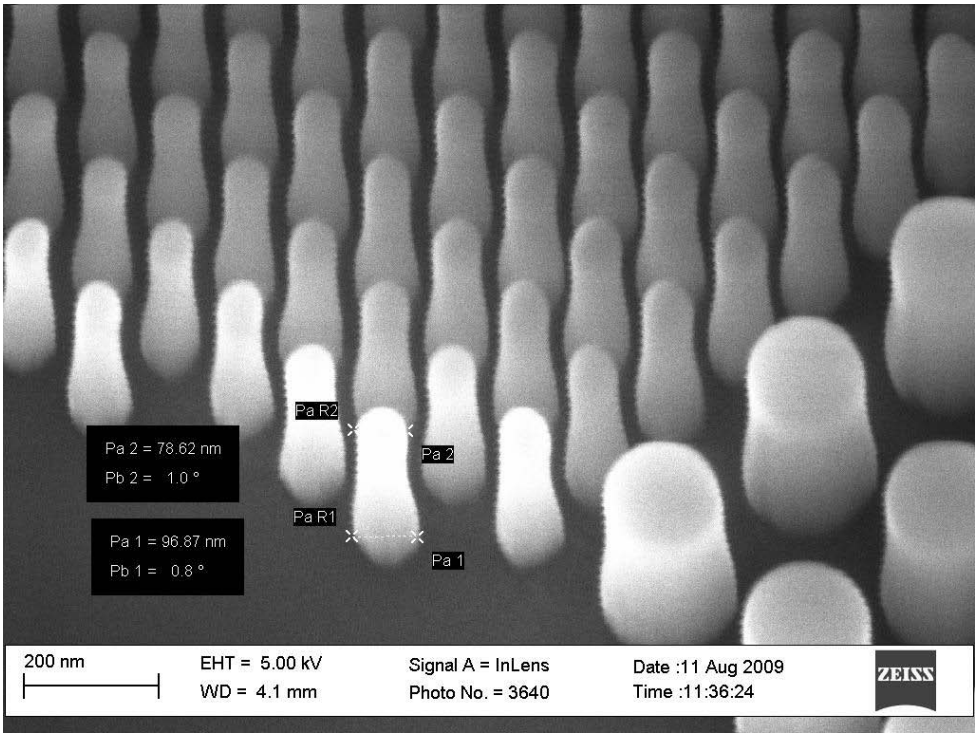

Figure 6-18: Side view of one of the larger nanorods in Device A, showing the non-uniformity obtained in the sidewall thickness as an effect of the etch process.

The second cloak structure, named Design B, is similar to Design A but reduced in size. In an effort to reduce the scattering losses in the device, the Design B cloak reduced the number of pillars, and therefore the number of scattering sources for the incoming light beam. The smaller cloak consists of a 143 x 53 nanorod array that reduces the device size to a 26.4μm x 26.4μm area. The cloaking area size was also reduced to 21.45μm x 7.95μm, with an identical Design A pillar spacing of a = 300nm. Design B is identical to the Design A layout except for the reduction in cloak and background nanorod array areas. A block diagram for Design B is shown in Figure 6-19. Using the same proximity correction and fabrication parameters as Design A, these cloaks had similar non-uniformities to the Design A devices due to the identical etch parameters being used. Figure 6-20 shows the smaller cloaking area in Device B post-measurement, with the damage in the outer pillars having been caused during the measurement characterization work.

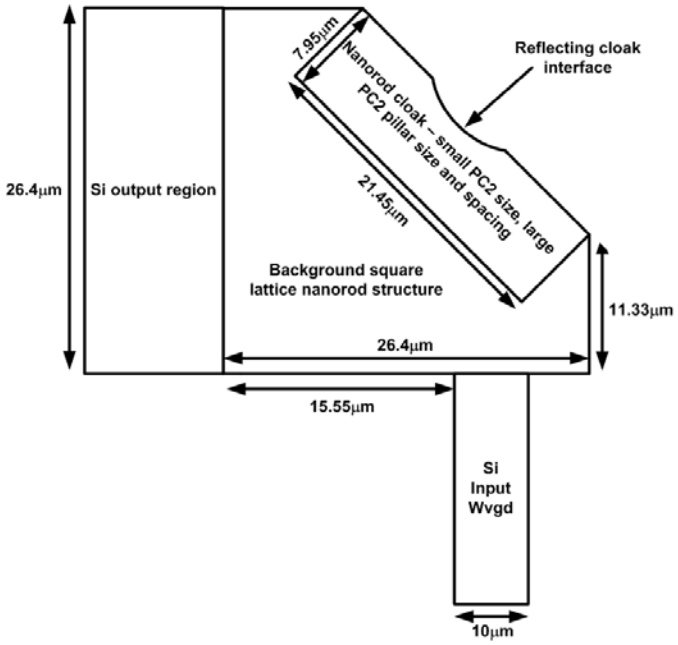

Figure 6-19: Block diagram of the Design B nanorod optical cloaking structure.

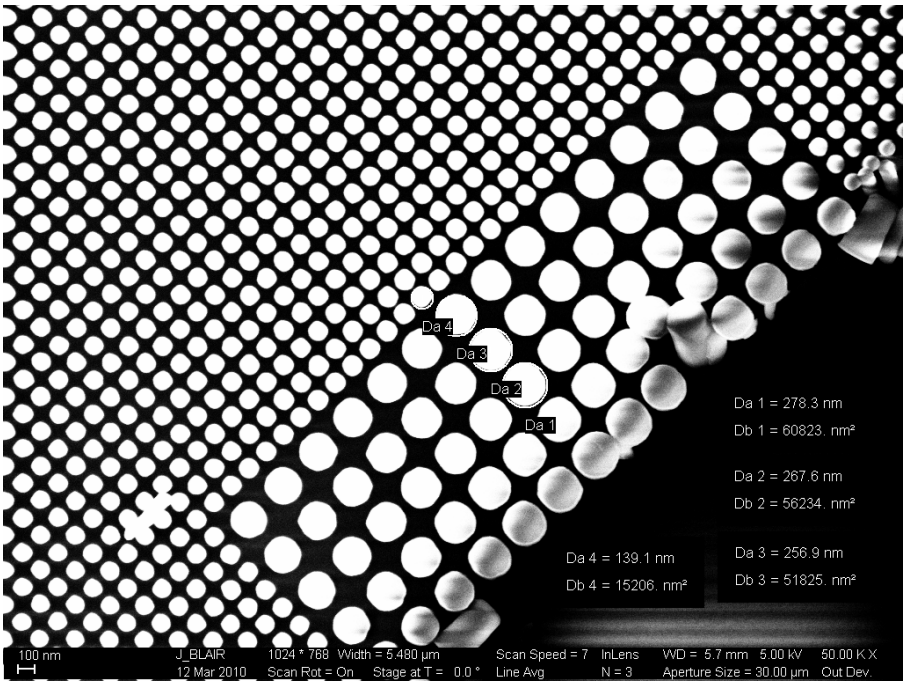

Figure 6-20: Close-up of the reduced cloaking area in Design B, damage to several pillars caused during the measurement phase of the device.

For the third design, called Design C, the background index was changed to implement 1.55 and 1.6 index structures, to see if changing the device match to the underlying silicon dioxide layer would also reduce scattering, thereby improving the device performance. This index match change required slight adjustments in the pillar sizes throughout the device. In this designs, the lattice constant was kept at a = 150nm for the cloaking section, re-creating the original design for a smaller 20nm pillar gap. The change in background index also resulted in slightly smaller nanorod diameters ranging from 0.35a to 0.84a or 52nm to 125nm. In addition, a simple square lattice photonic bandgap (PBG) structure was added in Design C to help minimize light leakage at the back of the cloaking area. The PBG structure consisted of a 62 x 10 array of 520nm spaced nanorods, each having a diameter of 312nm. This structure helps to enhance reflection of stray light that may inadvertently pass through the cloaking area by providing a PBG in the 1500nm wavelength range. The PBG in the band structure for this square lattice photonic crystal is standard for this type of structure and is detailed in other work [41]. A block diagram for Design C is shown in Figure 6-21.

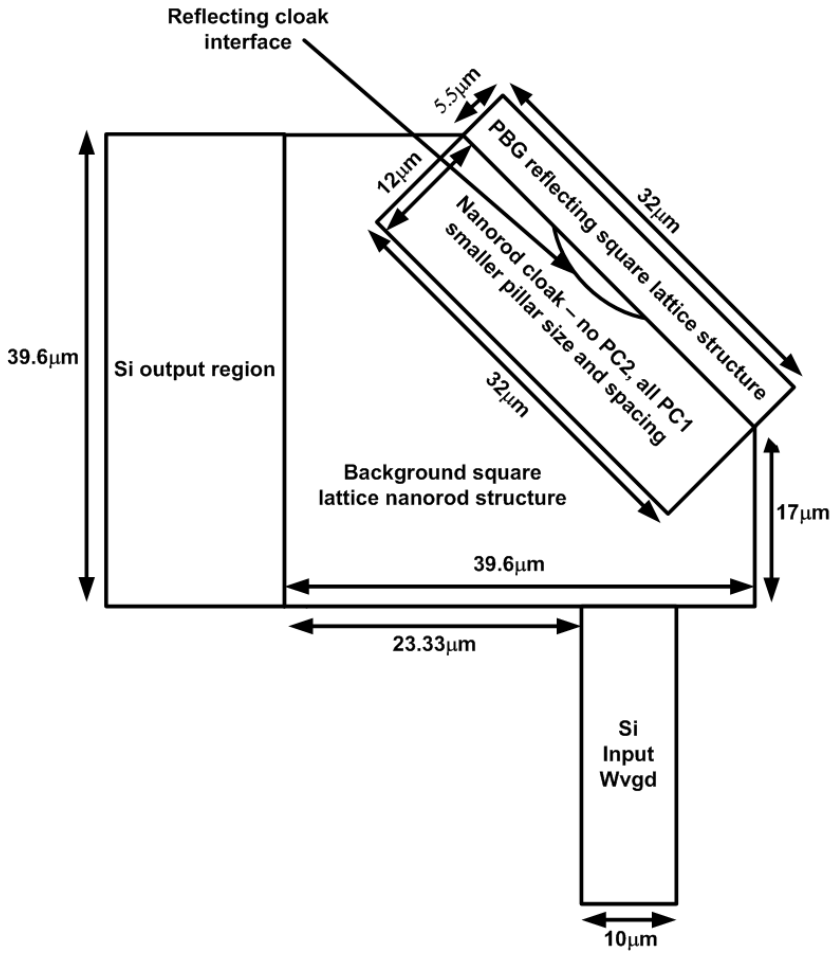

Figure 6-21: Block diagram of the Design C nanorod optical cloaking structure.

The proximity correction required for the fabrication for Design C proved more challenging to adjust to due smaller gaps between nanorods as compared to Design A. Initially, only the default forward scattering correction parameters were used as in Design A to fabricate the device. In this case, the central cloaking area nanorods are slightly overexposed resulting in over-sized structures leading to rod bridging in the central cloak area, while the side area nanorods were underexposed leading to missing and defective rod structures. This result is shown in Figure 6-22.

In order to correct for the electron beam proximity effects in Design C, both forward and back scattering corrections were required (adjustments to the Alpha and Beta values), as well as a process blur adjustment. Both the Alpha and Beta parameters were adjusted to 0.08 and 38.9, respectively, to compensate for the smaller feature sizes and gaps between nanorods. The process blur parameter Gamma1 describes the mid range scattering range of the electrons and was used to compensate for process related effects. The Neu1 parameter describes the ratio of the mid range Gaussian against the Alpha Gaussian, based on their stored energy. This correction required the process blur parameter Gamma1 to be set to 60nm and given a weight Nue1 of 0.20 or 20% to compensate for the additional scattering correction. Figure 6-23 shows the results of adding this additional proximity correction. Some bridging is evident in the largest pillar structures where the gap was designed to be 20nm, but this was found to be unavoidable due to the higher dose required to correctly expose the smaller cloak edge pillars. This bridging was expected to shift the operating frequency of the device slightly in the measurements.

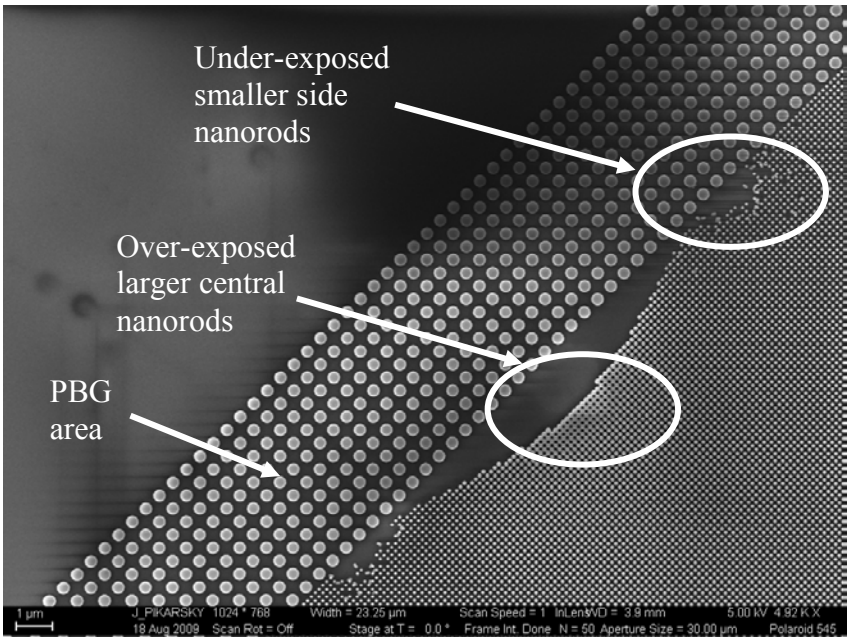

Figure 6-22: SEM illustrating the overexposure of the central nanorods (causing bridging) and underexposure of the side nanorods (causing missing structures) in the cloaking section of the Design C cloak when only forward proximity scattering correction is used.

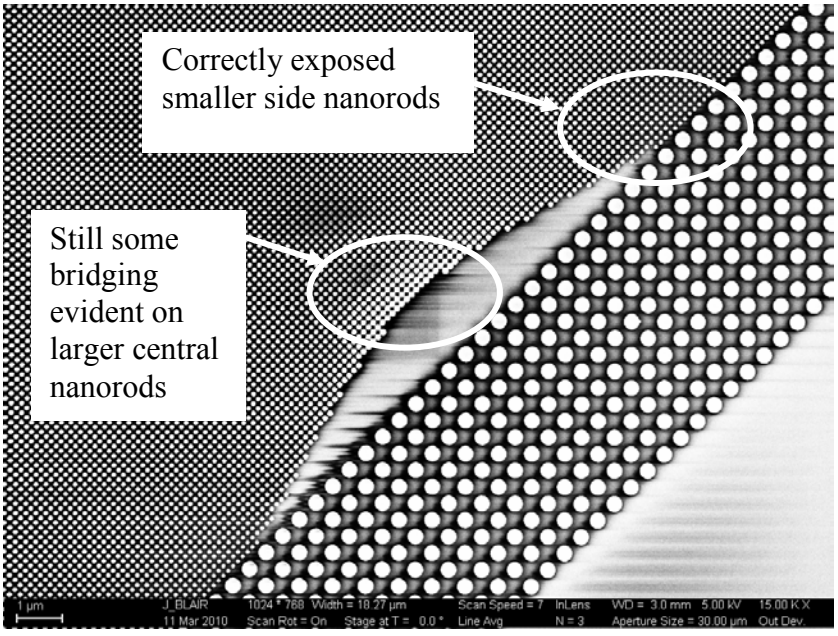

Figure 6-23: SEM image of the cloaking area in Design C, showing both the cloak and PC bandgap pillar structures. A small amount of bridging in the central cloak area can be seen, but the smallest side nanorods have been correctly patterned using both forward and back scattering proximity corrections.

6.6 Measurement Results and Discussion:

The fabricated cloak structures were investigated by near-field scanning optical microscopy (NSOM). For optical characterizations, three fiber-coupled lasers tunable between 1400nm -1602nm were used as light source. A polarization control paddle was used to set the correct polarization of the laser and the light output from the fiber was butt-coupled into the silicon input waveguide. The light that comes out of the fiber within the critical angle was captured by the input waveguide and fed into the nanorod array. The light propagation through the nanorod structure was then directly visualized by the near-field scanning optical microscopy (NSOM). Figure 6-24 shows an NSOM image for a Device A cloaking structure at a wavelength of 1500nm. A well-defined input beam was observed propagating vertically from the bottom of the figure into the cloaking structure, producing a spot of intense scattering visible at the reflecting interface. The out-of-plane scattering at the reflecting interface significantly reduces the reflected beam intensity, but is unavoidable in a 2D implementation, in which the guiding condition is compromised due to the abrupt interface. Despite losses at the reflecting interface, a clearly defined reflected beam was observed at a reflection angle of 45^{o} with respect to the reflecting interface. The reflected light beam does not reach the output waveguide, however, due to the propagation loss within the nanorod array and also because of scattering losses at the reflecting interface.

Similar behavior was observed at an operating wavelength of 1460nm in the Device B cloak as shown in Figure 6-25. The off-tuning of this device could be attributed to the non-uniform pillar profiles, as well as a slight change in index due to pillars being off in exact design dimensions within experimental tolerances. This

operating wavelength shift could also be attributed to the index matching of the design, which is close to the index of the SiO_2 underneath the Si guiding layer. The reduction in scattering due to the reduction of the background nanorod array area improved the strength of reflected beam at the same measurement wavelength as compared to the original Design A cloak. The output beam strength was again subject to propagation and scattering losses, but in this case they have been reduced significantly.

Figure 6-26 shows the results of an NSOM measurement on a Device C large cloak sample taken at a wavelength of 1420nm, showing a clearly defined output beam reflecting from the cloaking surface. The reduction of the spacing in the pillars in the cloaking area reduced the reflection from incoming light significantly, resulting in a more uniform output beam. The shift in operating wavelength may be due to the unavoidable bridging of some of the larger pillars that leads to a large index change than expected in that area. The strength and clarity of the output beam is much improved over Designs A and B however. The change in index match of the structure may also have helped improve the output, although it is hard to determine the exact effect based on the evidence from the experimental measurements.

All three cloak design structures are created from of non-resonant dielectric elements and are expected to operate well over a broad range of frequencies. Due to the high scattering of the output beam, far-field effects such as the coupling of the light into the output waveguide were not able to be observed. The performance of the devices could be improved through further reduction in the background PC size, as well as correcting for bridging pillars and non-uniform pillar etching which increases the index average of the cloak in the large pillar areas, shifting the operating wavelength of the

device. The change in background index of the cloak did not appear to have a noticeable effect on the device performance, although further investigation is required for a complete conclusion.

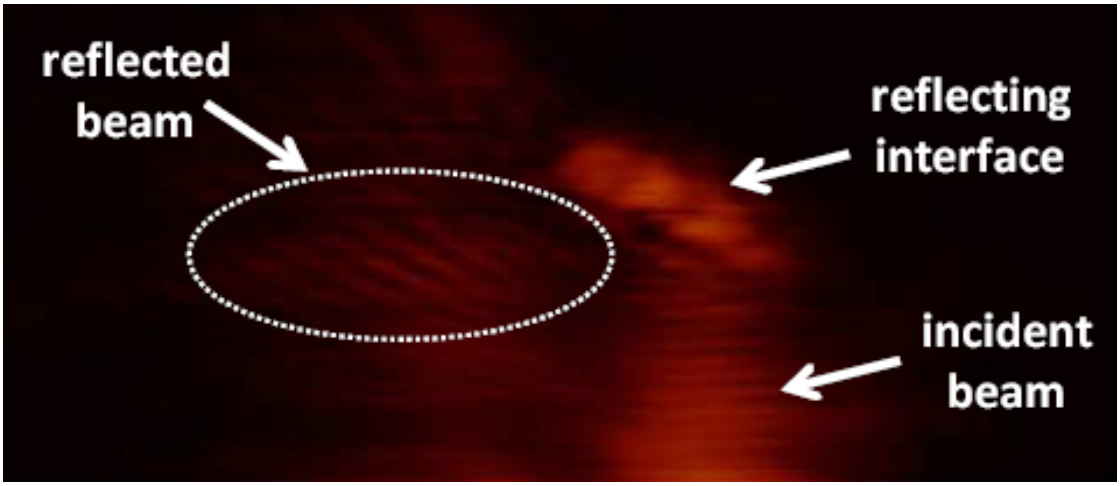

Figure 6-24: NSOM image for 1500nm laser light propagating off the Design A cloaking structure area.

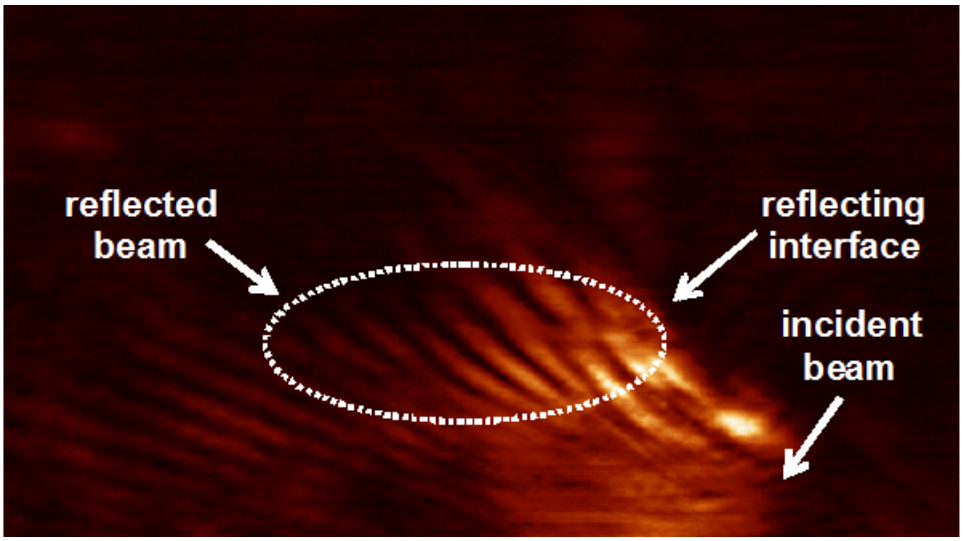

Figure 6-25: NSOM image for 1460nm laser light propagating off the cloaking area in Design B.

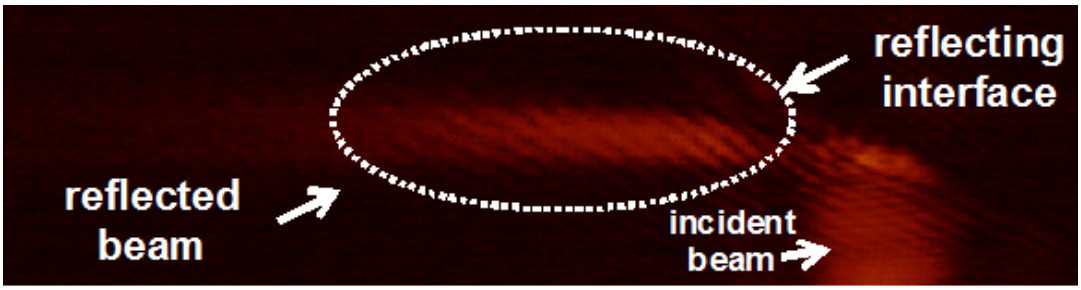

Figure 6-26: NSOM image for 1420nm laser light propagating off the cloaking area in Design C.

6.7 Static Tuning of the Optical Cloak Utilizing ALD

Based on the measurement results from the fabricated cloaks, Designs B and C were proven to have the best optical performance in terms of scattering losses and clearly defined output beam. However, the wavelength of laser light that provided the best optical response was not at the expected 1.55μm design wavelength. This shifting of the frequency response of the device could be attributed to a number of factors, such as the size uniformity in the background PC, as well as shifting errors due bridging pillars and non-uniform pillar etching which increases the index average of the cloak in the large pillar areas as mentioned in the previous section. These factors are inherent to the device fabrication process and are electron beam dose dependent. Simply changing the device dose during the electron beam patterning step does not provide a quick solution to correct the nanorod sizes across the device. The doses given in the proximity correction file and the structure sizes across the device are interdependent as shown in the previous chapter, so further optimization is difficult without a large deal of time and expense experimenting with changing the proximity correction software parameters manually. There are inherent technology limitations in the electron beam patterning and resist

exposure process accuracy inherent to this type of device fabrication, providing limits to how closely the nanorod structures can be sized to the original design specification. In addition, non-uniformities in the etch process will almost always be present due to the limits of uniformity that can be obtained by the particular recipe used to create the Si nanorods.

Since there are limitations on the accuracy of device fabrication with respect to obtaining the correct structure sizes, and thus the correct optical device tuning, we desire to find a method that will enable static tuning (i.e. tuning that cannot be electro-optically controlled) after fabrication. To this end, we have investigated the application of optical materials to the fabricated devices by use of atomic layer deposition (ALD) to accomplish this tuning. As discussed in the Introduction, ALD provides a method to apply atomic layer thickness films of optical material on various substrates. In this work to optically tune fabricated ground plane tuning devices, we will focus on two different optical materials we have available on our groups ALD system. Both of these materials are oxides, which makes them ideal for deposition on Si, and the native SiO_2 oxide layer present on them. The first material investigated for tuning purposes is titanium dioxide (TiO_2). This material is of medium optical index at the wavelength of operation, λ = 1500nm. TiO_2 has an index of $n = 2.31$, which is relatively lower compared to the higher index of Si at $n = 3.46$. This material is expected to provide course optical tuning of our cloaking devices when applied in small layer thicknesses. The second material that has been investigated is aluminum oxide (Al_2O_3), that provides a lower optical index than TiO_2. The index of Al_2O_3 is approximately $n = 1.8$, which is close to the index of SiO_2 at

n = 1.5 than that of Si. This optical material can be used for finer optical tuning than TiO_2 due to its lower index, again when applied in small layer thicknesses.

Due to the expense involved with fabricating multiple cloaking structures and the fact that the best optical cloaking behavior was obtained with the Design C samples, the ALD tuning work has been limited to two working fabricated samples of Design C. This work begins with an investigation of optically tuning the structures using thin layers of TiO_2 to examine if coarse tuning is possible. The following set of research investigates applying a second coating of Al_2O_3 to fine tune the structures to the desired 1500nm wavelength. In both cases, the process starts with ALD coating the samples, followed by an SEM measurement of the coating thickness, and concludes with an optical measurement of the device to determine how the optical tuning has been adjusted through the application of these thin films.

6.7.1 Coarse Tuning of the Optical Cloak Utilizing ALD Applied TiO_2

The first fabricated sample of Design C, which will be designated as Sample F, was designed for a background index of 1.55, using an electron beam dose of 2400 $\mu C/cm^2$ in the lithography process. The other Design C sample was designed for a background index of 1.6, with a lower base dose of 2600$\mu C/cm^2$, which will be called Sample G. The higher base dose lead to the slightly larger nanorod sizes in Sample G compared to Sample F. Figure 6-26 shows the previous NSOM image of a measurement that was taken of Sample G, showing that the device tuning was optimal at 1420nm. The goal is to use a TiO_2 ALD coating to shift this operating wavelength coarsely, that is by a large

amount, in both devices closer to the desired 1500nm operating wavelength. SEM images were taken of the devices before the application of the coating and are shown Figure 6-27 - Figure 6-29 for Sample F, and Figure 6-30 - Figure 6-32 for Sample G. Note that there is more nanorod bridging in the Sample G structure due to the higher electron beam dose used in its fabrication.

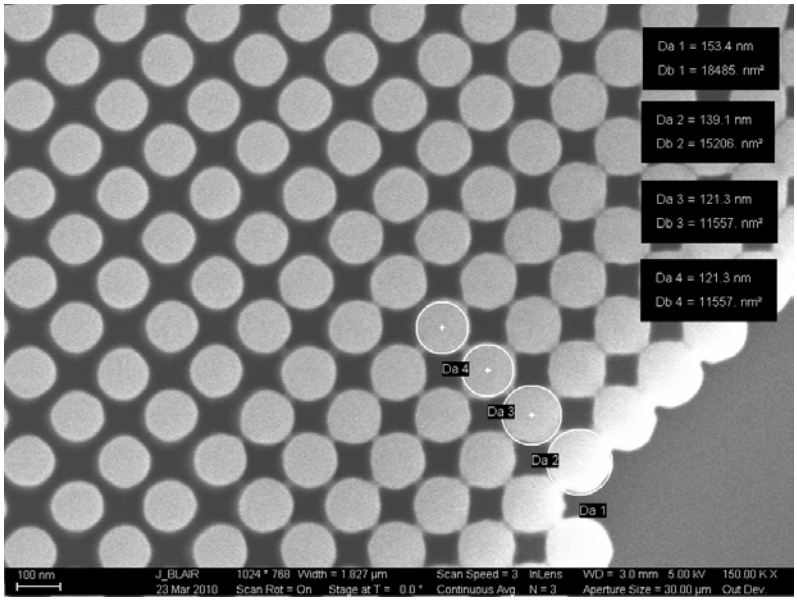

Figure 6-27: SEM image 1 of Cloak F with no ALD coating, showing the dimensions of the larger nanorods closest to cloaking area.

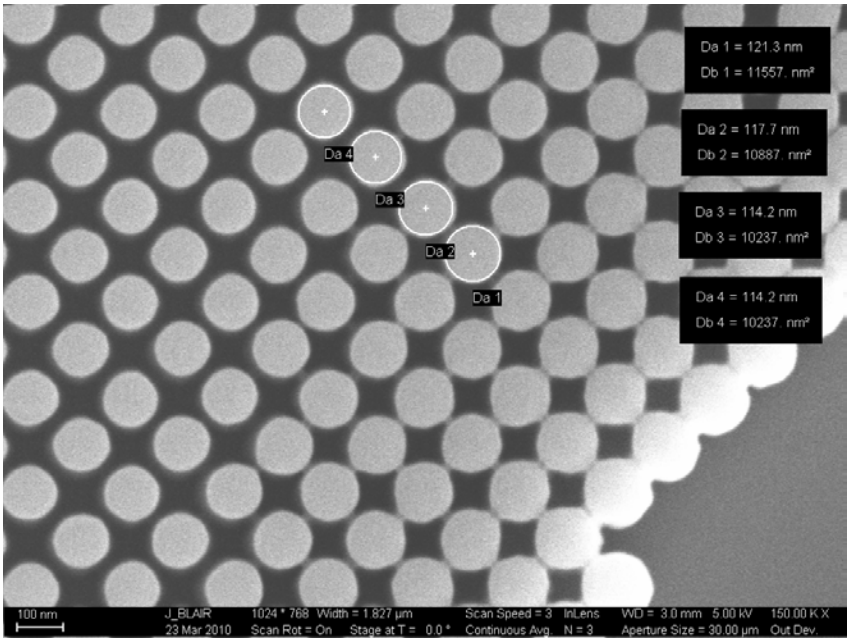

Figure 6-28: SEM image 2 of Cloak F with no ALD coating, showing the dimensions of the medium size nanorods further in from from the cloaking area.

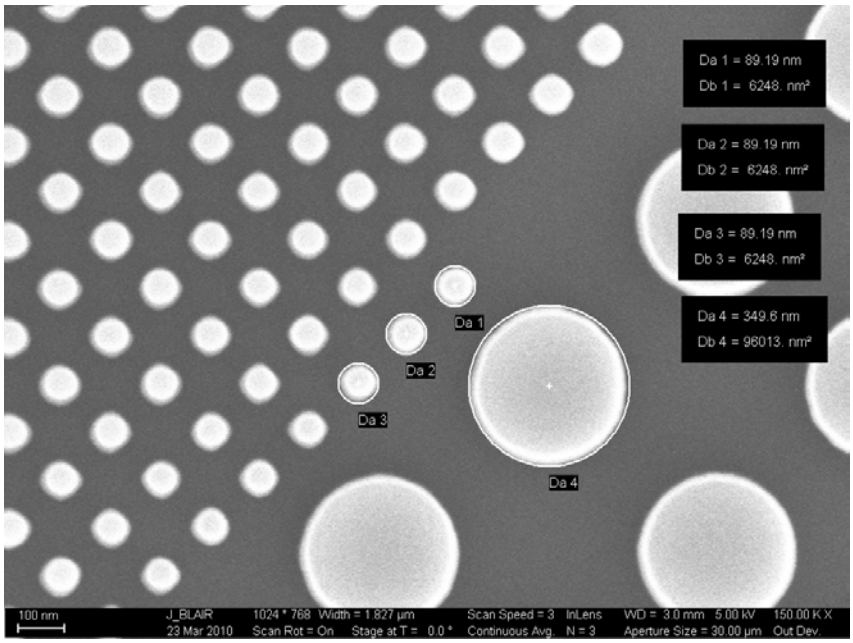

Figure 6-29: SEM image 3 of Cloak F with no ALD coating, showing the dimensions of the smallest nanorods near the edge of the cloaking area and the PBG nanorods.

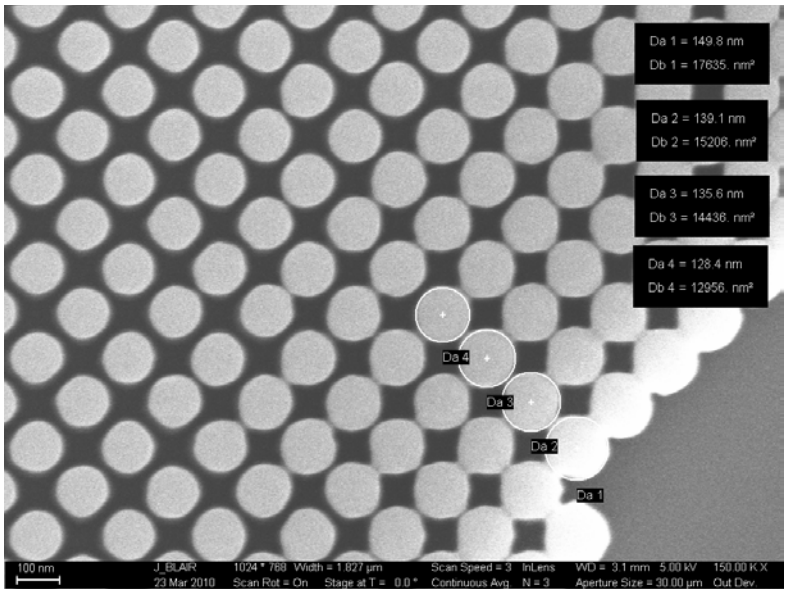

Figure 6-30: SEM image 1 of Cloak G with no ALD coating, showing the dimensions of the larger nanorods closest to cloaking area.

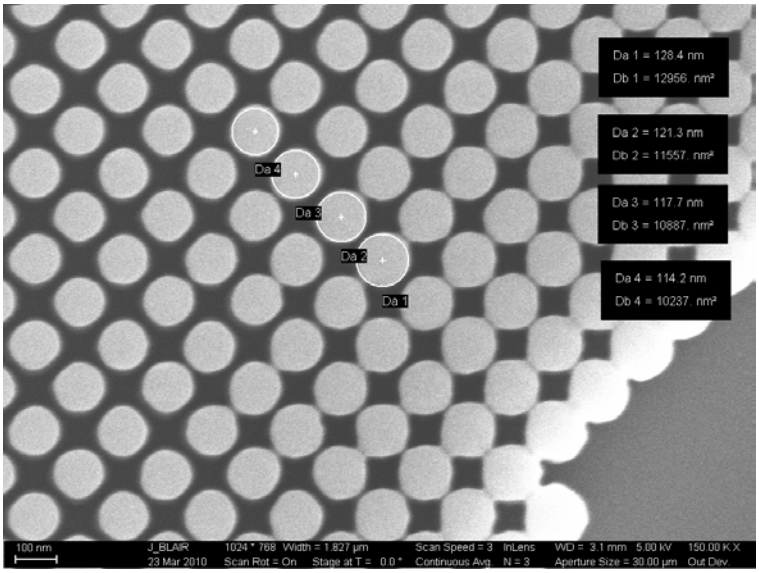

Figure 6-31: SEM image 2 of Cloak G with no ALD coating, showing the dimensions of the medium size nanorods further in from from the cloaking area.

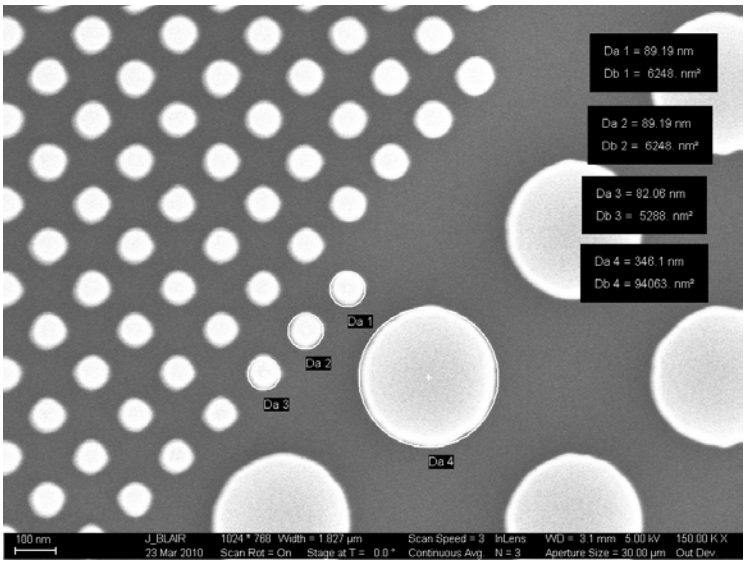

Figure 6-32: SEM image 3 of Cloak G with no ALD coating, showing the dimensions of the smallest nanorods near the edge of the cloaking area and the PBG nanorods.

The next step in the coarse static tuning of the devices was to apply the TiO_2 material directly to the structures using the ALD system. Through simulation work, it was determined that the coating thickness should be at least 5nm to provide a thick enough coating to see an operating wavelength shift in the device. It was decided that Sample F would receive a 10nm TiO2 coating, while Samples G would only receive a 5nm coating. Caution was taken to make sure that the coating was not too thick, as TiO2 has a medium optical index at index of $n = 2.31$ compared to $n = 3.46$ for Si. The operating wavelength of the measurement laser and output detector that the NSOM can operate at and measure is between 1400nm- 1600nm, so a large film thickness may tune the device outside the wavelength range, removing the capability of getting good measurement performance images. The two precursors that are used for this deposition are titanium chloride ($TiCl_4$) and water (H_2O). Each ALD cycle consists of four steps: 1) 8s pulse of the $TiCl_4$ precursor into the reaction chamber, 2) 20s purge of the $TiCl_4$

precursor out of the reaction chamber, 3) 8s pulse of H_2O into the reaction chamber, and 4) 20s purge of H_2O from the reaction chamber. Each cycle results in 0.075nm of growth of TiO_2 on the sample per four step cycle. Thus for a 5nm TiO_2 coating thickness, 67 ALD cycles were required.

After applying the TiO_2 ALD coating, SEMS were taken to examine the thickness, conformality, and smoothness of the deposited film on the two cloaks. As can be seen by the SEM images, the coating looked clean and conformal. Exact measurements of the coating thickness is difficult due to some coating creating bridging around the nanorods, however it appears 5nm and 10nm of TiO_2 were deposited at the correct thickness and film quality. SEM images of both devices were taken after the application of the thin film TiO2 coating, and are shown in Figure 6-33 - Figure 6-35 for Sample F and Figure 6-36 - Figure 6-39 for Sample G.

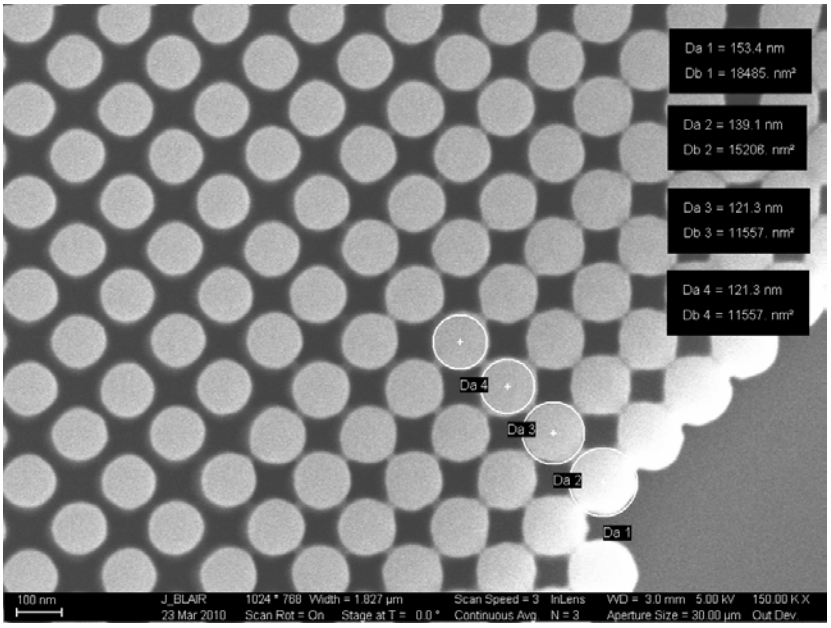

Figure 6-33: SEM image 1 of Cloak F with 10nm TiO_2 ALD coating, showing the dimensions of the larger nanorods closest to cloaking area. With the thicker coating, some bridging is evident between these nanorods.

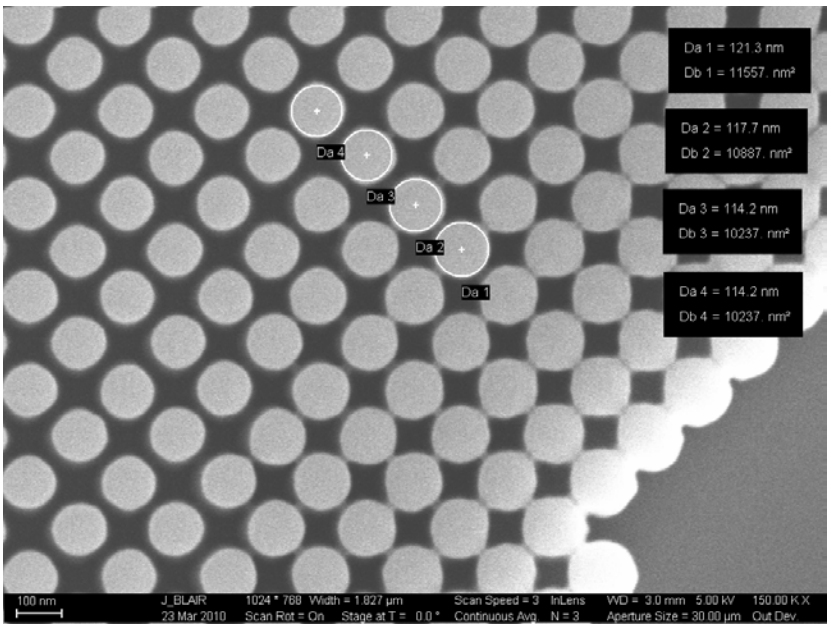

Figure 6-34: SEM image 2 of Cloak F with 10nm TiO_2 ALD coating, showing the dimensions of the medium sized nanorods closest to cloaking area.

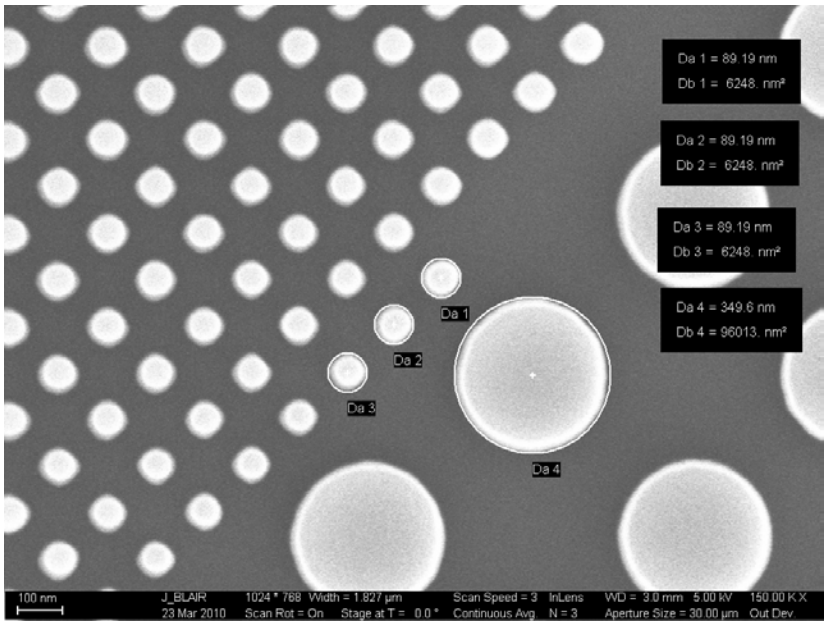

Figure 6-35: SEM image 3 of Cloak F with 10nm TiO_2 ALD coating, showing the dimensions of the smallest nanorods near the edge of the cloaking area and the PBG nanorods.

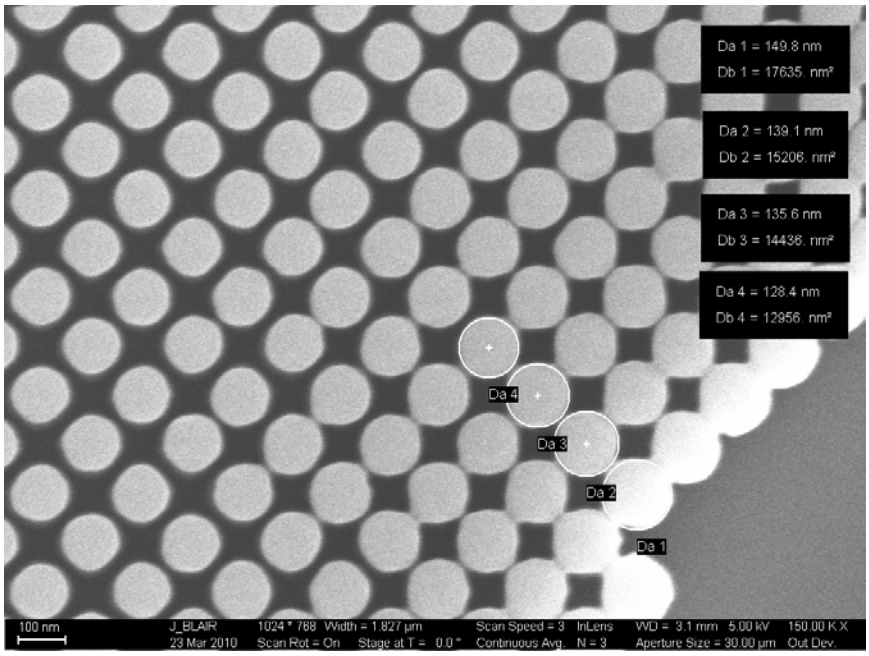

Figure 6-36: SEM image 1 of Cloak G with 5nm TiO_2 ALD coating, showing the dimensions of the larger nanorods closest to cloaking area.

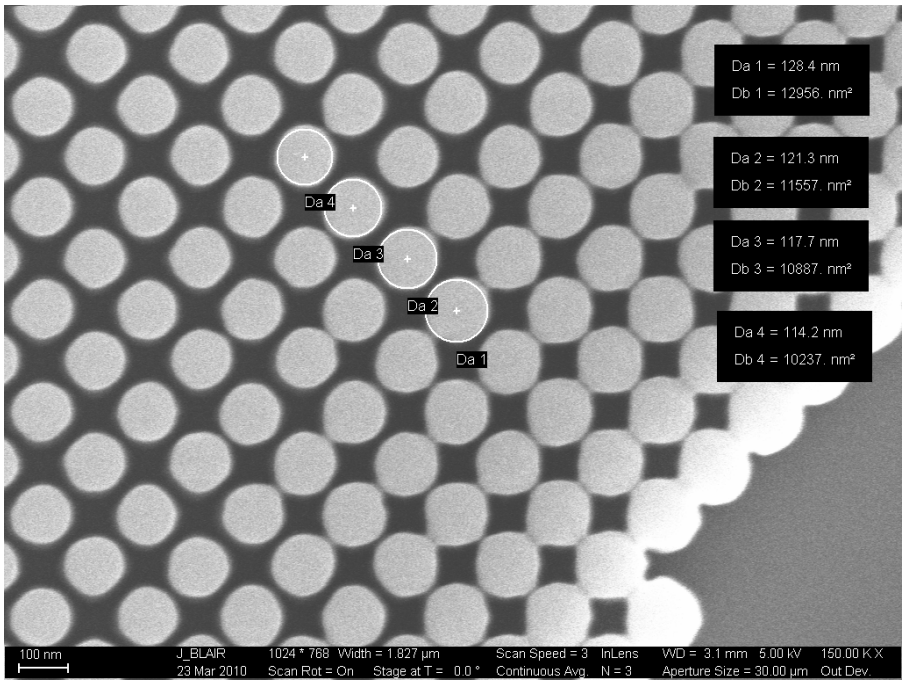

Figure 6-37: SEM image 2 of Cloak G with 5nm TiO_2 ALD coating, showing the dimensions of the medium sized nanorods closest to cloaking area. Note that there is more bridging present in this sample due to the application of the thin film coating.

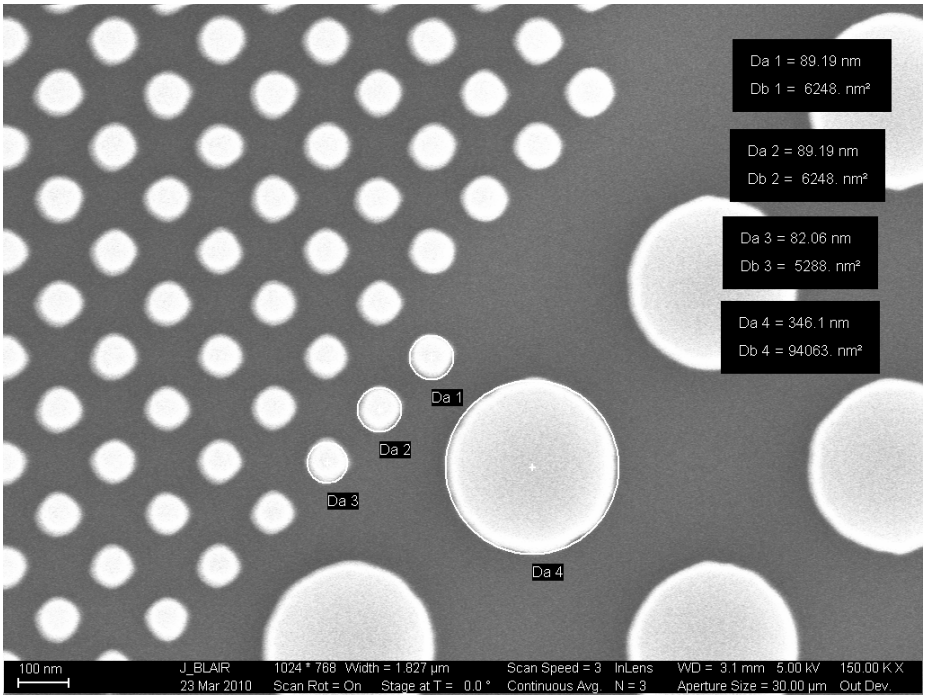

Figure 6-38: SEM image 3 of Cloak G with 5nm TiO_2 ALD coating, showing the dimensions of the smallest nanorods near the edge of the cloaking area and the PBG nanorods.

NSOM measurements we repeated on all cloaks to determine the amount of operating wavelength shift in the devices. Also, it was unknown whether that application of the coating would also increase scattering in the devices which would affect the strength of the output beam. Measurements on Cloak F with the thicker 10nm TiO2 coating had a noticeable tuning effect. The NSOM scan at 1572nm using 10mW of laser power revealed that the best cloaking performance at 1572nm. This is a significant shift from the original 1460nm operating wavelength obtained from the uncoated sample. A NSOM image showing the output fields at the new 1572nm operating frequency is shown in Figure 6-39. Unfortunately, Samples G that had only 5nm TiO2 did not show an appreciable shift in operating wavelength compared to Sample F. It is believed that a thicker coating, perhaps another 5 – 10nm of TiO2 would allow the device to exhibit improved cloaking behavior at higher wavelengths. Rather than coat these samples with

additional TiO2, it was decided to continue the experiment by coating Samples F and G with an additional layer of Al2O3 to see if a wavelength shift could be observed. This work in continued in the next section.

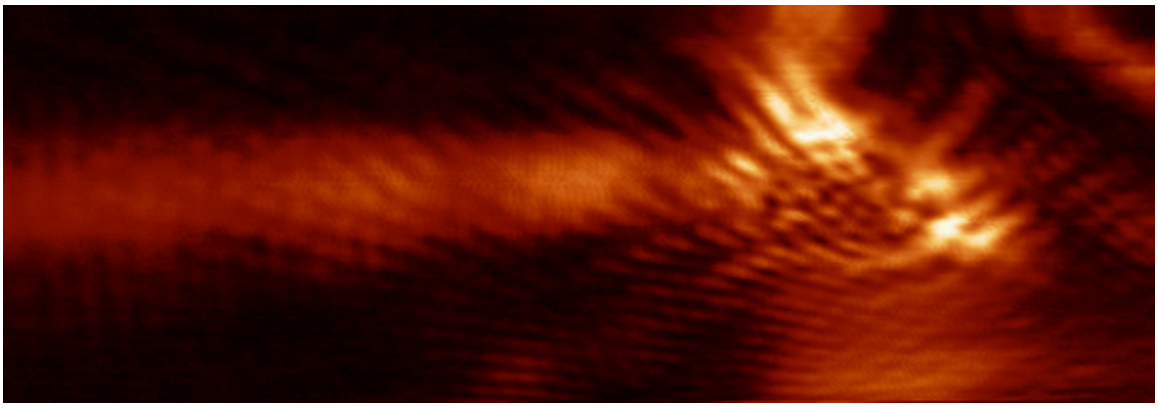

Figure 6-39: NSOM scanning image of Sample F with 10nm TiO2 coating for an operating wavelength of 1572nm.

6.7.2 Fine Tuning of the Optical Cloak Utilizing ALD Applied Al_2O_3

After the successful demonstration of obtaining a coarse operating wavelength shift in the cloaks using ALD applied TiO_2, a follow on experiment was done to see if the operating wavelength could be tuned further using coatings of low optical index Al_2O_3. This optical material has an index of n = 1.8 in the 1500nm wavelength range and should provide less shift in operating wavelength as compare to an identical thin layer film thickness application of TiO_2. Through repeated simulation work, it was determined that the coating thickness should be at least 10nm to provide a thick enough coating to see an operating wavelength shift in the device. It was decided to try 10nm of coating on Sample F and 20nm of coating on Sample G to provide some experimental spread in the data. Again, too thick of a coating of Al_2O_3 may shift the operating wavelength out of

the range that the NSOM can operate at and measure, so caution was taken to not make the coatings too thick The two precursors that are used for Al_2O_3 deposition are trimethyl aluminum (TMA) and water (H_2O). Each ALD cycle consists of four steps, similar to that of TiO_2: 1) 4s pulse of the TMA precursor into the reaction chamber, 2) 40s purge of the TMA precursor out of the reaction chamber, 3) 4s pulse of H_2O into the reaction chamber, and 4) 40s purge of H_2O from the reaction chamber. Each cycle results in 0.14nm of growth of Al_2O_3 on the sample per four step cycle. Thus for a 10nm Al_2O_3 coating thickness**,** 72 ALD cycles were required, while for a 20nm coating doubling the number cycles to 144 was sufficient.

After applying the Al_2O_3 ALD coating, SEMS were taken to examine the thickness, conformality, and smoothness of the deposited film on both cloaks. In this case the TiO_2 coating was still present on the samples, thus it provided a surface oxide material for the Al_2O_3 growth to start from. As can be seen by the SEM images of , the coating again looked clean and conformal. However, the growth thickness of the Al_2O_3 was grossly off. Instead of growths of 10nm and 20nm, we obtained growths of 20nm and 40nm repectively. This was not expected, and could possibly be attributed to the TiO_2 material providing a faster growth reaction at the surface compared to the Si/SiO_2 material that the original TiO_2 was grown on. In addition, the ALD system had been extensively renovated prior to the runs, and although many tests were run on Si to test the growth thickness of Al_2O_3, there may have still been problems with the system that caused the growth thickness to be off. Exact measurements of the coating thickness was now even more difficult due to more coating creating bridging around the nanorods.

SEM images of the coatings were taken after adding the additional 20nm and

40nm of Al_2O_3 to Samples G and H respectively. Note that the 5nm TiO_2 film coating remained underneath the new coating, so the nanorod sizes were compared to these images to determine the film thickness. It was now much more difficult to get exact nanorod diameters due to the fact that bridging between structures changed them from cylindrical to square shaped nanorod pillars. A best estimate was made based on the diameters of the PBG and smaller nanorod structures in both devices, as these remained cylindrical enough for an accurate measurement. SEMs of the two Al2O3 coated devices are shown in Figure 6-40 - Figure 6-42 for Sample F and Figure 6-43 - Figure 6-45 for Sample G.

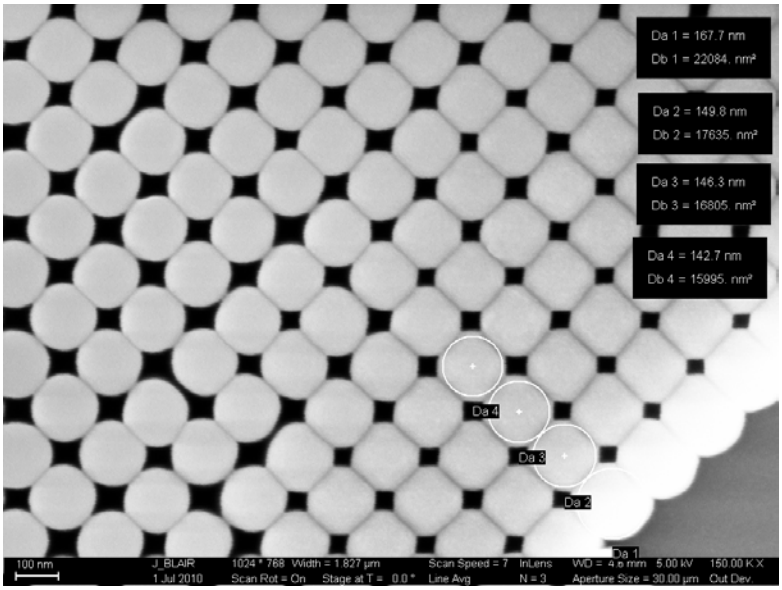

Figure 6-40: SEM image 1 of Cloak F with 20nm Al_2O_3 ALD coating, showing the dimensions of the larger nanorods closest to cloaking area. The pillars are bridging enough to cause them to obtain a square nanorod shape.

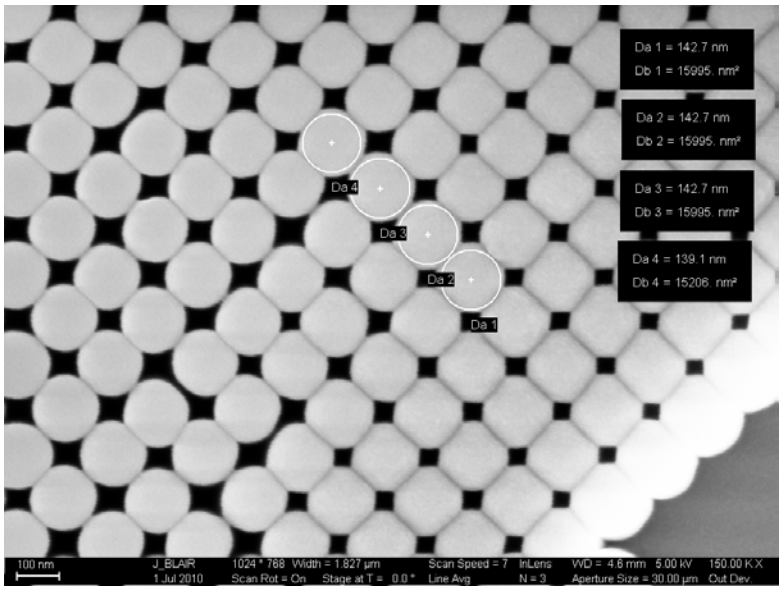

Figure 6-41: SEM image 2 of Cloak F with 20nm Al_2O_3 ALD coating, showing the dimensions of the medium sized nanorods closest to cloaking area. Note that there is more bridging present in this sample due to the application of the thin film coating.

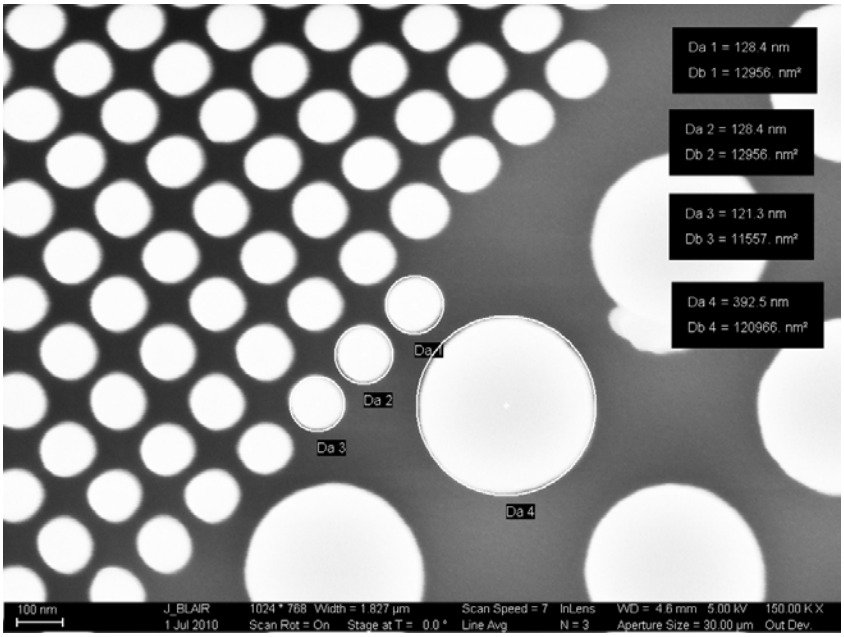

Figure 6-42: SEM image 3 of Cloak F with 20nm Al_2O_3 ALD coating, showing the dimensions of the smallest nanorods near the edge of the cloaking area and the PBG nanorods.

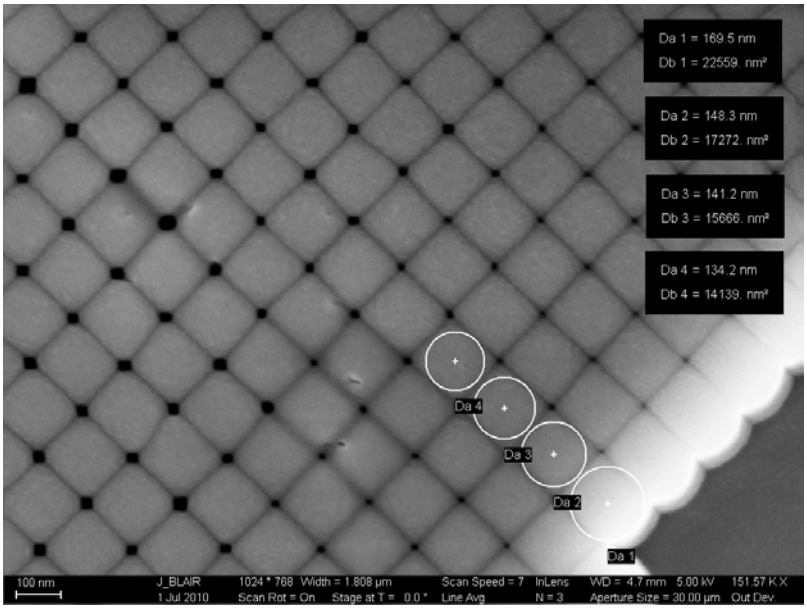

Figure 6-43: SEM image 1 of Cloak G with 40nm Al_2O_3 ALD coating, showing the dimensions of the larger nanorods closest to cloaking area. The pillars are bridging enough to cause them to obtain a square nanorod shape.

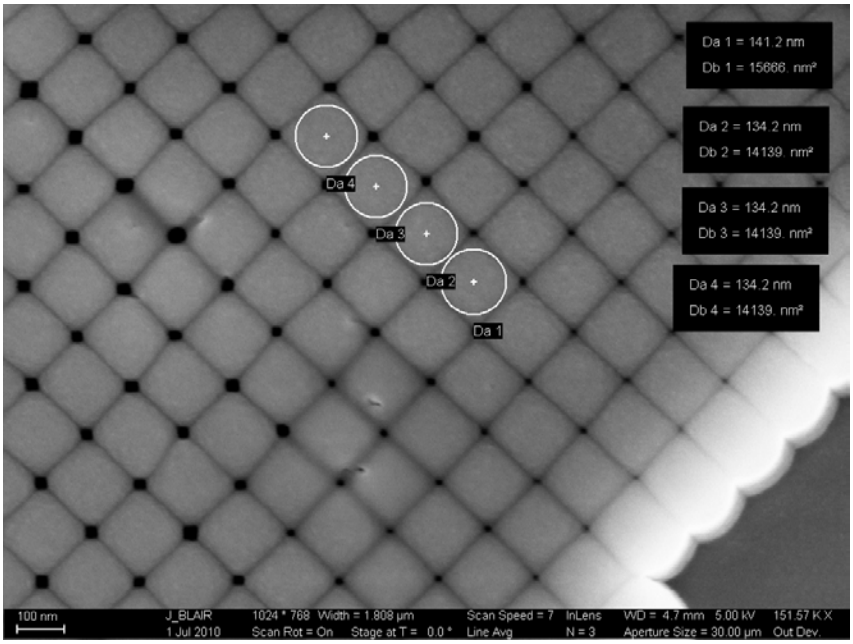

Figure 6-44: SEM image 2 of Cloak G with 40nm Al_2O_3 ALD coating, showing the dimensions of the medium sized nanorods closest to cloaking area. Note that there is more bridging present in this sample due to the application of the thin film coating.

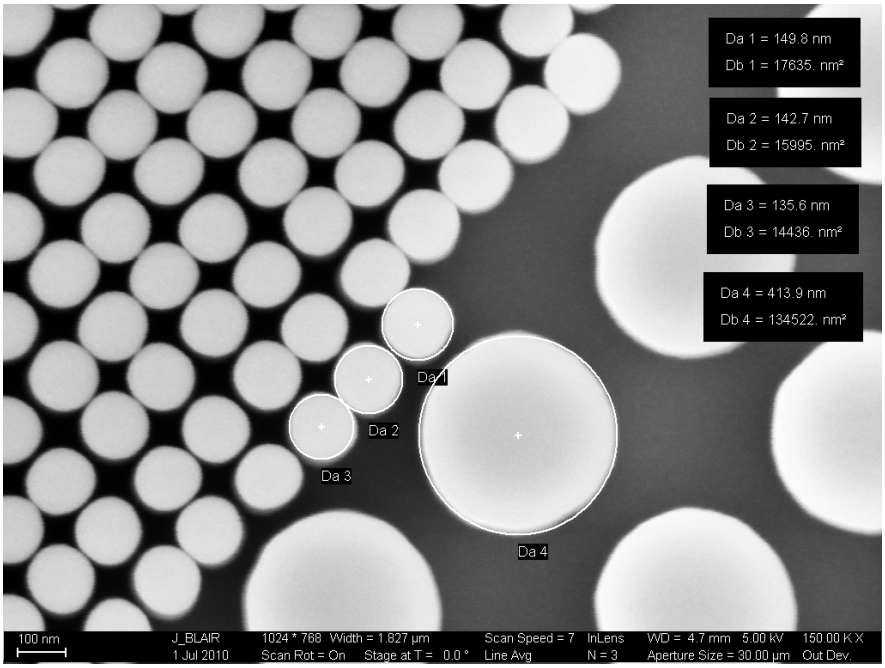

Figure 6-45: SEM image 3 of Cloak G with 40nm Al_2O_3 ALD coating, showing the dimensions of the smallest nanorods near the edge of the cloaking area and the PBG nanorods.

Unfortunately, at the time of this writing, the NSOM measurements were not available to determine the wavelength shift due to the equipment being out of service. However, it is expected that the sample would show a significant shift in operating wavelength. This research work is in progress and should be completed within the next month. The follow-on research to this work will start be fabricating a new set of fabricated Design C devices that are all identical. From this new set of devices, a varying coating thicknesses of materials will be applied to structures in a more methodical fashion. In this way, plots showing clear wavelength shifts versus the various coating types and thicknesses can be produced. This work will be used in a future publication based on the quality of results and conclusions drawn.

6.8 Conclusions and Future Work on Optical Cloaking

In conclusion, successful fabrication and characterization of an optical cloaking photonic crystal structure consisting of nanorods has been demonstrated using an in-house developed cleanroom process. Several fabrication parameters were key in fabricating the nano-size device features correctly. The selection of the best high-contrast resist exposure and development process for the electron-beam lithography step was critical in patterning the nanorod structures successfully. The adjustment of proximity correction parameters through multiple exposure runs was also key in replicating the difficult to fabricate nanorod structures, especially with each rod having a different size in this particular cloak design. Careful consideration of both forward (Alpha) and backward (Beta) scattering processes based on the feature size and spacing have to be taken into consideration when determining the optimum proximity correction parameters. In addition, further refinements to the mid range scattering processes using Gamma1 and Nue1 are necessary to compensate for additional features sizes and process dependent corrections. The choice of the plasma etch recipe is also critical in order to reduce scattering in the final device performance. Allowing for the creation of near-vertical rod side walls while maintaining a high selectivity ratio with the respect to the resist is important to successful cloaking behavior in the device.

Some refinements could be made to this set of processes to improve the device fabrication quality. Optimization of the plasma etch recipe to obtain more vertical side walls is one area for improvement, as the nanorods in the current process show some sidewall irregularities. Further adjustments to the proximity correction dose pattern and scattering correction may allow for improvement in the problem between

overdevelopment and underdevelopment of the various sized nanorods in the cloak arrays. For example, reducing the dose in the area of the largest nanorods by manually changing the proximity correction dose pattern may allow the bridging in this area to be eliminated.

This two-dimensional nanorod cloak design represents a first step in an exciting and innovative field of study that will have a significant impact on the field of transformation optics. While three dimensional carpet cloak has recently been demonstrated [76], 2D waveguide based transformation optical devices will continue to remain an important class of devices. As has been demonstrated in the carpet cloak, several slight different fabrication approaches have been employed. The e-beam lithography based approach presented in this paper provides precision control over the nanoscale geometries while at the same time capable of fabricating large area devices. We therefore believe it is one of the most efficient ways for manufacturing this new and exciting class of devices. Further work will explore adding passive and active tunability properties to the device by use of optical and electro-optical coatings and materials.

The static method of tuning the optical cloak wavelength utilizing the ALD coating technique has shown promise in provide a way to tune these devices after fabrication. Further work need to be taken in a more controlled fashion to correlate the tuning shift with the coating type and thickness. This work is under way and should be publishable within the next six months upon completion of this thesis.

This two-dimensional nanorod cloak design represents a first step in an exciting and innovative field of study that will have a significant impact on the field of

transformation optics. Further work will explore adding passive and active tunability properties to the device by use of optical and electro-optical coatings and materials.

Appendix

Appendix A: Sample MPB Code for Generating Dispersion Contour Data

```
% x-direction band contours

(set! num-bands 4)

(set! geometry-lattice (make lattice (size 1 2 no-size)))

(define-param kz 0)
(define-param k-mesh 150)
(set! k-mesh 150)
(set! k-mesh (- k-mesh 2))

(define x 0)
(define n1 (list (vector3 0 0 0) (vector3 0 0.5 0)))
(define n2 (list (vector3 0.5 0 0) (vector3 0.5 0.5 0)))

(set! n1 (interpolate k-mesh n1))
(set! n2 (interpolate k-mesh n2))

(while (<= x (+ k-mesh 1))(set! k-points (append k-points
(interpolate k-mesh (list (list-ref n1 x)
(list-ref n2 x)))))(set! x (+ x 1)))

(define-param si 3.464)
(define-param r1 0.35)
(define-param r2 0.3)
(define-param ehole1 1.0)
(define-param ehole2 1.0)
(set! default-material (make dielectric (index si)))

(set! geometry (list (make cylinder
                        (center 0) (material (make dielectric
(index ehole1)))
                   (radius r1) (height infinity))
                 (make cylinder
                        (center 0 1) (material (make dielectric
                   (index ehole2 ))) (radius r2) (height
infinity))))


(set! resolution 64)

(if (= kz 0)
    (begin
      (run-te
       ) )
    (run))
```

```
% y-direction band contours

(set! num-bands 4)

(set! geometry-lattice (make lattice (size 1 2 no-size)))

(define-param kz 0)
(define-param k-mesh 150)
(set! k-mesh 150)
(set! k-mesh (- k-mesh 2))

(define x 0)
(define n1 (list (vector3 0 0 0) (vector3 0.5 0 0)))
(define n2 (list (vector3 0 0.5 0) (vector3 0.5 0.5 0)))

(set! n1 (interpolate k-mesh n1))
(set! n2 (interpolate k-mesh n2))

(while (<= x (+ k-mesh 1))(set! k-points (append k-points
(interpolate k-mesh (list (list-ref n1 x)
(list-ref n2 x)))))(set! x (+ x 1)))

(define-param si 3.464)
(define-param r1 0.35)
(define-param r2 0.3)
(define-param ehole1 1.0)
(define-param ehole2 1.0)
(set! default-material (make dielectric (index si)))

(set! geometry (list (make cylinder
                       (center 0) (material (make dielectric
(index ehole1)))
                  (radius r1) (height infinity))
                (make cylinder
                       (center 0 1) (material (make dielectric
                  (index ehole2 ))) (radius r2) (height
infinity))))


(set! resolution 64)

(if (= kz 0)
    (begin
      (run-te
       ) )
    (run))
```

Appendix B: Sample MEEP Code to Generate An Effective 3D Index

```
;Test to compute effective index
; on Si slab waveguide structure  6/16/10
;  Here the PLZT is on index 2.598 biased

(set! geometry-lattice (make lattice (size 1 1 7)))

(set! geometry
       (list (make block (center 0 0 0) (size infinity infinity
0.5)
               (material (make dielectric (index 2.598))))))


(set-param! resolution 20)

(set! pml-layers (list (make pml (direction Z) (thickness
1.25))))

(define-param fcen 0.375) ; pulse center frequency
(define-param df 1.0) ; pulse freq. width: large df = short
impulse

(set! sources (list
             (make source
            (src (make gaussian-src (frequency fcen) (fwidth
df)))
            (component Hz) (center 0.123 0.234 0.123))))


(define Gamma (vector3 0 0 0))
(define X (vector3 1.5 0 0))

(define-param k-interp 33) ; # k-points to interpolate, otherwise

(run-sources+ 300
  (after-sources (harminv Hz (vector3 0.123 0.234 0.123) fcen
df)))


(run-k-points 500 (interpolate k-interp (list Gamma X)))
```

Appendix C: Matlab Code for Producing Dispersion Contours and Refraction Plots

```
% Matlab program used to plot x-y dispersion contours using MPB data
% from 2D photonic crystal simulations
% 3p band (column 9)

clear
clc
close

% Set contour frequency of interest

cf = [.259];
cfx=[0;.5];
[r s]=size(cf);

% Import data matrix, strip out first column (freqs: string) and first
% row using excel so matrix is all numerical first, .csv file

% Do the gamma-x to y-m direction lines first

kxpoints = 150;
matrix1=dlmread('sqrsl_dispcont_150x_20nmtio2_te.csv');
[m1,n1]=size(matrix1);
m=m1/kxpoints;
n=.5/(m-1);
ansxmatrix1=[];
ansymatrix1=[];
xmatrix1=[];
ymatrix1=[];

% Use instersections function to find crossings for x lines

for q=1:s
    rowcount=1;
    for p=1:m
        xmatrix1=matrix1(rowcount:rowcount+kxpoints-1,2);
        ymatrix1=matrix1(rowcount:rowcount+kxpoints-1,9);
        temp1=intersections(xmatrix1,ymatrix1,cfx,[cf(q);cf(q)]);
        ansxmatrix1=[ansxmatrix1;temp1];
        ansymatrix1=[ansymatrix1;.5*n*(p-1)*ones(size(temp1))];
        rowcount=rowcount+kxpoints;
    end
end

% Do the gamma-y to x-m directions second

kypoints = 150;
matrix2=dlmread('sqrsl_dispcont_150y_20nmtio2_te.csv');
[m2,n2]=size(matrix2);
t=m2/kypoints;
u=.5/(t-1);
```

```
ansxmatrix2=[];
ansymatrix2=[];
xmatrix2=[];
ymatrix2=[];

% Use instersections function to find crossings for y lines

for v=1:s
    rowcount=1;
    for w=1:t
        xmatrix2=matrix2(rowcount:rowcount+kypoints-1,3);
        ymatrix2=matrix2(rowcount:rowcount+kypoints-1,9);
        temp2=intersections(xmatrix2,ymatrix2,cfx,[cf(v);cf(v)]);
        ansymatrix2=[ansymatrix2;.5*temp2];
        ansxmatrix2=[ansxmatrix2;u*(w-1)*ones(size(temp2))];
        rowcount=rowcount+kypoints;
    end
end

% Plot the results in a scatter plot (not joined)

%scatter(ansxmatrix1,ansymatrix1,'.')
%axis equal
%axis([0 .5 0 .2885])
%box on
%hold on
%scatter(ansxmatrix2,ansymatrix2,'.')
%hold off

% Post processing

ansxmatrix3=[ansxmatrix1;ansxmatrix2];
ansymatrix3=[ansymatrix1;ansymatrix2];
startindex=find(ansymatrix3>.2485);
ansxmatrix4=ansxmatrix3(startindex);
ansymatrix4=ansymatrix3(startindex);
ansxmatrix5=ansxmatrix3;
ansymatrix5=ansymatrix3;
ansxmatrix5(startindex)=[];
ansymatrix5(startindex)=[];

% Use for aa=1:size(ansxmatrix3)-1 to start, then find cuttoff point

for aa=1:62
    bb=1;
    for bb=1:size(ansxmatrix5)
        distxmatrix1(bb)=(ansxmatrix4(aa)-ansxmatrix5(bb))^2;
        distymatrix1(bb)=(ansymatrix4(aa)-ansymatrix5(bb))^2;
        distmatrix1(bb)=sqrt(distxmatrix1(bb)+distymatrix1(bb));
    end
    [cc,dd]=min(distmatrix1);
    ansxmatrix4(aa+1)=ansxmatrix5(dd);
    ansymatrix4(aa+1)=ansymatrix5(dd);
    ansxmatrix5(dd)=[];
    ansymatrix5(dd)=[];
```

```
    distxmatrix1=[];
    distymatrix1=[];
    distmatrix1=[];
end

ansxmatrix4=ansxmatrix4.';
ansymatrix4=ansymatrix4.';
plot(ansxmatrix4,ansymatrix4)
axis equal
axis([0 .5 0 .25])
box on

% Incorporate rotation angle to plot four sections and put in new
matrix

quad3x=ansxmatrix4(1:62)-.5;
quad3y=ansymatrix4(1:62)-.25;
%quad3x=ansxmatrix4-.5;
%quad3y=ansymatrix4-.25;
quad4xtemp=-quad3x;
quad4ytemp=quad3y;
quad4x=quad4xtemp(end:-1:1);
quad4y=quad4ytemp(end:-1:1);
ansxmatrix6=[quad3x;quad4x];
ansymatrix6=[quad3y;quad4y];
quad12=rotation([ansxmatrix6,ansymatrix6],[0,0],180);
quad12x=quad12(:,1);
quad12y=quad12(:,2);
ansxmatrix7=[ansxmatrix6;quad12x];
ansymatrix7=[ansymatrix6;quad12y];
ansmatrix8=rotation([ansxmatrix7,ansymatrix7],[0,0],63.435);
ansxmatrix8=ansmatrix8(:,1);
ansymatrix8=ansmatrix8(:,2);

plot(ansxmatrix8,ansymatrix8,'.')
axis equal
box on

% Incorporate rotation angle to plot four sections and put in new
matrix

quad3x=ansxmatrix4(1:60)-.5;
quad3y=ansymatrix4(1:60)-.25;
%quad3x=ansxmatrix4-.5;
%quad3y=ansymatrix4-.25;
quad2xtemp=quad3x;
quad2ytemp=-quad3y;
quad2x=quad2xtemp(end:-1:1);
quad2y=quad2ytemp(end:-1:1);
ansxmatrix6=[quad2x;quad3x];
ansymatrix6=[quad2y;quad3y];
quad12=rotation([ansxmatrix6,ansymatrix6],[0,0],63.435);
quad12x=quad12(:,1);
quad12y=quad12(:,2);
%ansxmatrix7=[ansxmatrix6;quad12x];
%ansymatrix7=[ansymatrix6;quad12y];
```

```
%ansmatrix8=rotation([ansxmatrix7,ansymatrix7],[0,0],63.435);
ansxmatrix8=quad12x;
ansymatrix8=quad12y;


plot(ansxmatrix8,ansymatrix8,'.')
axis equal
box on


[a1,b1]=size(ansxmatrix8);

for a=1:a1-1
    slopematrix1(a,1)=(ansymatrix8(a+1,1)-
ansymatrix8(a,1))/(ansxmatrix8(a+1,1)-ansxmatrix8(a,1));
end

index1=1;
thetai=(index1*asin(ansxmatrix8)/cf(1,1))*180/pi;
thetar=atan(slopematrix1)*180/pi;
thetai(end,:)=[];


% Plot the results in a scatter plot (not joined)

plot(thetai,thetar,'.')
```

References

[1] S. John, "Strong localization of photons in certain disordered dielectric superlattices," *Physical Review Letters,* vol. 58, pp. 2486-9, 1987.

[2] E. Yablonovitch, "Inhibited spontaneous emission in solid-state physics and electronics," *Physical Review Letters,* vol. 58, pp. 2059-62, 1987.

[3] K. M. Ho, C. T. Chan, and C. M. Soukoulis, "Existence of a photonic gap in periodic dielectric structures," *Physical Review Letters,* vol. 65, pp. 3152-3155, 1990.

[4] E. Yablonovitch, T. J. Gmitter, and K. M. Leung, "Photonic band structure: the face-centered-cubic case employing nonspherical atoms," *Physical Review Letters,* vol. 67, pp. 2295-8, 1991.

[5] E. Yablonovitch, T. J. Gmitter, R. D. Meade, A. M. Rappe, K. D. Brommer, and J. D. Joannopoulos, "Donor and acceptor modes in photonic band structure," *Physical Review Letters,* vol. 67, pp. 3380-3383, 1991.

[6] J. B. Pendry and A. MacKinnon, "Calculation of photon dispersion relations," *Physical Review Letters,* vol. 69, pp. 2772-2775, 1992.

[7] J.-K. Hwang, H.-Y. Ryu, D.-S. Song, I.-Y. Han, H.-W. Song, H.-K. Park, Y.-H. Lee, and D.-H. Jang, "Room-temperature triangular-lattice two-dimensional photonic band gap lasers operating at 1.54 μm," *Applied Physics Letters,* vol. 76, p. 2982, 2000.

[8] O. Painter, R. K. Lee, A. Scherer, A. Yariv, J. D. O'Brien, P. D. Dapkus, and I. Kim, "Two-dimensional photonic band-gap defect mode laser," *Science,* vol. 284, pp. 1819-1821, 1999.

[9] T. Baba, N. Fukaya, and J. Yonekura, "Observation of light propagation in photonic crystal optical waveguides with bends," *Electronics Letters,* vol. 35, pp. 654-655, 1999.

[10] A. Chutinan and S. Noda, "Waveguides and waveguide bends in two-dimensional photonic crystal slabs," *Physical Review B (Condensed Matter),* vol. 62, pp. 4488-92, 2000.

[11] A. Yariv, Y. Xu, R. K. Lee, and A. Scherer, "Coupled-resonator optical waveguide: A proposal and analysis," *Optics Letters,* vol. 24, pp. 711-713, 1999.

[12] T. A. Birks, J. C. Knight, and P. St. J. Russell, "Endlessly single-mode photonic crystal fiber," *Optics Letters,* vol. 22, pp. 961-963, 1997.

[13] R. F. Cregan, B. J. Mangan, J. C. Knight, T. A. Birks, P. S. J. Russell, P. J. Roberts, and D. C. Allan, "Size-mode photonic band gap guidance of light in air," *Science,* vol. 285, pp. 1537-9, 1999.

[14] H. Miguez, C. Lopez, F. Meseguer, A. Blanco, L. Vazquez, R. Mayoral, M. Ocana, V. Fornes, and A. Mifsud, "Photonic crystal properties of packed submicrometric SiO₂ spheres," *Applied Physics Letters,* vol. 71, pp. 1148-50, 1997.

[15] S. G. Romanov, A. V. Fokin, V. V. Tretijakov, V. Y. Butko, V. I. Alperovich, N. P. Johnson, and C. M. Sotomayor Torres, "Optical properties of ordered three-dimensional arrays of structurally confined semiconductors," *Journal of Crystal Growth,* vol. 159, pp. 857-860, 1996.

[16] Y. A. Vlasov, X. Z. Bo, J. C. Sturm, and D. J. Norris, "On-chip natural assembly of silicon photonic bandgap crystals," *Nature,* vol. 414, pp. 289-293, 2001.
[17] J. E. G. J. Wijnhoven and W. L. Vos, "Preparation of photonic crystals made of air spheres in titania," *Science,* vol. 281, pp. 802-4, 1998.
[18] K. Yoshino, K. Tada, M. Ozaki, A. A. Zakhidov, and R. H. Baughman, "The optical properties of porous opal crystals infiltrated with organic molecules," *Japanese Journal of Applied Physics, Part 2 (Letters),* vol. 36, pp. 714-17, 1997.
[19] H. T. Miyazaki, H. Miyazaki, K. Ohtaka, and T. Sato, "Photonic band in two-dimensional lattices of micrometer-sized spheres mechanically arranged under a scanning electron microscope," *Journal of Applied Physics,* vol. 87, pp. 7152-8, 2000.
[20] M. Campbell, D. N. Sharp, M. T. Harrison, R. G. Denning, and A. J. Turberfield, "Fabrication of photonic crystals for the visible spectrum by holographic lithography," *Nature,* vol. 404, pp. 53-6, 2000.
[21] S. Shoji and S. Kawata, "Photofabrication of three-dimensional photonic crystals by multibeam laser interference into a photopolymerizable resin," *Applied Physics Letters,* vol. 76, pp. 2668-2670, 2000.
[22] H.-B. Sun, S. Matsuo, and H. Misawa, "Three-dimensional photonic crystal structures achieved with two-photon-absorption photopolymerization of resin," *Applied Physics Letters,* vol. 74, pp. 786-788, 1999.
[23] O. Toader and S. John, "Proposed square spiral microfabrication architecture for large three-dimensional photonic band gap crystals," *Science,* vol. 292, pp. 1133-1135, 2001.
[24] L. P. Biro, Z. Balint, K. Kertesz, Z. Vertesy, G. I. Mark, Z. E. Horvath, J. Balazs, D. Mehn, I. Kiricsi, V. Lousse, and J. P. Vigneron, "Role of photonic-crystal-type structures in the thermal regulation of a Lycaenid butterfly sister species pair," *Physical Review E,* vol. 67, pp. 21907-1, 2003.
[25] K. Kertesz, Z. Balint, Z. Vertesy, G. I. Mark, V. Lousse, J. P. Vigneron, M. Rassart, and L. P. Biro, "Gleaming and dull surface textures from photonic-crystal-type nanostructures in the butterfly cyanophrys remus," *Physical Review E (Statistical, Nonlinear, and Soft Matter Physics),* vol. 74, pp. 21922-1, 2006.
[26] R. O. Prum, R. H. Torres, S. Williamson, and J. Dyck, "Coherent light scattering by blue feather barbs," *Nature,* vol. 396, p. 28, 1998.
[27] P. Vukusic and J. R. Sambles, "Photonic structures in biology," *Nature,* vol. 424, pp. 852-855, 2003.
[28] J. P. Vigneron, M. Rassart, C. Vandenbem, V. Lousse, O. Deparis, L. P. Biro, D. Dedouaire, A. Cornet, and P. Defrance, "Spectral filtering of visible light by the cuticle of metallic woodboring beetles and microfabrication of a matching bioinspired material," *Physical Review E - Statistical, Nonlinear, and Soft Matter Physics,* vol. 73, p. 041905, 2006.
[29] I. R. Hooper, P. Vukusic, and R. J. Wootton, "Detailed optical study of the transparent wing membranes of the dragonfly Aeshna cyanea," *Optics Express,* vol. 14, pp. 4891-4897, 2006.
[30] T. Fuhrmann, S. Landwehr, M. El Rharbi-Kucki, and M. Sumper, "Diatoms as living photonic crystals," *Applied Physics B (Lasers and Optics),* vol. B78, pp. 257-60, 2004.

[31] L. P. Biro, K. Kertesz, Z. Balint, Z. Vertesy, G. I. Mark, V. Lousse, and J. P. Vigneron, "Photonic crystal type structures of biological origin: Structural and spectral characterization," *Current Applied Physics,* vol. 6, pp. 252-8, 2006.
[32] J. P. Vigneron, M. Rassart, Z. Vertesy, K. Kertesz, M. Sarrazin, L. P. Biro, D. Ertz, and V. Lousse, "Optical structure and function of the white filamentary hair covering the edelweiss bracts," *Physical Review E - Statistical, Nonlinear, and Soft Matter Physics,* vol. 71, p. 011906, 2005.
[33] L. P. Lee and R. Szema, "Inspirations from biological optics for advanced photonic systems," *Science,* vol. 310, pp. 1148-50, 2005.
[34] R. C. McPhedran, N. A. Nicorovici, D. R. McKenzie, G. W. Rouse, L. C. Botten, V. Welch, A. P. Parker, M. Wohlgennant, and V. Vardeny, "Structural colours through photonic crystals," Snowbird, UT, USA, 2003, pp. 182-5.
[35] A. P. Sommer and M. Gente, "Biomimetics: From teeth to photonic crystal solar light collectors," *Energy and Fuels,* vol. 20, pp. 2189-2191, 2006.
[36] S. Noda and T. Baba, *Roadmap on photonic crystals*: Dordrecht ; Boston : Kluwer Academic Publishers, 2003.
[37] K. Sakoda, *Optical properties of photonic crystals*, 2nd ed.: Berlin ; New York : Springer, 2005.
[38] T. Yamashita, "Unraveling Photonic Bands: Characterization of Self-Collimation Effects in Two Dimensional Crystals," PhD, Material Science and Engineering, Georgia Institute of Technology, Atlanta, 2005.
[39] C. Neff, "Optical Properties of Superlattice Photonic Crystals," PhD, Materials Science and Engineering, Georgia Institute of Technology, Atlanta, 2005.
[40] J. Li and J. B. Pendry, "Hiding under the carpet: A new strategy for cloaking," *Physical Review Letters,* vol. 101, 2008.
[41] R. D. M. John D. Joannopoulos, Joshua N. Winn., *Photonic crystals : molding the flow of light*: Princeton, N.J. : Princeton University Press, 1995.
[42] C. Kittel, *Introduction to solid state physics*, 8th ed. ed.: Hoboken, NJ : Wiley, 2005.
[43] K. S. Yee, "Numerical solution of initial boundary value problems involving Maxwell's equations in isotropic media," *IEEE Transactions on Antennas and Propagation,* vol. AP-14, pp. 302-307, 1966.
[44] M. Ritala, M. Leskela, J.-P. Dekker, C. Mutsaers, P. J. Soininen, and J. Skarp, "Perfectly conformal TiN and Al2O3 films deposited by atomic layer deposition," *Chemical Vapor Deposition,* vol. 5, pp. 7-9, 1999.
[45] W. a. S. Park, C.J, ""Tunable 2D photonic crystal slabs exhibiting extraordinary refraction and dispersion."," presented at the The Fourth International Workshop on Photonic and Electromagnetic Crystal Structures, 2002.
[46] B. D. a. S. Cullity, S.R., *Elements of X-Ray Diffraction*, 3rd ed.: Prentice Hall, 2001.
[47] C. Kittel, *Introduction to Solid State Physics*, 7th ed., 1996.
[48] J. P. Dowling and C. M. Bowden, "Anomalous index of refraction in photonic bandgap materials," *Journal of Modern Optics,* vol. 41, pp. 345-51, 1994.
[49] P. S. J. Russell and T. A. Birks, *Block wave optics in photonic crystals: physics and applications*: Kluwer Academic Publishers, 1996.

[50] S.-Y. Lin, V. M. Hietala, L. Wang, and E. D. Jones, "Highly dispersive photonic band-gap prism," *Optics Letters,* vol. 21, pp. 1771-1771, 1996.
[51] H. Kosaka, T. Kawashima, A. Tomita, M. Notomi, T. Tamamura, T. Sato, and S. Kawakami, "Superprism phenomena in photonic crystals: Toward microscale lightwave circuits," *Journal of Lightwave Technology,* vol. 17, pp. 2032-2038, 1999.
[52] M. Notomi, "Negative refraction in photonic crystals," *Optical and Quantum Electronics,* vol. 34, pp. 133-143, 2002.
[53] W. Park and C. J. Summers, "Extraordinary refraction and dispersion in two-dimensional photonic-crystal slabs," *Optics Letters,* vol. 27, pp. 1397-1399, 2002.
[54] C. W. Neff and C. J. Summers, "Photonic crystal superlattices in electro-optic slab waveguides," Denver, CO, United States, 2004, pp. 104-111.
[55] C. W. Neff and C. J. Summers, "A photonic crystal superlattice based on triangular lattice," *Optics Express,* vol. 13, 2005.
[56] D. P. Gaillot, E. Graugnard, J. Blair, and C. J. Summers, "Dispersion control in two-dimensional superlattice photonic crystal slab waveguides by atomic layer deposition," *Applied Physics Letters,* vol. 91, 2007.
[57] K. Busch and S. John, "Liquid-crystal photonic-band-gap materials: The tunable electromagnetic vacuum," *Physical Review Letters,* vol. 83, pp. 967-970, 1999.
[58] S. W. Leonard, J. P. Mondia, H. M. Van Driel, O. Toader, S. John, K. Busch, A. Bimer, U. Gosele, and V. Lehmann, "Tunable two-dimensional photonic crystals using liquid-crystal infiltration," *Physical Review B (Condensed Matter),* vol. 61, pp. 2389-92, 2000.
[59] W. Park, J. S. King, C. W. Neff, C. Liddell, and C. J. Summers, "ZnS-based photonic crystals," *Physica Status Solidi B,* vol. 229, pp. 949-60, 2002.
[60] D. Scrymgeour, N. Malkova, S. Kim, and V. Gopalan, "Electro-optic control of the superprism effect in photonic crystals," *Applied Physics Letters,* vol. 82, pp. 3176-3178, 2003.
[61] S. Xiong and H. Fukshima, "Analysis of light propagation in index-tunable photonic crystals," *Journal of Applied Physics,* vol. 94, pp. 1286-1288, 2003.
[62] K. Yoshino, Y. Shimoda, Y. Kawagishi, K. Nakayama, and M. Ozaki, "Temperature tuning of the stop band in transmission spectra of liquid-crystal infiltrated synthetic opal as tunable photonic crystal," *Applied Physics Letters,* vol. 75, pp. 932-934, 1999.
[63] W. Park and J. B. Lee, "Mechanically tunable photonic crystals," *Optics & Photonics News,* vol. 20, pp. 40-5, 2009.
[64] K. Yoshino, Y. Kawagishi, M. Ozaki, and A. Kose, "Mechanical tuning of the optical properties of plastic opal as a photonic crystal," *Japanese Journal of Applied Physics, Part 2: Letters,* vol. 38, pp. L786-L788, 1999.
[65] S. W. Leonard, J. P. Mondia, H. M. Van Driel, O. Toader, S. John, K. Busch, A. Bimer, U. Gosele, and V. Lehmann, "Tunable two-dimensional photonic crystals using liquid-crystal infiltration," *Physical Review B (Condensed Matter),* vol. 61, pp. 2389-92, 2000.
[66] J. B. Pendry, D. Schurig, and D. R. Smith, "Controlling electromagnetic fields," *Science,* vol. 312, pp. 1780-1782, 2006.

[67] D. Schurig, J. B. Pendry, and D. R. Smith, "Calculation of material properties and ray tracing in transformation media," *Optics Express,* vol. 14, 2006.
[68] D. Schurig, J. J. Mock, B. J. Justice, S. A. Cummer, J. B. Pendry, A. F. Starr, and D. R. Smith, "Metamaterial electromagnetic cloak at microwave frequencies," *Science,* vol. 314, pp. 977-80, 2006.
[69] D. R. Smith, J. B. Pendry, and M. C. K. Wiltshire, "Metamaterials and negative refractive index," *Science,* vol. 305, pp. 788-792, 2004.
[70] D. R. Smith, W. J. Padilla, D. C. Vier, S. C. Nemat-Nasser, and S. Schultz, "Composite medium with simultaneously negative permeability and permittivity," *Physical Review Letters,* vol. 84, pp. 4184-4184, 2000.
[71] R. Liu, C. Ji, J. J. Mock, J. Y. Chin, T. J. Cui, and D. R. Smith, "Broadband ground-plane cloak," *Science,* vol. 323, pp. 366-9, 2009.
[72] J. H. Lee, J. Blair, V. A. Tamma, Q. Wu, S. J. Rhee, C. J. Summers, and W. Park, "Direct visualization of optical frequency invisibility cloak based on silicon nanorod array," *Opt. Express,* vol. 17, pp. 12922-12928, 2009.
[73] J. B. V. A. Tamma, J. H. Lee, Q. Wu, S. J. Rhee, C. J. Summers and W. Park, "Near-Infrared Ground Plane Cloak Based on Silicon Nanorod Array," in *Frontiers in Optics 2009: The Optical Society of America Annual Meeting*, San Jose, CA, Oct. 11-15, 2009.
[74] L. H. Gabrielli, J. Cardenas, C. B. Poitras, and M. Lipson, "Silicon nanostructure cloak operating at optical frequencies," *Nat Photon,* vol. 3, pp. 461-463, 2009.
[75] J. Valentine, J. Li, T. Zentgraf, G. Bartal, and X. Zhang, "An optical cloak made of dielectrics," *Nature Materials,* vol. 8, pp. 568-571, 2009.
[76] N. Liu, H. Guo, L. Fu, S. Kaiser, H. Schweizer, and H. Giessen, "Three-dimensional photonic metamaterials at optical frequencies," *Nature Materials,* vol. 7, pp. 31-37, 2008.